TECHNISCHE UNIVERSITÄT WIEN
Vienna University of Technology
Technische Universität Wien

# Investigations and technology developments for a final cooling scheme in muon colliders

**Doktorarbeit**

Ausgeführt am Atominstitut
der Fakultät für Physik
an der Technischen Universität Wien,
in Zusammenarbeit mit der
Europäischen Organisation für Kernphysik.

Durchgefürt von
**Bernd Stechauner**

Unter der Anleitung von

Univ.Prof. Dipl.-Phys. Dr.rer.nat. Jochen Schieck, und
Dipl.-Phys. Dr.rer.nat. Daniel Schulte

Bernd Stechauner
Matrikelnummer: 1426914
Großau, am 11. September 2025

# Abstract

This thesis investigates the beam dynamics of the final cooling stage in a multi-TeV muon collider, where ionization cooling reduces the normalized transverse emittance to its target value. Achieving this enables the collider to reach peak luminosities necessary for precision studies of the Higgs boson, leptonic parton distribution functions, and other fundamental phenomena. As a transformative tool for high-energy physics, the muon collider drives advancements in accelerator technologies.

Ionization cooling is a fast-acting technique that reduces muon beam emittance within the muons' short lifetime, primarily through interactions with material combined with high-field solenoids. This work incorporates a semi-Gaussian scattering model, parameterized with the Bethe-Wentzel model, into the RF-Track code. The implementation is compared to established tracking software, which confirms the suitability of RF-Track to simulate ionization cooling and allows future studies of collective beam effects.

The Bethe-Wentzel model is further useful for the analytic evolution of the transverse emittance reduction, showing unprecedented agreement with the simulation. This innovation allows optimizing initial beam parameters in final cooling cells without relying on time-intensive macro-particle simulations. Furthermore, an analytical calculation for energy deposition estimates pressure increases in hydrogen absorbers, revealing that earlier assumptions underestimated the pressure increase within hydrogen. A new design with density-adjusted liquid and vapor hydrogen is proposed to mitigate excessive pressure buildup.

A critical contribution of this thesis is the development of an adiabatic ramping method to match the beam to a 40 T solenoid. This ensures smooth beam transport from low-field to high-field solenoids incorporated with hydrogen. A refined RF-solenoid beamline layout is introduced, improving compactness and realism over previous designs. The proposed final cooling lattice comprises nine uniquely configured cells, each with adjusted hydrogen properties and beam windows, offering a more practical and effective solution of the final cooling in a muon collider.

# Kurzfassung der Dissertation

In dieser Arbeit wird die Strahldynamik in der letzten Kühlphase einer hoch energetischen Myonen-Kollisionsmaschine untersucht, indem die Ionisationskühlung die normalisierte transversale Emittanz auf den Zielwert reduziert wird. Dadurch kann der Kollisionsbeschleuniger maximale Luminositäten erreichen, die für Präzisionsstudien des Higgs-Bosons, leptonischer Partonverteilungsfunktionen und anderer fundamentaler Phänomene erforderlich sind. Als bahnbrechendes Werkzeug für die Hochenergiephysik treibt die Kollisionsmaschine mit Myonen die Weiterentwicklung der Beschleunigertechnologien voran.

Die Ionisationskühlung ist eine schnell wirkende Technik, die die Emittanz von Myonenstrahlen innerhalb ihrer kurzen Lebensdauer vor allem durch Wechselwirkungen mit Material reduziert. In dieser Arbeit wird ein Semigaußsches Streumodell, parametrisiert mit dem Bethe-Wentzel-Modell, in das RF-Track Programm integriert. Die Implementierung wird mit etablierter Software verglichen, was die Eignung von RF-Track zur Simulation der Ionisationskühlung bestätigt und künftige Studien über kollektive Strahleffekte ermöglicht.

Das Bethe-Wentzel-Modell wird außerdem für analytische Rechnungen zur transversalen Emittanzverringerung verwendet, wie eine beispiellose Übereinstimmung mit der Simulation zeigt. Diese Innovation ermöglicht die Optimierung der anfänglichen Strahlenparameter in den Zellen des finalen Kühlens, ohne auf zeitintensive Makroteilchensimulationen angewiesen zu sein. Darüber hinaus schätzt dieses analytische Modell für die Energiedeposition den Druckanstieg in Wasserstoffabsorbern, wobei sich herausstellt, dass frühere Annahmen den Druckanstieg im Wasserstoff nicht berücksichtigt haben. Es wird ein neues Design mit dichteangepasstem Wasserstoff vorgeschlagen, um einen materialschädigenden Druckanstieg zu vermeiden.

Ein entscheidender Beitrag dieser Arbeit ist die Entwicklung einer adiabatischen Hochfahr-Methode zur Strahlanpassung an ein 40 T starkes Solenoid mit Wasserstoff. Dadurch wird ein angepasster Strahltransport von Solenoiden mit niedrigen in hohe Felder gewährleistet. Es wird ein verfeinertes Sytem aus RF-Kavitäten und Solenoiden eingeführt, das die Kompaktheit und Realitätsnähe gegenüber früheren Designs verbessert. Das vorgeschlagene Endkühlungsdesign umfasst neun konfigurierte Zellen, jede mit angepassten Dichten des Wasserstoffes mit inkludierten Strahlfenstern, und bietet eine praktischere und effektivere Lösung für das final Myonenkühlen.

# Declaration

In lieu of oath, I declare that I wrote this thesis and carried out the associated research myself, using only the literature cited in this volume. If text passages from sources are used literally, they are marked as such. I confirm that this work is original and has not been submitted for examination elsewhere nor is it currently under consideration for a thesis elsewhere.

Several studies and results presented in Chapters 2 to 4 have already been published. A summary of these references is given below.

**Chapter 2:** R. Capdevilla, F. Garosi, D. Marzocca and B. Stechauner, *"Testing the neutrino content of the muon at muon colliders"*, J. High Energ. Phys. 2025, 168 (2025), https://doi.org/10.1007/JHEP04(2025)168

**Chapter 3:** B. Stechauner, J. A. Ferreira Somoza, E. Fol, C. Rogers, J. Schieck and D. Schulte, *"Thermodynamic characteristics of hydrogen in an ionization cooling channel for muon colliders"*, JACoW IPAC, Venice, 2023, https://cds.cern.ch/record/2884555

B. Stechauner, E. Fol, A. Latins, C. Rogers, J. Schieck and D. Schulte, *"Comparison of tracking codes for beam-matter interaction"*,JACoW IPAC, Venice, 2023, https://cds.cern.ch/record/2889399.

B. Stechauner, R. Frühwirth, A. Latina, J. Schieck and D. Schulte, *"Introducing a semi-Gaussian mixture model for simulating multiple Coulomb scattering in RF-track"*, JACoW IPAC, Nashville, 2024,
https://doi.org/10.18429/JACoW-IPAC2024-WEPR31.

**Chapter 4:** B. Stechauner, E. Fol, C. Rogers, J. Schieck and D. Schulte, *"Searching for the best initial beam parameters for efficient muon ionization cooling"*, JACoW IPAC, Nashville, 2024, https://cds.cern.ch/record/2913551.

Signature, Bernd Stechauner:

# Funding Acknowledgment

The work presented in this thesis was made possible through the generous support of several funding sources:

- The majority of the funding was provided by the **CERN - Austrian Doctoral Student Program**, supported by the *österreichisches Bundesministerium für Wissenschaft und Forschung* (Austrian Federal Ministry of Science and Research).
- Additional support was received from the **International Muon Collider Collaboration (IMCC)**.
- This research also benefited from funding through the **MuCol Project**, which is *co-funded by the European Union*.
- Further support was provided for **PhD student participation in conferences and related scientific events** from the TU Wien.

I gratefully acknowledge all these contributions, without which this work would not have been possible.

# Acknowledgment

First and foremost I am grateful to my CERN supervisor, **Dr. Daniel Schulte**, whose mentorship shaped my path to accelerator physics. His vast experience, admirable dedication, and steady guidance were instrumental in my development as a scientist. The collaboration between his direction and my own innovative contributions helped me grow into the researcher I am today. I am truly grateful for the opportunity to learn from him.

I also deeply appreciate my university supervisor, **Prof. Jochen Schieck**, for his continuous support, patience, and the time he always took to listen to me. Our conversations, especially during our moments together in Restaurant 1 at CERN, were more than just enjoyable—they provided me with valuable insights into scientific management and the broader world of research leadership. I learned a lot from him, both professionally and personally.

I am grateful to **Dr. Chris Rogers** for his invaluable support. His expertise in muon cooling and the July 2024 visit to his institute were pivotal for my understanding of beam dynamics in solenoids. I owe thanks to **Dr. Rebecca Taylor** for joining the cooling team; her clarity and support were critical during my intense work, making her not only a colleague, but a friend. I also thank **Dr. Helmut Eberl** for nurturing my interest in theoretical physics, guiding my problem solving with patience. His knowledge of particle physics inspired and motivated my research towards a future muon collider.

I sincerely thank my colleagues and friends at CERN and in the Muon Collider Collaboration for their camaraderie. Special thanks to **Dr. Andrea Latina** for introducing me to computational programming, **Dr. Christian Carli** for insightful discussions on accelerator physics during coffee breaks. I would also like to thank my colleague and friend **Dr. Jacqueline Keintzel** for our pleasant lunch conversations, and **Daniele Calzolari**, my flatmate, for the stimulating discussions about the future of collider physics.

I would like to express my heartfelt gratitude to my **parents** for their unwavering support throughout my university years. I am also very grateful to my siblings, **Martin, Babsi, and Clarissa**, for always being there for me. A very special thank you goes to **Laura**, whose steadfast support and encouragement carried me through the highs and lows of this journey. I am grateful and happy that she is by my side as I look forward to new and exciting journeys in the future.

*To my grandfather, Alfred Stechauner,*
*the hero of my childhood.*
*Wherever you may be, I hope you're looking down on me with pride.*

# Contents

# Chapter 1.

# Introduction

The concept of accelerating muons for collision has been considered since the 1960s and 1970s [1–4]. However, because of the short lifespan of the muon, it is imperative to explore innovative acceleration technologies and methodologies. One such technology is a final cooling channel based on muon ionization cooling, i.e. this technology is essential for sufficient luminosity of collision, and ensures a reasonable beam size for downstream components. The beam dynamics and technical aspects of this technology constitute the principal subject of this thesis.

This introduction provides a concise overview of the fundamental questions in physics that remain unresolved and how a muon collider could contribute to elucidating these queries. It will further elaborate on the luminosity of a muon collider and compare it to other prospective collider design concepts. Additionally, a brief overview of the muon collider's design components will be presented. A discussion regarding the feasibility of hosting a muon collider at the CERN site will also be included. Finally, this chapter outlines the structure of this thesis.

## 1.1 The Standard Model's brightness in the dark

Within the field of particle physics, the discovery of the Higgs boson in 2012 [5, 6], at CERN, marked the identification of the final particle within the Standard Model (SM). The SM comprehensively predicts all fundamental forces on the micro-scale, with the notable exception of gravitation. The field associated with the Higgs particle provides the mechanism through which matter particles acquire their mass.

Physicists aim for an all-encompassing and thorough description of nature. Although the list of 25 (26[1]) parameters (particle masses, mixing angles, and couplings) within the SM is seemingly complete, it is far from conclusive. In the SM, a **grand unification** of

[1]Within the framework of Quantum Chromodynamics, there exists a $26^{\text{th}}$ parameter that results in CP violation within the strong interaction; however, its magnitude is exceedingly small [7].

all three micro forces is not acknowledged. The SM can be seen as a building block of a more complete and new theory. This unknown theory has to incorporate the SM or even reproduce it.

Beyond the scope of the SM, numerous scientific phenomena remain poorly understood, and scientists continue their explorations in uncertainty. In particular, the matter particles accounted for by the SM represent a mere 4% of the total composition of the universe [8]. The subsequent sections address several unresolved physical explanations regarding the composition of the universe.

- **Dark matter** has not been directly detected, but its existence is strongly supported by multiple astrophysical observations. Observations of galaxy clusters by F. Zwicky [9] showed that the velocity dispersion of galaxies in the Coma cluster was too high to be explained by visible matter alone. Later, V. Rubin and W. Ford [10] found that the rotation curves of spiral galaxies remained flat at large radii, contradicting expectations from Keplerian motion. These anomalies suggested the presence of an unseen mass component, leading to the hypothesis of dark matter.
- The expansion of the universe has been accelerating since around 5 billion years ago, as revealed by observations of distant supernovae. This acceleration is attributed to dark energy, a mysterious force that counteracts gravity and drives the expansion of the universe to accelerate over time [11, 12].
- The visible universe is predominantly composed of matter, such as particles, with only a minor proportion consisting of antimatter. Upon interaction, matter and antimatter particles undergo annihilation, releasing energy in the form of radiation. It is hypothesized that in the initial moments of the universe, there existed a symmetry between matter and antimatter particles. The reasons behind matter's dominance and the disappearance of antimatter remain unresolved questions, and the mechanism behind that is called **Baryogenesis** [13].
- Although **gravitation** is evident on a large scale (explaining why we remain on Earth's surface), its microscopic origins remain uncertain [14]. The integration of general relativity with fundamental particles, known as quantum gravitation, continues to be an area with untapped experimental discoveries.

The muon collider also provides an optimal environment as an observatory for rare events, as it can detect features in the high-energy sector and can provide precision measurements of these events. One potential avenue for addressing these fundamental questions is in-depth investigation of the Higgs particle. Given that the Higgs boson is responsible for generating masses, it may have a connection to dark-matter particles [15, 16]. Furthermore, some research indicates that the self-coupling of the Higgs boson could be involved in baryogenesis [17]. Further investigation of Higgs and the enhancement of statistical data concerning it form a key strategy in the future of high-energy physics [18]. Lepton colliders are considered the most suitable **Higgs factories** for this purpose.

The subsequent sections outline various types of lepton colliders, with a special focus on **muon colliders**.

## 1.2 Future collider landscape

The **Large Hadron Collider** (**LHC**), situated at CERN near Geneva, Switzerland, stands as the most powerful particle accelerator to date. It conducts collisions of proton $p^+$ bunches, classified as hadrons, reaching center-of-mass (cm) energies exceeding $\sqrt{s} = 13\,\text{TeV}$, successfully detecting the Higgs boson [5, 6]. Although it primarily collides protons, occasionally, the LHC also facilitates collisions involving ions. Plans are underway to enhance the LHC's **luminosity** (HL-LHC) [19], with operations anticipated to commence around the mid-2030s. Luminosity is an indicator of beam brightness in a collider and will be examined in greater detail subsequently.

In principle, the acceleration of hadrons to elevated energy levels can be achieved by expanding the collider-ring infrastructure or through the development of high-field bending magnets. However, given that hadrons are made up of quarks and gluons, the complete cm energy $\sqrt{s}$ is not fully accessible during collisions. This limitation arises because $\sqrt{s}$ is factorized among the constituents of hadrons.

Replacement of hadrons with leptons, which are elementary particles, is an alternative. Positron-Electron ($e^+e^-$) colliders have had successful operation in the past and still operate in present. However, a drawback of electron-like particles is their low mass, which causes them to emit synchrotron radiation when accelerated or bent within ring colliders. To minimize this bending of electrons, one approach is to expand the circumference of the collider's ring structure. Concepts for such **$e^-e^+$-ring colliders**, including the Future Circular Collider (FCC-ee) and the Circular Electron-Positron collider (CEPC), are being explored [20, 21]. These designs plan a collider circumference of $90 - 100\,\text{km}$, operating with a maximum cm energy of $365\,\text{MeV}$. A proposal has been put forward for a reduced version within the current LHC tunnel, identified as the third run of the Large Electron Positron collider (LEP3) [22].

Synchrotron radiation constrains the ability to operate at high energies in $e^-e^+$ ring colliders. To address this, **linear $e^-e^+$ colliders** have been developed as an alternative. These colliders are capable of achieving energies on the TeV scale, as illustrated by the proposed designs for the Compact Linear Collider (CLIC) [23] and the International Linear Collider (ILC) [24]. However, the expense associated with linear colliders increases with their length. Additionally, once the lepton bunch passes the interaction point, it cannot be recycled for another collision.

The benefits of employing $e^+e^-$ colliders are attributed to the small background during collision events. Nevertheless, the feasibility of achieving high-energy collisions is

constrained in ring configurations by synchrotron radiation, and in linear colliders by financial considerations.

## 1.3 What about muons?

Based on the preceding discussion, the optimal collider configuration should encompass:

1. a ring-design collider to facilitate multiple bunch collisions,
2. a high-mass particle to minimize synchrotron radiation,
3. collide fundamental particles, such as leptons.

A muon collider meets these specifications because:

1. The mass of a muon is about 200 times that of an electron. Synchrotron radiation is proportional to $m^{-4}$, with $m$ representing the mass of the particle. That electron-muon mass difference reduces synchrotron radiation by a factor of $1.6 \times 10^9$, making synchrotron radiation negligible in a muon collider.
2. Therefore, a muon collider ring can be compact and the cm energy can be higher compared to $e^-e^+$ ring machines. The ring size and energy are limited by the field strengths of the bending magnets.
3. The muon is a fundamental particle and provides a cleaner background at the interaction point compared to hadron machines. However, the primary challenge is that the muon decays and has a mean lifetime of $\tau_0 = 2.2\,\mu s$ in its rest frame. Consequently, innovative accelerator technologies and concepts need to be developed, and this thesis focuses on one such concept.

In the field of high energy physics, the primary objective is the generation of rare events, the rate of which is quantified in $\sigma \cdot \mathcal{L}_{\text{Lum}}$. The cross section, as detailed in $\sigma$, serves as a measure of the probability of the occurrence of a specific particle interaction, being expressed in units of area. It can be derived through either theoretical or experimental methods. Within collider operations, the luminosity $\mathcal{L}_{\text{Lum}}$ is predominantly dependent on the parameters of the collider apparatus. The luminosity is a measure of the rate of particle collisions per unit of area and time.

The muon collider luminosity for a single collision point can be analytically estimated by

$$\mathcal{L}_{\text{Lum}} = \frac{\gamma^2 \tau_0 c}{2C} \frac{N_0^2}{4\pi\ \varepsilon_{\perp,\text{N}}\ \beta^*} f_{\text{r}}\ F_{\text{h}}\ H_{\text{D}} \tag{1.1}$$

which is more detailed discussed in Appendix A.1 and also in the reference [25]. In case of two interaction points in the collider design, the luminosity is doubled.

In Eq. (1.1), the variable $C$ represents the circumference of the collider ring, while $\beta^*$ refers to the transverse two-dimensional betatron function[2] at the interaction point and $\gamma$ is the Lorentz factor. The number of muons per bunch at the time of injection is labeled as $N_0$ in Eq. (1.1), and $f_r$ stands for the repetition rate[3]. The normalized transverse emittance $\varepsilon_{\perp,N}$ in Eq. (1.1) signifies the phase-space area of the particles in the bunch, which must be minimized to achieve higher luminosities. Mastering $\varepsilon_{\perp,N}$ requires a specialized technique in accelerator physics, which forms the core subject of this work. Furthermore, Eq. (1.1) includes the hourglass effect $F_h$, approximately valued at 0.75 for the muon collider, with more details provided in Appendix A.2. The parameter $H_D$ is an enhancement factor, elaborated in Appendix A.3. Reference [26] provides a summary of the luminosity in a muon collider in relation to the beam-beam interactions by means of numerical evaluations.

The proposed design for a muon collider as presented in [25] indicates an initial phase of operation at $\sqrt{s} = 3\,\text{TeV}$, followed by an upgraded phase at $\sqrt{s} = 10\,\text{TeV}$. Drawing upon the target parameters outlined in [27] and substitute them into Eq. (1.1), the estimated luminosity of the muon collider is approximately:

| $\sqrt{s}$ [TeV] | $\mathcal{L}_{\text{Lum}} \times 10^{34}$ [$\text{cm}^{-2}\,\text{s}^{-1}$] |
|---|---|
| 3 | 2.0 |
| 10 | 21.5 |

Figure 1.1 presents a comparative analysis of the luminosities of muon colliders versus those of alternative prospective collider design concepts. Muon colliders at 3 TeV achieve luminosities that are comparable with those of linear colliders. Moreover, the muon collider at 10 TeV achieves luminosities similar to those proposed in emerging designs for hadron colliders, such as the FCC-hh[4] [28] or the SppC[5] [29], which are described as $90 - 100\,\text{km}$ proton ring colliders operating at $\sqrt{s} = 100\,\text{TeV}$. Additionally, K. Long et al. [30] examine a muon collider operating at 14 TeV, which can attain luminosities of $\mathcal{L}_{\text{Lum}}^{14\text{TeV}} = 42.2 \times 10^{34}\ \text{cm}^{-2}\,\text{s}^{-1}$, almost double the luminosity at 10 TeV. This is attributed to the quadratic relation of the energy in cm expressed by $\gamma$ as shown in Eq. (1.1). According to a survey by earlier carrier US scientists in collider physics, the muon collider is the preferred future option [31].

[2]The betatron function is unique to each accelerator and will be explained further in the Chapter 4.
[3]Denoting the number of bunch injections into the collider ring per second.
[4]Future Circular Collider, hadron-hadron option
[5]Super proton-proton Collider

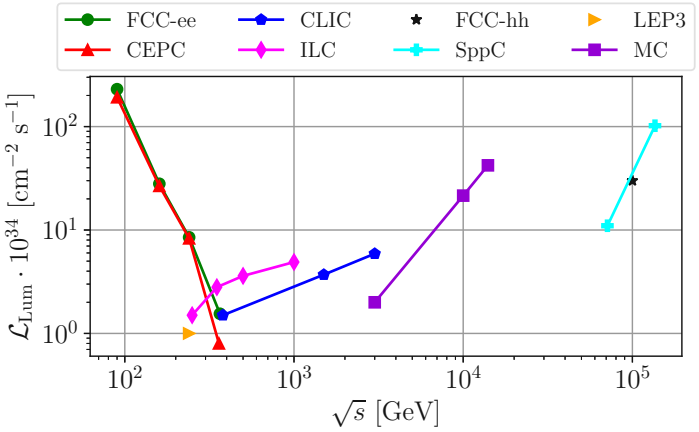


**Figure 1.1.:** Comparative analysis of the luminosities of muon colliders against those of alternative prospective collider design concepts. Muon colliders at 3 TeV achieve luminosities comparable to those of linear colliders. Moreover, the muon collider at 10 TeV reaches luminosities similar to those proposed for future hadron colliders, such as the FCC-hh or the SppC.

## 1.4 Design overview and possible CERN implementation

The conceptual design of a muon collider was initially formulated by the **Muon Accelerator Program**[6] (**MAP**) [32], under the leadership of the United States, and subsequently advanced by the **International Muon Collider Collaboration**[7] (**IMCC**) [25]. The schematic representation of the muon collider is shown in Fig. 1.2, comprising five stages as outlined in

1. the proton driver,
2. the target and pion decay channel,
3. the muon cooling stage,
4. fast acceleration systems, and
5. the collider ring.

[6] From 2011 to 2015.
[7] Started in 2022.

## Muon collider design overview

The following paragraphs succinctly characterize each stage accompanied by the respective citation.

As depicted in Fig. 1.2, the **proton complex** constitutes the initial component of the muon collider complex, characterized by a high-power acceleration section. A proton beam of $5 - 10\,\mathrm{GeV}$ with $2 - 4\,\mathrm{MW}$ is delivered to a target in order to produce a high flux of positively and negatively charged pions [33].

The second box from the left in Fig. 1.2 showcases the **target and decay channel**. A proton beam impinges on a **graphite target** [34], producing charged pions. These pions are transported through a tapered solenoid channel, where they decay into $\mu^+$ and $\mu^-$. Each proton pulse produces approximately $4.5 \times 10^{13}$ positive muons and an equal number of negative muons. Subsequently, the muons are organized into 21 micro-bunches per charge using an RF-system composed of a buncher and a phase rotator [35].

As depicted in the third box of Fig. 1.2, the solenoid chicane system is employed to segregate the train of micro-bunches according to their charge species in preparation for the **ionization cooling system**. The expansive phase space of the micro-bunches necessitates its reduction or cooling. Each micro bunch undergoes longitudinal and transverse cooling within a **rectilinear cooling** channel [36]. At a specific juncture, from a sequence of 21 micro-bunches, 3 micro-bunches are longitudinally merged. Subsequently, the seven remaining intermediate micro bunches are transversely combined into a single bunch [37], which proceeds through further cooling within a second rectilinear cooling channel. Subsequently, the muon bunch will experience exclusive transverse cooling within the **final cooling** channel. The objective of the final cooling stage is to minimize the transverse emittance to the greatest extent while simultaneously mitigating the growth of longitudinal emittance to the fullest extent possible. The final cooling channel is the main focus of this thesis. It centers on beam dynamics and the selection of a technical design, which will be elaborated upon in the following chapters.

In the penultimate step illustrated in Fig. 1.2, it is imperative that the cooled muon bunches be accelerated to the TeV scale expeditiously to mitigate muon losses. The initial channel is a multi-pass **recirculating linear accelerator** (**RLA**) wherein each muon bunch charge is accelerated from 250 MeV to 63 GeV. Subsequently, the bunches will be arranged in four **rapid cycling synchrotron** (**RCS**) units to achieve acceleration of each beam from 63 GeV to 1.55 TeV. A hybrid synchrotron design is employed to realize exceptionally rapid acceleration. This design incorporates interspersed superconducting high-field bending magnets [38] and ultra-fast, normal conducting ramped bending magnets (multiple $\mathrm{kT\,s^{-1}}$).

The final segment of Fig. 1.2 illustrates the inclusion of the collider ring. For both 3 TeV and 10 TeV muon colliders, two racetrack-type rings with different circumferences have been proposed. Theoretically, the 3 TeV alternative could be accommodated within the 10 TeV ring to make the best use of the available resources. However, this strategy leads to a reduction in luminosity, as demonstrated by Eq. (1.1). The 10 TeV collider ring has a circumference of approximately 10 km, with a lattice design proposed by K. Skoufaris [39].

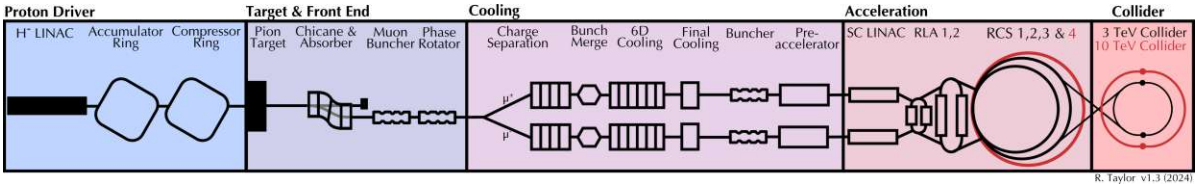


**Figure 1.2.:** A layout of the muon collider accelerator and collider complex. [27]

## A muon collider at CERN

An initial choice for the installation of the collider considers the **CERN** site as a viable location, using existing tunnels and technical infrastructure. The proposed design for the muon collider features an elongated circular ring with straight sections housing two interaction points (IP), as depicted in Fig. 1.3 as the stars at the red solid line[8]. It should be emphasized that Fig. 1.3 serves merely as a schematic representation and does not correspond to any finalized design plans[9].

A key consideration in this design is the high flux of neutrinos generated along the long straight sections, which will create a significant dose at the Earth's surface [45]. To optimize safety and efficiency, the collider configuration is designed to direct neutrino flux from IPs to non-built-up regions. These regions include a Jura mountain range area on one side and the Mediterranean Sea on the other side [46].

A muon collider option at CERN would reduce the environmental footprint. Importantly, all surface structures for the complex would be built on CERN-owned land across the CERN-Meyrin and CERN-Prévessin sites, thereby minimizing territorial and ecological disturbances. Furthermore, maximizing reuse of the existing CERN infrastructure simplifies environmental impact studies, facilitates public acceptance, and reduces costs and $CO_2$ emissions compared to completely new construction in a greenfield site [47].

[8] Muon collider ring for the 10 TeV option.

[9] The data points delineating the borders of the Swiss cantons, Geneva and the Lake-Geneva were sourced from Data [40–42]. Map construction was facilitated through the use of the Python GeoPandas package [43].

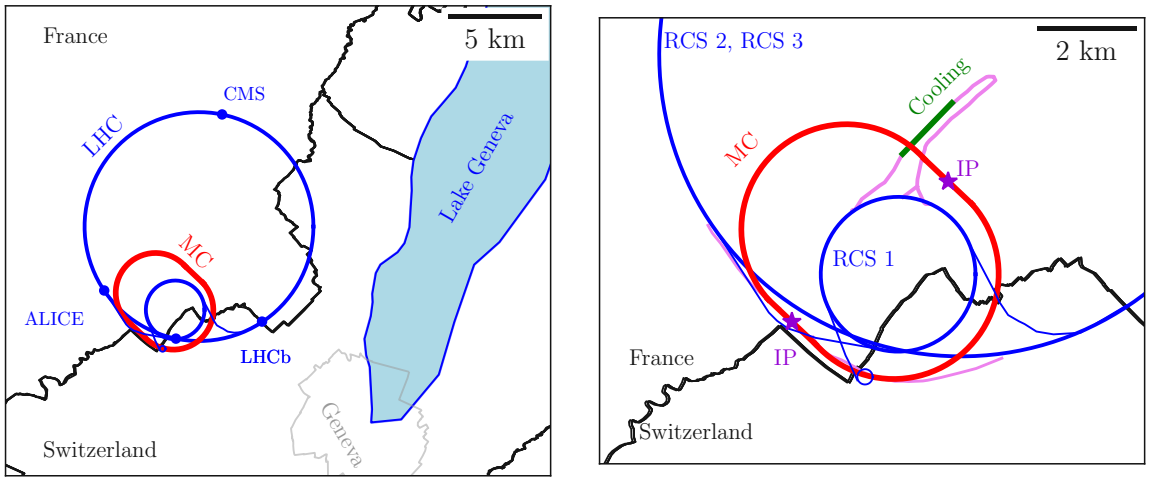


**Figure 1.3.:** A schematic illustration delineates a prospective design option for a muon collider situated within the Geneva basin. The suggested 10 TeV muon collider ring is depicted by the red solid line. Based on civil engineering analyses [44], a collider ring along with several transfer and cooling beam lines requiring construction would span a total length exceeding 10 km. The acceleration arrangement [RCS1, RCS2, RCS3, RCS4] can be integrated within the existing LHC and SPS tunnel infrastructure, classifying it as reutilized CERN infrastructure.

The technical framework for reusing the LHC tunnel to accommodate a muon collider at CERN is contingent upon the maintenance status of the Super Proton Synchrotron (SPS) at CERN. There is an optics design that fits into the LHC tunnel and will incorporate two RCS systems [48].

## 1.5 Thesis goals

This thesis is centered on muon ionization cooling, with a specific emphasis on the **final cooling channel**. Before delving into that subject, an overview of two potential topics in particle physics is collected in Chapter 2. This chapter examines **lepton-parton distribution functions** (**LePDF**) based on SM principles. Neutrino LePDFs in a muon collider are detected through partonic muon collsions with neutrinos, analyzing the final-state photons. The differential cross section amplifies at small forward angles, enhancing the precision of the event as predicted by SM. In general, Chapter 2 covers essential topics in particle physics that drive the development and exploration of accelerator technologies for a muon collider. An brief discourse on the principal mechanism of **Higgs boson production** will be presented in Chapter 2.

In the process of ionization cooling, muon beams traverse low-$Z$ materials, hydrogen being the preferred choice. Many accelerator design software programs do not incorporate material-beam interactions in their algorithms. Chapter 3 examines the interaction between charged particles and materials, detailing the integration of these physical processes into RF-Track software, a LINAC design tool developed at CERN. For the scattering model, a **semi-Gaussian** particle deflection model was implemented, using the **Bethe-Wentzel cross section** to simulate **multiple Coulomb scattering**. The benchmark results of RF-Track against other comparable codes demonstrate excellent performance. The addition of particle-matter physics to RF-Track is driven by its integration of an extensive range of collective-effects models. Research into collective effects within ionization cooling channels is a completely novel area that RF-Track could explore in future studies.

Chapter 4 will explore the dynamics of charged particles within solenoid and RF accelerating structures. The chapter will cover the beam dynamics involved in ionization cooling, highlighting a refined analytical **cooling equation** that aligns accurately with multi particle simulations. Additionally, an analytical method for determining the **optimal initial beam energy** for final cooling will be introduced. Chapter 4 will dive further into the often overlooked aspects of beam windows and hydrogen pressures, emphasizing their critical importance.

Chapter 5 is the most critical as it incorporates the main efforts of the study. This chapter details a strategy for matching muon beams in ultra-high field solenoids using a newly developed optimization algorithm named **adiabatic ramping**, unique to this thesis. In Chapter 5, a final cooling cell design is suggested, comprising two high-field solenoids integrated with hydrogen absorber systems. The reverse polarity of these solenoids not only enhances the efficiency of ionization cooling but also effectively decouples the beam in both transverse planes. The proposed cooling design includes beam windows and adapted hydrogen pressures. The cooling channel is made up of 9 cells: the first four use liquid hydrogen, and the remainder utilize hydrogen vapor to maintain reduced pressures. Additionally, Chapter 5 addresses the longitudinal phase-space adjustments made through phase rotating cavities within the final cooling cell. Finally, it presents an RF re-acceleration pathway between two final cooling cells, which remains a focal point for further development and refinement. This thesis was an essential step to ensure an increasingly realistic final cooling system and has made important insights into the dynamics of the beam throughout the key elements of this system.

# Chapter 2.

# Testing the parton nature of leptons in muon colliders

The muon is an elementary particle. Thus in a muon collider the complete center-of-mass (cm) energy is available for particle production during collisions. This is in contrast to hadrons, which are composed of quarks and gluons, resulting in the cm energy being distributed among these constituents. In comparison to circular electron colliders, the synchrotron radiation emitted by muons within the collider ring is negligible. This is attributed to the muon mass, which is approximately 200 times heavier than the electron, resulting in more than a billion times less synchrotron radiation compared to electron machines. Consequently, muons can be accelerated in a collider ring to energies much higher than those of electrons. The primary technical challenge involves promptly cooling the muon beam and accelerating it swiftly, because of the muon's decaying properties. This thesis focuses primarily on muon cooling, which will be elaborated in subsequent chapters.

**Firstly**, neutrinos originating from muon decay are included within the muon bunch. At the collider's collision point, neutrinos have the potential to interact with particles from the opposing bunch. These types of interaction can be investigated using the **lepton-parton distribution functions** (**LePDF**), and a few processes will be described in this chapter. Prior to delving into these studies, a brief overview of the Standard Model in particle physics will be provided.

An essential component of European strategies in particle physics [18] is the investigation of the Higgs boson, recognized as the most recent fundamental particle discovered at CERN. **Secondly**, in the context of a TeV-scale muon collider, **vector boson fusion** (**VBF**) stands out as the dominant mechanism for generating Higgs bosons. This chapter aims to provide a comprehensive overview of Higgs production through VBF processes of leading order. It will serve as the basis for a discussion on applying lepton PDFs on the Higgs production.

## 2.1 Standard Model of particle physics in a nutshell

In quantum mechanics, particles can be described as waves or as point-like objects, a concept known as wave-particle duality. In the field of high-energy physics, particles are frequently characterized as excitations within a quantum field. The processes of interaction among particles are described by the so-called **quantum field theory** (**QFT**). The dynamic behavior in QFT is represented using Lagrange densities, commonly referred to as Lagrangians.

The Lagrangian of the **Standard Model** (**SM**) of paticle phyisics can be represented essentially by

$$\begin{aligned}\mathcal{L}_{\text{SM}} =& -\frac{1}{4}F^{\mu\nu}F_{\mu\nu} \\ &+i\overline{\psi}\,\not{D}\,\psi \\ &+|D_\mu\phi|^2 - V(\phi) \\ &+i\overline{\psi}_i\, y_{ij}\,\psi_j\,\phi + \text{h.c.}\end{aligned} \tag{2.1}$$

Eq. (2.1) summarizes the three fundamental microscopic forces of nature, excluding gravity, named electromagnetic, strong, and weak interactions. The interactions of all particles are represented by Eq. (2.1) and can be illustrated using Feynman diagrams. H. Eberl's lecture notes [49] and the work of J. Romão et al. [50] provide a comprehensive overview and explanation of these diagrams. Feynman rules and computation methods are covered in the textbook by M. Thomson [7], with e.g. further detailed treatment in the literature of M. Peskin and D. Schroeder [51]. Both the Feynman diagram and the Feynman rules enable the calculation of cross sections for any particle interaction. In particle physics, the cross section quantifies the transition rate to a specific final state, typically expressed in units of surface area.

### 2.1.1 Description of the Standard Model's Lagrangian

The next paragraphs will briefly outline the meaning of these terms within Eq. (2.1). It is important to highlight that Eq. (2.1) serves as a compact mathematical representation of the SM. Each term in Eq. (2.1) is a condensation of several Lagrangians. The term $-\frac{1}{4}F^{\mu\nu}F_{\mu\nu}$ is known as the kinetic term and describes the dynamics of gauge bosons, the force carriers in the SM. The particles responsible for transmitting forces include gluons $g$ for the strong force, $W^\pm$ and $Z^0$ bosons for the weak force, and the photon $\gamma$ for the electromagnetic force.

The interaction of gauge bosons with fermions (matter fields) is summarized as $i\overline{\psi}\,\not{D}\,\psi$. The object $\psi$ is a spinor multiplet with four components and is known as the Dirac

spinor. This Dirac spinor is used for leptons and quarks, including also the fermionic and anti-fermionic character of the particles.

The term $|D_\mu \phi|^2$ is the interaction between the weak gauge bosons and the Brout-Englert-Higgs field $\phi$. Due to an infinite set of minima in the potential $V(\phi)$ of the Brout-Englert-Higgs field. Spontaneous symmetry breaking via the Higgs mechanism gives mass to the $W$ and $Z$ bosons while leaving the photon massless. The term $i\overline{\psi}_i \, y_{ij} \, \psi_j \, \phi$ describes the interaction between the Brout-Englert-Higgs field $\phi$ and fermion spinors $\psi$ and is the mechanism that causes matter particles to be massive. The Yukawa matrix, denoted by $y_{ij}$, is crucial in defining the masses of quarks and leptons, excluding neutrinos. Neutrinos interact with the Brout-Englert-Higgs field by virtue of the theoretical framework; however, they exhibit no coupling with the Higgs boson itself. Nevertheless, their masses have been substantiated through the phenomenon of neutrino oscillations. Various models have been proposed to explain the mechanism of neutrino mass generation, though none have been experimentally verified so far. The notation h.c. signifies the Hermitian conjugate of $i\overline{\psi}_i \, y_{ij} \, \psi_j \, \phi$.

The discovery of the Higgs boson in 2012 at CERN [5, 6] completed the SM. Prospective muon colliders feature a limited range of discovery potential beyond the SM [52], but serve as Higgs factories with vector boson fusion as the predominant process. An in-depth analysis of the Higgs particle may act as a gateway to uncovering phenomena beyond the SM. The following step involves a discussion on the cross section, which is an important parameter for analyzing particle events.

### 2.1.2 Cross section calculations

In high energy physics, the number of a specific interaction event generated during a particle collision per second can be expressed by

$$\text{Rate} = \mathcal{L}_{\text{Lum}} \cdot \sigma_{\text{tot}}. \tag{2.2}$$

In Eq. (2.2), the luminosity is indicated by $\mathcal{L}_{\text{Lum}}$, which is based on the technical specifications of the collider machine. For the muon collider the luminosity was presented in Eq. (1.1) of Chapter 1.3. The total cross section $\sigma_{\text{tot}}$ in Eq. (2.2) is dependent upon the specific particle process, which may be assessed through theoretical predictions or empirical observations. The cross section $\sigma$ quantifies the probability of a scattering process and its calculation comes from

$$d\sigma = \frac{\langle |M|^2 \rangle}{\text{flux}} d^n\text{Lips}, \tag{2.3}$$

In Eq. (2.3) the Lorentz invariant components include the averaged squared matrix element $\langle |M|^2 \rangle$, the flux factor, and the $n$-body phase space $d^n$Lips. Lorentz invariance

ensures that these quantities remain unchanged under Lorentz transformations. The flux factor depends on the 4-momenta of incoming particles $p_1^\mu$ and $p_2^\nu$ and is defined as

$$\text{flux} = 4\sqrt{(p_1 p_2)^2 - m_1^2 m_2^2}, \tag{2.4}$$

with the masses of these particles denoted as $m_1$ and $m_2$. A relativistic 4-momentum vector encapsulates the total energy $E$ and the spatial momentum $\vec{p}$ as $p^\mu = (E, \vec{p})^\top$. The Lorentz invariant phase space $d^n\text{Lips}$ describes the kinematics of $n$ final-state particles and is generally given by

$$d^n\text{Lips} = \prod_{k=1}^{n} \frac{d^3\vec{p}_k}{(2\pi)^3 2E_k}. \tag{2.5}$$

The quantity $\langle |M|^2 \rangle$ is averaged over the initial states $i$ and sums over all spin states and is defined as

$$\langle |M|^2 \rangle = \frac{1}{\text{Spin}} \sum_{\text{Spin}} M_{fi}\, M_{fi}^\dagger. \tag{2.6}$$

For a specific particle interaction process, the matrix element $M_{fi}$ can be evaluated by constructing a Feynman diagram and applying the Feynman rules. This study will go through two significant events that can be created and analyzed in a potential muon collider. The investigation will commence with an analysis of the interaction between a muon and a muon-neutrino, utilizing lepton parton distribution functions (LePDF). The LePDF framework is anticipated by SM calculations, and a muon collider possesses the potential to validate these theoretical predictions. Additionally, an overview of the vector boson fusion processes, which represent the predominant mechanisms for Higgs boson production in a muon collider, will be provided. Furthermore, the influence of the LePDF framework on vector-boson fusion will be examined and evaluated to determine whether the calculated cross sections exhibit significant deviations from those obtained without the application of LePDF.

## 2.2 Exploring the lepton PDF with muon colliders

At high energy levels, quantum corrections enable "valence" leptons to become a neutrino by emitting a gauge boson. These resulting particles can be considered as partons, allowing the application of methodologies established in hadron-hadron collision studies. At muon energies around the TeV range, the neutrino PDF of the muon increases significantly with increasing momentum fraction $x \simeq 1$. This distribution dominates over the gauge boson PDFs, which makes neutrino collisions with an approaching beam probable and even measurable.

This section examines a specific candidate for a scattering process capable of probing the parton distribution function of a neutrino within a muon beam. These precise

measurements would confirm that LePDF at muon collider energies accurately predict certain processes and establish that a muon collider can also operate as a neutrino collider.

### 2.2.1 Overview of LePDFs

Leptons are foundational constituents within the SM. However, at high energy levels, collinear initial state radiations appear and cause a reduction in the cm energy [53]. These initial-state radiations can be factorized into **PDF**s $f_i(x, Q)$, akin to proton-like particles. The function $f_i(x, Q)$ delineates the probability density of encountering a constituent parton $i$, be it a quark, a boson, or a lepton, in high-energy interactions. This parton possesses a fraction $x$ of the momentum $\sqrt{s}/2$ of a parent particle on a specified energy scale $Q$. At extremely high energies of a lepton, collinear emissions of $W^{\pm}$ and $Z^0$ emerge. The PDF relevant to a neutrino is derived from the contribution of a lepton splitting at elevated energies resulting from initial-state radiation into a $W$ boson and a neutrino.

In contrast to the PDFs of proton-like particles, the **lepton PDF**s (**LePDF**) are derived from the first principles investigated in the work of F. Garosi et al. [54]. Notably for a multi-TeV muon collider the neutrino-PDF of the muon increases as with $x \to 1$. This phenomenon is illustrated in Fig.2.1, where the LePDFs of several other particles are also depicted on factorization scales of $Q = 1.5\,\text{TeV}$ and $Q = 5\,\text{TeV}$. Subsequently, a scattering process will be introduced to facilitate the measurement of $f_{\nu_\mu}$ within the environment of a multi-TeV muon collider.

### 2.2.2 Observing the neutrino content of muon beams

This discussion focuses on the analysis of SM processes that exhibit significant sensitivity to the PDF of neutrinos. Specifically, the main focus in the following is $\mu\bar{\mu} \to \gamma W$, where $\mu(\bar{\mu})$ represents the muon (anti-muon) beam that includes its full parton content. There exists a second process sensitive to the PDF of neutrinos, as indicated by $\mu\bar{\mu} \to e\nu_e$. This particular process is not addressed in the current discussion, but is instead referenced in [54].

The $\gamma$-$W^-$ production via a $\mu\bar{\mu} \to \gamma W$ scattering event is predominantly influenced by the contribution of $\nu_\mu$-PDF, when $x \simeq 1$. At the parton level, these processes are $\mu^-\bar{\nu}_\mu \to \gamma W^-$ and $\mu^+\nu_\mu \to \gamma W^+$. Taking into account, for example, the initial generation of parton states $\mu^-$ and $\bar{\nu}_\mu$, $\gamma W^-$ can be facilitated by an s-channel scattering process, as shown in the Feynman diagram on the left of Fig. 2.2, or by a t-channel illustrated on the right of Fig. 2.2.

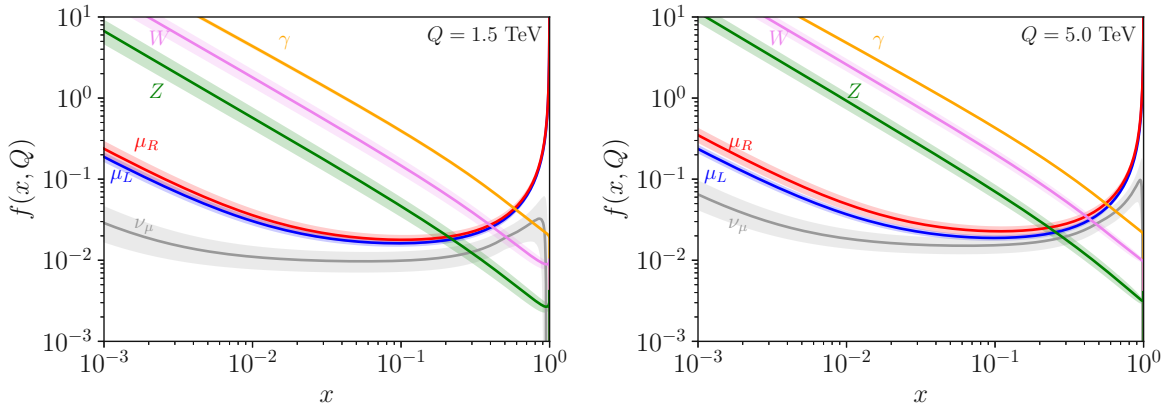


**Figure 2.1.:** Lepton parton distribution functions (**LePDF**) of various particles at factorization scales $Q = 1.5\,\text{TeV}$ (**left**) and $Q = 5\,\text{TeV}$ (**right**). The increase in the neutrino PDF $f_{\nu_\mu}$ of the muon appears as $x \to 1$. The uncertainty bands corresponds to $Q/2$ and $2Q$ in both diagrams. The figures were generated with the interpolation [55] of data that are publicly accessible from [56].

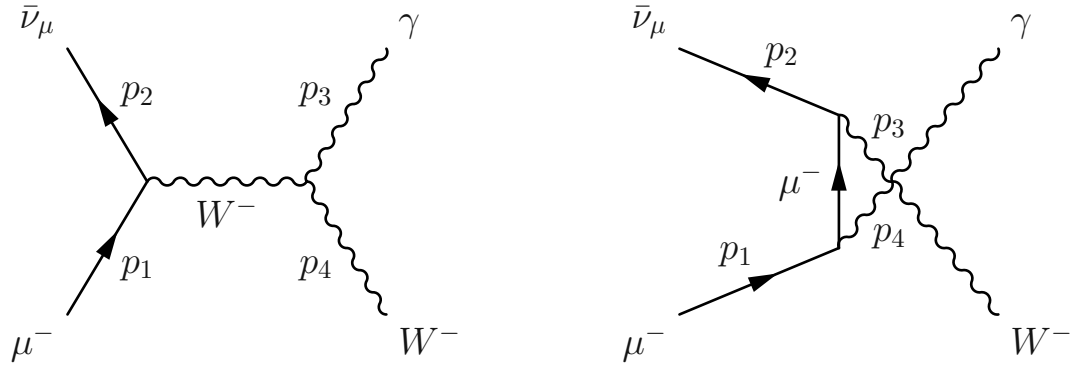


**Figure 2.2.:** Feynman diagrams illustrating the production of a $\gamma W^-$ final state from an initial parton state $\mu^-$ and $\bar{\nu}_\mu$. The **left** diagram represents the **s-channel** scattering process, while the **right** diagram depicts the **t-channel** scattering. Equivalent diagrams exist also for the processes of $\mu^+\nu_\mu \to \gamma W^+$.

The kinematics are delineated so that the four-momentum, as denoted in $p_1$, refers to the parton $\mu^-$ and $p_2$ of the initial-state parton $\bar{\nu}_\mu$. The four-momentum associated with the final-state bosons is characterized by $p_3$, corresponding to $\gamma$, and $p_4$ corresponding to $W^-$. The Mandelstam variables for the processes in Fig. 2.2 are defined as

$$\hat{s} = (p_1 + p_2)^2, \qquad \hat{t} = (p_1 - p_3)^2. \tag{2.7}$$

The notation of a hat $\hat{}$ above the Mandelstam variables signifies the partonic cm energy, as defined in $\hat{s} = x_1 x_2 s$. Here, $x_1$ represents the fraction of energy associated with the parton in $\mu$, while $x_2$ denotes that of the opposing $\bar{\mu}$. To compute the differential cross

section, it is essential to evaluate the total squared amplitude. The expression for the squared amplitude of the s-channel is evaluated by applying the Feynman rules to the corresponding Feynman diagram and is given by

$$\left\langle |M|^2 \right\rangle_s = \frac{e^2 g^2}{2\left[(\hat{s} - m_W^2)^2 + m_W^2 \Gamma_W^2\right]} \left[ \frac{\hat{s}(\hat{s}^2 + \hat{s}\hat{t} + \hat{t}^2)}{m_W^2} - m_W^2(\hat{s} - 5\hat{t}\,) - 4\hat{s}^2 - 6\hat{s}\hat{t} - 5\hat{t}^2 \right], \tag{2.8}$$

where the electrical charge is denoted as $e$ and $\Gamma_W$ represents the $W$ boson's decay width. Similarly, the squared amplitude for the t-channel is represented by

$$\left\langle |M|^2 \right\rangle_t = \frac{g^2\, e^2}{2\,\hat{t}\, m_W^2} \left[ 2m_W^4 - 2m_W^2(\hat{s} + \hat{t}\,) + \hat{s}\hat{t}\,\right]. \tag{2.9}$$

The derivation of the t-channel as well of the s-channel can be both verified in Appendix B.2.1 and Appendix B.2.2. The combined squared amplitude for both the s- and t-channels is expressed as

$$\left\langle |M|^2 \right\rangle_{\text{tot}} = \left\langle |M_t + M_s|^2 \right\rangle = \left\langle |M|^2 \right\rangle_s + \left\langle |M|^2 \right\rangle_t + 2\left\langle \text{Re}\left(M_s\, M_t^\dagger\right)\right\rangle. \tag{2.10}$$

The subsequent task involves deriving the physical differential cross section by incorporating the LePDF associated with the muon $f_\mu(x_1, Q)$ and the anti-muon neutrino $\bar{f}_{\bar{\nu}_\mu}(x_2, Q)$. The factorization energies related with the LePDF functions were evaluated on the basis of the beam energies $Q = \sqrt{s}/2$ outlined in the proposed muon collider concepts, specifically at $Q = 1.5\,\text{TeV}$ and $Q = 5\,\text{TeV}$, and $\sqrt{s}/4$ and $\sqrt{s}$ as uncertainties. The physical differential cross section is specified as [51]

$$\frac{d\sigma(s)}{d(\cos\vartheta)} = \int_0^1 dx_1 \int_0^1 dx_2\, f_\mu\,(x_1, Q)\, \bar{f}_{\bar{\nu}_\mu}\,(x_2, Q)\, \frac{d\sigma(\hat{s})}{d(\cos\vartheta)}. \tag{2.11}$$

The next step involves the evaluation of the differential cross section in a range of the scattering angle of $\gamma$ within the laboratory frame $10^\circ < \vartheta_{\text{Lab}} < 170^\circ$. Angle restrictions were taken from the nozzle geometry as defined in the muon collider detector proposal, which was designed specifically for radiation shielding purposes [57]. Consequently, integrating requires the transformation of the scattering angle from the laboratory frame to the parton frame. The results of a $\mu\bar{\mu}$ collision at $\sqrt{s} = 3\,\text{TeV}$ and $\sqrt{s} = 10\,\text{TeV}$ are presented in Fig. 2.3.

At low values of $\vartheta_{\text{Lab}}$, the differential cross section is significantly enhanced. Recent research [54, Fig. 8] examined and compared background processes for $\sqrt{s} = 3\,\text{TeV}$ and $\sqrt{s} = 10\,\text{TeV}$, resulting in promising findings. In particular, it demonstrates that for a specific transverse momentum threshold $p_T$, the $\gamma W$ production resulting from neutrino-muon scattering at the parton level exceeds the background at small values of

$\vartheta_{\text{Lab}}$. These findings indicate that a muon collider possesses the ability to probe the neutrino content of a muon.

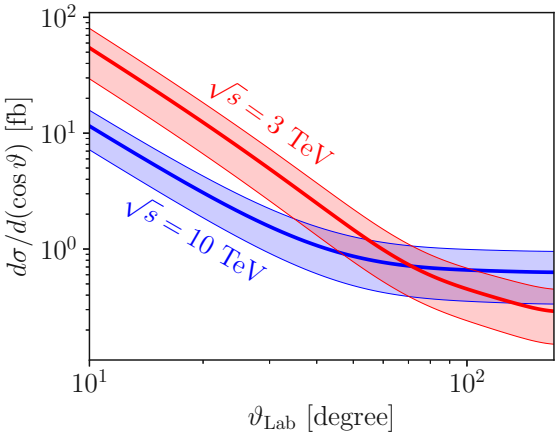


**Figure 2.3.:** Differential cross section as a function of the laboratory-frame scattering angle $\vartheta_{\text{Lab}}$ for $\mu\bar{\mu}$ collisions at 3 TeV and 10 TeV. The calculation incorporates the transformation from parton frame to the laboratory frame. A pronounced enhancement of the differential cross section is observed at low $\vartheta_{\text{Lab}}$.

## 2.3 Do lepton PDFs influences the Higgs production?

The use of lepton colliders results in reduced background noise in the detectors and makes the analysis of rare events more straightforward. One of such rare events is the production of Higgs bosons. In a muon collider, its primary production channel is through vector-boson fusion. These processes are well understood and will be briefly described in this section. The primary aim of this analysis is to determine whether lepton PDFs significantly affect Higgs production, and this will be thoroughly examined in this section.

### 2.3.1 Vector boson fusion overview

Vector Boson Fusion (VBF) is a fundamental process in particle physics in which two weak gauge bosons are emitted from high-energy fermion beams and subsequently fuse to produce rare final-state particles. Typically, these particles are Higgs bosons, accompanied by two additional fermions. The Higgs boson can be generated through the fusion of a $W^+$ and a $W^-$ boson or through two $Z^0$ bosons. The Feynman diagram for

the fusion $W^+W^-$ is shown in Fig. 2.4 **left**, while the fusion $Z^0Z^0$ is illustrated as the diagram on the **right**.

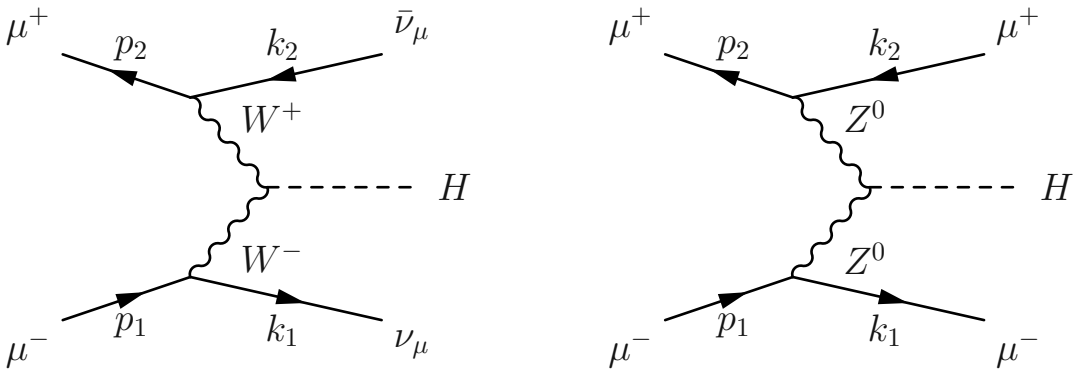


**Figure 2.4.:** Feynman diagrams illustrating Vector Boson Fusion (VBF) processes at a muon collider. The **left** diagram shows a Higgs boson production via $W^+W^-$ fusion, while the **right** diagram depicts the Higgs production through $Z^0Z^0$ fusion.

The VBF process is a $1 + 2 \to 3 + 4 + 5$ scattering event that produces three final-state particles. The complete derivation of the Lorentz invariant phase space $d^3\text{Lips}$ is presented in the Appendix B.3.2 and is given by

$$\mathrm{d}^3\mathrm{Lips} = \frac{1}{(2\pi)^4}\frac{1}{16\sqrt{s}}\int_0^{2\pi}\mathrm{d}\phi^*\int_0^{\pi}\sin\theta^*\,\mathrm{d}\theta^*\int_0^{\pi}\sin\theta\,\mathrm{d}\theta\int_0^{\sqrt{s}-m_H} m_{12}k\,dm_{12}. \tag{2.12}$$

The final-state particles include a Higgs boson with momentum $k_3$, and a pair of neutrinos $(\nu_\mu, \bar{\nu}_\mu)$ or charged leptons $(\mu^-, \mu^+)$ with momenta $k_1$ and $k_2$. These leptonic momenta are combined into a single effective four-momentum $K^\mu_{12} = (E_{12},\ \vec{k})^\top$ with energy $E_{12} = \sqrt{m_{12}^2 + k^2}$. This transformation reduces the original $2 \to 3$ process to an effective $2 \to 2$ process, where the final lepton system is represented by a composite particle with invariant mass $m_{12}$ and spatial momentum $\vec{k}$. The magnitude of $\vec{k}$ is

$$k = \frac{\lambda^{1/2}(s, m_{12}^2, m_{\mathrm{H}}^2)}{2\sqrt{s}}, \tag{2.13}$$

where $m_{\mathrm{H}}$ is the mass of the Higgs boson and $\lambda$ is the Källén function, defined in Appendix B.1.2. The average squared amplitude of $\mu^-\mu^+ \to W^-W^+ \to \nu_\mu\bar{\nu}_\mu H$ is

$$\overline{\langle|M|^2\rangle}^{WW\to\nu\bar{\nu}H} = m_W^2\, g^6 \frac{(p_1k_2)(p_2k_1)}{\left[2(p_1k_1) + m_W^2\right]^2\left[2(p_2k_2) + m_W^2\right]^2}, \tag{2.14}$$

where $m_W$ is the $W$ boson mass and $g$ is the weak coupling constant. The momenta $p_1$ and $p_2$ refer to the initial-state muons, while $k_1$ and $k_2$ correspond to the final-state

leptons. The expressions in brackets in Eq. (2.14) are referred as Lorentz products of two 4-momenta. The full derivation of Eq. (2.14) is outlined in detail in Appendix B.3.3.

The average squared amplitude of the process $\mu^-\mu^+ \to Z^0Z^0 \to \mu^-\mu^+H$ results to

$$\overset{ZZ\to\mu^-\mu^+H}{\langle|M|^2\rangle} = \frac{m_Z^2\, g'^6}{8} \frac{4C_1\,(p_1k_2)(p_2k_1) + C_2\, s\, m_{12}}{\left[2(p_1k_1) + m_Z^2\right]^2 \left[2(p_2k_2) + m_Z^2\right]^2}, \tag{2.15}$$

which includes the mass $m_Z$ of the $Z^0$ boson and $g'$ is its coupling constant. The expressions $C_1$ and $C_2$ are composed of the vector and axial constants, $c_V$ and $c_A$, of the muon to $Z^0$ which are defined as

$$C_1 = c_V^4 + c_A^4 + 6c_V^2c_A^2, \qquad C_2 = (c_V^2 - c_A^2)^2. \tag{2.16}$$

The cross sections of the VBF processes is the substitution of the Lorentz invariant phase space Eq. (2.12), the flux Eq. (2.4) and the average squared amplitudes of Eq. (2.14) and Eq. (2.15) into the definition Eq. (2.3). The evaluation of the multidimensional integral in Eq. (2.12) over Eq. (2.14) and Eq. (2.15) necessitates a numerical approach, e.g. Monte Carlo integrations [58, 59].

The results of the total cross section of VBF are illustrated in Fig. 2.5. In the total cross section, the contribution from Higgs strahlung processes was also included with further information provided in the Appendix B.3.4. Within the muon collider operation energies 3 TeV and 10 TeV, the difference in the total cross section between the $W^+W^-$ and $Z^0Z^0$ fusion channels is approximately an order of magnitude. A comparison of the Higgs production rates in different collider types is summarized in the Appendix B.3.5. It is identified there that a 10 TeV muon collider is capable of producing a Higgs boson every 6 s only through the $W^+W^-$ fusion channel, which is an order of magnitude higher than what $e^+e^-$ ring colliders achieve.

### 2.3.2 Influences of LePDF on the Higgs production

Since VBF occurs through processes of the t channel, outgoing leptons, $\mu^-(\mu^+)$ or $\nu_\mu(\bar{\nu}_\mu)$, tend to be scattered at small angles relative to the direction of the beam. This means that they appear in the forward regions of the detector. As a result, the momentum transfers $q_1$ and $q_2$ associated with the exchanged vector bosons are relatively small. The involvement of neutrinos of the initial state at the parton level in the context of Higgs production is negligible. This is due to the fact that the scaling factor $Q$ is minor, leading to a correspondingly small neutrino LePDF. At low $Q$, the muon does not divide into weak bosons. Instead, it emits photons, leaving the muon intact but with a small reduced cm energy, which effect is more pronounced in $e^+e^-$ colliders.

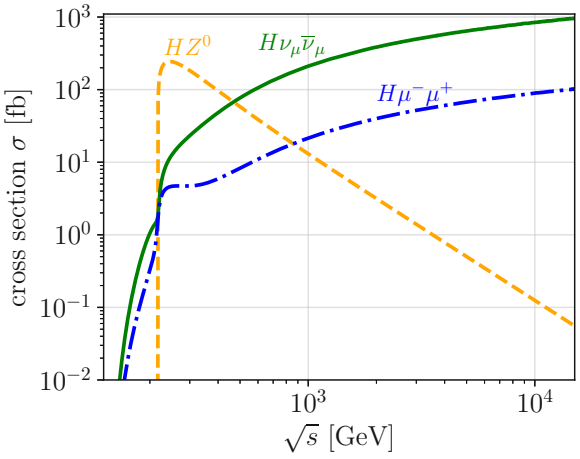


**Figure 2.5.:** Total cross sections of vector boson fusion (VBF) Higgs production via $W^-W^+$ fusion (green solid line) and $Z^0Z^0$ fusion (blue dashed-pointed line). For comparison the Higgs strahlung, which is the leading Higgs production porcess in $e^+e^-$ ring colliders (orange dashed line).

However, the cross section of the single Higgs productions should not be affected by LePDFs. To test this, the PDF approach can be applied to muons in the initial state in VBF as depicted in Fig. 2.6. To maintain simplicity, the unpolarized partonic cross sections are computed and then convoluted with LePDFs of $\mu^-$ and $\mu^+$ summed over different helicities. Detailed cross sections are presented in Tables 2.1, illustrating scenarios at Muon Colliders with energies of 3 TeV and 10 TeV. The scaling factors for $Q = [100, 200, 400]$ GeV were used and compared with the cross sections of VBF calculated. The parton cross sections for the VBF are $1 - 7\%$ smaller relative to the non-LePDF cross section, making their effect on Higgs production insignificant.

| $W^+W^- \to \nu_\mu\bar{\nu}_\mu H$ | no PDF | $Q = 100$ GeV | $Q = 200$ GeV | $Q = 400$ GeV |
|---|---|---|---|---|
| $\sigma_{3\,\text{TeV}}$ [fb] | 496.6 | 486.9 | 483.4 | 467.2 |
| $\sigma_{10\,\text{TeV}}$ [fb] | 845.1 | 833.9 | 828.6 | 783.3 |
| $Z^0Z^0 \to \mu^-\mu^+ H$ | | | | |
| $\sigma_{3\,\text{TeV}}$ [fb] | 51.8 | 50.8 | 50.4 | 50.0 |
| $\sigma_{10\,\text{TeV}}$ [fb] | 89.3 | 88.1 | 87.7 | 86.9 |

**Table 2.1.:** Comparison of the total cross section between the two VBF channels at muon colliders for energies of $\sqrt{s} = 3$ TeV and $\sqrt{s} = 10$ TeV and compared with the LePDF cross section. The partonic cross section are within a few percentages smaller.

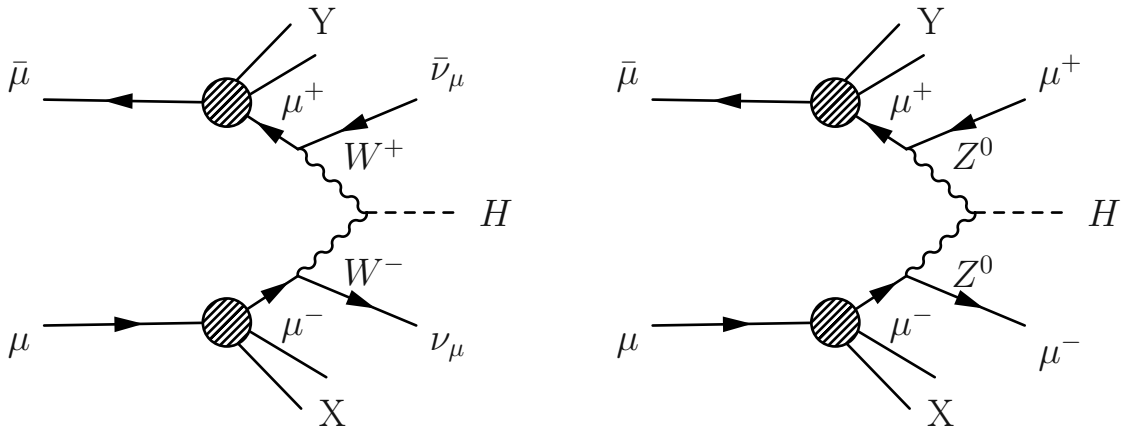


**Figure 2.6.:** Singl Higgs production via VBF in the parton picture. Due to the initial state radiation, a $\mu(\bar{\mu})$ splits into a leptonic parton $\bar{\mu}(\mu^+)$ and $X(Y)$. The inital state partons $\mu^-$ and $\mu^+$ further create a Higgs via VBF.

## 2.4 Conclusion of testing the parton nature of leptons in muon colliders

A muon collider represents an optimal apparatus for performing precise measurements of the Standard Model (SM) due to the reduced incidence of background events within the interaction region. The examination of rare events may lead to the discovery of novel physics or, more significantly, facilitate the direct observation of new laws in nature.

In this chapter a detailed examination of a specific precision study is presented, emphasizing the potential analysis of lepton-parton distribution functions (LePDF). The theoretical framework of LePDF can be derived from the fundamental principles of the SM. In the muon collider, the neutrino LePDF can be identified through processes $\mu(\mu^-)\bar{\mu}(\bar{\nu}_\mu) \to \gamma W^-$ and $\mu(\nu_\mu)\bar{\mu}(\mu^+) \to \gamma W^+$ by observing and analyzing the final-state photon $\gamma$. The angle-dependent differential cross section was evaluated to be enhanced at small forward angles. Examining events within this angle interval in a detector can observe high-precision events caused by the partonic characteristics of leptons, as predicted by the SM.

A muon collider operates as a Higgs factory, facilitating a comprehensive study of this scalar boson. Higgs boson production is mainly through vector boson fusion (VBF), with $W^-W^+$-fusion processes being an order of magnitude more dominant than $Z^0Z^0$ fusions. This analysis includes LePDFs in Higgs production via VBF, but scaling factors $Q$ at low energies keep the cross sections nearly unchanged, regardless of LePDF inclusion.

# Chapter 3.

# Charged particles in material

This chapter explores the advancement of models for charged particle interactions with materials within RF-Track particle tracking software [60]. These models are vital for simulating ionization cooling in future muon colliders. For an accurate beamline design simulating muon ionization cooling, computational capabilities must be embedded in a tracking code. These computational capabilities should include:

- intersecting electromagnetic fields,
- decay processes of particles,
- interactions between charged particles and atomic materials.

This chapter outlines the models concerning the interaction of charged particles with materials. Previously, RF-Track had integrated models for particle decay and electromagnetic fields. In addition, an advanced solenoid field model is included in this thesis and will be covered in detail in Chapter 4. The primary interactions between particles and materials that are significant for ionization cooling are as follows:

- energy loss along with its fluctuations,
- scattering events of charged particles within matter.

In implementing the Bethe equation for the model of average energy loss of charged particles, it demonstrates remarkable consistency with comparable tracking software. Although the model still requires updates with respect to energy loss fluctuations, this was beyond the scope of this study.

In the charged particle scattering model, an innovative semi-Gaussian mixture model, parameterized using the Bethe-Wentzel scattering formula, was integrated into RF-Track. The significant results emphasize that this is the first application of this kind of model within a beamline tracking code. This chapter demonstrates that the convolution property of the semi-Gaussian mixture model surpasses the scattering models commonly

employed in other tracking software. Additionally, benchmarking the RF-Track scattering angles in liquid hydrogen and lithium hydride against other simulation tools reveals strong agreement.

The RF-Track software provides enhanced functionality for simulating linear accelerators, taking into account collective effects. This motivated the integration of charged particle interactions with materials into the RF-Track code. This integration is essential because the study of collective effects in muon ionization cooling channels is an unexplored area in beam physics that should be investigated in future research.

## 3.1 Tracking codes for ionization cooling

The movement of charged particles with charge $q$ and mass $m_0$ in any electromagnetic field is governed by electrodynamic laws. The path followed by a particle through an electromagnetic field is determined by the Lorentz force, expressed as

$$\frac{d\vec{p}(\vec{r},t)}{dt} = q\left[\vec{E}(\vec{r},t) + \vec{v}(\vec{r},t) \times \vec{B}(\vec{r},t)\right]. \tag{3.1}$$

The force presented in Eq. (3.1) encompasses the influence of the electric field $\vec{E}(\vec{r},t)$, which imparts a force along its field lines on the charge, and the magnetic field $\vec{B}(\vec{r},t)$, which exerts a force perpendicular to both the velocity $\vec{v}(\vec{r},t)$ of the charged particle and the magnetic field. Equation (3.1) is time-dependent and varies with the position vector $\vec{r} = (x,\, y,\, z)^\top$.

The velocity $\vec{v}$ of a point charge is a vector quantity that indicates how its position changes over time. The path of the particle is represented as $s(t)$, with its total velocity given by $v = |\vec{v}(\vec{r},t)|$ at a certain time and location, and specifically as $v(t) = \partial s/\partial t$. In accelerator physics, velocity is expressed in terms of angles to provide information about the particle's direction. The conversion of velocity into angular terms is represented as:

$$\vec{v}(\vec{r},t) \equiv \dot{\vec{r}}(t) = \frac{\partial \vec{r}(t)}{\partial t} = \frac{\partial \vec{r}(t)}{\partial s}\frac{\partial s}{\partial t} \equiv v\,\vec{r}\,'(t). \tag{3.2}$$

In Eq. (3.2), the angle is given by $\vec{r}\,' = (x',\, y',\, z')^\top = (\partial x/\partial s,\, \partial y/\partial s,\, \partial z/\partial s)^\top$.

In the field of accelerator physics, the transverse angles $x'$ and $y'$ are described in terms of the relationship between transverse and longitudinal momentum. When these angles are small ($\sin\vartheta \approx \vartheta$), they can be approximated by the expressions:

$$x' \approx \frac{p_x}{p_z} \quad y' \approx \frac{p_y}{p_z}. \tag{3.3}$$

The scalar of the total momentum $p = m\,\partial r/\partial s = mv$ is determined by multiplying the relativistic mass by the total velocity of a particle. Here, the relativistic mass is expressed as $m = \gamma m_0$, with $\gamma$ representing the relativistic gamma factor and $m_0$ being the mass of the particle at rest. In this context, Eq. (3.1) can be reformulated in terms of $\vec{r}$ together with its first and second derivatives. This formulation results in a second-order differential equation, expressed as

$$\vec{r}'' = \frac{q}{pv}\vec{E}(\vec{r}) + \frac{q}{p}\left(\vec{r}' \times \vec{B}(\vec{r})\right) = \mathbf{\Gamma}\left(s, \vec{r}, \vec{r}'\right), \tag{3.4}$$

In Eq. (3.4), the function denoted by $\Gamma$ signifies the second derivative of $\vec{r}$ with respect to $s$. At this point, it has to be mentioned that the time dependency is of Eq. (3.4) is covered in $\vec{r}'$.

In scenarios characterized by inhomogeneous fields, such as optical elements in particle accelerators, the precise analytical solution of Eq. (3.4) is unfeasible. Consequently, numerical approaches are necessary to approximate solutions with precision. The Runge-Kutta-Nyström method is a particularly effective approach to resolving such complexities, especially with regard to second-order differential equations [61]. For a single integration step $ds$ along the particle's trajectory, ranging from $s$ to $s+ds$, the approximate solution is modeled by two recursive functions:

$$\begin{aligned} \vec{r}_{n+1} &= \vec{r}_n + \vec{r}_n'\,ds + \frac{ds^2}{6}\left(k_1 + k_2 + k_3\right), \\ \vec{r}_{n+1}' &= \vec{r}_n' + \frac{ds}{6}\left(k_1 + 2k_2 + 2k_3 + k_4\right), \end{aligned} \tag{3.5}$$

which update both the position and orientation of the particle at each incremental step. The quartet of intermediary terms $[k_1, k_2, k_3, k_4]$ delineated in Eq. (3.5) is outlined in the following table.

| Integration step | intermediate position | intermediate angle | intermediate term |
|---|---|---|---|
| $z_1 = s_n$ | $\vec{\varrho}_1 = \vec{r}_n$ | $\vec{\varrho}_n' = \vec{r}_n'$ | $k_1 = \mathbf{\Gamma}\left(z_1, \vec{\varrho}_1, \vec{\varrho}_1'\right)$ |
| $z_2 = s_n + ds/2$ | $\vec{\varrho}_2 = \vec{r}_n + \vec{r}_n'\,ds/2 + k_1 ds^2/8$ | $\vec{\varrho}_2' = \vec{r}_n' + k_1 ds/2$ | $k_2 = \mathbf{\Gamma}\left(z_2, \vec{\varrho}_2, \vec{\varrho}_2'\right)$ |
| $z_3 = s_n + ds/2$ | $\vec{\varrho}_3 = \vec{r}_n + \vec{r}_n'\,ds/2 + k_1 ds^2/8$ | $\vec{\varrho}_3' = \vec{r}_n' + k_2 ds/2$ | $k_3 = \mathbf{\Gamma}\left(z_3, \vec{\varrho}_3, \vec{\varrho}_3'\right)$ |
| $z_4 = s_n + ds$ | $\vec{\varrho}_4 = \vec{r}_n + \vec{r}_n'\,ds + k_3 ds^2/2$ | $\vec{\varrho}_4' = \vec{r}_n' + k_3 ds$ | $k_4 = \mathbf{\Gamma}\left(z_4, \vec{\varrho}_4, \vec{\varrho}_4'\right)$ |

The necessity of evaluating electric and magnetic fields at three different positions per step is replaced by an innovative strategy suggested by R. Frühwirth's textbook [62]. These positions are $\vec{r}_n$, $\vec{r}_n + \vec{r}_n'\,ds/2 + k_1 ds^2/8$, and $\vec{r}_n + \vec{r}_n'\,ds + k_3 ds^2/2$. If the field at the conclusive position $\vec{r}_{n+1}$, which is chosen as the starting position for the subsequent step, is approximated using the field of $k_4$, only two evaluations per step are required. This strategy thus accelerates computation.

In the case of additional perturbation of the particles angles coming from interactions between the particle and a material in the presence of an electromagnetic field, the second line of the equation can be modified according to

$$\vec{r}'_{n+1} = \vec{r}'_n + \frac{ds}{6}(k_1 + 2k_2 + 2k_3 + k_4) + \Delta\vec{r}'. \tag{3.6}$$

The transverse components of the perturbation term $\Delta\vec{r}'$ characterize angles $\vartheta_x$ and $\vartheta_y$. These angles arise because of the deflection of the particle caused by the Coulomb forces exerted by the nuclei of the material. The longitudinal disturbance $\Delta r'_z = \delta_p$ accounts for the fluctuations in energy loss experienced along the longitudinal path of the particle.

Within this thesis, Eqs. (3.5) with its perturbative modification in Eq. (3.6) were utilized to assess the particle-material interaction models prior to their adaptation and incorporation into the existing RF-Track code. The particularities of the particle-material interaction models, encompassing both implementation and evaluation, will be elaborated upon in subsequent sections. However, this section first provides a concise historical overview of ionization cooling codes and the contemporary computational tools used to design ionization cooling beamlines.

### 3.1.1 Overview of ionization cooling software

Software designed to track charged particles during ionization cooling must address several critical issues. As already mentioned in the introduction of the chapter, these include the overlap of magnetic fields, the decay of particles, and the interactions between charged particles and materials. The following overview gives a brief history of the development of tracking codes in ionizatin cooling base on [63].

In the late twentieth century, laboratories in the United States began to explore the idea of a high-luminosity muon collider [64]. Although they had a conceptual framework, they lacked detailed simulations at the time. Initial simulations were carried out using the MARS program [65], and later the ICOOL [66] software was developed to enhance these efforts.

In the early 2000s, CERN initiated efforts toward building a neutrino factory based on a muon storage ring [67, 68]. To simulate beam dynamics related to pion decay and muon cooling, they utilized the PATH [69] and MARS programs.

Although simulation tools for ionization cooling were already available, the detailed description of its beam dynamics was provided a few years later. G. Penn introduced the angular momentum depending beam envelope equation for a solenoid system that included energy-absorbing material [70]. B. Holzer proposed an alternative approach by

developing a particle count technique based on 4D and 6D hyperellipsoids to analyze the beam dynamics in a cooling channel [71].

### 3.1.2 ICOOL

ICOOL [72] is a Fortran-based code specifically designed to simulate muon ionization cooling. Initially, it used the physics model for charged particle interactions in materials from GEANT-3 [73]. However, discrepancies between the ICOOL simulations and the experimental data from the MuScat experiment [74], particularly those involving liquid hydrogen, required updates and improvements to the model.

ICOOL performs integration through an electromagnetic field. This field can either be read from a pre-defined field map or generated by various accelerator components included within the code. The tracking of particle integration is performed in longitudinal space, and the phase space coordinates of each particle are saved in a data. The beam parameter analysis can be performed using integrated analysis techniques in ICOOL or, as recommended, with the ECALC9 Fortran program developed by G. Penn [75].

### 3.1.3 G4Beamline

G4Beamline is a single-particle tracking code developed by T. Roberts [76], based on the Geant4 toolkit [77]. It simulates arbitrary particles as they traverse electromagnetic fields and materials. The software is designed to be user-friendly and does not require C++ programming skills [78], although installing it from the source may present some challenges. MacBook Pro users who have an Intel processor can also choose the G4Beamline-App software, which offers a simpler installation process.

G4Beamline includes a variety of beamline elements that can be arranged within the G4Beamline environment, allowing for the creation of custom electromagnetic fields through which particles are tracked. One of its key advantages is the graphical user interface, which enables users to visualize the beamline elements and particle trajectories, facilitating easy validation and error correction.

Additionally, G4Beamline can determine the beam parameters using integrated analysis tools. Similarly to ICOOL, G4Beamline generates a data file that can be analyzed with external programs such as ECALC9.

### 3.1.4 RF-Track

RF-Track [60], coded by A. Latina, was initially developed to support the design of a high-gradient proton LINAC known as TULIP [79]. Since then, it has been continuously refined and expanded for use in various advanced applications. One of its current functions includes helping to design DEFT [80], a new medical therapy system based on the FLASH effect [81].

In the field of future particle colliders, RF-Track plays a key role in the design and optimization processes for projects such as CLIC [82] and the FCC-ee, specifically for the FCC-ee injector and positron source [83]. For this thesis, particle interactions with matter were implemented for the study of ionization cooling in muon colliders.

For interfacing with RF-Track, users can select Python3 [84] (Python3.10 used in this thesis) or Octave [85], offering adaptability based on their chosen computing environment. Beyond collider applications, RF-Track is a versatile tool used for particle dynamics studies to simulate processes such as inverse Compton scattering [86], time-dependent electromagnetic 3D field maps and simulating particle behavior independent of mass, charge lifetime, or relativistic limit. To ensure accuracy and efficiency, RF-Track employs advanced, higher-order algorithms for the numerical integration of particle equations of motion. The software tool incorporates both collective and single-particle effects into its simulations. Collective effects include space-charge forces, short- and long-range wakefields, and beam loading phenomena. RF-Track accounts for incoherent synchrotron radiation and magnetic multipole kicks.

In this study, multiple Coulomb scattering was implemented and tested for single-particle interactions and energy losses. The subsequent sections provide a detailed physical overview of particle-matter interactions, accompanied by a comprehensive benchmarking analysis. The discussion begins with an exploration of energy loss, followed by an in-depth examination of multiple Coulomb scattering.

## 3.2 Energy loss of charged particles in materials

The primary mechanism in ionization cooling is the loss of energy of the particles during their passage through the material. The main particle-stopping process is the interaction of the electrons of the materials with the charged particles when they are heavier than the electrons. This chapter provides a discussion of the quantum electrodynamical (QED) principles that underlie energy dissipation in matter. It also demonstrates how the RF-Track energy-loss model is consistent with simulations from both ICOOL and G4Beamline.

### 3.2.1 Main quantum electrodynamics scatter process

The QED scattering process in the t-channel delineates the elastic deflection of two charged particles, $\ell_1$ and $\ell_2$. This deflection results from their interaction through Coulomb forces by photon exchanges, as shown in Fig. 3.1. The Coulomb force is associated with a charge $e$, which can be positive or negative, and is quantified by an integer $Z$. Let the charges of the particles involved in the process be $Z_1e$ and $Z_2e$. The cross section for the QED t-channel scattering process can be derived using various methods. Within this context, the trace technique for Feynman diagrams is utilized, as introduced and applied in the preceding physics chapter.

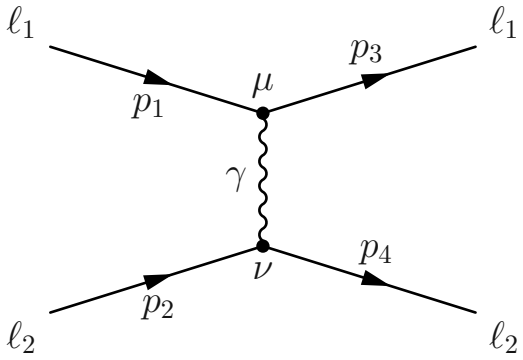


**Figure 3.1.:** The QED t-channel interaction involves two charged particles, $\ell_1$ and $\ell_2$. These particles carry charges $Z_1e$ and $Z_2e$, respectively. The interaction is facilitated by the exchange of a photon $\gamma$ at the vertices $\mu$ and $\nu$ via the electromagnetic force.

To evaluate the cross section of the process in Fig. 3.1, the initial task is to calculate the matrix element. As per the Feynman rules, the expression for the matrix element is given by

$$M_{fi} = \xi \cdot \overline{u}(p_3)\gamma^{\mu}u(p_1)\overline{u}(p_4)\gamma_{\mu}u(p_2), \quad \text{where } \xi = \frac{Z_1 Z_2 e^2}{t}. \tag{3.7}$$

The Lorentz-invariant Mandelstam variable $t$ in Eq. (3.7) is defined as $t = (p_1 - p_3)^2 = (p_4 - p_2)^2$. To evaluate the squared amplitude, the initial step involves finding the complex conjugate of the matrix element mentioned in Eq. (3.7). The subsequent procedure involves averaging the spins of the two initial particles, thereby considering all possible spin states. For situations with spin-half initial particles, the spin-averaged squared amplitude is expressed as

$$\begin{aligned}\left\langle |M|^2 \right\rangle = \frac{\xi^2}{4} &\left( \sum_{\text{Spin}} u(p_1)\overline{u}(p_1) \right) \gamma^{\nu} \left( \sum_{\text{Spin}} u(p_3)\overline{u}(p_3) \right) \gamma^{\mu} \\ &\left( \sum_{\text{Spin}} u(p_2)\overline{u}(p_2) \right) \gamma_{\nu} \left( \sum_{\text{Spin}} u(p_4)\overline{u}(p_4) \right) \gamma_{\mu}.\end{aligned} \tag{3.8}$$

By employing the Feynman trace method to simplify Eq. (3.8), the squared amplitude refines to

$$\left\langle |M|^2 \right\rangle = \frac{\xi^2}{4} \operatorname{Tr}\left\{ (\not{p}_1 + m_1 c)\gamma^\nu (\not{p}_3 + m_1 c)\gamma^\mu \right\} \operatorname{Tr}\left\{ (\not{p}_2 + m_2 c)\gamma_\nu (\not{p}_4 + m_2 c)\gamma_\mu \right\}, \quad (3.9)$$

where the mass of particle $\ell_1$ is represented as $m_1$. The mass $m_2$ corresponds to that of $\ell_2$. The left trace in Eq. (3.9) can be represented as

$$p_1^\alpha p_3^\beta \left[ \operatorname{Tr}\left\{ \gamma^\alpha \gamma^\nu \gamma^\beta \gamma^\mu \right\} + m_1 c \operatorname{Tr}\left\{ \gamma^\alpha \gamma^\nu \gamma^\mu \right\} + m_1 c \operatorname{Tr}\left\{ \gamma^\nu \gamma^\beta \gamma^\mu \right\} + m_1^2 c^2 \operatorname{Tr}\left\{ \gamma^\nu \gamma^\beta \right\} \right] = 4 \left[ p_1^\mu p_3^\nu + p_1^\nu p_3^\mu - (p_1 p_3) g^{\nu\mu} + m_1^2 c^2 g^{\nu\mu} \right].$$

Traces that include an odd count of gamma matrices evaluate to zero, thus the second and third terms in the mentioned equation are eliminated. The second trace term in Eq. (3.9) is treated in a manner similar to the first, resulting in the final expression for the squared amplitude given by

$$\left\langle |M|^2 \right\rangle = 8\xi^2 \left[ (p_1 p_2)(p_3 p_4) + (p_1 p_4)(p_2 p_3) - m_1^2 (p_2 p_4) - m_2^2 (p_1 p_3) + 2 m_1^2 m_2^2 \right]. \quad (3.10)$$

Equation (3.10) serves as the cornerstone for the following investigation of energy dissipation and multi-particle scattering, elaborated in further detail in this chapter.

### 3.2.2 Quantitative description of the energy loss of charged particles in matter

When a charged particle, like a muon, penetrates and travels through matter, it engages in interactions with the electrons of the atoms contained within the material. First, consider the elastic interaction between the muon and an individual electron. Considering that the muon has a mass significantly larger than that of the electron, it is rational to expect that the muon has negligible deflection, though it does experience a slight loss of energy. Furthermore, because the binding energy of the electron $I$ within the atom is significantly lower than the muon energy, the electron can be approximated as free within the material.

Using the notation of Fig. 3.1, the following quantities are defined: $\ell_1 \to e^-$, $\ell_2 \to \mu$, $m_1 \to m_e$ and $m_2 \to m_\mu$. For the calculations that follow, the sign of the muon charge is irrelevant due to the presence of the square in the term $\xi^2$ in Eq. (3.10). The number of charges of both particles is $Z_1 = Z_2 = 1$. Under the next assumption, the calculation is conducted in the rest frame of the muon and their initial 4-momenta are

$$\begin{aligned} p_1 &= \begin{pmatrix} p & 0 & 0 & p \end{pmatrix}^\top, & p_2 &= \begin{pmatrix} m_\mu & 0 & 0 & 0 \end{pmatrix}^\top, \\ p_3 &= \begin{pmatrix} p & p\sin\vartheta & 0 & p\cos\vartheta \end{pmatrix}^\top, & p_4 &= \begin{pmatrix} m_\mu & 0 & 0 & 0 \end{pmatrix}^\top. \end{aligned} \quad (3.11)$$

The momentum of the electron in Eq. (3.11) is denoted as $p$. Due to the low electron mass, the electron's total energy is approximated its momentum $E \approx p$. Now that the momenta have been established and inserted into Eq. (3.10), the differential cross section (Mott scattering [87]) is observed in the charged muon's rest frame. It is given by

$$\frac{d\sigma}{d\Omega} = \frac{\alpha^2}{p^2\beta^2 \sin^4 \vartheta/2}(1 - \beta^2 \sin^2 \vartheta/2), \tag{3.12}$$

where $\beta$ is the velocity of the electron relative to $c$, and $\alpha = e^2/4\pi \approx 1/137$ stands for the Sommerfeld fine-structure constant. From these variables, the spin correction term, $-\beta^2 \sin^2 \vartheta/2$, reduces the value of Eq. (3.12) as the scattering angle becomes smaller. The energy transfer is defined as $q^2 = 4p^2 \sin^2 \vartheta/2$ and Eq. (3.12) can be reformulated as the cross section per transferred energy

$$\frac{d\sigma}{dq^2} = \frac{8\pi\alpha^2}{\beta^2 q^4}\left(1 - \beta^2 \frac{q^2}{4p^2}\right). \tag{3.13}$$

H. Bethe [88, 89] assumed that $(1 - \beta^2 \sin^2 \vartheta/2) = (1 - \beta^2 T/T_{\max})$, where the maximum possible energy transfer from the muon to electron is

$$T_{\max} = \frac{2m_e\beta^2\gamma^2}{1 + 2\gamma m_e/m_\mu + (m_e/m_\mu)^2}. \tag{3.14}$$

In the rest frame of the electron, the squared transferred momentum can likewise be expressed as $q^2 = 2m_e T$, where $T$ represents the kinetic energy imparted to the electron following the interaction with the muon. Therefore, the cross section per energy reduction scales to

$$\frac{d\sigma}{dT} = \frac{4\pi\alpha^2}{\beta^2 m_e T^2}\left(1 - \beta^2 \frac{T}{T_{\max}}\right). \tag{3.15}$$

Taking into account the interactions of the muon with multiple electrons in a unit volume $dV = ds \cdot dA$, the average energy loss of the muon is

$$-\langle dE \rangle = n_e\, ds \int_{T_{\min}}^{T_{\max}} T \frac{d\sigma}{dT} dT. \tag{3.16}$$

In Eq. (3.16), the number of electrons per unit volume is characterized by $n_e = \rho N_A Z/A$, which incorporates $Z$ as the atomic number of the material, the Avogadro number $N_A$, the density of the material $\rho$ and the atomic weight $A$. The integration limits are specified by the lower limit $T_{\min} = I^2/2m_e\gamma^2\beta^2$ and the upper limit $T_{\max}$, which was already defined in Eq. (3.14). The average energy loss per unit of distance $ds$ traversed in the material, described by the Bethe formula without additional correction terms, is

represented by the expression

$$-\left\langle \frac{dE}{ds} \right\rangle = 4\pi N_{\mathrm{A}} \frac{\alpha^2}{m_e} \frac{\rho Z}{A} \frac{1}{\beta^2} \left[ \frac{1}{2} \ln \frac{2m_e \gamma^2 \beta^2 T_{\max}}{I^2} - \beta^2 \right]. \tag{3.17}$$

An additional factor of $1/2$ was incorporated in front of the logarithmic term in Eq. (3.17). This adjustment comes from the approach considering the impact parameter, described through N. Bohr's semi-classical framework [90, 91]. Eq. (3.17), known as the Bethe formula, has been confirmed to be accurate within a few percent for the range $0.1 < \beta\gamma < 1000$ [92]. For the purpose of ionization cooling, Eq. (3.17) is adequate and does not require additional correction terms. A density correction, mentioned in reference [92], is unnecessary because it becomes relevant only at energy levels that exceed those utilized in ionization cooling.

### 3.2.3 Energy loss results in RF-Track and benchmarking

The best candidates for ionization cooling are liquid hydrogen (LH) and lithium hydride (LiH). Initially, LH in its liquid state serves as the preferred ionization cooling medium, necessitating the use of containment windows. LiH is considered a viable option for these windows. As mentioned in the beginning of this chapter, the first scattering experiments using these materials were conducted at the MuScat facility at the TRIUMF laboratory [86]. Simulations of the Geant4 version 6.7 scattering model, using LH, showed significant discrepancies compared to experimental data [74]. Only the ELMS model form W. Allison et al. [93], implemented in ICOOL [94], demonstrated a close alignment with the scattering angles observed in the MuScat experiment. Later scattering experiments with MICE [95] showed much closer agreement with simulated scattering data from Geant4 version 9.4. ICOOL and G4Beamline later updated their scattering models in their codes.

This subsection presents the benchmarking performance of RF-Track compared to ICOOL and G4Beamline. Comparisons with experimental data sets were not included, as ICOOL and G4Beamline have already been benchmarked against these experimental results.

The selection of momentum values, absorber materials, and thicknesses was based on experimental parameters from the MICE study. The test parameters specific to LH were drawn from M. Bogomilov et al. [96], while the data for the reference of solid LiH were referenced from a separate study of M. Bogomilov et al. [97]. A comprehensive summary of the beam and material parameters used in these studies is provided in Table 3.1.

| Material | Liquid hydrogen |
|---|---|
| Parameter | Magnitude |
| Thickness [mm] | 349.6 |
| Density [g cm$^{-3}$] | 0.07053 |
| $E_{\mathrm{Kin}}$ [MeV] | 90.2, 119.7, 153.9 |
| Thickness [mm] | 10 |
| Density [g cm$^{-3}$] | 0.07053 |
| $E_{\mathrm{Kin}}$ [MeV] | 4.2 |

| Material | Lithium hydride |
|---|---|
| Parameter | Magnitude |
| Thickness [mm] | 65.37 |
| Density [g cm$^{-3}$] | 0.69 |
| Li6 mass fraction | 0.814 |
| Li7 mass fraction | 0.043 |
| H mass fraction | 0.143 |
| $E_{\mathrm{Kin}}$ [MeV] | 95.9, 120.5, 156.4 |

**Table 3.1.:** For benchmarking RF-Track against ICOOL and G4Beamline, the initial beam and material parameters were chosen to match those used in the MICE experiment.

### Energy loss benchmarking in LH

To benchmark the energy loss of LH in RF-Track compared to ICOOL, the data of Table 3.1 are taken into account. For higher muon energies, an LH absorber length of 364.9 mm was used. For the lower energy case, an absorber length of 10 mm was chosen. The muon energies under 4 MeV in LH are typically regarded as stopped.

Each simulation begins at the entrance of the absorber element, using a monoenergetic pencil beam consisting of $10^5$ muons. The six-dimensional muon coordinates are evaluated in 50 integration steps, identical in both RF-Track and ICOOL.

Considering the six-dimensional particle coordinates, the energy loss of the muons was analyzed in detail. Fig. 3.2 summarizes the mean energy loss of all muons simulated using RF-Track and ICOOL in LH. For higher energy simulations, the relative error is below 0.10%, demonstrating strong agreement between the RF-Track results and the calculations of the ICOOL data. The relative error between the a set of evaluated data from RF-Track $\mathcal{X}_{\mathrm{RF}}$ and G4Beamline/ICOOL are $\mathcal{X}_{\mathrm{G4BL/ICOOL}}$ for is defined as

$$\mathrm{Err} = \left| \frac{\mathcal{X}_{\mathrm{RF}} - \mathcal{X}_{\mathrm{G4BL/ICOOL}}}{\mathcal{X}_{\mathrm{G4BL/ICOOL}}} \right|. \tag{3.18}$$

The lower right plot in Fig. 3.2 shows a comparison of RF-Track and ICOOL simulations for low-energy scattering analysis. As the absorber length increases, the error grows exponentially as a result of muon losses within the absorber. This loss leads to an increase in relative error as the data points are reduced. For this particular absorber and beam configuration, muon transmission is approximately 10% in both the RF-Track and ICOOL simulations.

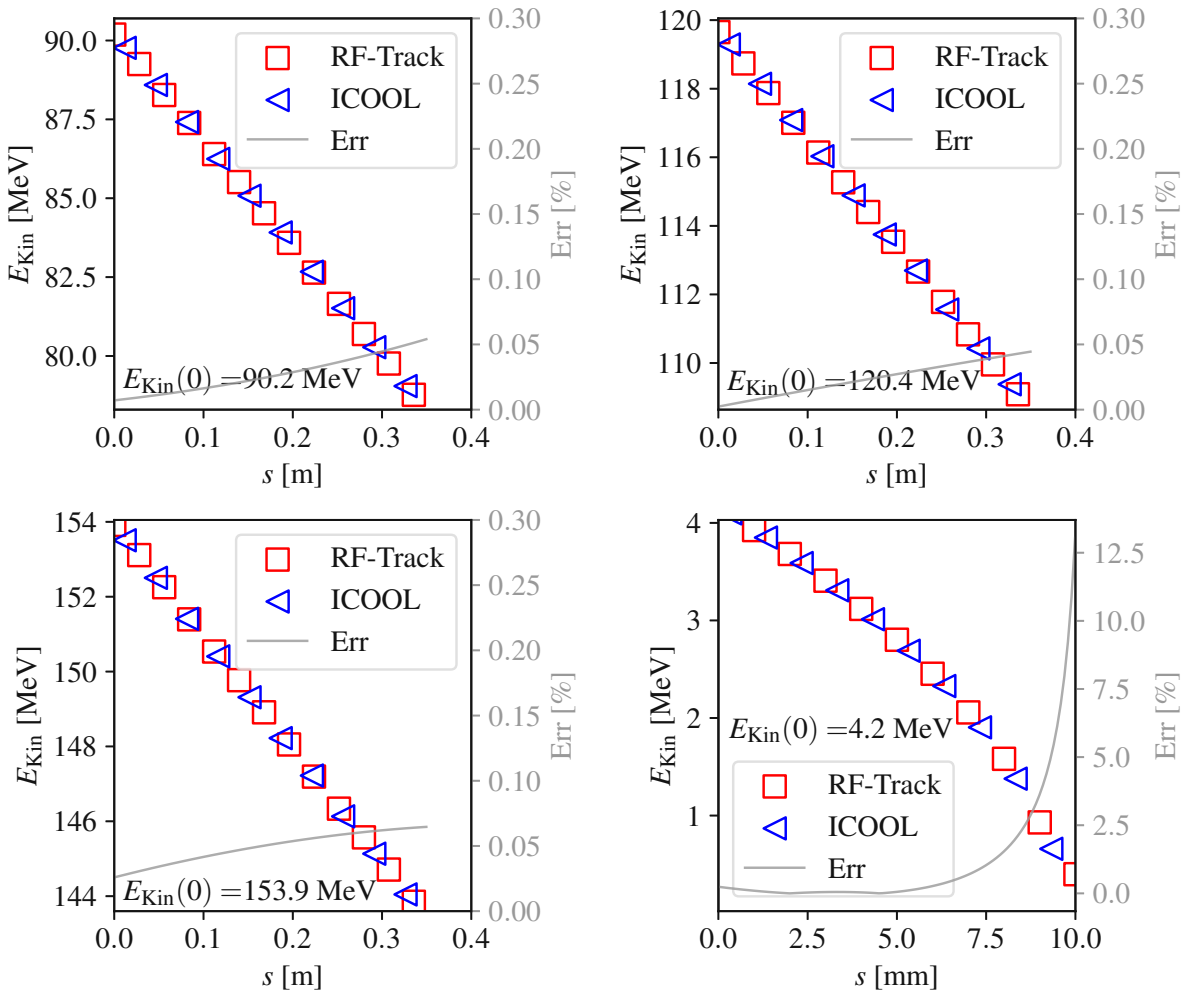


**Figure 3.2.:** The energy loss of muons in LH was compared using RF-Track and ICOOL simulations. These simulations were initiated with a monoenergetic pencil beam containing $10^5$ muons, each traversing a 349.6 mm LH element at initial kinetic energies of $E_{\mathrm{Kin}} = [90.2, 119.7, 153.9]$ MeV, and a 10 mm LH sample with $E_{\mathrm{Kin}} = 4.2$ MeV. For the higher energy scenario, the relative error, depicted as the gray lines, falls within a range below 0.10%, while for the lower energy case, the relative error increases exponentially with absorber length due to muon losses.

### Energy loss benchmarking in LiH

LiH has a solid structure and is composed of Li and H atoms. Naturally occurring Li consists of approximately 90% Li-7, with the remaining 10% being Li-6. ICOOL uses data based on natural Li to define LiH in its absorber list. In contrast, the MICE composition of Table 3.1 uses a configuration enriched with Li-6 and Li-7 in LiH [97].

This particular LiH configuration is enriched with Li-6, which is the standard material used at the US nuclear materials facility [98].

The ICOOL reference manual [72] does not provide a straightforward method for manually mixing a specific absorber configuration. To address this limitation, the LiH benchmark study of RF-Track was conducted using G4Beamline. It should be noted that energy loss benchmarking between ICOOL and G4Beamline was not carried out in this study, as both are well-established and extensively benchmarked codes. The following paragraph will present a code example for mixing materials in G4Beamline, using the LiH configured with MICE as an illustrative case.

In G4Beamline, the material `Li` defaults to natural lithium but can be redefined with specific isotopes by specifying their atomic number, mass, and density. For compounds like LiH, fractional compositions must sum up to one and the total density must be specified. Hydrogen is predefined as `H`, so no redefinition is needed. Below is an example of G4Beamline code for setting up a LiH sample similar to MICE:

```
material Li6 Z=3 A=6 density=0.539
material Li7 Z=3 A=7 density=0.534
material LiH Li6,0.814 Li7,0.043 H,0.143 density=0.69
```

In RF-Track, specific materials mix differently. For example, with LiH, the RF-Track generates volumes for each of the lithium isotopes and an equivalent volume for hydrogen, overlapping these volumes at the same position. For defining a material in the RF-Track composed of molecules, the volumes of each constituent element are overlapped, and their densities are scaled according to their respective contributions to the total density of the compound.

```
rho_LiH = 0.69 #density of MICE LiH in g/cm^3
len = 0.06537 #absorber length in mm
Li6 = RF_Track.Absorber(len, RadLen_Li6, Z=3, A=6, rho_LiH*0.814, I=40.)
Li7 = RF_Track.Absorber(len, RadLen_Li7, Z=3, A=7, rho_LiH * 0.043, I=40.)
H = RF_Track.Absorber(len, RadLen_H, Z=1, A=1, rho_LiH * 0.143, I=21.)
```

To benchmark the energy loss of LiH in RF-Track compared to G4Beamline, key material parameters are presented on the right side of Table 3.1. In the simulations, a LiH absorber of length 65.37 mm was used.

Fig. 3.3 shows the mean energy loss of all simulated muons in RF-Track. It also presents the results of G4Beamline, using LiH as the absorber material. For all three energy scenarios used, the relative error between the RF-Track and G4Beamline results does not exceed 0.2%. This is still below the statistical error of $1/\sqrt{N} = 1/\sqrt{10^5} \approx 0.3\%$, indicates strong agreement between the two approaches.

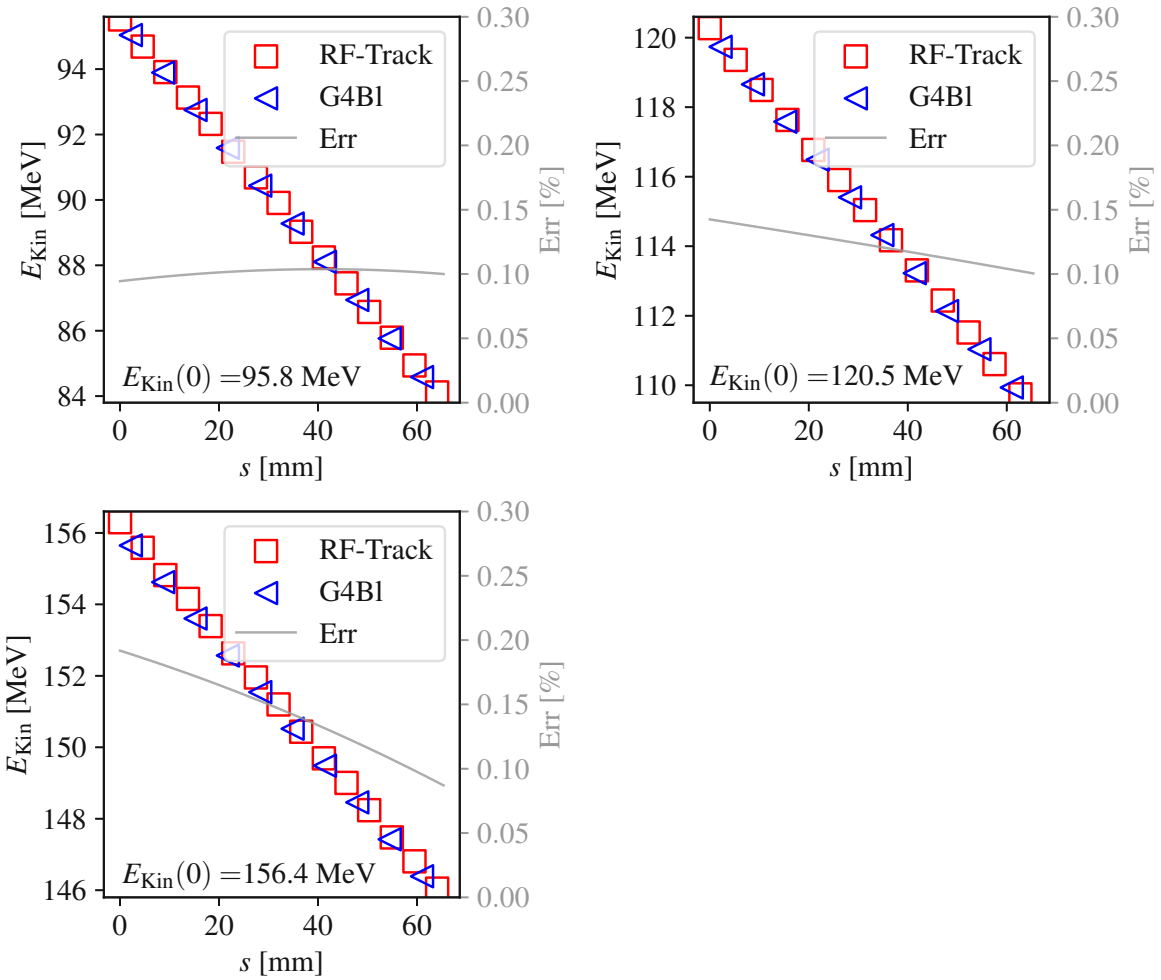


**Figure 3.3.:** The muon energy loss in LiH was examined by comparing simulations from RF-Track and G4Beamline. These simulations began with a monoenergetic pencil beam of $10^5$ muons, each passing through a 65.37 mm LiH element at initial kinetic energies of $E_{\mathrm{Kin}} = [95.9, 120.5, 156.4]$ MeV. The relative error, in gray lines, in these comparisons is below 0.2%.

### 3.2.4 Energy loss fluctuations

As muons or other charged particles traverse a material, their energy loss undergoes stochastic fluctuations, via a phenomenon called energy straggling. The fluctuation is asymmetric around the most probable value of the energy loss distribution. These fluctuations arise mostly from electronic scattering interactions in the material and rarely from the nuclei. The Bethe formula in Eq. (3.17) represents merely an averaged value of the energy loss induced by electronic scattering. Fundamentally, the energy transfer

from a charged particle to matter is small.

However, on occasion, there can be transfers of higher energy, resulting in high-energy recoil electrons. These recoil electrons, termed delta rays [92], introduce tails into the energy loss distribution of a charged particle beam in a material. In the theoretical treatment of energy loss fluctuations [99], a straggling parameter is introduced.

$$\kappa = \frac{\xi}{T_{\max}}, \quad \xi = \frac{k\rho}{\beta^2 m_e} \frac{Z}{A} ds, \tag{3.19}$$

$k = 2\pi N_A r_e^2 m_e \approx 0.157\,\mathrm{MeV\,cm^2\,mol^{-1}}$. The characteristic energy loss $\xi$ simplifies from Eq. (3.17) by omitting the term on the right within the brackets and considering that the logarithm equals one. The maximum energy transfer is indicated by $T_{\max}$ and was defined already in Eq. (3.14).

Upon examining the ICOOL source code [100], it is evident that several energy-loss distributions are utilized depending on the value of $\kappa$, as outlined in the associated table:

| Ranges | $\kappa \leq 0.01$ | $0.01 < \kappa \leq 10$ | $\kappa > 10$ |
|---|---|---|---|
| Distribution | Landau [101] | Vavilov [102] | Gauss [103] |

In the existing version 2.3 of RF-Track, the Gaussian distribution is the only probabilistic representation implemented within the code. The standard deviation of a Gaussian energy loss distribution per unit path length is described in

$$\frac{d\sigma_E^2}{ds} = k \frac{Z}{A} \rho \gamma^2 \left(1 - \frac{\beta^2}{2}\right). \tag{3.20}$$

A comparative analysis of the energy loss distribution patterns is illustrated in Fig. 3.4, comparing ICOOL and RF-Track. Both simulations used an identical material thickness and a 100 MeV monoenergetic pencil muon beam. The energy distribution after the thickness of the material in the RF-Track shows a symmetric Gaussian profile, whereas the distribution of ICOOL is asymmetric. The implementation of this distribution in RF-Track is beyond the scope of this thesis, but has been identified as a necessary update for the developers.

## 3.3 Scattering of charged particles in matter

The deflection of charged particles in matter, known as multiple Coulomb scattering (MCS), plays a crucial role in various areas of physics. Direct simulation of particles that undergo repeated interactions with atomic nuclei is computationally intensive.

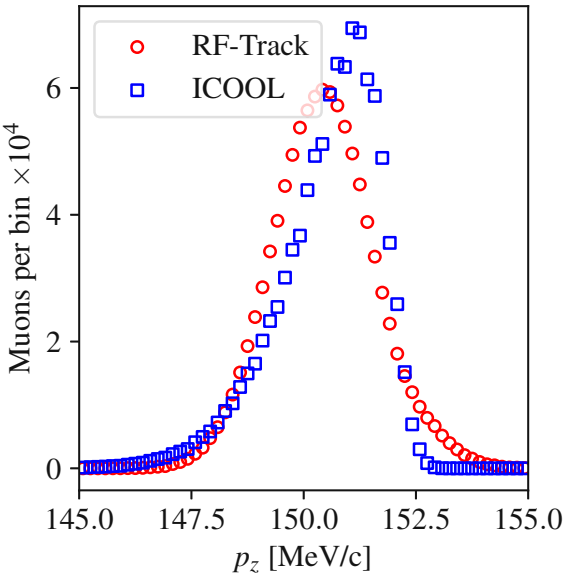


**Figure 3.4.:** The longitudinal distribution of muons from an initial 100 MeV monoenergetic muon pencil beam is presented in the form of a histogram after passing through 164 mm of LH material. The energy straggling distribution within RF-Track exhibits a symmetric Gaussian profile. To facilitate a benchmark against ICOOL simulations, it is necessary to incorporate an implementation of both the Landau and Vavilov distributions into the code.

Therefore, probabilistic scattering models, such as G. Molière's framework [104] and subsequent refinements by H. Bethe [105] and W. Scott [106], provide practical approximations. Although MCS has a fundamentally non-Gaussian character, it is commonly approximated with a Gaussian core and non-Gaussian tails generated by single scattering events. This approximation is especially relevant for the advancement of cooling simulations in this thesis.

Precise modeling of ionization cooling is based on an accurate representation of MCS events. This section describes the enhancements of RF-Track through the integration of a swift and novel MCS model. These enhancements extend the utility of RF-Track in the design of the cooling channels for muon colliders. The new model employs a semi-Gaussian mixture approach, parameterized with the Bethe-Wentzel deflection width. This section begins with a compact theoretical and historical review of single-scattering models and then presents the semi-Gaussian algorithm. In the end, this section benchmarks the RF-Track results against those of comparable ICOOL and G4Beamline simulations and interprets the findings in the concluding remarks.

### 3.3.1 Motivation for scattering analysis in low-$Z$ materials

The mathematical model of ionization cooling for low-$Z$ materials significantly diverges from the measurements, which will be demonstrated in this section and in the following chapter. The discrepancy arises because the theoretical framework for ionization cooling is based on the Lynch-Dahl modification [107] of the Highland formula [108]. This framework was popularized by the Particle Data Group [92].

Such a scattering formula encounters two primary issues when applied to light-atomic materials. First, it accounts for the atomic number $Z$ indirectly through the radiation length, which is based on an approximation that lacks precision for light materials. Highland introduced an additional logarithmic term to the Rossi-Greisen formalism [109]. This was done to adjust the dependence on $Z$, factoring in the length of the absorber. However, this modification presents another significant problem. When Highland's equation is applied for particle tracking algorithms, the results become significantly sensitive to the step size due to the non-convoluting nature of a logarithmic term. This dependency creates inconsistencies that compromise the accuracy of the modeling process.

### 3.3.2 Rutherford scattering

If a muon passes close enough to the Coulomb field of a nucleus, both exchange virtual QED force carriers, photons, which is the actual scattering process. The Coulomb force is assumed to originate between the muon charge $\pm e$ and the nucleus charge $Ze$. To determine the elastic deflection angle of the muon in the nucleus, the analytical approach described in Section 3.2.1 can be used. Referring to Fig. 3.1, $\ell_1$ represents the muon possessing mass $m_1 = m_\mu$, while $\ell_2$ denotes the nucleus with mass $m_2 = m_\mathrm{N}$.

Within the laboratory frame-of-reference, the muon is moving towards a stationary nucleus. By employing the Rutherford approximation, the recoil of the nucleus is treated as negligible, thus enabling a compact representation of the momenta as follows:

$$\begin{aligned} p_1 &= \begin{pmatrix} E & 0 & 0 & p \end{pmatrix}^\top, & p_2 &= \begin{pmatrix} m_N & 0 & 0 & 0 \end{pmatrix}^\top, \\ p_3 &= \begin{pmatrix} E & p\sin\vartheta & 0 & p\cos\vartheta \end{pmatrix}^\top, & p_4 &= \begin{pmatrix} m_N & 0 & 0 & 0 \end{pmatrix}^\top. \end{aligned} \tag{3.21}$$

The variables $p$ and $E$ denote the momentum and energy of the muon in Eq. (3.21), while $\vartheta$ corresponds to its scattering angle. Substituting the four-momenta from Eq. (3.21) into Eq. (3.8) results in an squared average amplitude denoted by

$$\left\langle |M|^2 \right\rangle = \xi^2 m_\mu^2 m_N^2 \left(1 + \beta^2\gamma^2 \cos^2\vartheta/2\right), \quad \xi^2 = \frac{Z^2 e^4}{p^4 \sin^4\vartheta/2}. \tag{3.22}$$

In Eq. (3.22) the terms $\beta$ and $\gamma$ refer to the Lorentz factors of the muon. The cross section within the laboratory frame, as derived from [7], is articulated under the Rutherford approximation, under the premise that the nuclear mass significantly exceeds the muon energy $E$, allowing the differential cross section to be approximated as

$$\frac{d\sigma}{d\Omega} = \frac{1}{64\pi^2} \frac{1}{(m_N + E - E\cos\vartheta)^2} \left\langle |M|^2 \right\rangle \approx \frac{1}{64\pi^2} \frac{1}{m_N^2} \left\langle |M|^2 \right\rangle . \tag{3.23}$$

In the context of Rutherford scattering, it is assumed that the muon is non-relativistic ($\beta\gamma < 1$), and the bracket in Eq. (3.22) is considered to be one. Furthermore, applying the small angle approximation $\sin\vartheta/2 \approx \vartheta/2$, the Rutherford differential cross section consequently scales to

$$\frac{d\sigma}{d\Omega} \approx \frac{Z^2\Xi}{\vartheta^4}, \quad \text{with} \quad \Xi = \left(\frac{2\alpha}{\beta p}\right)^2 . \tag{3.24}$$

### 3.3.3 Rossi and Greisen formula

This section begins with the Rossi and Greisen formula to derive the scattering angle, which will be integrated into the RF-Track. B. Rossi and K. Greisen presented a first characterization of the MCS [109]. In their analysis, they considered an MCS probability density function derived from Eq. (3.24) and the concentration of atoms per unit area $N_\mathrm{A}\rho ds/A$ within a thickness layer of material $ds$. They represented the variance of MCS per unit path length as

$$\frac{\langle\vartheta^2\rangle}{ds} = \int_{\vartheta_\mathrm{min}}^{\vartheta_\mathrm{max}} \vartheta^2 \frac{d\sigma}{d\Omega} \frac{N_\mathrm{A}}{A} \rho d\Omega. \tag{3.25}$$

The angular boundaries $\vartheta_\mathrm{min}$ and $\vartheta_\mathrm{max}$ in Eq. (3.25) are given by

$$\vartheta_\mathrm{min} = \frac{2.66 \cdot 10^{-6}\, Z^{1/3}}{p[\mathrm{GeV}]}, \quad \text{and} \quad \vartheta_\mathrm{max} = \frac{0.14}{A^{1/3}\, p[\mathrm{GeV}]}. \tag{3.26}$$

The definition of the minimum scattering angle, $\vartheta_\mathrm{min}$, presented in Eq. (3.26) is derived from a semi-classical scattering theory [99]. This theory considers the impact parameter to be equivalent to the atomic radius of the Thomas-Fermi potential and incorporates the uncertainty principle. The Rutherford cross section becomes invalid when the wavelength of the charged particle reaches the nuclear radius $r_\mathrm{n}$. This invalidation is analogous to the first minimum observed in the diffraction pattern for an object of size $r_\mathrm{n}$, the scattering angles are confined such that $\vartheta \leq \vartheta_\mathrm{max}$ [110]. For angles $\vartheta > \vartheta_\mathrm{max}$, the inelastic scattering theory is more appropriate, characterized by smaller cross sections and thus insignificant for low-energy muons.

In Eq. (3.25), the small angle approximation can be applied to the differential solid angle

as $d\Omega \approx \vartheta d\vartheta d\varphi$. The resolution of the integral in Eq. (3.25) results in a scaling expressed by

$$\frac{d\langle\vartheta^2\rangle}{ds} = 2\pi\Xi \frac{\rho N_\mathrm{A}}{A} Z^2 \ln\left[\frac{\vartheta_\mathrm{max}}{\vartheta_\mathrm{min}}\right]. \tag{3.27}$$

Assuming $A \approx 2Z$, the logarithmic component in Eq. (3.27) is reduced to

$$\ln\left[\frac{\vartheta_\mathrm{max}}{\vartheta_\mathrm{min}}\right] = \ln\left[229.25^2\, Z^{-2/3}\left(\frac{Z^{1/6}}{A^{1/6}}\right)^2\right] \approx 2\ln\left[\frac{204.24}{Z^{1/3}}\right]. \tag{3.28}$$

Using the definition of the electron radius as given in $r_\mathrm{e} = \alpha/m_\mathrm{e}$, Eq. (3.24) transforms to

$$\frac{d\langle\vartheta^2\rangle}{ds} = 4\pi\left(\frac{m_\mathrm{e}}{p\beta}\right)^2 4r_\mathrm{e}^2 N_\mathrm{A}\frac{\rho Z^2}{A}\ln\left[\frac{204.24}{Z^{1/3}}\right]. \tag{3.29}$$

Rossi and Greisen [109] observed that certain parameters and the logarithmic term in Eq. (3.29) exhibit similarities to the radiation length formula

$$L_\mathrm{R}^{-1} = 4\alpha N_A \frac{Z^2}{A}\rho\, r_e^2 \ln\left(183 Z^{-1/3}\right). \tag{3.30}$$

The root mean square of the Rossi-Greisen scattering angle within a transverse plane, as specified in $\vartheta_0 = \sqrt{\langle\vartheta^2\rangle/2}$, culminates in

$$\vartheta_0 = \frac{E_\mathrm{s}}{\beta p}\sqrt{\frac{s}{L_\mathrm{R}}}, \quad \text{with} \quad E_\mathrm{s} = \sqrt{\frac{4\pi\, m_e^2}{2\alpha}} \approx 15\,\mathrm{MeV}. \tag{3.31}$$

Later, V. Highland [108] compared in his work Eq. (3.31) the Molière-Bethe theory [105] and found inconsistencies for lower $Z$ materials. He adjusted Eq. (3.31) with a fitting parameter and an additional logarithmic term. G. Lynch and O. Dahl [107] fine-tuned Highland's idea and found the final analytical expression

$$\vartheta_0 = \frac{13.6[\mathrm{MeV}]}{\beta p}\sqrt{\frac{s}{L_\mathrm{R}}}\left[1 + 0.038\ln\left(\frac{s}{L_\mathrm{R}}\right)\right], \tag{3.32}$$

with an accuracy of 11% for $10^{-3} < s/L_\mathrm{R} < 10^2$. Eq. (3.32) gives a quick analytical estimate of 98% of the central distribution and is also quoted in [92].

Despite this, Eq. (3.32) is unsuitable for tracking simulations due to the non-additive nature of the logarithmic term. If the integration step of a generic tracking is set to 10% of the radiation length, the fitting parameter would be adjusted to 12.4 MeV. In contrast, when 1% of the radiation length is used, it changes to 11.22 MeV, which clearly violates the convolution property. The initial integration of a scattering model into the

RF-Track code involved omitting the logarithmic component of Eq. (3.32) to

$$\vartheta_0 = \frac{13.6[\mathrm{MeV}]}{\beta p}\sqrt{\frac{s}{L_\mathrm{R}}}. \tag{3.33}$$

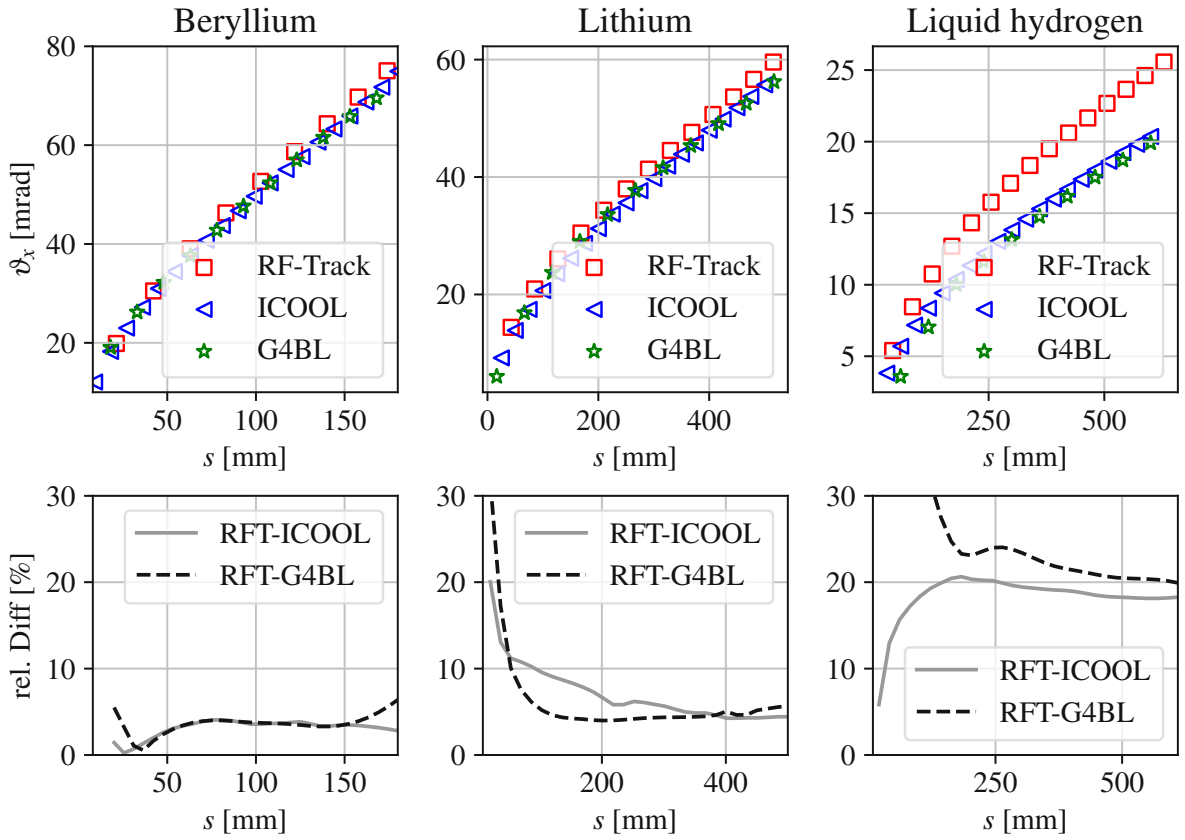


**Figure 3.5.:** The scattering angles of muons were compared using the simulation codes ICOOL, RF-Track, and G4Beamline, with Be, Li, and LH as test materials due to their low atomic numbers. For LH, RF-Track simulations show significant discrepancies in scattering angles compared to the results from ICOOL and G4Beamline. The relative differences are shown below the scattering angle graphs. The dashed line represents the relative error between RF-Track and G4Beamline, while the solid line shows the relative difference between RF-Track and ICOOL. For Be and Li, the deviation remains around the 5% line, whereas for LH, the discrepancy stabilizes at approximately 20%.

For comparison, a muon pencil beam was generated with RF-Track, ICOOL, and G4Beamline and guided through a slab of Be, Li, and LH, using the following beam and material parameters as listed in Table 3.2. The initial kinetic energy of the pencil beam is 100 MeV consisting of $10^5$ positively charged muons.

| [MeV] | $L$ [cm] | $L_{\mathrm{R}}$ [cm] | $\rho$ [g cm$^{-3}$] |
|---|---|---|---|
| Be | 18 | 35.28 | 1.848 |
| Li | 50 | 155 | 0.534 |
| LH | 60 | 890.5 | 0.0708 |

**Table 3.2.:** Parameters of the beam and material for the comparative scattering study involving RF-Track, G4Beamline, and ICOOL. The absorber's thickness is noted as $L$, its radiation length is indicated by $L_{\mathrm{R}}$ and the absorber's density by $\rho$

The standard deviations of the scattered muons for Li and Be were compared, revealing a agreement with the results of ICOOL and G4Beamline, as shown in Fig. 3.5. The relative error for these material tests is approximately 5%. However, Fig. 3.5 demonstrates a significant overestimation for LH, which is the main material of interest for ionization cooling simulations. The relative error between RF-Track and G4Beamline / ICOOL is for LH around 20%.

It is not surprising that the error increases as $Z$ decreases. This trend arises from the approximation of the scattering length used in the Eq. (3.32). The assumption that $A$ is roughly twice $Z$ holds well for heavier elements, but not e.g. LH with $Z \approx A$. Consequently, it is necessary to identify an improved analytical approximation compared to Eq. (3.32), leading to the result outlined below.

### 3.3.4 Bethe-Wentzel scattering

J. Cobb and T. Carlisle [111, 112] put forward a scattering model in low-$Z$ materials derived from Bethe and Wentzel, incorporating electron- and nucleus interactions [105, 113]. The Rutherford differential cross section in Eq. (3.24) can be adjusted by implementing the minimum cut-off angle $\vartheta^{-4} \to (\vartheta^2 + \vartheta^2_{\mathrm{min}})^{-2}$ from Eq. (3.26) to prevent singularities. Additionally, it can be modified with contributions from electron screening by replacing $Z^2$ with $Z(Z+1)$. The variance of multiple Coulomb scattering per unit length can be divided into nuclear and electronic components, with the aforementioned adjustments, leading to

$$\frac{d\langle\vartheta^2\rangle}{ds} = \frac{\Xi\,\rho\,N_{\mathrm{A}}}{A}\left[\int_{\vartheta_{\mathrm{min}}}^{\vartheta_{\mathrm{max}}} \vartheta^2 \frac{Z^2\,d\Omega}{(\vartheta^2+\vartheta^2_{\mathrm{min}})^2} + \int_{\vartheta^{\mathrm{e}}_{\mathrm{min}}}^{\vartheta^{\mathrm{e}}_{\mathrm{max}}} \vartheta^2 \frac{Z\,d\Omega}{(\vartheta^2+\vartheta^2_{\mathrm{min}})^2}\right]. \tag{3.34}$$

The bounds for the integration of the second component, the screening contribution, in Eq. (3.34) are determined in [110, 112]. These are given by

$$\vartheta^{\mathrm{e}}_{\mathrm{min}} = \arccos\frac{p^2 - I(m_{\mathrm{e}}+E)}{p\sqrt{(E-I)^2 - m_\mu^2}}, \quad \vartheta^{\mathrm{e}}_{\mathrm{max}} \approx \frac{m_{\mathrm{e}}}{m_\mu}. \tag{3.35}$$

The resulting expression for the scattering variance per unit length in a single dimension can be written as

$$\frac{d\langle\vartheta^2\rangle}{ds} = \rho\frac{m_e\, k}{2A}\left(\frac{Z}{\beta p}\right)^2\left[F\left(\frac{\vartheta_{\max}}{\vartheta_{\min}}\right) + \frac{1}{Z}F\left(\frac{\vartheta^e_{\max}}{\vartheta^e_{\min}}\right) - 1.19\left(1+\frac{1}{Z}\right)\right]. \tag{3.36}$$

The auxiliary function, the solution of the integral in Eq. (3.34), is defined as

$$F(x) = \frac{1}{1+x^2} + \ln\left(1+x^2\right). \tag{3.37}$$

### 3.3.5 The Semi-Gaussian mixture model

The semi-Gaussian mixture model, introduced by R. Frühwirth [114], offers an effective approach to track particles in materials that include MCS. Its main component adopts a Gaussian shape within the MCS, complemented by supplementary non-Gaussian tail distributions. These tails account for single scattered particles, as detailed in Eq. (3.24) and remain applicable in thicker materials. The marginal mixture density function is expressed as

$$f(\vartheta) \propto (1-\epsilon)\frac{\vartheta e^{\frac{-\vartheta^2}{2\sigma^2}}}{\sigma^2} + \epsilon\frac{2a^2\vartheta}{\left(\vartheta^2+a^2\right)^2} \tag{3.38}$$

where the initial term represents the Gaussian core, while the latter term accounts for the extended tails. The variable $\epsilon$ in Eq. (3.38) describes the amount of particles participating in the core and in the tails of the distribution.

In the literature, a Gaussian tail approximation is also observed [115]. However, this method is recommended for layer thicknesses greater than the radiation length of the material. In an ionization cooling channel, the absorber length is usually an order of magnitude smaller than their radiation length.

Random scattering angles are determined via two inverse cumulative distribution functions, represented as:

$$\vartheta = \begin{cases} \sigma\sqrt{-2\ln u}, & \text{if } v > \epsilon, \\ ab\sqrt{\dfrac{1-u}{ub^2+a^2}}, & \text{if } v < \epsilon. \end{cases} \tag{3.39}$$

The initial term in Eq. (3.39) is used for creating the Gaussian core. The second term is relevant to long-range tails. In Eq. (3.39), $u$ and $v$ represent uniform random variables within the interval [0,1]. The coefficients $(\sigma, a, b, \epsilon)$ in Eq. (3.39) are calculated following the procedures described in [116]. The values of these coefficients are influenced by the type of particle and the properties of the material used. Given the material thickness

$ds$ and the particle velocity $\beta$, two critical functions are introduced:

$$n = Z^{0.1} \ln \overline{N}, \quad \text{with} \quad \overline{N} \approx \frac{2.215 \cdot 10^4 \cdot Z^{\frac{4}{3}}}{\beta^2 A} ds. \tag{3.40}$$

The variance for the Gaussian component in Eq. (3.39) is expressed as

$$\sigma^2 = 0.1827 + 0.01803n + 0.0005782n^2. \tag{3.41}$$

The tail parameter is determined using

$$a = 0.2822 + 0.09828\, n - 0.01355\, n^2 + 0.001330\, n^3 - 4.590 \times 10^{-5}\, n^4. \tag{3.42}$$

The third parameter of the single scattering distribution is expressed as

$$b = \frac{\vartheta_{\max}}{\vartheta_{\min}} \Bigg/ \sqrt{\overline{N} \left( \ln \frac{\vartheta_{\max}}{\vartheta_{\min}} - 0.5 \right)}. \tag{3.43}$$

After calculating $a$, $b$ and $\sigma$, the tail weight factor can calculated according to

$$\epsilon = \frac{1 - \sigma^2}{a^2 \left( \ln \left( a/b \right) - 0.5 \right) - \sigma^2}, \tag{3.44}$$

that controls whether the scattered particle contributes to the core or to the tail of the distribution. The projected angles in the $x$ and $y$ directions are perpendicular to the longitudinal particle propagation $s$. They are connected via the azimuth angle $\varphi$,

$$\vartheta_x = \vartheta \cos \varphi, \quad \vartheta_y = \vartheta \sin \varphi, \tag{3.45}$$

where $\varphi$ follows a uniform distribution in the range $[0, 2\pi)$. These two angles are not correlated, but are not independent. The total variance of the generated angles from Eq. (3.39) is equal to one and must be parameterized with Eq. (3.34).

### 3.3.6 Convolution property of the MCS distribution

The statistical properties of MCS should adhere to the convolution property. The convolution principle defines that the same scattering is provided, regardless of the number of steps in the simulation. That means, a slab of material with thickness $d$ should be equivalent to the scattering distribution resulting from slabs of $n$ of the same material, each with a thickness of $d/n$.

The Central Limit theorem states that the sum of a large number of independent random variables converges towards a normal distribution. As shown in Fig. 3.6, the semi-

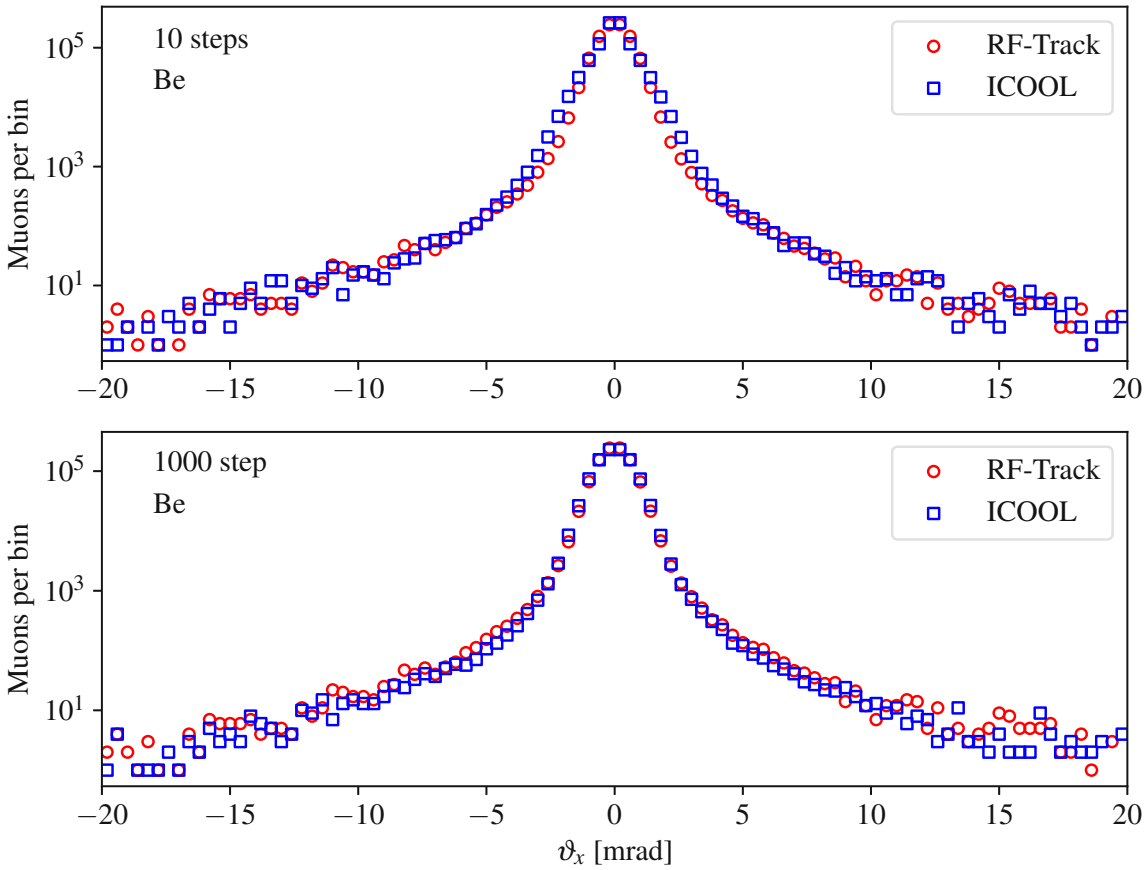


**Figure 3.6.:** The scattering distributions of muons in beryllium (1% radiation length) were compared between RF-Track and ICOOL simulations using a 1 GeV pencil beam of $10^6$ muons with tracking steps of $10^1$ and $10^3$. RF-Track results show consistent scattering distribution tails regardless of step size, while ICOOL exhibits slight changes in the core distribution shape for 10 steps compared to 1000 steps, highlighting a lack of step-size convolution in its current model.

Gaussian mixture model retains its elongated tail. Despite executing a substantial number of integration steps, it does not achieve convergence to a normal distribution. It is crucial to highlight that the scattering distributions' tails persist even after multiple tracking steps.

To analyze muon deflections, the size of the computational step in RF-Track and ICOOL was varied. Beryllium was used in the first test simulation, with a thickness of 1% of its radiation length. In Fig. 3.6, the resulting RF-Track distributions were compared with those obtained from ICOOL. Both programs used a 1 GeV pencil beam of $10^6$ muons to penetrate the samples, with simulations repeated for the $10^1$ and $10^3$ tracking steps.

In Fig. 3.6, modifying the integration step size does not affect the tail sections of the scattering distribution. In the current ICOOL model, the convolution property is lacking at different step sizes. For the $10^1$ steps, the shape of the core distribution pattern in ICOOL changes slightly compared to the case with the $10^3$ steps.

A distribution based on a semi-Gaussian mixture parameterized with Bethe-Wentzel scattering is a novel charged-particle deflection solution in material. The semi-Gaussian mixture model demonstrates that the accuracy of the scattering distribution is maintained even with reduced integration step sizes. Consequently, RF-Track can employ smaller integration steps in the simulation of an ionization cooling channel, thereby optimizing computational efficiency.

The following analysis concentrates on materials relevant to ionization cooling, specifically LH and LiH. The lengths of these materials and the initial energies of the muons are enumerated in Table 3.1 related to the MICE test samples. For comparison of muon scattering distribution patterns, a pencil beam of positively charged muons $10^6$ is generated at the entrance of each material slab in the simulations. At the end of each absorber sample, the angle of each muon was recorded and compared with other simulations. Throughout every simulation, the number of integration step sizes is kept at $10^2$ to ensure that ICOOL and G4Beamline produce precise distribution patterns. The analysis of scattering distributions for the 4 MeV scenario in Table 3.1 was excluded from the comparison. The exclusion was attributed to the significant muon losses detected in that specific simulation.

The benchmarking of LH was conducted using ICOOL and evaluated against RF-track's novel semi-Gaussian mixture model. The comparison involving LiH was made using G4Beamline. This was initiated by the distinct composition of Li-6 and Li-7 from the MICE experiment, which is not included in the standard ICOOL material database.

The results are depicted in Fig. 3.7, with LH histograms presented in the left column and LiH plots positioned on the right. In each histogram, the core distributions exhibit substantial agreement between all simulation codes. It is apparent that both ICOOL and G4Beamline accommodate particles exhibiting extensive scattering distances, whereas the RF-Track's semi-Gaussian model demonstrates a truncation in its tail distribution. The occurrence of extensively scattered particles in ICOOL and G4Beamline ranges from 50 to 100. In contrast, compared to $10^6$ macro particles, the incidence of such long-range particles is markedly lower. Nevertheless, in the context of ionization cooling simulations, the presence of these particles is likely to introduce distortions in the beam parameter results, and thus they should be excluded from the analysis.

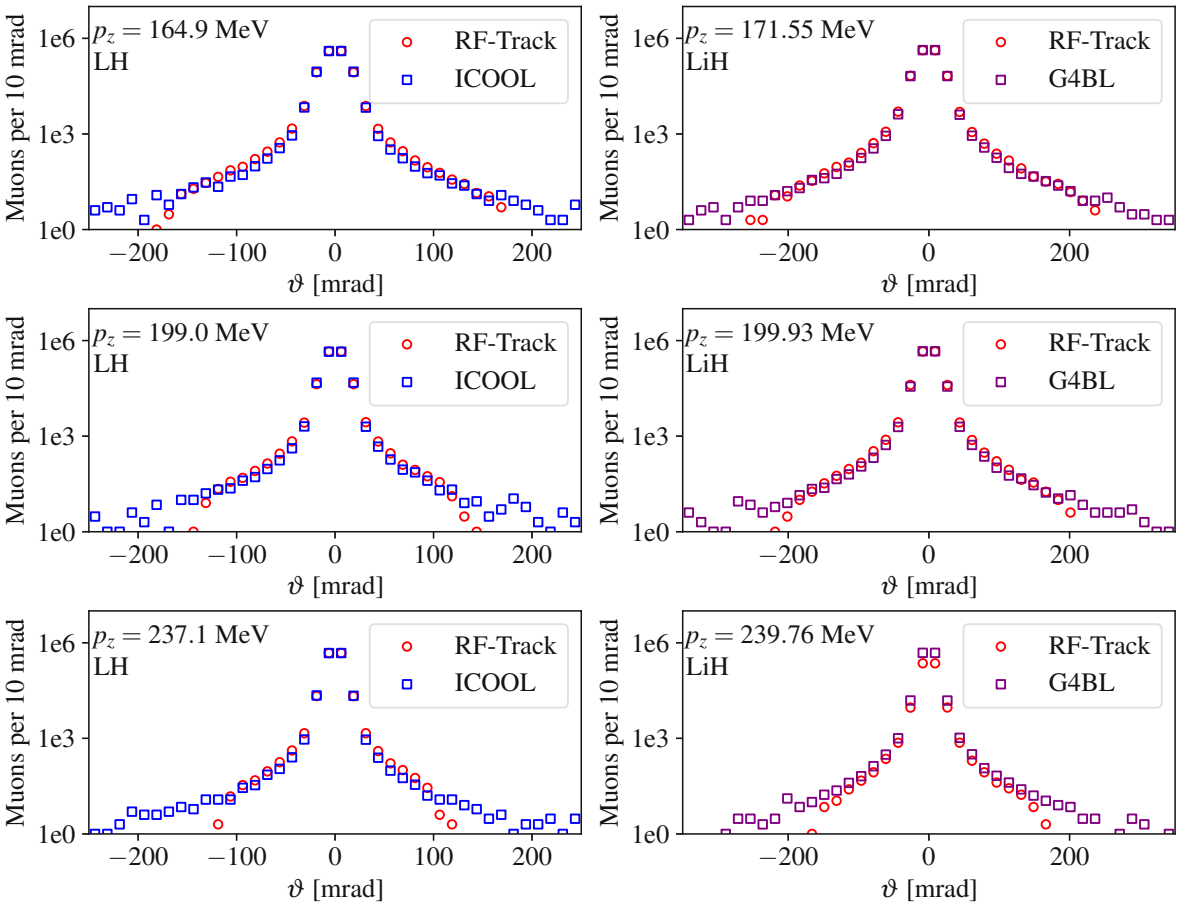


**Figure 3.7.:** The results show that the core distributions are consistent across all simulation codes. ICOOL and G4Beamline capture particles with significant scattering distances, while RF-Track's semi-Gaussian model truncates the tail distribution. The occurrence of very high scattered particles in ICOOL and G4Beamline ranges in the order of 100, compared to a total particle number of $10^6$. These long-range particles can distort beam parameter results in ionization cooling simulations and should be excluded from the analysis.

### 3.3.7 Deflection angle comparisons

The scattering angles were evaluated and compared at different material thicknesses. The conditions for the beam and the material were consistent with those in the previous analysis of the scattering pattern. However, a particle muon count of $10^5$ was selected to accelerate the simulation speed. The number of integration steps for all simulations was established at 30. The scattering angles were investigated after each step. The LH scattering angle benchmark was performed using both ICOOL and RF-Track, as shown

in Fig. 3.8. This figure also presents the analytical solution of Eq. (3.36).

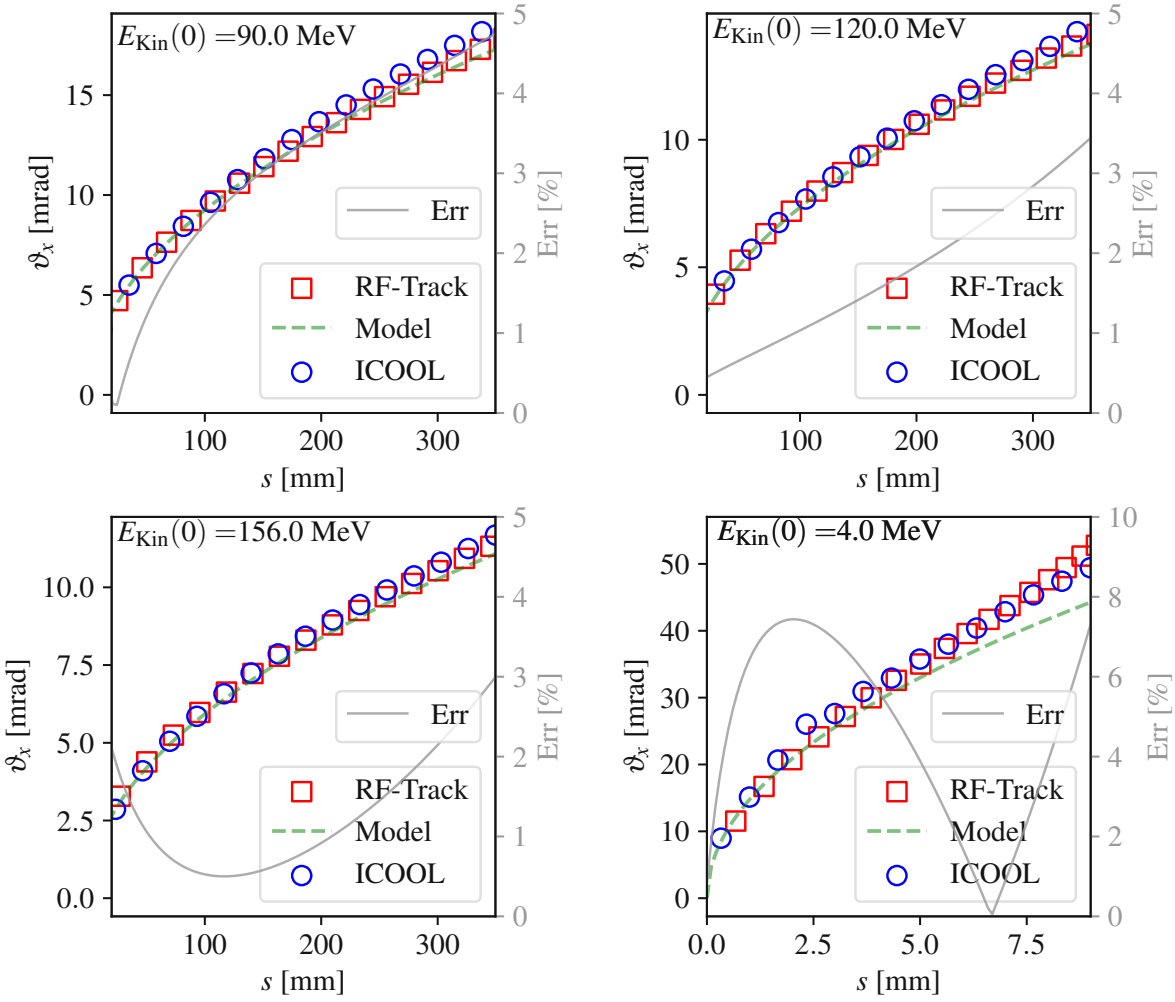


**Figure 3.8.:** In energy scenarios of [90.2, 119.7, 153.9] MeV, the benchmarks demonstrate strong agreement, with relative errors consistently below 5%. These errors follow a systematic pattern due to differences in the scattering models of RF-Track and ICOOL: they increase with the path length through the material. This behavior highlights compatibility between RF-Track's semi-Gaussian mixture approach and ICOOL's MCS model. In the lower-energy scenario of 4 MeV, relative errors are higher. This is primarily due to significant particle losses as muons stop and decay within the material, resulting in increased simulation error from information loss.

In the context of higher-energy scenarios, the benchmarks exhibit a high degree of consistency, as illustrated in Fig. 3.8. Relative errors consistently remain below 5%, similar to the results for Be and Li in Fig. 3.5. However, the relative errors reveal a systematic pattern attributable to the distinct scattering models employed by RF-Track and

ICOOL. Specifically, as the material lengths of the tracked particles increase, the relative error increases slightly. This earlier observation suggests that RF-Track's semi-Gaussian mixture method is well-matched with the MCS model used by ICOOL.

In the low-energy analysis shown in the bottom right graph of Fig. 3.8, the relative error is greater compared to that observed at higher energy levels. This can be explained, as mentioned earlier, by substantial particle losses occurring when muons are completely stopped and decay within the material. From a statistical perspective, this loss of particles translates to a loss of information in the simulation, resulting in an increased error.

Finally, the analysis was performed using the beam kinetic energies referenced in 96 MeV and 156 MeV, on a LiH material of thickness 65.37 mm. The benchmark results, obtained through RF-Track and G4Beamline, are illustrated in Fig. 3.9. These results demonstrate a relative error behavior analogous to that in Fig. 3.8. The marginally higher relative error can be attributed to the disparate materials mixture methodologies employed by RF-Track and G4Beamline, as previously elucidated in Section 3.2.3.

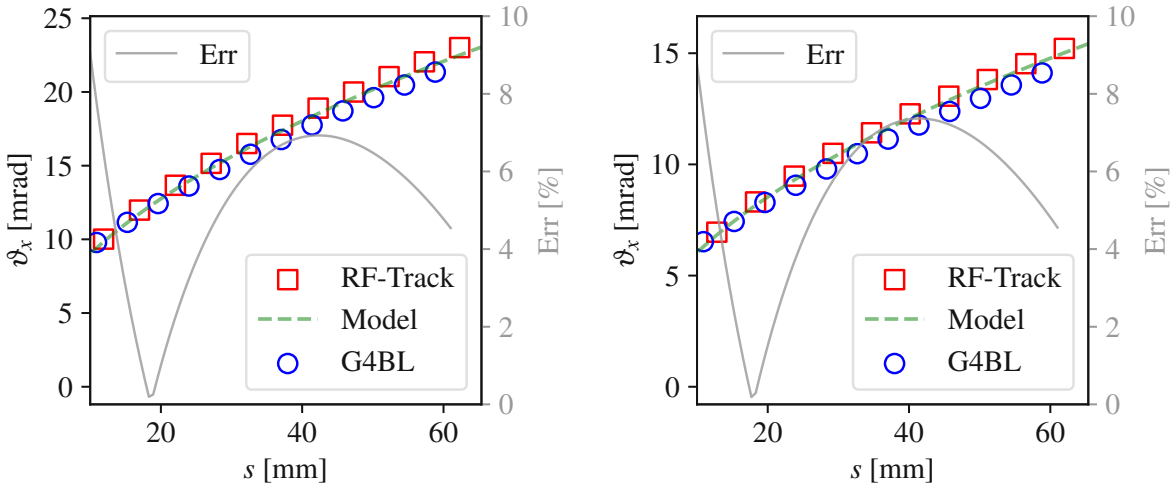


**Figure 3.9.:** The benchmark study was conducted on LiH material. The results demonstrate a trend of relative error similar to prior observations in LH, albeit with slightly higher errors. This variance can be attributed to the differing material combination methods used by RF-Track and G4Beamline, as discussed earlier.

## 3.4 Summary of charged particle interaction in RF-Track

The key interactions between charged particles and matter relevant to ionization cooling involve electronic energy losses and their related fluctuations. In addition, these interactions include nuclear multiple Coulomb scattering (MCS). The theoretical framework for representing energy losses is founded on the Mott differential cross section, with the inclusion of spin corrections. For MCS, the fundamental element is the Rutherford cross section, serving as the foundation for developing statistical models of charged particle deflection. An enhanced formula conceived by Cobb and Carlisle [111, 112] has been developed, which describes the Wentzel-Bethe deflection approach. It is embedded within RF-Track to more accurately represent the statistical variability of scattering. This addresses the issue that existing approximations for deflection angles of charged particles in liquid hydrogen (LH) either do not preserve the convolution property or are overly accurate.

A semi-Gaussian mixture model for MCS in RF-Track was developed and implemented. This model consists of a Gaussian core distribution and non-Gaussian tails, and it is parameterized using the Bethe-Wentzel scattering angle approach. The model maintains long-range scattering tails over a number of integration steps. It shows strong agreement with comparable ICOOL and G4Beamline simulations.

Comparisons of the mean energy loss in RF-Track with both ICOOL and G4Beamline show remarkable consistency. Similarly, benchmarking of the MCS standard deviation angles in RF-Track against ICOOL and G4Beamline yields impressive results. The new scattering model introduced in RF-Track is suitable for particles that are heavier than electrons and positrons.

The motivation for beginning simulation studies of ionization cooling using RF-Track lies in its sophisticated implementation of collective effects. Compared to ICOOL and G4Beamline, RF-Track offers a wider range of collective effect models in its software. The exploration of these collective effects within ionization cooling channels is still relatively unexplored territory in muon collider research. RF-Track offers a strong platform for expanding this knowledge, but could greatly improve by fine-tuning certain elements, particularly by enhancing the energy-straggling model. Presently, the energy loss fluctuations are based on a Gaussian approximation, which does not entirely capture the real physics of the phenomenon.

# Chapter 4.

# Beam dynamics in ionization cooling

In accelerator physics, beam dynamics involves particles traveling through structures consisting of magnets and RF cavities. In the final cooling channel, the reference trajectory is a straight line as it incorporates only solenoids and RF systems. Additionally, the solenoids are filled with energy-absorbing material, which always manipulates the normalized phase space in each degree of freedom.

In this chapter, a practical current sheet model for solenoids was implemented in RF-Track and benchmarked against G4Beamline, providing an accurate and efficient method for evaluating 3D magnetic fields. The transverse beam dynamics in solenoidal fields was explored using a modified Courant-Snyder formalism that incorporates canonical angular momentum to account for coupling effects.

Analytical models that describe the evolution of the emittance in solenoids with absorbers were developed, enhancing Neuffer's cooling equation[1] and showing excellent agreement with simulations. These models enable efficient optimization of the initial beam energies. Finally, the chapter examines the deposition of energy in absorbers and windows, providing key insights into the critical thermal behavior of cooling channel design.

## 4.1 How to cool muon beams

A muon beam, generated from pion decays, occupies a large volume in phase space. The emittance characterizes the volume the beam occupies in phase space and has to be reduced to reach high luminosities for future $\mu^-\mu^+$ -collisions. The target emittances are achieved within the final cooling channel of the muon collider accelerator complex [25]. To push minimal transverse emittance, it is essential to employ solenoid fields at their maximum capacity for very strong focusing.

[1] This is presented in Chapter 4.5 in Eq. (4.51).

Each segment of this channel contains a **solenoid** that features an extremely strong field (40 T). Inside the solenoid, an **energy absorbing material** is placed, followed by an **RF acceleration cavity** located next to the solenoid. While muons penetrate the absorber, they lose momentum in all three spatial directions. Muons gain longitudinal momenta through the re-acceleration in an RF cavity, as illustrated in Fig. 4.1, while the transverse velocities remain unchanged.

Coulomb scattering of muons by the absorber's nuclei reduces the cooling effect because it increases the transverse momenta of the muons within the bunch. The strong magnetic fields of the solenoid diminish the absorber-induced divergence increase of the muon beam. Low atomic number materials have more energy loss per scatter and counteract the transverse momentum increases. The muon beam traverses through multiple final cooling cells, analogous to Fig. 4.1, until the target emittance values are attained.

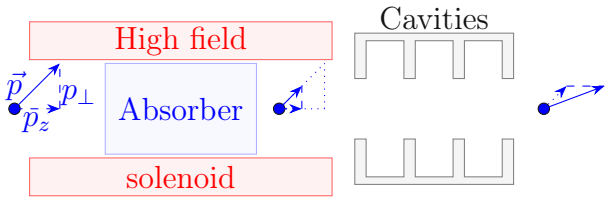


**Figure 4.1.:** A final cooling cell initially reduces the momenta of muons in all spatial directions. A longitudinal re-acceleration results to a decrease the divergence of the momenta. The strong fields of the solenoid counteracts divergence growth induced by scattering effects of the absorber.

This chapter provides a summary of a comprehensive theoretical framework, the tools of which will be utilized for the final cooling design in Chapter 5. Furthermore, this chapter expands on the theoretical ionization cooling framework, contributing not only to the design of the final cooling cells but also potentially aiding future research in this area.

## 4.2 Analytical field model for solenoids

An electric current passing through a wire creates a circular magnetic field around it, as described by the Biot-Savart law. A solenoid, composed of wire coiled in a spiral form, produces a magnetic field along its length when current flows. The magnetic field can theoretically be determined by adding the fields of each individual coil, although this method is inefficient.

There is an analytic solution for the magnetic field produced by a cylindrically symmetrical current sheet. A solenoid can be represented as a series of coaxially arranged current

sheets. This model, referred to as the finite current sheet model, offers an analytic solution for a practical solenoid.

This section provides a mathematical summary of the finite current sheet model. The implementation of this model into the RF-Track code facilitates the execution of ionization cooling simulations. A comparative tracking study was conducted that involved muons within equivalent solenoids using both RF-Track and G4Beamline. The benchmarking results demonstrate a high degree of consistency, thereby establishing RF-Track as a sophisticated tool for muon cooling investigations.

### 4.2.1 Current sheet model

A solenoid is assembled by integrating the contributions of a multitude of identical coaxial loops. In an initial approximation, the thickness of these wires is considered to be infinitesimally small. The loops are uniformly distributed along their longitudinal axis for finite length $L$. For the sake of simplification, these loops may be represented as an infinitesimally thin conductive and cylinder symmetric current sheet. Within cylindrical coordinates $(\varrho\ \varphi\ z)^\top$, the vector potential at a position $(\varrho, z)$ of a current sheet is articulated as

$$A_\varphi(\varrho,z) = \frac{\mu_0 I}{2\pi L}\sqrt{\frac{r}{\varrho}}\left[\zeta\, k\left(K(k^2)\frac{h^2+k^2-h^2k^2}{h^2k^2} - E(k^2)\frac{1}{k^2} + \frac{h^2-1}{h^2}\Pi(h^2,k^2)\right)\right]_{\zeta_-}^{\zeta_+}, \quad (4.1)$$

with the comprehensive derivation provided in Appendix C.1.2. In Eq. (4.1), $r$ refers to the radius of the sheet with a current $I$. The variables in Eq. (4.1) are defined as

$$\zeta_\pm = z \pm \frac{L}{2}, \quad k^2 = \frac{4\varrho\, r}{(\varrho+r)^2}, \quad h^2 = \frac{4\varrho\, r}{(\varrho+r)^2+\zeta^2}. \quad (4.2)$$

The functions $K, E$ and $\Pi$ are specified as complete elliptic integrals of the first, second, and third kinds, and are detailed in Eq. (C.15). To ensure completeness in Eq. (4.1), the constant $\mu_0$ is specified as the vacuum permeability.

From the vector potential in Eq. (4.1), the radial field component of the current sheet at

$$B_\varrho(\varrho,z) = \frac{\mu_0 I}{2\pi L}\sqrt{\frac{r}{\varrho}}\left[\frac{k^2-2}{k}K(k^2) + \frac{2}{k}E(k^2)\right]_{\zeta_-}^{\zeta_+}, \quad (4.3)$$

while the longitudinal component yields to

$$B_z(\varrho,z) = \frac{\mu_0 I}{4\pi L}\frac{1}{\sqrt{r\varrho}}\left[\zeta\, k\left(K(k^2) + \frac{\varrho-r}{r+\varrho}\Pi(h^2,k^2)\right)\right]_{\zeta_-}^{\zeta_+}. \quad (4.4)$$

The radial field on-axis ($\varrho = 0$) is $B_z(\varrho = 0, z) = 0$, while the longitudinal component scales to

$$B_z(\varrho = 0, z) = \frac{\mu_0 I}{2L}\left(\frac{z + L/2}{\sqrt{r^2 + (z + L/2)^2}} - \frac{z - L/2}{\sqrt{r^2 + (z - L/2)^2}}\right). \tag{4.5}$$

### 4.2.2 Multiple current sheets

In practice, a solenoid possesses a limited thickness $t$, and to utilize a sheet model on an actual solenoid, one can assume the following. The solenoid may be divided into an arbitrary number of coaxial rings with thickness $dt$, as depicted in the left sketch of Fig. 4.2. In the model, each ring is floated with the same current density, $dJ = J/N_{\text{Sheets}}$, while the total current density of the solenoid is described by Eq. (4.6).

$$J = \frac{I}{(r_{\text{out}} - r_{\text{in}})L}. \tag{4.6}$$

In Eq. (4.6), the inner radius of the solenoid is denoted by $r_{\text{in}}$, while the outer radius is represented by $r_{\text{out}}$. Consequently, the solenoid thickness is defined as $t = r_{\text{out}} - r_{\text{in}}$. The total magnetic field of the solenoid is the superposition of $N_{\text{Sheets}}$ sheets within the thickness $t$. The plot on the right in Fig. 4.2 illustrates an example of a solenoid field composed of $N_{\text{Sheets}} = 10$ sheets. This model aligns with realistic solenoid fields as the number of sheets increases.

### 4.2.3 RF-Track solenoid model benchmarks

To carry out ionization cooling simulations within RF-Track, it is essential to have a precise representation of the field map of a solenoid. Accordingly, Eq. (4.3) and Eq. (4.4) from the finite current sheet model were integrated into the RF-Track code. For benchmarking purposes, G4Beamline was employed, and the ensuing results will be detailed below.

Due to the computationally intensive nature of the elliptic integrals in Eq. (4.3) and Eq. (4.4), RF-Track follows the specific strategy. In an RF-Track simulation, when a solenoid is being defined, RF-Track initially generates a 3D mesh-grid that encompasses a volume centered around the solenoid. The magnetic field at these data points will be calculated first by Eq. (4.3) and Eq. (4.4) and will be further used as an input of a 3D interpolation function. The trajectory of the particle is subsequently computed by solving the equations of motion, utilizing the field information returned from the interpolation function. This approach markedly improves computational efficiency by

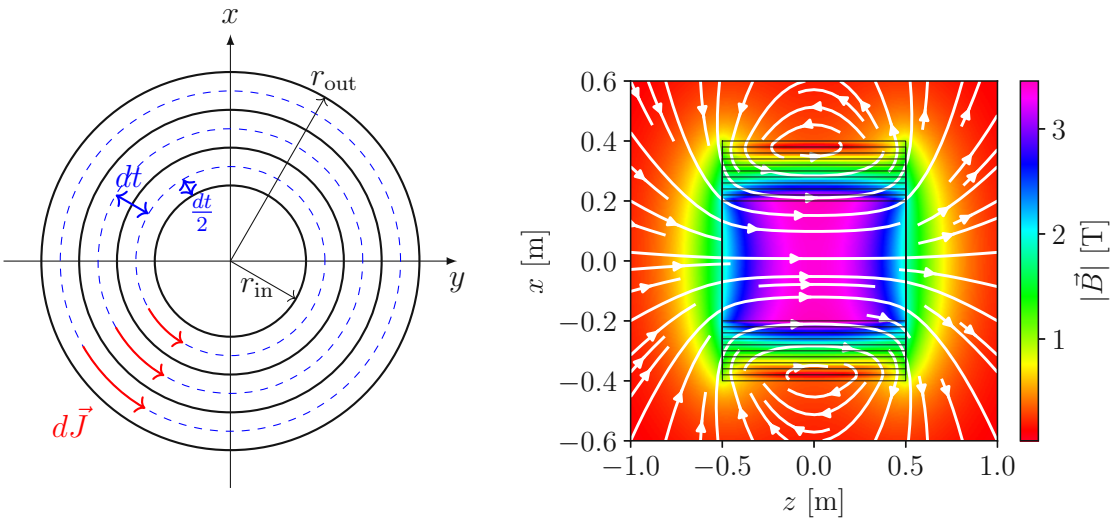


**Figure 4.2.: Left** figure: a solenoid with finite thickness $t$ can be modeled using a sheet approximation by dividing it into an arbitrary number of coaxial rings with thickness $dt$. **Right** figure: An example of a solenoid field composed of 10 finite current sheets with a length of 1 m centered at the origin.

employing interpolation. By doing so, it avoids the need to compute a set of elliptic integrals for each particle at every spatial position.

For the purpose of benchmarking the RF-Track solenoid model using G4Beamline, the solenoid shall be represented by a single cylindrically symmetric block composed of 20 current sheets. The optical parameters of the solenoid are summarized in Table. 4.1. A group of $\mu^+$ test particles will begin tracking from a position 0.5 m upstream of the solenoid's center. The final position of the particle at 0.5 m downstream in both simulations, RF-Track and G4Beamline, will be analyzed and compared for comparative analysis. Initially, 41 $\mu^+$ will have a momentum of 200 MeV/c in the $z$ direction and will be distributed radially at intervals of 10 mm. Fig. 4.2 provides a detailed overview of the particle specifications.

The final positions of the particles as computed by the RF-Track and G4Beamline simulations are illustrated to the left in Fig. 4.3. As depicted in the right-hand graph of Fig. 4.3, the benchmark analysis indicates that the relative error increases with greater radial offset. This suggests that the magnetic fields between G4Beamline and RF-Track are not perfectly aligned, leading to discrepancies in particle trajectories. The source of this misalignment is the mesh-grid interpolation. Despite these differences, both simulations exhibit high accuracy, indicating that RF-Track is capable of effectively modeling complex ionization cooling lattices.

| Coil parameter | Unit | Value |
|---|---|---|
| Inner radius | mm | 250.0 |
| Radial thickness | mm | 169.3 |
| Outer radius | mm | 419.3 |
| Length | mm | 140.0 |
| Current density | A/mm$^2$ | 500.0 |

**Table 4.1.:** Solenoid parameters used for the benchmarking between RF-Track and G4Beamline.

| $\mu^+$ parameter | Unit | Value |
|---|---|---|
| Momentum | MeV/c | 200.0 |
| $z$ start | mm | -500.0 |
| $z$ end | mm | 500.0 |
| Radial spacing | mm | 10.0 |
| Maximum radius | mm | 200.0 |

**Table 4.2.:** In the context of benchmarking, 41 $\mu^+$ will be monitored as they traverses the solenoid. The detailed parameters of the particle are provided above.

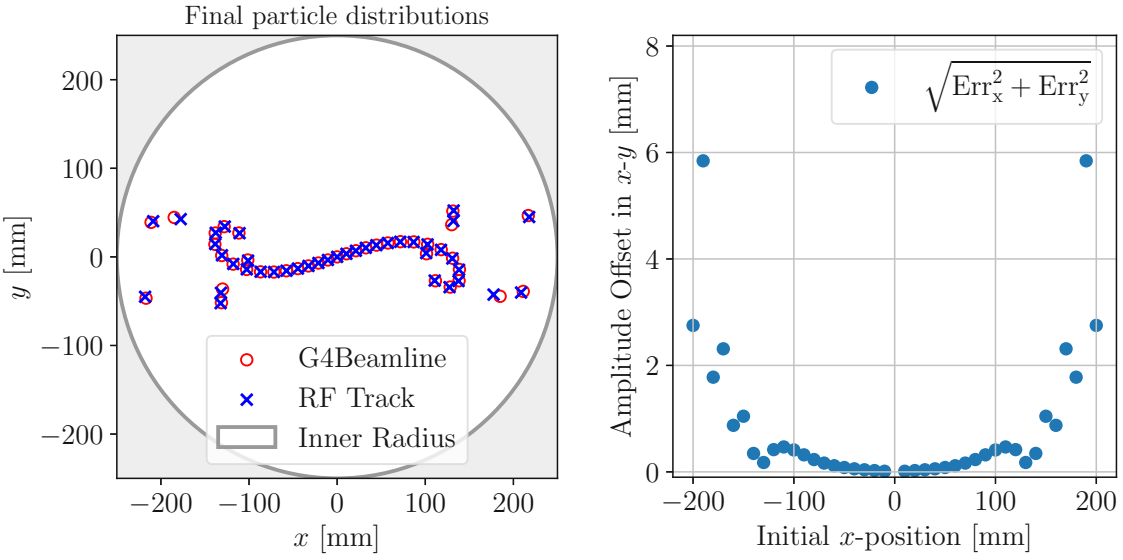


**Figure 4.3.:** Final particle positions from RF-Track and G4Beamline simulations (**left**). The benchmark analysis (**right**) shows increasing relative error with radial offset, suggesting magnetic field misalignment due to mesh-grid interpolation. Despite this, both simulations demonstrate high accuracy.

## 4.3 Linear and transverse beam dynamics in solenoids

Particles in a beam propagating along an accelerator lattice[2] exhibit position and momentum deviations, resulting in oscillations around a reference orbit. These movements are known as betatron oscillations. The dynamics within the transverse plane will be analyzed on the basis of the referenced literature [117–119]. In the transverse plane,

[2]In accelerator physics, the term lattice refers to a beamline comprising designated optical elements.

each particle within a bunch will be represented by its spatial coordinates $(x, y)$ and momentum components $(p_x, p_y)$ relative to a reference particle. The transverse motion is described relative to a reference particle traveling along the beam axis $s$, using a Frenet-Serret coordinate system (Fig. 4.4).

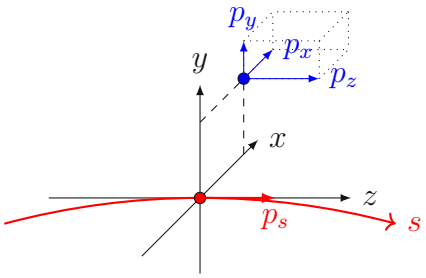


**Figure 4.4.:** A Frenet-Serret system is a type of coordinate system that travels along with a reference particle, which has momentum $p_0$, on its path designated as the reference orbit $s$. In this Frenet-Serret system, the phase space coordinates of every particle in a bunch are defined.

In an accelerator design, curvatures in $s$ occur within lattice elements with non-zero transverse fields, such as dipoles. The present design for the final cooling channel currently excludes dipole components. The set of spatial and momentum coordinates $(x, p_x, y, p_y)$ defines the transverse phase space, with $(x,\, p_x)$ and $(y,\, p_y)$ representing the horizontal and vertical components, respectively.

The transverse momenta are often normalized with respect to the reference momentum, which, under the paraxial approximation, corresponds to the angles

$$x' \approx \frac{p_x}{p_s}, \quad y' \approx \frac{p_y}{p_s}. \tag{4.7}$$

The collection of spatial and angle coordinates $(x, x', y, y')$ is alternatively referred to as the trace space coordinates. In accelerator physics, beam dynamics is commonly described using Hamiltonian mechanics. In this framework the momenta are expressed as canonical variables which are defined as

$$\tilde{p}_x = p_x + qA_x, \quad \tilde{p}_y = p_y + qA_y, \tag{4.8}$$

where $q$ is the charge of the particle and $A_x$ and $A_y$ are the transverse components of the vector potential. The spatial canonical variables are congruent to their mechanical counterparts within the transverse plane, thus denoted by $x = \tilde{x}$ and $y = \tilde{y}$.

In linear beam dynamics, the propagation of a particle from position $s_0$ to $s_1$ along a beamline is described using a transfer matrix $R$ typically computed by solving the

equation of motion derived from the Hamiltonian or Hill's equation. The following discussion focuses on the linear transverse beam dynamics in the single-particle, decoupled regime (Chapter 4.3.1). This frame work is also extended to statistical ensembles of particles with given distributions, characterized by beam parameters consistent with the Courant-Snyder theory.

Since the final cooling channel employs only solenoids for transverse focusing, an analysis of the transfer map of a solenoid will be presented in Chapter 4.3.2. Solenoids inherently couple the horizontal and vertical motion of the charged particle beam. Thus, a description of beam evolution within a coupled dynamics framework that introduces the concept of canonical angular momentum will be provided. Understanding the evolution of beam parameters is crucial to accurately design the final cooling lattice. This topic will be elaborated on in Chapter 5. The theory of linear and uncoupled beam dynamics serves as the foundation for describing beam parameters in the coupled motion from solenoids, as will be detailed in the following.

### 4.3.1 Linear and uncoupled beam dynamics

The beam parameters are determined by the field characteristics of the accelerator lattice. These parameters can describe the behavior of individual particles inside this lattice. In particular, the beam parameters are intrinsic properties of the lattice rather than the beam itself; however, when the beam is appropriately matched to the lattice, these parameters can equivalently characterize the beam. Including couplings, collective effects, and other unrelated factors, one can calculate beam parameters within a beamline using two methods. Applying a linear transfer map to the beam parameter at $s_0$, it is possible to determine them at $s_1$. An alternative approach involves solving the beam envelope equation, which is derived from Hill's equation, and propagating the beam parameters from $s_0$ to $s_1$. The beam parameters are described using the Courant-Snyder formalism, which will be elaborated upon in the subsequent discussion.

#### Courant-Snyder formalism

The characterization of the uncoupled two-dimensional beam is derived from the linear transfer matrix $R$. A transfer map of this kind may describe the tracking of particles through a specific optical element or a segment of a beamline. A stable beamline segment may either comprise solely focusing elements, such as solenoids within a final cooling channel, or a combination of focusing and defocusing optics, which are quadrupole optics in LINACs and rings.

Transfer maps, derived from Hamiltonian mechanics, are inherently symplectic. Symplecticity is characterized by transformations that maintain the phase space's volume[3] of a particle distribution in an accelerator. As $R$ is derived from the Hamiltonian equations, the symplectic condition for a transfer map satisfies

$$R^\top S\, R = S. \tag{4.9}$$

Since this section discusses only the transverse planes, the 4-dimensional symplectic matrix is defined as

$$S = \begin{pmatrix} 0 & 1 & 0 & 0 \\ -1 & 0 & 0 & 0 \\ 0 & 0 & 0 & 1 \\ 0 & 0 & -1 & 0 \end{pmatrix} = \begin{pmatrix} S_2 & 0 \\ 0 & S_2 \end{pmatrix}. \tag{4.10}$$

When examining a 2-dimensional and uncoupled transfer matrix $R_x$ within the horizontal plane, the horizontal transfer map can be generalized as

$$R_x = \mathbb{I}_2 \cos\mu_x + S_2\, A_x \sin\mu_x. \tag{4.11}$$

The symbol $\mathbb{I}_2$ in Eq. (4.11) represents the 2-dimensional identity, accompanied by a symplectic matrix $A_x$ and a parameter $\mu_x$. The relationship expressed in Eq. (4.11) is applicable to both the vertical and longitudinal planes. The paramters of $\alpha_x$, $\beta_x$, and $\gamma_x$ are known as the horizontal Courant-Snyder [120] or Twiss parameters [121] and are elements of the matrix

$$A_x = \begin{pmatrix} \gamma_x & \alpha_x \\ \alpha_x & \beta_x \end{pmatrix}. \tag{4.12}$$

The parameter $\beta_x$ is often referred to as the betatron function or simply the beta function [122]. The Courant-Snyder parameters $\alpha_x$ and $\beta_x$ are independent of each other, while $\gamma_x$ depends on both $\alpha_x$ and $\beta_x$. Inserting Eq. (4.11) into Eq. (4.9) results in

$$\beta_x\gamma_x - \alpha_x^2 = 1, \tag{4.13}$$

indicating that the horizontal Twiss-gamma is given by $\gamma_x = (1+\alpha_x^2)/\beta_x$. Initially, a particle's position was depicted using phase- or trace-space coordinates.

In the preceding discussion, the particle motion was described by using phase-space (or trace-space) coordinates. An alternative approach is to characterize it using action and angle variables, which will be introduced in the following.

[3] The Liouville theorem states that when particle propagation adheres to Hamiltonian equations, the density of particles within a beamline remains conserved.

### Action-angle variables

The action $J_x$ alongside angle $\varphi_x$ can be described by a synthesis of Courant-Snyder parameters in conjunction with $x$ and $x'$. In the uncoupled case, the definition of the horizontal action is

$$J_x = \frac{1}{2} \begin{pmatrix} x & x' \end{pmatrix} A_x \begin{pmatrix} x \\ x' \end{pmatrix}. \tag{4.14}$$

The invariant variable $J_x$ is also often known as the single-particle emittance. In a stable and periodic beamline structure of length $L$, plotting $x$ and $x'$ of a single particle over multiple periods of that structure forms an ellipse in the trace space frame. The shape of this ellipse is determined by the Courant-Snyder parameters $(\alpha_x, \beta_x, \gamma_x)$. Although the form of an ellipse may vary with the observation point $s_0$ within the beamline, its area remains constant and is precisely $2\pi J_x$.

By monitoring the individual particle after each segment of the periodic beamline, the trajectory on the ellipse aligns to a particular phase. This phase is characterized as the angle variable expressed as

$$\tan \varphi_x = -\beta_x \frac{x'}{x} - \alpha_x. \tag{4.15}$$

The conversion from action-angle variables to trace-space coordinates is dictated by the Courant-Snyder parameters, resulting in the expressions:

$$x = \sqrt{2\beta_x J_x} \cos \varphi_x, \tag{4.16}$$

$$x' = -\sqrt{\frac{2J_x}{\beta_x}} \left( \sin \varphi_x + \alpha_x \cos \varphi_x \right). \tag{4.17}$$

To obtain Eq. (4.17) from Eq. (4.16), the following conditions must be met:

$$\begin{aligned} \frac{d\varphi_x}{ds} &= \frac{1}{\beta_x}, \\ \alpha_x &= -\frac{1}{2} \frac{d\beta_x}{ds}. \end{aligned} \tag{4.18}$$

The derivation of the beam envelope equation starts by utilizing Eq. (4.16) alongside Eq. (4.17), in combination with Hill's equation. In linear beam dynamics, beyond the transfer maps, the beam envelope equation serves as an alternative method to compute the Courant-Snyder variables in a beamline.

### Hill's equation

Within the context of uncoupled beam dynamics, the Hamiltonian for each degree of freedom aligns with an equation of motion given by

$$x'' = -k(s)\,x, \tag{4.19}$$

which is widely known as Hill's equation. It resembles the motion of a harmonic oscillator, although the key difference is that $k(s)$ changes with position. Here, $k(s)$ represents the focusing strength of the linear optical component at position $s$. For a solenoid, the strength takes the form $k(s) = \kappa^2(s)$, which is defined in Eq. (4.31).

To address Eq. (4.19), the approach involves using the expressions given in Eq. (4.16) and Eq. (4.17) as the starting point. By separating and setting the resulting sine and cosine terms to zero, the uncoupled envelope equation yields to

$$2\beta_x''\beta_x - (\beta_x')^2 + 4\beta_x^2\kappa^2 - 4 = 0. \tag{4.20}$$

In Section 4.3.2, the envelope equation will be presented specifically for a solenoid under coupled conditions. Eq. (4.20) serves as a crucial analytical tool to design the beamline in a final cooling channel, which will be detailed in Chapter 5. Before exploring the methodology of coupled beam dynamics in solenoids, this subsection concludes with the Courant-Snyder parameterization of particle distributions in a bunch. It also introduces the geometrical and normalized emittance, which is an important figure of merit in ionization cooling.

### Description of particle distributions with Courant-Snyder parameter

In previous discussions, the focus was on the dynamics of an individual charged particle in a stable and periodic lattice. The action $J_x$ remains constant the beamline while the angle $\varphi_x$ and the Courant-Snyder parameter vary in position $s$. The Courant-Snyder parameters describe not only the single-particle motions but also the particle distribution in a beam. A collection of particles arranged according to a particular distribution is called a bunch. When multiple such bunches are spaced at regular intervals, they collectively form a beam.

Taking into account the statistical variance of a distribution of particles, the average of the square of Eq. (4.16) at a certain point in the beamline is

$$\left\langle x^2 \right\rangle = 2\beta_x \left\langle J_x \cos^2 \varphi_x \right\rangle. \tag{4.21}$$

Assuming the angles of the particles $\varphi_x$ are uniformly distributed from 0 to $2\pi$. The average of the squared cosine[4] is 1/2 leading to

$$\langle x^2 \rangle = \beta_x \langle J_x \rangle = \beta_x \varepsilon_x. \tag{4.22}$$

The average value of the action is called the geometric emittance $\varepsilon_x = \langle J_x \rangle$ of the beam. In Eq. (4.22), the beta function $\beta_x$ is related to the beam, as opposed to an individual particle. In general, the distribution of a beam is Gaussian, with the size of the root mean square (rms) $\sigma_x$ defined as $\sqrt{\langle x^2 \rangle}$[5]. It should be noted that the definitions provided are applicable to both the vertical and longitudinal planes.

The geometrical emittance is a statistical quantity in beam dynamics that defines the rms area occupied by the particles in the 2-dimensional trace/phase space. If the beam gets accelerated $\varepsilon_x$ is no longer conserved. To maintain this conservation, the emittance that remains unchanged under Lorentz transformation is referred to as normalized emittance, defined by

$$\varepsilon_{x,\mathrm{N}} = \beta\gamma\, \varepsilon_x. \tag{4.23}$$

The factors $\beta$ and $\gamma$ are Lorentz factors and not Couraunt-Snyder parameters. To differentiate them, this thesis consistently uses subscripts on the Courant-Snyder parameters. In contrast, unindexed $\beta$ and $\gamma$ symbols refer to the relativistic Lorentz factors associated with the beam's longitudinal motion.

The correlational between $x$ and $x'$ is defined as

$$\langle x x' \rangle = -\alpha_x\, \varepsilon_x \tag{4.24}$$

and the variance of the beam's divergence is

$$\langle x'^2 \rangle = \frac{1+\alpha_x^2}{\beta_x} \varepsilon_x = \gamma_x\, \varepsilon_x. \tag{4.25}$$

In terms of the beam distributions, the geometrical emittance can be expressed when inserting Eq. (4.22), Eq. (4.24) and Eq. (4.25) into the identity Eq. (4.13) which leads to

$$\varepsilon_x = \sqrt{\langle x^2 \rangle \langle x'^2 \rangle - \langle x x' \rangle^2}. \tag{4.26}$$

An useful method in beam dynamics is to extract the covariance matrix of a beam distribution, which is often referred to as a sigma matrix $\Sigma_x$. The sigma matrix is characterized as

$$\Sigma_x = \langle \vec{x}\vec{x}^{\top} \rangle = \begin{pmatrix} \langle x^2 \rangle & \langle x x' \rangle \\ \langle x' x \rangle & \langle x'^2 \rangle \end{pmatrix} = \begin{pmatrix} \beta_x & -\alpha_x \\ -\alpha_x & \gamma_x \end{pmatrix} \varepsilon_x. \tag{4.27}$$

[4] Calculation: $\langle \cos^2 \varphi_x \rangle = \frac{1}{2\pi} \int_0^{2\pi} d\varphi_x \cos^2 \varphi_x = \frac{1}{2}$

[5] When the beam is centered: $\langle x \rangle = 0$

The components of covariance matrix are the second momenta of the beam distribution.

### 4.3.2 Coupled beam dynamics in solenoids

In the Courant-Snyder framework, which characterizes both individual particle motion and multi-particle distributions, the horizontal and vertical motions are treated as independent of each other. Nevertheless, a solenoid simultaneously focuses charged particles in both the vertical and horizontal planes, coupling their motion across these dimensions. The Courant-Snyder parametrization is no longer applicable to coupled beam distributions. This summary characterizes the Courant-Snyder parameter in coupled solenoid motions through the invariant property of canonical angular momentum. The beam envelope equation for solenoid beam dynamics will be shown, which is a practical tool for designing lattices for the final cooling channel.

#### Canonical angular momentum

The solenoid field is cylinder symmetric, hence the Hamiltonian is invariant under rotation about the axis of symmetry . The generator of rotation about the axis of symmetry, the canonical angular momentum, is invariant. The canonical angular momentum for a beam is given by

$$\langle L_{\text{can}} \rangle = \langle \tilde{x}\tilde{y}' - \tilde{y}\tilde{x}' \rangle, \tag{4.28}$$

which utilizes the canonical variables described in Eq. (4.8). By examining a field that is both static and homogeneous within a solenoid, it is assumed that the fringe fields occupy an infinitesimally small region. This region is located precisely at the solenoid boundary. To effectively define the canonical momenta of a particle within a solenoid, it is imperative to evaluate the vector potential, defined as

$$\vec{B} = \begin{pmatrix} 0, & 0, & B_0 \end{pmatrix}^\top \rightarrow \quad \vec{A} = \begin{pmatrix} \frac{1}{2}B_0 y, & -\frac{1}{2}B_0 x, & 0 \end{pmatrix}^\top . \tag{4.29}$$

According to Eq. (4.8), the canonical variables in the linear approximation of the vector potential can be defined as $\tilde{x} = x$, $\tilde{y} = y$, and

$$\tilde{x}' = x' + \frac{qB_0}{2p_0}y, \quad \tilde{y}' = y' - \frac{qB_0}{2p_0}x. \tag{4.30}$$

It is evident from Eq. (4.30) that as particles enter the solenoid, they acquire a transverse momentum kick of $\mp qB_0 x/2p_0$ and $\pm qB_0 y/2p_0$, depending on both their charge and the direction of the magnetic field. The expression $qB_0/2p_0$ represents the solenoid's focusing

strength. The focusing strength has the units of inverse length and is typically expressed as

$$\kappa = \frac{cB[\mathrm{T}]}{2p_0[\mathrm{eV}]}. \tag{4.31}$$

The canonical angular momentum in terms of kinetic variables can be get by inserting Eq. (4.30) into Eq. (4.28) and yields to

$$\langle L_{\mathrm{can}} \rangle = \langle xy' - yx' \rangle + \kappa(\langle x^2 \rangle + \langle y^2 \rangle). \tag{4.32}$$

The term $\langle xy' - yx' \rangle$ is called the kinetic angular momentum. The term in parentheses in Eq. (4.32) is geometrically the interpretation of a radius, and as defined in [70], it is related to the betatron function in a solenoid as follows

$$\beta_\perp = \frac{\langle x^2 \rangle + \langle y^2 \rangle}{2\varepsilon_\perp} \tag{4.33}$$

For a beam that is cylinder symmetric, the solenoid's beta function reduces to $\langle x^2 \rangle / \varepsilon_\perp$, although it does not match the two-dimensional beta function stated in Eq. (4.22). The distinction lies in the application of the four-dimensional emittance, defined as

$$\varepsilon_\perp = \sqrt[4]{\det(\Sigma_{4\mathrm{D}})}, \tag{4.34}$$

where $\Sigma_{4\mathrm{D}}$ represents the four-dimensional covariance matrix. In the context of the Courant-Snyder evolution within a solenoid lattice, the normalized canonical angular momentum is defined as

$$\mathcal{L} = \frac{\langle L_{\mathrm{can}} \rangle}{2\varepsilon_\perp}. \tag{4.35}$$

### Envelope equation in solenoids

Beam coupling arises in elements such as dipoles, skew quadrupoles, solenoids or due to misalignments. D. Edwards and L. Tang [123] proposed a decoupling method by block diagonalizing the sigma matrix to extract Courant-Snyder parameters, though the transformation is not uniquely defined. The coupled motion in solenoids can be analyzed in the rotating Larmor frame [119], where the transfer matrix becomes block-diagonal if and only if $L_{\mathrm{can}} = 0$. For $L_{\mathrm{can}} \neq 0$, the Larmor frame is offset from the beam axis and full decoupling is not possible [124].

In beam dynamics of solenoids, the baseline approach of G. Penn introduced a modified transverse action, $J_\perp = \sqrt{1 + \mathcal{L}^2}(J_x + J_y) - 2\mathcal{L}L_{\mathrm{can}}$, leading to the second order differential equation of $\beta_\perp$, although with less clarity on its derivation [70, 125, 126]. In Penn's

finding, the betatron function in solenoids for a matched beam is defined as

$$\beta_\perp = \beta_\mathrm{p}\sqrt{1+\mathcal{L}^2}, \tag{4.36}$$

with $\beta_\mathrm{p} = 1/\kappa$. The beta-function in Eq. (4.36) interpreted as a kind of effective value, which grows with additional normalized canonical angular momentum $\mathcal{L}$ of the beam. Substituting $\beta_\mathrm{p}$ from Eq. (4.36) into Eq. (4.20) gives the **envelope equation** in a solenoid:

$$2\beta_\perp\beta_\perp'' - (\beta_\perp')^2 + 4\beta_\perp^2\kappa^2 - 4(1+\mathcal{L}^2) = 0. \tag{4.37}$$

When designing the lattice for a final cooling channel, Eq. (4.37) is the primary guide to follow a matched beam through a solenoid system, which includes both absorbers and RF components. Chapter 5 will dive deeper into the analysis of beam dynamics within the final cooling optics. Subsequently, the second moments for a matched beam within a solenoid will be discussed using Cartesian coordinates.

### Courant-Snyder parameters in solenoids

The parameter $\beta_\perp$ in a solenoid was expressed already in Eq. (4.33). In an analogous manner, the transverse cylindrically symmetric alpha function is defined by Penn [70], which is

$$\alpha_\perp = -\frac{1}{2\varepsilon_\perp}\left(\langle xp_x\rangle + \langle yp_y\rangle\right). \tag{4.38}$$

In the final cooling channel, the muon beam is assumed to be round and cylinder-symmetric. Consequently, the second-order moments are given by $\langle xp_x\rangle = \langle yp_y\rangle$ and $\langle xp_y\rangle = -\langle yp_x\rangle$. This results in the formation of a symmetric covariance matrix expressed as

$$\Sigma = \begin{pmatrix} \langle x^2\rangle & \langle xp_x\rangle & 0 & -\langle yp_x\rangle \\ \langle xp_x\rangle & \langle p_x^2\rangle & \langle yp_x\rangle & 0 \\ 0 & \langle yp_x\rangle & \langle x^2\rangle & \langle xp_x\rangle \\ -\langle yp_x\rangle & 0 & \langle xp_x\rangle & \langle p_x^2\rangle \end{pmatrix} \tag{4.39}$$

The square root of the second moments matrix determinant is given by

$$\varepsilon_\perp^2 = \langle x^2\rangle\langle p_x^2\rangle - \langle xp_x\rangle^2 - \langle yp_x\rangle^2 = \varepsilon_\perp^2\left(\beta_\perp\gamma_\perp - \alpha_\perp^2 - (\kappa\,\beta_\perp - \mathcal{L})^2\right) \tag{4.40}$$

which leads to the cylinder symmetric gamma function

$$\gamma_\perp = \frac{1+\alpha_\perp^2+(\kappa\,\beta_\perp-\mathcal{L})^2}{\beta_\perp}. \tag{4.41}$$

The beam characteristics in solenoids can be explained similarly using the Courant-Snyder parameterization, with the inclusion of the canonical angular momentum. The

solenoid transfer map was transformed into a straightforward rotation matrix. By doing so, one can obtain the envelope equation for cylindrically symmetric Courant-Snyder parameters. This forms the foundation for designing the final cooling channel in the transverse plane elaborated in Chapter 5.

This section provided an overview of the basic transverse beam dynamics in solenoids. For the final cooling channel, adjustments to the particles must occur within the longitudinal phase space. To achieve this, RF cavities are employed as optical elements. The subsequent section will dive into specific topics related to longitudinal beam dynamics, applicable to the final cooling design.

## 4.4 Longitudinal beam dynamics in LINACs

Despite of solenoids, RF cavities are the second optical elements in the final cooling channel of muon colliders. This segment provides a concise summary of the longitudinal beam dynamics of low-energy beams in LINACs, drawing on the textbook by S.Y. Lee [118] in this section. The impact on the transverse beam dynamics within the cavities was not considered. RF cavities in a final cooling channel serve several purposes. They phase focus the muon beam and accelerate it. Moreover, they refine the energy distribution by employing particular methodologies discussed in Chapter 5.3 and 5.5.2.

The canonical phase-space variables, time $t$ and energy $E$, are selected as coordinates for the individual particles. Phase-focusing and the acceleration of a charged particle bunch occur through the action of a sinusoidal electromagnetic RF wave in a cavity gap. The reference time $t_s$ is indicative of a distinct phase $\psi_s = \omega t_s$ of the RF at the moment when the particle reaches the center of the cavity. The RF frequency is expressed as $f = 2\pi\omega$, while the reference particle's energy is represented by $E_s$.

Non-reference particles are described using variables $t$, $\psi$, and $E$, where the phase space variables respective to the reference particle are

$$\Delta\psi = \psi - \psi_s, \quad \Delta E = E - E_s. \tag{4.42}$$

The electric field experienced by an arbitrary particle within the cavity gap is expressed as

$$\mathcal{E} = \mathcal{E}_0 \sin(\psi_\mathrm{s} + \Delta\psi), \tag{4.43}$$

where $\mathcal{E}_0$ is the electric peak field. The rate of change of $\Delta\psi$ along the beam axis $s$ is described by

$$\frac{d\,\Delta\psi}{ds} = \omega\left(\frac{dt}{ds} - \frac{dt_s}{ds}\right) \approx -\omega\frac{\Delta v}{v_\mathrm{s}^2}, \tag{4.44}$$

where $v_s$ is the reference velocity. Employing the relationship $d\beta = d\gamma/\beta\gamma^3$, the initial first energy-phase motion equation can be formulated as:

$$\frac{d\,\Delta\psi}{ds} = -\frac{\omega\,\Delta E}{c\beta^3\,\gamma^2 E_s}. \tag{4.45}$$

The Lorentz factors $\beta$ and $\gamma$ are identical to those of the reference particle. The amount of energy acquired by a particle carrying a charge $q$ as it traverses a cavity gap of length $g$ is described by the second energy-phase relation:

$$\delta E = q\mathcal{E}\,g = q\mathcal{E}_0 \int_0^g \sin\left(\omega\frac{s}{\beta c}\right) ds = q\mathcal{E}_0 T g. \tag{4.46}$$

The time transition factor

$$T = \frac{\sin(\pi g/\beta\lambda)}{\pi g/\beta\lambda}. \tag{4.47}$$

in an RF cavity accounts for the reduction in accelerating efficiency. This is due to the finite length $g$ of the cavity, as charged particles experience a varying electric field while traversing it. The parameter $\lambda$ corresponds to the wave length of the RF. The dynamics of particle motion within an RF cavity can be expressed through the mapping equations as follows:

$$\begin{aligned} \psi_{n+1} &= \psi_n - \frac{\omega\,\Delta E_n}{c\beta_s^3\gamma_s^2\,E_s} g, \\ \Delta E_{n+1} &= \Delta E_n + q\mathcal{E}_0 T g\left[\sin(\psi_{n+1}) - \sin(\psi_s)\right]. \end{aligned} \tag{4.48}$$

The equations presented in Eq. (4.48) are interlinked to maintain symplecticity, and can be unified through the Hamiltonian

$$H(\Delta\psi, \Delta W) = -\frac{\omega(\Delta W)^2}{2\gamma_s^2\beta_s^3 c\,W} + q\mathcal{E}_0 T g\left[\cos(\Delta\psi) - \Delta\psi\sin(\psi_s)\right]. \tag{4.49}$$

The equipotential lines from the Hamiltonian Eq. (4.49) indicate constant energy paths within the $(\Delta\psi, \Delta E)$-space. In the context of longitudinal beam dynamics, these lines trace the motion of particles in the longitudinal phase space. As shown in Fig. 4.5, the contours can form closed or open trajectories. The area enclosed by closed trajectories is considered stable and is separated from the unstable region by the separatrix, shown as the thick red line in the plots of Fig. 4.5. The diagram on the left in Fig. 4.5 illustrates the scenario for $\psi_s = 0$, where the separatrix is known as the stationary bucket. In the acceleration phase, where $0 < \psi_s < \pi/2$, the separatrix takes the shape of an asymmetric running bucket, as shown in the right plot of Fig. 4.5.

Particle distributions should always remain within the stable regions of an RF bucket. Inside this bucket, particles undergo rotational motion, known as phase-focusing or synchrotron motion. Particles outside the separatrix drift away from the bunch and are

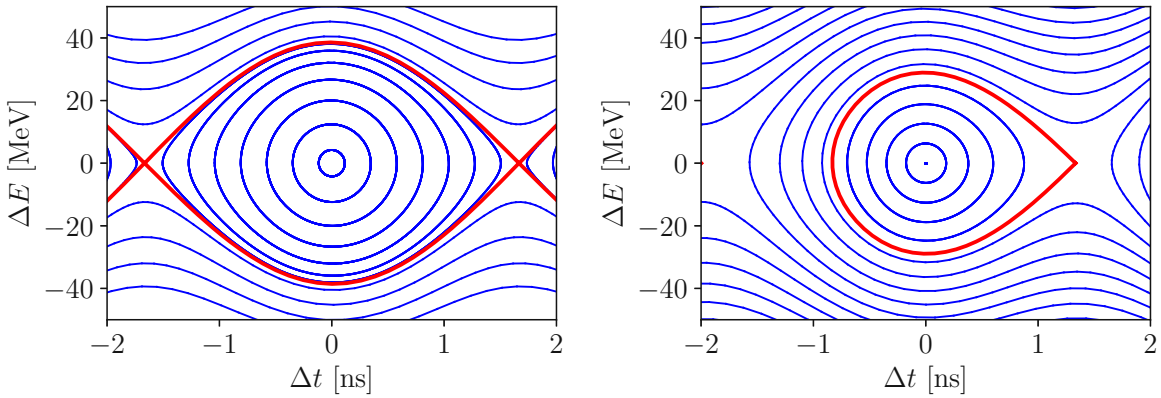


**Figure 4.5.:** The equipotential lines illustrate particle motions in the longitudinal phase space. Closed contours correspond to stable regions, while the separatrix, shown as a thick red line, marks the boundary between stable and unstable motion. The left plot depicts the case for $\psi_0$, where the separatrix forms a stationary bucket. In the accelerating phase $0 < \psi_0 < \pi/2$, the separatrix deforms into a running bucket, as shown in the right plot.

eventually lost. To prevent bunch filamentation, the equipotential lines should closely match the shape of the bunch distribution. If they do not, the longitudinal emittance increases.

Given the relationship $\Delta t = \Delta\psi/\omega$, the normalized longitudinal emittance is expressed as

$$\varepsilon_{\mathrm{L,N}}[\mathrm{eV\,s}] = \sqrt{\det\left(\mathrm{Cov}[\Delta t, \Delta E]\right)} \tag{4.50}$$

This expression represents the square-root determinant of the covariance matrix for particles in the $(\Delta t, \Delta E)$ phase space, when coupling in both horizontal and vertical planes are excluded. It is in units of eV s or in m for particles with mass $m$, that can be evaluated when multiplying $c/m$ on Eq. (4.50).

## 4.5 Emittance changes in ionization cooling

This section performs an analysis of the transverse cooling equation of a muon beam undergoing ionization cooling. The innovation herein lies in the incorporation of the Bethe-Wentzel scattering model within this cooling equation. Previous research employed the simplified Lynch-Dahl model, which resulted in discrepancies when compared with simulations to analyze the beam's transverse emittance. A comparison of the transverse equilibrium emittance between the ICOOL simulations and the analytical

model, enhanced through the Bethe-Wentzel approach, demonstrates a high degree of concordance.

Furthermore, the evolution of the longitudinal emittance within an ionization cooling cell was compared with results from ICOOL simulations, using beam parameters comparable to those in a final cooling channel. The comparison shows a good agreement between the analytical approach and the simulation results. Combined with the improved analytical expression for the transverse emittance rate, this provides a framework for determining optimal beam parameters for a final cooling cell analytically. As a result, the design of ionization cooling channels can be significantly accelerated, reducing the reliance on time-consuming multiparticle simulations.

### 4.5.1 Ionization cooling

Muons originate from the decays of charged pions, which are produced when protons collide with a fixed target, classifying muons as second-generation particles. Once produced, muons, both positively and negatively charged, occupy a large phase space. To achieve smaller emittances and subsequently increase luminosities, per Eq. (1.1), this phase space must be contracted. The term "cooling" in accelerator physics refers to the reduction of the normalized emittance in one or multiple degrees of freedom. As explained in Chapter 4.3.1, Liouville's theorem indicates that the normalized emittance stays unchanged as the beam passes through optical elements. However, during beam cooling, non-Hamiltonian effects are introduced that break the conservation of the phase-space density.

Various cooling methods are available, such as laser cooling, stochastic cooling, and electron cooling. However, these techniques are too time-consuming for muons due to their short lifetime of 2.2 µs in their rest frame, causing the muon to decay before sufficient cooling can occur. The only method capable of reducing the emittance within a relatively short duration is ionization cooling.

During the ionization cooling process, as the muon traverses an absorber, its total momentum decreases, and then longitudinal acceleration follows within an RF cavity configuration. A secondary consequence is that the interaction of muons with atomic nuclei and electrons within the absorber results in an unwanted increase of the longitudinal and transverse emittances. To counteract these effects, the absorber is situated inside a solenoid. This solenoid needs a very high magnetic field, which helps to reduce the spread of the transverse momentum due to multiple scattering. The arrangement of an ionization cooling cell was previously outlined in Fig. 4.1.

The final cooling channel of the muon collider complex is dedicated to decreasing the normalized emittance in both transverse planes. Key challenges include minimizing the

increase in longitudinal normalized emittance, selecting optimal absorber and window configurations, and designing an accurate beamline with the help of numerical tracking simulations. To simplify the beamline design process, an analytic depiction of the beam dynamics within an ionization cooling cell is crucial. The forthcoming analysis will examine the rate at which the normalized transverse emittance cools within an absorber when subjected to a solenoid field. It uses an updated analytical model that shows remarkable results compared to previous studies.

### 4.5.2 Transverse cooling equation

As previously discussed in Chapter 4.3.2, the transverse emittance is characterized as the 4-dimensional emittance $\varepsilon_\perp = \varepsilon_{4\mathrm{D}}$ in accordance with Eq. (4.34). The evolution of $\varepsilon_{\perp,\mathrm{N}}$ in an ionization cooling cell can be analytically expressed in detail in the Appendix C.3. D. Neuffer [127] firstly described the behavior of transverse emittance during ionization cooling along the beam path $s$ by

$$\frac{d\varepsilon_{\perp,\mathrm{N}}}{ds} = -\frac{\varepsilon_{\perp,\mathrm{N}}}{\beta^2 E}\left\langle\frac{\partial E}{\partial s}\right\rangle + \frac{\beta_\perp\, p_s c}{2\, m_\mu c^2}\frac{d\langle\vartheta^2\rangle}{ds}. \tag{4.51}$$

In Eq. (4.51), the left term accounts for the reduction in $\varepsilon_{\perp,\mathrm{N}}$ and is referred to as the cooling term. This reduction is influenced by the beam energy $E$, the relativistic factor $\beta$ and the average muon stopping power $\langle\partial E/\partial s\rangle$, equivalent to the Bethe formula in Eq. (3.17). In the final cooling channel, it is essential to select a beam energy within the range of 5 to 200 MeV to achieve high values of $\langle\partial E/\partial s\rangle$.

The heating term in the right part of Eq. (4.51) is driven by the variance of the scattering per unit length $d\langle\vartheta^2\rangle/ds$ suppressed by the betatron function $\beta_\perp$. This term can be reduced by focusing the beam strongly with a solenoid, leading to a smaller beta function $\beta_\perp = 2p_s\sqrt{1+\mathcal{L}^2}/cB$. Achieving low $\beta_\perp$ values requires high magnetic fields, low particle momenta, and the absence of canonical angular momentum.

An alternative approach to reduce the influence of heating is by carefully selecting the absorptive material to decrease the squared scattering rate $d\langle\vartheta^2\rangle/ds$. Low-$Z$ materials are effective in reducing muon scattering, with liquid hydrogen being the optimal option for ionization cooling. Among all materials, hydrogen provides the best balance with minimal scattering effects, delivering the highest energy deposition by muons, compared to the amount of induced scattering angle per unit length.

### 4.5.3 Modification of the cooling equation by the Bethe-Wentzel scattering model

The analytical description of $d\langle\vartheta^2\rangle/ds$ in the cooling equation originally incorporated the scattering model by G. Lynch and O. Dahl [107], which was extensively discussed in Chapter 3.3.3. A drawback of this scattering model is the presence of an additional logarithmic term in Eq. (3.32). Neuffer excluded this logarithmic term which modifies the mean squared scattering rate to

$$\frac{d\langle\vartheta^2\rangle}{ds} = \left(\frac{13.6[\mathrm{MeV}]}{\beta pc}\right)^2 \frac{1}{L_\mathrm{R}}, \tag{4.52}$$

and substituted it into Eq. (4.51). In the research outlined in Chapter 3.3.3, it is demonstrated that the scattering model from Eq. (4.52) exhibits an error margin of approximately 20% in liquid hydrogen, as shown in Fig. 3.5. Consequently, the Lynch-Dahl formula without the logarithmic term is unsuitable for precise analytical emittance calculations in the context of ionization cooling, when liquid hydrogen serves as the absorber.

A different method involves identifying a scattering model that better represents the scattering of charged particles in liquid hydrogen. This can be achieved using the approach developed by G. Wentzel and H. Bethe [105, 113], which has been elaborated for the scattering algorithm in RF-Track as detailed in Chapter 3.3.4. To recapitulate, the Bethe-Wentzel model modifies the Rutherford cross section by introducing a minimum cutoff angle $\vartheta_\mathrm{min}$ and considering the scattering from constituent electrons within the material's atoms. The variance in scattering per unit length of the Bethe-Wentzel model is presented in Eq. (3.36). By substitution Eq. (3.36) into Eq. (4.51), the modified transverse cooling equation yields

$$\frac{d\varepsilon_{\perp,\mathrm{N}}}{ds} = -\frac{\varepsilon_{\perp,\mathrm{N}}}{\beta^2 E}\left|\left\langle\frac{\partial E}{\partial s}\right\rangle\right| + \frac{\beta_\perp\, pc}{2\, m_\mu c^2}\frac{d\langle\vartheta^2\rangle}{ds}, \tag{4.53}$$

$$\frac{d\langle\vartheta^2\rangle}{ds} = \frac{k\rho}{2A}\left(\frac{Z}{\beta pc}\right)^2\left[F\left(\frac{\vartheta_\mathrm{max}}{\vartheta_\mathrm{min}}\right) + \frac{1}{Z}F\left(\frac{\vartheta^\mathrm{e}_\mathrm{max}}{\vartheta^\mathrm{e}_\mathrm{min}}\right) - 1.19\left(1+\frac{1}{Z}\right)\right], \tag{4.54}$$

$$F(x) = \frac{1}{1+x^2} + \ln\left(1+x^2\right). \tag{4.55}$$

In Eq. (4.54), the variable $A$ represents the atomic mass, $\rho$ stands for the material's density, and $k$ is approximately $0.157\,\mathrm{MeV^2 cm^2 mol^{-1}}$. The smallest and largest nuclear scattering angles are $\vartheta_\mathrm{min}$ and $\vartheta_\mathrm{max}$, as indicated in Eq. (3.26). For electron scattering, these angles are denoted by $\vartheta^\mathrm{e}_\mathrm{min}$ and $\vartheta^\mathrm{e}_\mathrm{max}$, as defined in Eq. (3.35).

The forthcoming discussion is dedicated to a comparative analysis of the analytical models pertaining to both the traditional Lynch-Dahl and novel Bethe-Wentzel transverse cooling equations, in conjunction with ICOOL simulation results. A viable approach to this effort involves conducting a benchmarking study of the equilibrium emittance, an undertaking that has yet to be realized.

### 4.5.4 Equilibrium emittance comparisons

To evaluate the Lynch-Dahl and Bethe-Wentzel scattering models using particle tracking simulations, the transverse equilibrium emittance is taken into consideration. Given the parameters of particle energy, choice of material, and the strength of the solenoid field, the equilibrium emittance, where the rates of heating and cooling balance each other, is calculated according to Eq. (4.51) as:

$$\varepsilon_{\perp,\mathrm{N}}^{\mathrm{eq}} = \beta^2 E \frac{d\langle\vartheta^2\rangle/ds}{|\langle\partial E/\partial s\rangle|} \frac{\beta_\perp pc}{2m_\mu c^2}. \tag{4.56}$$

To facilitate cooling, it is imperative that the initial value of $\varepsilon_{\perp,\mathrm{N}}$ in a cooling celle consistently exceeds that of $\varepsilon_{\perp,\mathrm{N}}^{\mathrm{eq}}$. In contrast, under the condition $\varepsilon_{\perp,\mathrm{N}} < \varepsilon_{\perp,\mathrm{N}}^{\mathrm{eq}}$, the heating term prevails, leading to an increase in the emittance, which must be avoided. Eq. (4.56) is analyzed using the scattering models expressed in terms of $d\langle\vartheta^2\rangle/ds$, where Equations (4.52) and (4.54) are substituted with the data generated by ICOOL.

To determine $\varepsilon_{\perp,\mathrm{N}}^{\mathrm{eq}}$ using ICOOL, the following approach was used: Simulations were performed with a constant solenoid field strength $B$ and kinetic beam energy $E_{\mathrm{Kin}}$, while varying the initial normalized transverse emittance $\varepsilon_{\perp,\mathrm{N}}^{\mathrm{i}}$. The muons were tracked in liquid hydrogen and the final emittance values $\varepsilon_{\perp,\mathrm{N}}^{\mathrm{f}}$, were recorded. The equilibrium emittance was obtained by interpolating the curve of $\varepsilon_{\perp,\mathrm{N}}^{\mathrm{i}}$ versus $\Delta\varepsilon_\perp = \varepsilon_{\perp,\mathrm{N}}^{\mathrm{i}} - \varepsilon_{\perp,\mathrm{N}}^{\mathrm{f}}$. The equilibrium point corresponds to the intersection of this curve with the horizontal zero line. The ICOOL analysis was further extended by varying the $E_{\mathrm{Kin}}$ at field strengths of 30, 40 and 50 T. The density of liquid hydrogen employed was $0.0708\,\mathrm{g\,cm^{-3}}$.

Fig. 4.6 illustrates that the ICOOL data align well with the Bethe-Wentzel model as described in Eq. (4.54), whereas the Lynch-Dahl scattering approximation evidently overestimates the results. It is the first agreement of the transverse cooling equation with tracking simulations.

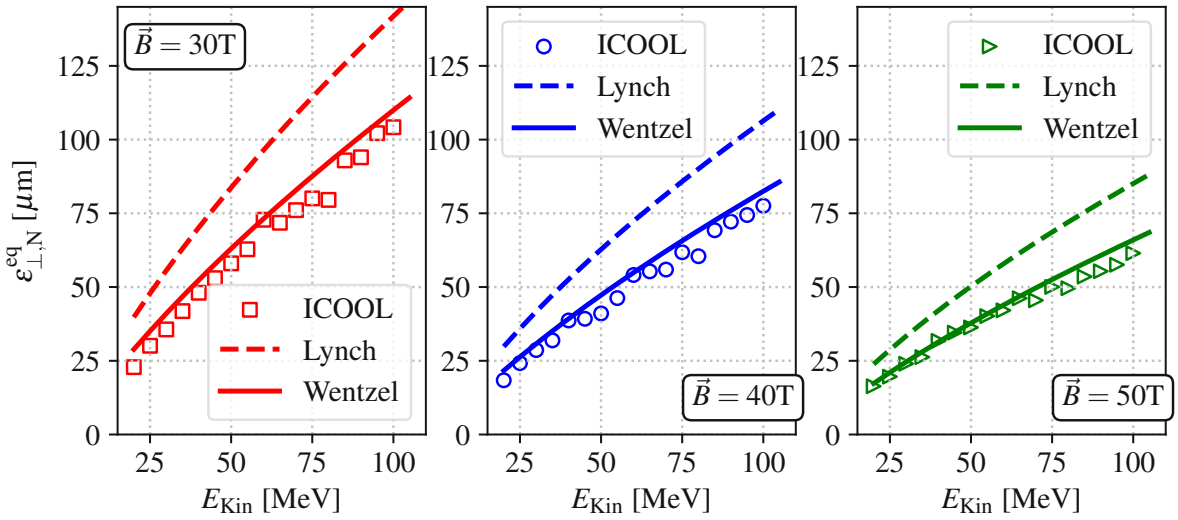


**Figure 4.6.:** The equilibrium emittance of liquid hydrogen subjected to a longitudinal static field of 30, 40, and 50 T is assessed using ICOOL. The results shows remarkable consistency with the analytical model when the Bethe-Wentzel scattering assumption is considered.

### 4.5.5 Canonical angular momentum in ionization cooling

The consideration of canonical angular momentum in the context of ionization cooling is crucial, as it directly influences the envelope equation as indicated in Eq. (4.37). The subsequent discourse will concisely examine the perspective of angular momentum from a single-particle perspective. It will then succinctly explore the evolution of canonical angular momentum for a collection of particles in ionization cooling, which has a significant influence in a final cooling cell.

Examine the depiction of an individual charged particle, defined by its longitudinal momentum $p_z$ and transverse position $x$, as it progresses from free space into a solenoid. Assume that the canonical angular momentum $\mathcal{L}$ is zero. After entering the solenoid, the particle follows a helical path that intersects the central solenoid axis at regular intervals. The gyration of the particle is caused by the azimuthal kick at the entrance of the solenoid and causes non-zero kinetic angular momentum $L_{\text{Kin}} = (xp_y - yp_x)$. This gain of $L_{\text{Kin}}$ is exactly $-qBr^2/2$. This is necessary to preserve the canonical angular momentum according to Eq. (4.32). Here, $r$ is the radial displacement relative to the beam axis.

In an ionization cooling cell, the solenoid is filled with energy-absorbing material. As a consequence of the particle's momentum reduction within the solenoid-absorber configuration, there is a contraction of the helical radius. This phenomenon is illustrated as the

dashed line in Fig. 4.7, where the magnetic field initially goes from left to right. Should the single particle remain in its current configuration, it will move closer to the Larmor center of its spiral trajectory. Considering multiple particles, the transverse dimensions of the beam cannot be effectively minimized, making emittance reduction less efficient.

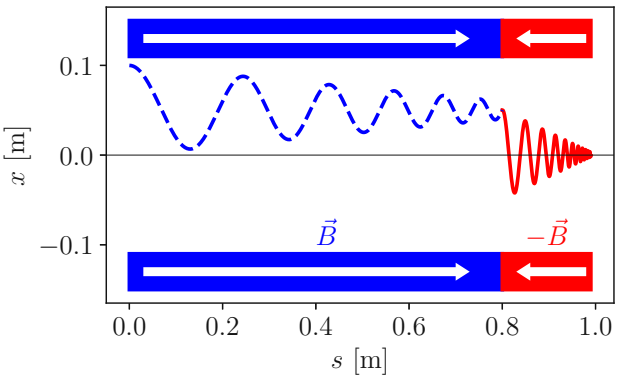


**Figure 4.7.:** The blue dashed line represents the contraction of the helical radius due to momentum reduction in the solenoid-absorber configuration. To enhance emittance reduction, the solenoid's magnetic field polarity is reversed, leading to shift the Larmor center toward the optical axis. The resulting particle trajectory is shown as the red solid line.

One solution involves reversing the polarity of the solenoid's magnetic field. Upon exiting the initial solenoid and entering the solenoid with reversed polarity, the particle experienced enhanced azimuthal forces, resulting in displacement of the Larmor center closer to the optical axis. Consequently, the particle orbits around the reference trajectory depicted as the solid line in Fig. 4.7. It is important to note that Fig. 4.7 is intended as an instructional example and does not represent the actual structure of a realistic final cooling cell. A more accurate model will be explored in Chapter 5.

The progression of the canonical angular momentum, on average, was established and confirmed through ICOOL simulations performed by G. Penn [125]. The expression for the rate of canonical angular momentum in its normalized form is given by

$$\frac{d\mathcal{L}}{ds} = \frac{\beta_\perp \kappa}{\beta E^2} \left\langle \frac{\partial E}{\partial s} \right\rangle - \frac{\mathcal{L}}{\varepsilon_{\perp,\mathrm{N}}} \frac{\beta_\perp pc}{2m_\mu c^2} \frac{d\langle \vartheta^2 \rangle}{ds}. \tag{4.57}$$

A detailed mathematical derivation of Eq. (4.57) is provided in [128]. Eq. (4.57) demonstrates that the magnitude of $\mathcal{L}$ increases as the beam traverses the ionization cooling setup. This leads to a weaker focus since the betatron function in a solenoid depends on the canonical angular momentum according to Eq. (4.36). Lower values of the beta function are desirable, as they correspond to reduced emittance heating, as expressed on the

right-hand side of Eq. (4.51). Additionally, an increase in canonical angular momentum results in stronger coupling of the beam in both horizontal and vertical planes.

As illustrated by the single-particle example in Fig. 4.7, altering the field polarity proves advantageous for diminishing the canonical angular momentum of the beam. The design of a final cooling cell featuring solenoids with inverted fields and absorbers will be carefully examined and assessed in Chapter 5.2. Regardless of the particle dynamics involved in ionization cooling within the transverse plane, the subsequent analysis will focus on the longitudinal behavior of particles.

### 4.5.6 Longitudinal emittance change in ionization cooling

The variation in longitudinal emittance within an ionization cooling cell arises from the dynamics related to the energy spread of the bunch $\sigma_E$. This modification of the energy spread is influenced by systematic and stochastic fluctuations encountered by the bunch as it passes through specific materials. This section provides a concise discussion on both effects and compares them using simulations that employ beam parameters relevant to the final cooling process.

The variation in systematic energy spread within a material is due to the distinct momenta of individual particles in a bunch relative to the reference particle. According to Bethe's equation in Eq. (3.17), particles with lower momentum experience a greater energy loss compared to those with higher momentum. An evolution of the energy spread through matter is expressed by D. Neuffer [129] as

$$\frac{d\sigma_E^2}{ds} \approx -2\frac{d\left\langle \partial E/\partial s \right\rangle}{ds}\sigma_E^2. \tag{4.58}$$

To evaluate the model described in Eq. (4.58), macro particle tracking was carried out using ICOOL. This software has the ability to selectively deactivate certain single-particle effects. During the simulation, particles released energies inside the material, but any form of energy fluctuations was deactivated to test the systematic effects. Lower and higher kinetic beam energies, as indicated in $E_{\mathrm{Kin}} = [7, 50, 100]$ MeV, were used for benchmarking, complemented by the corresponding and arbitrary initial energy spreads, as noted in $\sigma_E = [0.7, 3, 5]$ MeV. These energies and spreads are comparable to those utilized in the final cooling channel. In ICOOL, the particles were tracked while passing through a section of liquid hydrogen, which is the material used in ionization cooling studies. The comparative results between ICOOL and the model are depicted in Fig. (4.8). It is evident that the model demonstrates excellent performance in relation to the simulations.

Randomly, high-energy charged particles, such as muons, may interact directly with electrons present in a material [130]. Although this interaction does not significantly

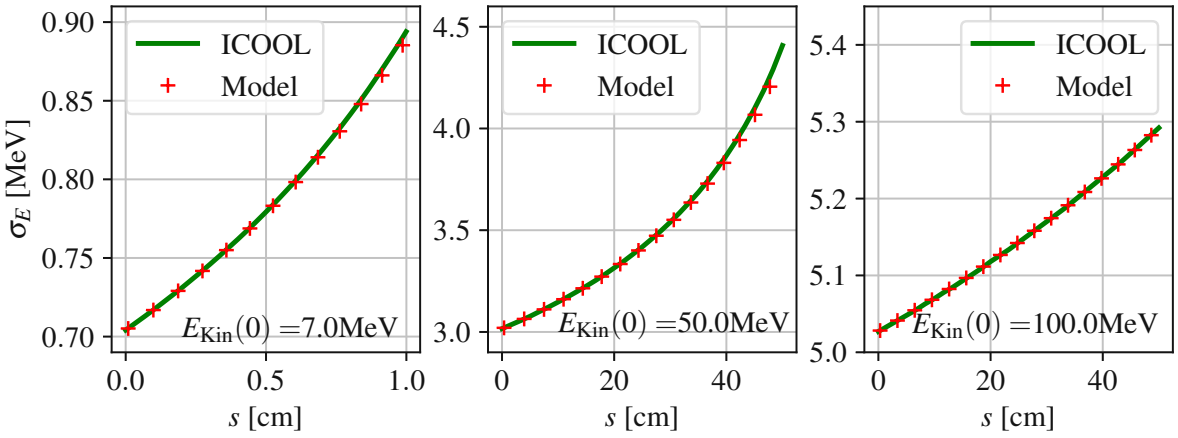


**Figure 4.8.:** To evaluate the systematic energy spread evolution, macro particle tracking was performed using ICOOL. Benchmarking was conducted using a range of kinetic beam energies, $E_{\mathrm{Kin}} = [7, 50, 100]$ MeV, along with corresponding and arbitrary initial energy spreads, $\sigma_E = [0.7, 3, 5]$ MeV, consistent with values typical of the final cooling channel. The comparison between ICOOL and the model shows that the model performs well in reproducing the simulated results.

alter the trajectory of the particles, it does result in an energy loss from the collision. This type of statistical fluctuation in energy losses is referred to as straggling. The progression of statistical energy distribution in the material is expressed by

$$\frac{d\sigma_E^2}{ds} = k\frac{Z}{A}\rho\gamma^2\left(1-\frac{\beta^2}{2}\right). \tag{4.59}$$

The total energy spread of a bunch penetrating a material can be summarized by combining Eq. (4.58) with Eq. (3.20) to

$$\frac{d\sigma_E^2}{ds} = -2\frac{d\langle\partial E/\partial s\rangle}{dE}\sigma_E^2 + \frac{d(\Delta E^2_{\mathrm{Stoch}})}{ds}. \tag{4.60}$$

In the comparison involving Eq. (4.60), the same methodology used in the previous analysis was used. Although the same absorber material and initial parameters $E_{\mathrm{Kin}}$ and $\sigma_E$ were used, the stochastic fluctuations inherent in the ICOOL simulations were considered. Fano straggling, as documented in the ICOOL reference manual [72], was applied for these simulations. The comparison findings of ICOOL with Eq. (4.60) are illustrated in the graphs of Fig. 4.9 and demonstrate a commendable agreement.

The evolution of the spread of energy within the material can be utilized to assess the dynamics of the longitudinal emittance in an ionization cooling cell. As demonstrated

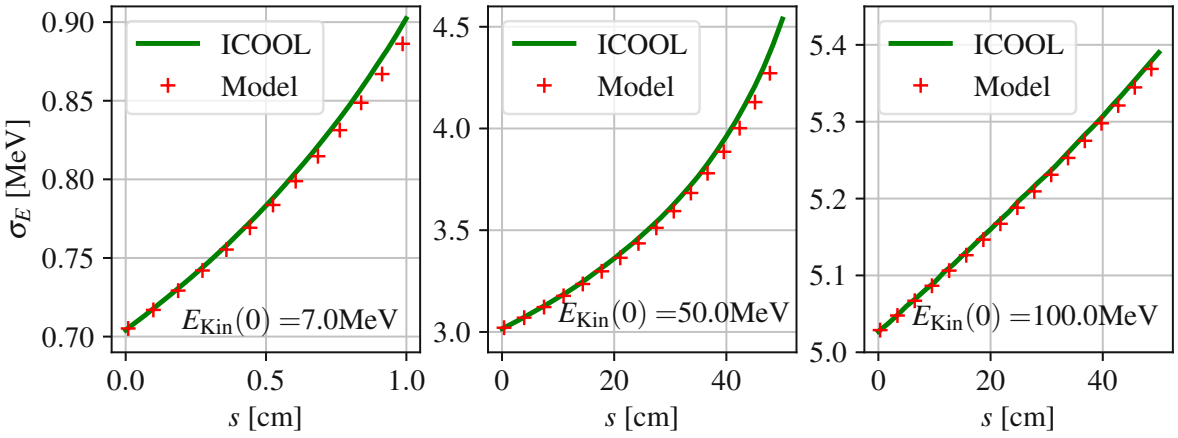


**Figure 4.9.:** The same methodology as before was used to evaluate Eq. (4.60), with identical absorber material and initial parameters $E_{\mathrm{Kin}}$ and $\sigma_E$. The stochastic straggling effects were included. The results show good agreement between ICOOL simulations and the model.

in Eq. (4.60), the longitudinal emittance unavoidably increases within a material. The techniques used in 6D cooling channels [36] have discovered methodologies to increase longitudinal emittance by incorporating beam dispersions and the choice of specific absorber geometries.

The main aim during the final cooling phase in the muon-collider complex is to reduce the transverse emittance while keeping the increase in longitudinal emittance as minimal as possible. The transverse and longitudinal analytical behavior of a muon beam within an ionization cooling cell are detailed in Eq. (4.51) and Eq. (4.60). With these equations, it becomes possible to determine the optimal initial beam parameters to be utilized in a final cooling cell. This aspect will be further elucidated in the subsequent discussion.

## 4.6 Best initial energy for ionization cooling

The optimal cooling parameters of a muon collider aim to minimize transverse emittance while simultaneously limiting longitudinal emittance growth. This approach results in optimal luminosities within the collider ring. As indicated by Eq. (1.1), the expression for luminosity is proportional to

$$\mathcal{L}_{\mathrm{Lum}} \propto \frac{1}{\varepsilon_{\perp,\mathrm{N}} \cdot \varepsilon_{\mathrm{L,N}}}, \tag{4.61}$$

implying that both the transverse and longitudinal normalized emittance should be minimized[6]. In the subsequent discussion, an analytical technique that facilitates the determination of the optimal initial beam energy for a final cooling cell will be presented.

### 4.6.1 Steps to identify the best beam energy

For a specified solenoid field strength $B$ and absorber, it is imperative to determine the optimal initial kinetic energy $E_{\mathrm{Kin}}$ for the beam as it enters the final cooling cell. Within a matched beamline external to the cooling cell, $\varepsilon_{\perp,\mathrm{N}}$ and $\varepsilon_{\mathrm{L,\,N}}$ remain invariant. Upon entering the cooling cell with a designated energy spread $\sigma_E$, a scan can be performed on $E_{\mathrm{Kin}}$ of the beam. The analysis is guided by the minimization of the tradeoff function $-\Delta\varepsilon_{\mathrm{L,\,N}}/\Delta\varepsilon_{\perp,\mathrm{N}}$ to reach maximum luminosity, as delineated by Eq. (4.61).

The phenomenon of particle losses is not considered in this study, as it predominantly occurs during the long re-acceleration phase, which is outside the scope of this analysis. To elucidate this matter through an example, a comprehensive energy scan in liquid hydrogen was performed, referencing $\varepsilon_{\perp,\mathrm{N}} = 200\,\mu\mathrm{m}$, $\varepsilon_{\mathrm{L,\,N}} = 1\,\mathrm{mm}$, and $B = 40\,\mathrm{T}$. This involves solving Eq. (4.51) and Eq. (4.60) numerically utilizing a fourth-order Runge-Kutta algorithm, to ensure high precision. The results, depicted in the plot to the **left** of Fig. 4.10, relate to various initial conditions $\sigma_E$. It is evident from the results that the optimal initial kinetic energy, represented as the minimum of the curves, increases as the spread of energy $\sigma_E$ increases.

### 4.6.2 Comparison with Simulations from ICOOL

The subsequent stage involves identifying the optimal initial energy for muon cooling corresponding to each initial transverse emittance $\varepsilon_{\perp,\mathrm{N}}$. A kinetic energy scan is performed at $\varepsilon_{\mathrm{L,\,N}} = 1\,\mathrm{mm}$ with a relative momentum spread of $\delta_{p_z} = 2\%$, and the energy is subsequently attenuated to 90% of its initial value. A static magnetic field of $B = 40\,\mathrm{T}$ is applied within liquid hydrogen using ICOOL, and the simulation produces a minimal trade-off function to determine the optimal energy for the initial transverse emittance. The results, depicted in Fig. 4.10 **right**, are evaluated against the analytical model that employs Eq. (4.51) in combination with Eq. (4.60). As shown in the **right** graph of Fig. 4.10, there is a reasonable level of agreement; however, when the analytical evaluation starts with small initial emittances, it starts to deviate from the trend depicted by the ICOOL simulation data.

[6] At the muon collider as discussed in [25], the beta-function $\beta^*$ is chosen to be equal to the bunch length $\sigma_z$ due to reasons of the hourglass effect (Appendix A.2). The normalized longitudinal emittance is connected to the length of the bunch ($\varepsilon_{\mathrm{L,N}} \propto \sigma_z$).

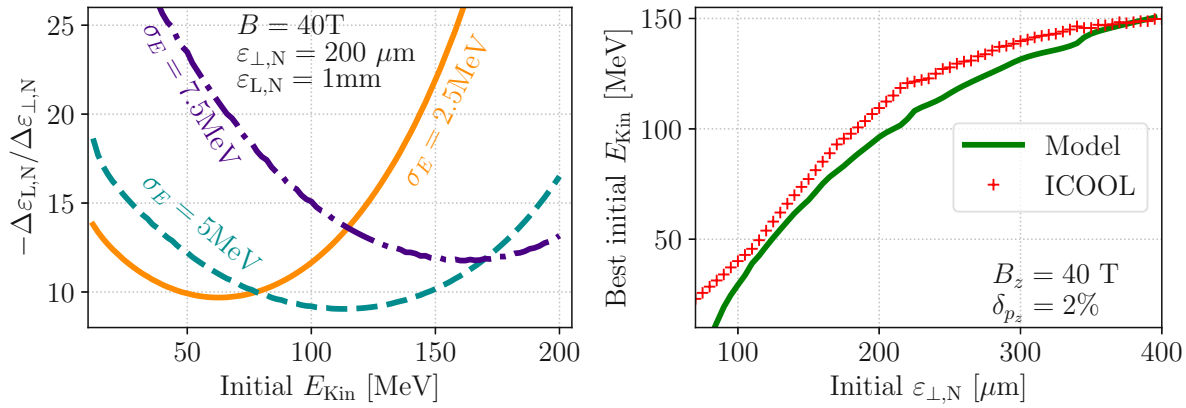


**Figure 4.10.: Left**: For specified beam and machine conditions, the optimal initial beam energy can be determined by identifying the minimum of the trade-off function $-\Delta\varepsilon_{\mathrm{L,\,N}}/\Delta\varepsilon_{\perp,\mathrm{N}}$. **Right**: The optimal initial kinetic beam energy for ionization cooling, applicable to various initial normalized transverse emittances in a scenario involving liquid hydrogen cooling under a magnetic field as described in 40 T, has been both simulated using ICOOL and derived from the analytical model.

An analytical study was performed to identify the ideal initial energy of muons for each phase of ionization cooling. In this investigation, Neuffer's transverse cooling equation in Eq. (4.51) was refined using the Bethe-Wentzel scattering model of Eq. (4.54). This model demonstrated superior agreement with the ICOOL simulations compared to the Lynch-Dahl model previously employed in ionization cooling research. An equilibrium emittance comparison of both methodologies with ICOOL confirms the precision of the Bethe-Wentzel approach. This facilitated the elucidation of the optimal initial beam energy for ionization cooling, exhibiting strong alignment with ICOOL simulations. Armed with a robust analytical model of both the transverse and longitudinal emittance rates within an ionization cooling setup, the design process for a cooling cell can be conducted with enhanced efficiency. Compared to macro-particle simulation programs, these analytical models enable more rapid predictions of the ideal parameters.

## 4.7 Thermodynamic characteristics of hydrogen absorbers and beam windows in ionization cooling

Using hydrogen as an absorber makes it possible to significantly reduce the normalized transverse emittance of a muon beam. This method is particularly effective during the final cooling stage, where it is combined with strong solenoidal magnetic fields and low beam energies. Under these conditions, the beam approaches a small equilibrium emittance, as described by Eq. (4.56).

As a result, the beam size becomes smaller, concentrating the energy deposition into a small volume. According to Bethe's formula for energy loss Eq. (3.17), lower beam energies also cause muons to deposit more energy into the material. Together, the reduced beam size and lower energy lead to a high energy density in the absorber.

This section estimates the energy deposited in a material by a passing muon beam. The analysis helps evaluate the resulting temperature rise and, more importantly, the pressure increase within hydrogen absorbers. This study is significant because the pressures generated by the beam and their impact on the absorber windows have not been previously investigated. A brief analysis of heat transfer through the beam windows is also included.

### 4.7.1 Energy storage in absorbers

In this analysis, the specific internal energy $u$ of a hydrogen absorber will be calculated after the passage of a muon beam. This makes it possible to evaluate the increase in pressure $p$ and temperature $T$ inside the absorber. The focus will be on the beam conditions in the final cooling cell, which represents the most extreme case. At this stage, the beam reaches its smallest normalized transverse emittance of $\varepsilon_{\perp,\mathrm{N}} = 25\,\mu\mathrm{m}$. Furthermore, muons will have a kinetic energy of approximately 4 to 5 MeV as they exit the absorber, and therefore the beam energy deposition in the absorber will be maximum.

A muon bunch passing through the absorber releases a kind of channel inside with changed thermodynamic conditions as depicted in Fig. 4.11. Since the bunch is Gaussian distributed, it is not obvious to delineate the beam transversely. Only muons within the **mean absolute deviation** (MAD) of the beam size will be used as a transverse limitation. It will define a characteristic radius around the beam axis, which is

$$r = \sigma_r \sqrt{2/\pi}, \tag{4.62}$$

where $\sigma_r$ is the radial rms beam size. The MAD is used because it signifies the core of a Gaussian distribution, where the particles in the bunch exhibit the highest concentration. Within the MAD size, 27% of the total number $N$ of muons in the bunch is contained.

Assuming the muon beam can be modeled as a symmetric cylindrical distribution, the energy is deposited within a small volume defined by a length $\Delta s$ and a cross-sectional area of $\pi r^2$. Taking the beam radius to be the mean absolute deviation (MAD) size, the volume becomes:

$$\Delta V = \frac{\varepsilon_{\perp,\mathrm{N}} \beta_\perp}{\beta\gamma} \Delta s \tag{4.63}$$

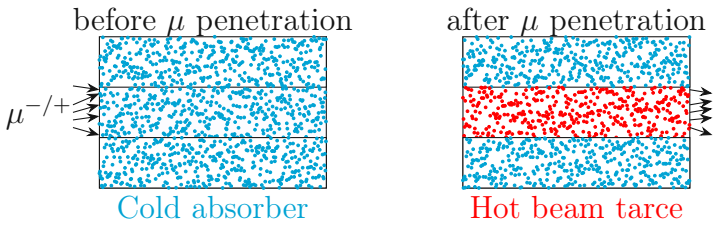


**Figure 4.11.:** The muons cause a hot beam path inside the absorber

The specific internal energy deposited within this volume is given by:

$$\Delta u[\mathrm{J\,kg^{-1}}] = \frac{0.27 \times Ne\,|\langle \partial E/\partial s \rangle|\,\Delta s}{\Delta m} = \beta\gamma \frac{0.27 \times Ne\,|\langle \partial E/\partial s \rangle|}{\rho\ \varepsilon_{\perp,\mathrm{N}} \beta_\perp}, \tag{4.64}$$

with the electrical charge $e \approx 1.6022 \times 10^{-19}\,\mathrm{C}$.

By evaluating $\Delta u$, it further gives the possibility of evaluating the increase in pressure and temperature within the beam path. In previous final cooling studies [131, 132], the absorbers are made of liquid hydrogen with a density of $\rho = 70.8\,\mathrm{kg\,m^{-3}}$. Thermodynamic calculations with fluids need additional program, such as CoolProp [133]. CoolProp is an open-source thermophysical property library that provides accurate and consistent fluid and gas properties for a wide range of engineering applications.

By evaluating $\Delta u$, it becomes possible to estimate the resulting increase in pressure and temperature along the beam path. In previous final cooling studies [131, 132], the absorbers were composed of liquid hydrogen, with a density of $\rho = 0.0708\,\mathrm{kg\,m^{-3}}$. To perform accurate thermodynamic calculations for fluids such as liquid hydrogen, external software is required; one such tool is CoolProp [133]. CoolProp is an open-source thermophysical property library that provides reliable and consistent fluid and gas properties for a wide range of engineering applications.

The preliminary study conducted by B. Palmer in 2011 [131] was used to assess the increase in pressure within the absorbers of a final cooling channel. This reference provided tabulated data on the initial and final energy values for each final cooling cell. Moreover, the progression of the transverse emittance and absorber lengths for each cell was graphically depicted. The solenoid field strength used in this study was established as detailed in 40 T. Using these parameters and substitute them into Eq. (4.64), the pressure increase can be calculated for each cell using CoolProp, which is summarized in Fig. 4.12. In performing the calculations, it was assumed that the initial pressure of the liquid hydrogen absorbers corresponds to the conditions specified in 1 bar. In the computation, each group utilized $N = 6 \times 10^{12}$ muons, which is a higher value than the ones obtained from the parameter list [27].

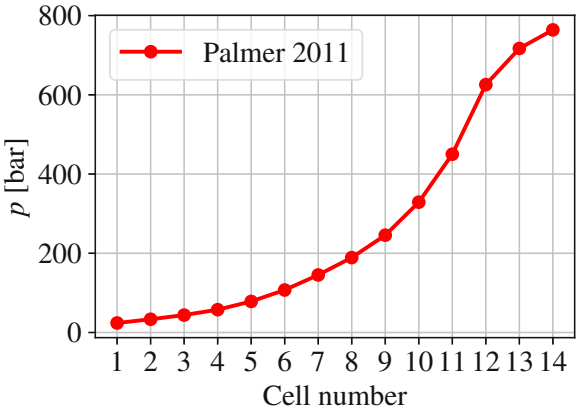


**Figure 4.12.:** Liquid hydrogen pressure increase in each absorber cell of the final cooling channel, based on the preliminary study by B. Palmer [131]. The resulting pressures are computed using CoolProp. After the beam passes through, the resulting pressures remain extremely high, with the last cell reaching nearly 900 bar. The results highlight the significant engineering challenge of designing ultra-thin absorber windows capable of withstanding such extreme conditions.

Subsequent to the beam's passage through the absorber, the resultant pressures remain exceptionally high. In Palmer's study, the last cell attains a pressure approaching 900 bar. The principal issue is that the absorber must be confined as a result of its liquid state. The interface at which the beam enters the absorber is referred to as the window. The window thickness must be minimized to avoid complete stopping of muons. Furthermore, the window material should ideally be composed of a low-$Z$ material to mitigate the heating of the emittance. As illustrated in Fig. 4.12, the fabrication of extremely thin materials capable of withstanding such high pressures presents significant technical challenges.

These high pressure increases have a significant impact on the conceptualization of a final cooling channel. To reduce the pressure within the absorbers following the passage of a muon beam, it is necessary to adjust the initial hydrogen pressure and density. Consequently, some absorbers may transition from a liquid state to a vapor state.

The length of the absorber can also be extended, as beam depositions in lower densities will be lower. Longer absorbers will contribute to minimizing the number of final cooling cells. All these considerations will be examined in Chapter 5.4.3, where the selection of hydrogen absorbers will be discussed in more detail.

### 4.7.2 Window heat dissipation

The absorber also includes windows where the energy of the beam is deposited. Unlike the hydrogen absorber, the window is made of solid material. It is important to assess whether the energy accumulated in the window reaches a critical threshold. As a first-order estimation, one can assess how the heat produced in the beam-interaction zone flows into the colder, non-irradiated regions of the window.

The energy deposition in the window can be estimated as in the discussion previously. The region of heating caused by the cylindrical beam is illustrated in **left** sketch of Fig. 4.13 as the red zone, which has a radius of $a$. The focus is on heat transport from the irradiated area to the rest of the window. This can be evaluated by

$$\frac{dQ}{dt} = -\lambda\, A\, \nabla T, \tag{4.65}$$

which is a differential equation, that describes the time depended heat flow $dQ/dt$ through a surface $A$ by the temperature gradient $\nabla T$ [134]. Like the **left** figure in Fig. 4.13 illustrates, the window is approximated as a cylinder with radius $b$ and thickness $d$. In this example, heat flow is assumed to be only in the radial direction. Therefore, any heat exchange through the surfaces that face the absorber or the vacuum were neglected in this example. Given these conditions, the rate of radial heat transfer can be articulated as follows:

$$\int_{T_{\text{in}}}^{T_{\text{out}}} \mathrm{d}T = -\frac{\Delta Q}{\Delta t \cdot \lambda}\,\frac{1}{2\pi d}\int_a^b \frac{\mathrm{d}r}{r} \quad \Rightarrow \quad \frac{\Delta Q}{\Delta t} = 2\pi d\,\lambda\,\frac{T_{\text{in}} - T_{\text{out}}}{\ln(b/a)}, \tag{4.66}$$

where $T_{\text{in}}$ is the temperature at the window area impacted by the beam, and $T_{\text{out}}$ is the window's initial temperature.

The use of a 5 mm thick lithium hydride (LiH) window and a 3 µm silicon nitride ($Si_3N_4$) layer is considered, as these materials are strong candidates for windows in the final cooling channel. A detailed analysis of the specific stages at which each material is used is provided in Chapter 5.4.3. LiH offers the advantage of being composed of low-$Z$ material, making it suitable for the early stages of the final cooling channel. In contrast, $Si_3N_4$ can be manufactured as an extremely thin film and is better suited for use in the later stages.

In the final cooling channel, a bunch of muons pass through the absorbers every 0.2 s [27]. The number of muons per bunch at this stage is estimated to be approximately $6 \cdot 10^{12}$, which is higher than the target value of $4 \cdot 10^{12}$ at the collision point. This higher initial count accounts for expected muon losses due to decay in the pre-accelerator complex between the final cooling stage and the collision point.

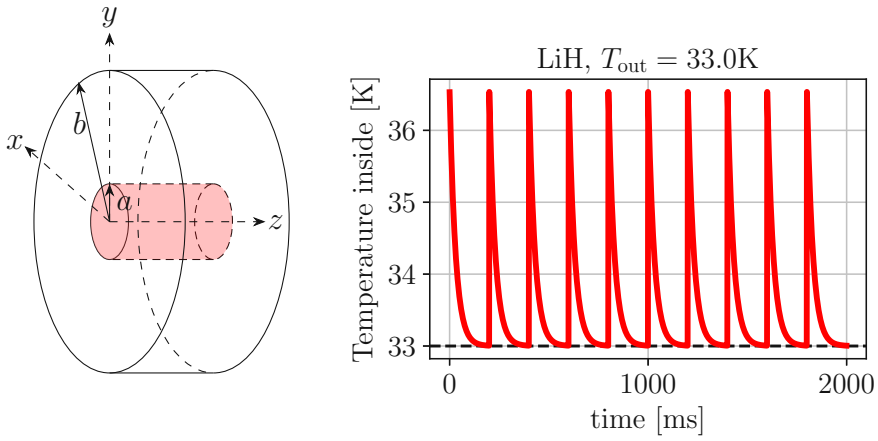


**Figure 4.13.:** The **left** side visualize a cylindrical beam window with its geometrical parameters. The **right** plot shows the cooling rate for a cylindrical LiH window. The peaks in the **right** diagram illustrate the energy deposition when a muon bunch goes through the window every 0.2 s.

The evolution of temperature in the center of the window, where the beam passes through, is analyzed using Eq. (4.65), with the specific parameters summarized in Table 4.3. The thermal conductivity of LiH is taken to be $\lambda = 100\,\mathrm{W\,m^{-1}\,K^{-1}}$, as reported in the reference in [135]. Due to the lack of available thermal conductivity data for $Si_3N_4$ at low temperatures, only LiH was considered in this analysis.

| Parameter | LiH |
|---|---|
| $\varepsilon_{\perp,\mathrm{N}}$ | 94 µm |
| $d$ | 5 mm |
| $b$ | 2.5 cm |
| $T_{\text{out}}$ | 33.0 K |
| $\lambda$ | $100\,\mathrm{Wm^{-1}K^{-1}}$ |
| $E_{\text{Kin}}$ | 20.6 MeV |

**Table 4.3.:** Parameters for the beam and the window in calculating the heat dissipation are described. The normalized transverse emittance is denoted by $\varepsilon_{\perp,\mathrm{N}}$, and the average kinetic energy of the beam is given as $E_{\text{Kin}}$. The thickness and radius of the LiH window are represented by $d$ and $b$, respectively, while the thermal conductivity is indicated by $\lambda$. The initial temperature of the window, prior to muon beam exposure, is referred to as $T_{\text{out}}$.

Inside a 40 T solenoidal magnetic field, the transverse size of the muon beam is approximately 1.3 mm. Under these conditions, the temperature in the center of the window increases by about 36.5 K. This occurs for a muon bunch containing $6 \times 10^{12}$ particles,

assuming an initial window temperature of 33 K. This particular case was taken from the final cooling cell 4 in Table 5.5 of the next chapter.

Following beam impact, the localized temperature increase, which forms a hot trace along the beam path, decays exponentially, returning to its initial value within a time frame of 0.2 s, as illustrated in Fig. 4.3 **right**. Successive bunches do not lead to significant temperature accumulation, although heat transfer from the window to the absorber was not considered in this analysis.

These results represent a first-order analytical approximation, which provides a satisfactory understanding of the thermal behavior. As a next step, it would be beneficial to extend the same calculations to the case of $Si_3N_4$. However, this can only be achieved if reliable thermal conductivity data at low temperatures are available. $Si_3N_4$ windows will be used for the last cooling stages, where the beam has low energies and low transverse emittances.

## 4.8 Summary of beam dynamic in ionization cooling

The comparison of the RF-Track solenoid model against G4Beamline demonstrates that RF-Track can reliably simulate particle trajectories through a cylindrically symmetric solenoid structure. Minor discrepancies arise, particularly at larger radial offsets. However, the overall agreement between the two simulation tools confirms the accuracy and robustness of RF-Track in the tracking of macro-particles in solenoids.

This chapter presented a refined analytical model for ionization cooling by integrating the Bethe-Wentzel scattering approach into the transverse cooling equation. This enhancement leads to significantly improved agreement with ICOOL simulation results, both for transverse equilibrium emittance and longitudinal emittance evolution.

The study in this chapter underscores the critical role of emittance minimization in achieving optimal luminosity for a muon collider. By highlighting the inverse relationship between luminosity and both transverse and longitudinal normalized emittances, it becomes clear that careful control of the beam parameters is essential. The foundation is laid for an analytical approach to identify the optimal initial beam energy for the final cooling cell, providing a strategic pathway to enhance collider performance through precise beam optimization.

Although hydrogen enables a significant reduction in the transverse emittance, the resulting high energy density owing to small beam sizes and low energies leads to notable energy deposition and pressure build-up within the absorber. These effects require careful adjustment of absorber parameters, such as initial pressure, density, and length, to

maintain stability and efficiency. In addition, the thermal response of the absorber windows was evaluated, particularly under repeated impacts of the beam, to avoid material failure. The analytical estimates presented provide an essential first look at these effects and establish a basis for future studies, including the evaluation of $Si_3N_4$ windows in later cooling stages.

# Chapter 5.

# Beam dynamics study in a final cooling lattice design

A highly effective final cooling channel is crucial for high-luminosity muon colliders; however, it is challenging to design due to the increase in longitudinal emittance when attempting to decrease transverse emittance. The emittance targets for the muon collider study are set to 25 µm for the transverse emittance and 70 mm for the longitudinal emittance [25]. During an earlier phase of the muon collider complex, specifically in the 6D-cooling channel [36], the muon beam is designed to obtain transverse emittances of 300 µm and longitudinal emittances of 1.5 mm[1]. In the final cooling channel, the muon beam will undergo further transverse cooling to meet these target specifications.

The strategy for this final cooling design follows a systematic and realistic methodology, which is different from previous designs [131, 132]. This chapter presents four novel methods for analyzing the beam dynamics within a final cooling lattice cell. In Section 5.1.2, the **first** method involves beam matching from low to high field solenoids to prevent increase in emittance and introduces a novel adiabatic beam matching technique. In Section 5.2, the **second** technique reverses the accumulation of canonical angular momentum in the final cooling cells, which is vital for effective cooling and maintenance of the decoupled beams. In Section 5.3, the **third** element involves the continuous fine-tuning of the energy spread through RF systems, which is crucial for managing the increase in longitudinal emittance. The **forth** method, described in Section 5.4, focuses on the windows and hydrogen density in the final cooling channel, areas that earlier studies had considered less essential. These iterative techniques led to the attainment of a final transverse emittance of 27.2 µm, with additional potential for further enhancement of the longitudinal emittance.

[1]Recent studies of 6D cooling reach transverse emittances lower than 300 µm [48].

## 5.1 Solenoid matching technique

Effective ionization cooling requires strong solenoid fields, such as the CERN high-field solenoid which is designed to achieve up to 40 T [136] while maintaining field uniformity to optimize cooling efficiency. Beam machine techniques such as adiabatic ramping; minimizing the betatron function; and using specialized matching coils; all ensure stable beam conditions, with simulations demonstrating that optimized matching prevents transverse-emittance growth.

### 5.1.1 CERN-type high-field solenoids in tracking simulations

CERN's magnet group has proposed a conceptual and realistic design for high-field solenoids. This section elucidates how the design developed by CERN's magnet experts integrates into tracking codes. Some adjustments in the simulations improve computational efficiency. As detailed in a recent design report [47], solenoids with a peak field of 40 T will be available in the next decade. Although the final cooling design is capable of supporting higher magnetic fields, the 40 T option was chosen for consideration in this thesis.

The final stage of ionization cooling necessitates extremely strong solenoid fields to counteract the effects of emittance heating from scattering. This topic was explored in detail in the previous chapter. Due to the equilibrium emittance, achieving the desired normalized emittance of 25 µm requires field strengths exceeding 30 T [131].

The strength of these high-field solenoid influences the length of the channel. As the field strength increases, the channel becomes shorter due to enhanced cooling effects. This not only has impacted the cost of the beamline, but also offers benefits for the longitudinal beam parameters. However, fields higher than 40 T later stages could be beneficial for longitudinal emittance, but this has to be investigated in another study.

Here, a brief summary of previous research evaluates how the cooling design and lattice length are affected by the maximum solenoid field strength. H. Sayed et al. [132] used fields of 25 T to 30 T, achieving a normalized transverse end emittance of 55 µm and a normalized longitudinal emittance of about 76 mm. They achieved these results with a transmission rate lower than 50%, resulting in a cooling design that spans approximately 140 m.

B. Palmer and colleagues, as outlined in [131], propose the use of high-field solenoids with a magnetic strength of 40 T. This includes an additional single 50 T solenoid for the last cooling cell in the channel. This structure successfully achieves the target transverse emittance. The normalized longitudinal emittance is 72 mm with a transmission of 67%.

The total beamline is about 75 m, which proves that a stronger high-field solenoid indeed shrinks the final cooling channel.

This chapter adopts B. Palmer's scheme utilizing a 40 T magnet, while excluding the 50 T magnet in the last cell. A primary challenge in final cooling is to ensure that the solenoid's field homogeneity at the absorber location remains minimal. In other terms, it implies that the field strength within the absorber must remain as uniform as possible. Neglecting this factor will result in simulations performing worse than analytical predictions due to lower field strengths at the absorbers entry and exit areas. For extremely small normalized transverse emittances near the desired target parameter, this inconsistency may lead to emittance-heating effects as a result of the emittance reaching below its equilibrium.

The proposed CERN solenoid employs a high-temperature superconductor (HTS) to meet the need for a high-field solenoid essential for final cooling. The proposed solenoid employs a high-temperature superconductor made of rare-earth barium copper oxide, better known as **ReBCO**.

The solenoid is constructed in a modular fashion using identical ring-shaped units known as pancakes. These pancakes are wound with ReBCO wires. Each pancake includes a hole with a diameter of 50 mm, an external radius of 90 mm, and a thickness of 12 mm. In the design proposal of B. Bordini et al. [136], 46 pancakes are electrically connected in series. They are separated by stiff support plates that prevent the axial Lorentz forces. To achieve a maximum field of 40 T, each pancake model has a current density of 650 A mm$^{-2}$.

To achieve consistent **uniformity** in the bore of the solenoid, **three** additional **corrector pancakes** are added at both the entrance and exit of the solenoid. These pancakes retain the same inner radius and current density, but have **different outer radii**. In the CERN design, the high-field solenoid, which includes the corrector pancakes, measures a total of 73 cm in length. The following discusses potential modifications to this dimension. The calculation of the homogeneity of the axial field is given by $1 - B(s)/B_{\text{peak}}$. In the CERN design, the solenoid remains below 1% within the length 50 cm. The absorber is proposed to be placed in this low homogeneity region in order to maximize the ionization cooling efficiency.

In principle, it is possible to create a similar design of this CERN-type solenoid model using G4Beamline and RF-Track. However, the process of computing the field for each pancake module requires significant time. This is due to the requirement of solving elliptical integrals for each pancake module, which is lengthy. Although performing a single simulation is not problematic, beam matching demands excessive time due to the optimizer's search for matched beam conditions across numerous field configurations.

An effective strategy to minimize total elliptic integrals is to substitute a set of equal pancake modules with a single solenoid. To maintain field uniformity within the solenoid,

only corrector pancakes will be retained. These corrector modules will be added to both the entry and exit of this single solenoid. This simplified design achieves a peak field of 40 T at a current density of 535.3 A mm$^{-2}$. It can be assumed that the 18% reduction in current density, relative to the CERN-design, is due to the exclusion of gaps between each pancake module which are essential for a realistic design.

An illustration of such a simple solenoid used for G4Beamline and RF-Track simulations is provided in Fig. 5.1. The left side of Fig. 5.1 shows the magnetic field strength on the axis. The corresponding homogeneity plot is shown in the plot on the left. The right plot of Fig. 5.1 features a color map illustrating the total magnetic field strength $|\vec{B}|$ and its field line configuration. Additionally, Fig. 5.1 shows the three corrector pancakes on both ends of the solenoid, characterized by their different radii. Those ensure the field lines remain long and parallel to the beam axis.

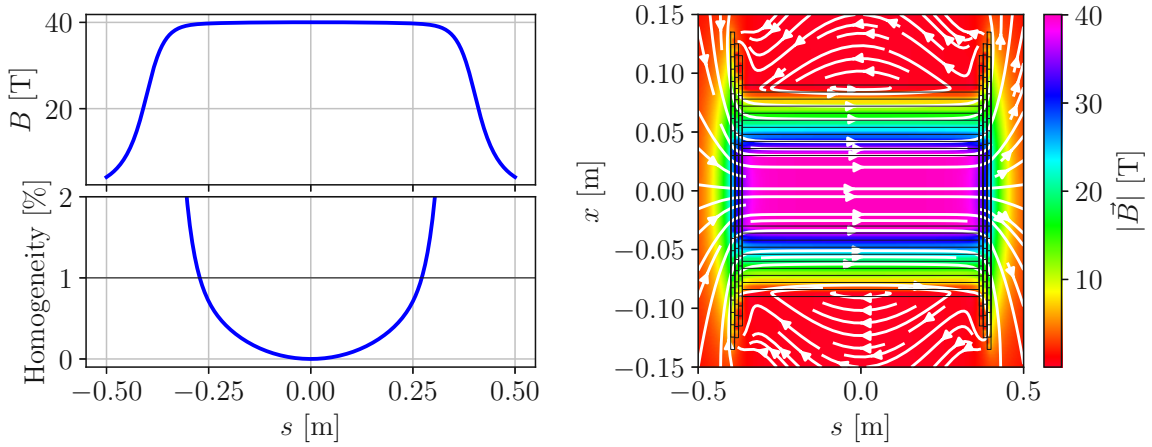


**Figure 5.1.:** Illustration of the solenoid's magnetic field on its axis (**left top**) and the corresponding homogeneity plot (**left bottom**). The plot on the **right** showcases a colormap depicting the lateral cross section of the total magnetic field strength $|\vec{B}|$, alongside the configuration of the field lines. It also illustrates the corrector pancakes which ensure that the field lines remain long and straight within the solenoid.

For this study on final cooling, non-liquid hydrogen absorbers were utilized for the first time. Because of their lower density, these absorbers typically need to be longer than those with liquid hydrogen. Consequently, the absorber length will be capped at a maximum of 90 cm, which is the 1%-homogeneity range of the solenoid of 1.2 m CERN type.

The proposed design in the later sections of this chapter necessitates three distinct lengths for high-field solenoids. Table 5.1 provides the total lengths of these CERN-type solenoids, as well as the section lengths where homogeneity is with the 1% variation. For this study, slightly longer CERN-type solenoids were considered. The solenoid of

minimal length is indicated as 80 cm, and it is the model exhibited in Fig. 5.1 on the right side.

| Total solenoid length [cm] | 1% homogeneity [cm] |
|---|---|
| 80 | 57 |
| 100 | 73 |
| 120 | 90 |

**Table 5.1.:** Summary of total lengths for the proposed high-field solenoids and sections with homogeneity below 1%.

### 5.1.2 Single particle matching and adiabatic ramping

The subsequent sections will discuss a method for matching a single particle within a beamline composed of low- and high-field solenoids. This approach can be utilized for a particle distribution which is Gaussian, axially symmetric, and monoenergetic, provided the radial beam size is adequately small. To maintain an optimal transverse condition for ionization cooling of the muon beam, consistent matching is crucial. The main factors involve:

- ensuring that the cylindrically symmetric betatron function $\beta_\perp$ attains its minimum value inside the absorber,
- avoiding mismatches, which lead to transverse filamentation and consequently an increase in the normalized transverse emittance.

Firstly, betatron oscillations in the absorber reduce the effectivity of ionization cooling. The reason is that scattering-induced heating can be minimized when the beta-function reaches its lowest value. Secondly, betatron oscillations inside a CERN-type solenoid with an absorber cause mismatches and lead to additional transverse emittance increases. A later section will explore the increase in transverse emittance resulting from optical mismatches.

As discussed in Chapter 4.3, the dynamics of charged particles in a beam can be described by the solenoid's envelope equation, given by

$$2\beta_\perp\beta_\perp'' - (\beta_\perp')^2 + 4\beta_\perp^2\kappa^2 - 4(1-\mathcal{L}^2) = 0. \tag{5.1}$$

In Eq. (5.1), $\beta_\perp(s) = \beta_\perp$ refers to the cylindrically symmetric betatron function, where $\beta_\perp'$ and $\beta_\perp''$ represent its first and second derivatives with respect to the path length $s$ ($\prime = \partial/\partial s$). The parameter $\kappa = \kappa(s) = 0.3B(s)/2p_z$ quantifies the solenoid's focusing

strength and $\mathcal{L}$ represents the conserved normalized average canonical angular momentum.

Typically, a beam is considered matched when its phase space ellipse is in alignment with the machine's ellipse [117]. In a static and homogenetic solenoid, the beta-function remains both constant and minimized if $\beta''_\perp = \beta'_\perp = 0$ and leads to

$$\beta_\perp = \frac{1}{\kappa}\sqrt{1+\mathcal{L}^2}, \tag{5.2}$$

when $\mathcal{L}$ is non-zero.

Apart from a high-field CERN-type solenoid, the final cooling channel is comprised of multiple other solenoids, each with unique magnetic-field configurations. Parameters $\beta_\perp$ and $\beta'_\perp$ can be determined along the beamline by solving Eq. (5.1) numerically. This determination is possible given the magnetic field configuration of solenoids from position $s_0$ to $s_1$ and knowing the initial conditions $\beta_\perp(s_0) = \beta_{\perp,0}$ and $\beta'_\perp(s_0) = \beta'_{\perp,0}$. The numerical solution of the Eq. (5.1) was performed using the `odeint` function of the Scientific-Python (SciPy) library [55].

### Coil arrangements around a CERN-type solenoid

The following paragraphs outline the method for transferring the beam between solenoids. An example is intended to illustrate the process of transporting a muon bunch from a region of low magnetic field to an area of high magnetic field. For the high-field area, the CERN-designed solenoid is used.

In order to transport a beam from one solenoid to another, a distinct system of coils with specific characteristics must be placed between them. These coils guarantee that the beam is aligned with the optics of both solenoids. These particular coils are known as **matchers**. Fig. 5.2 presents an example comprising two low-field solenoids, L1 and L2, situated on either side of a CERN-type high-field solenoid. Positioned between L1 and the high-field device are four upstream matching coils, labeled MU1, MU2, MU3 and MU4. An analogous arrangement of downstream matching coils, designated MD1, MD2, MD3 and MD4, is situated between the high-field solenoid and L2. This configuration is used to transfer the beam into and out of the high-field solenoid. The dimensions of the low-field solenoids and the matching coils were assumed to use conventional, more affordable conductors or superconductors, resulting in them being larger than the high-field solenoid in Fig. 5.2.

In this case, the optical systems L1, L2, and the CERN solenoid satisfy the condition specified in Eq.(5.2). The MU1-MU4 and MD1-MD4 matchers ensure matching conditions within L1, L2, and the CERN solenoid, provided that unique coil parameters

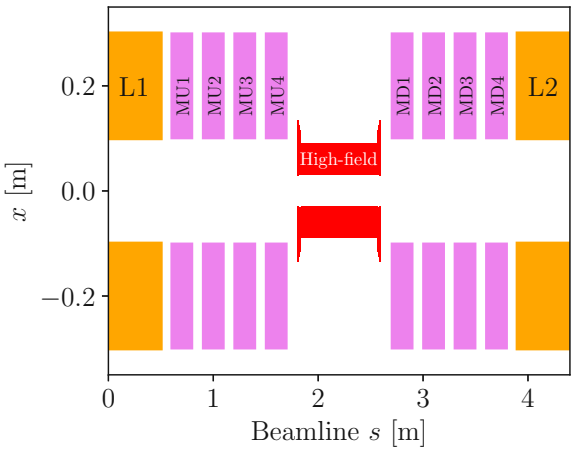


**Figure 5.2.:** The figure should show a lateral cross-section of the solenoid system, with low-field solenoids L1 and L2 flanking a central CERN-type high-field solenoid. Four upstream matching coils (MU1–MU4) are located between L1 and the high-field solenoid, while four downstream matching coils (MD1–MD4) are between the high-field solenoid and L2. The larger size of the low-field solenoids and matching coils reflects the use of conventional conductors.

for the matchers are identified. These parameters include **current densit**y, **inner** and **outer radii**, and the **positions** of the matching coils. To avoid spatial conflicts, for this study, the **current density** was selected as the unique adjustable parameter for each matching coil. For a mono-energetic bunch, a theoretically lower matching coil number than four could be chosen for each transfer between solenoids. For strategic reasons, which are detailed in the next section, discussing beams with momentum spread, four were selected.

### Optimization techniques for beam matching in solenoids

Optimization of the current density $J_i$ of each matching coil was performed using the function `scipy.optimize.minimize` [55], applying the Nelder-Mead algorithm [137]. The method is well-suited for multidimensional unconstrained optimization problems. It enabled the precise adjustment of solenoid parameters to achieve the desired magnetic-field profile. The Nelder-Mead algorithm facilitated efficient fine-tuning of the system by iteratively minimizing a defined objective function. This process enabled the system to meet constant and minimum beta values inside L1, L2, and the high-field solenoid.

To start with the optimization, a cost function $f_{\text{err}}$ must be established and which has to be minimized by the optimizer. A cost function in an optimizer quantifies the difference

between the predicted outputs of a model and the actual target values, serving as a measure of error. In this particular scenario, the values of the predicted parameters are defined as $\beta_\perp(s_i)$ and $\beta'_\perp(s_i)$. The target values are $\beta_{\perp,0}(s_i)$ and $\beta'_{\perp,0}(s_i)$, evaluated at one or several positions $s_i$. The optimizer uses this function to adjust the model's parameters iteratively, with the aim of minimizing the error between the target and the actual values. For the solenoid matching process, the cost function is defined as follows:

$$\begin{aligned} f_{\text{err}} &= \sum_i \left\{ \left[\beta_{\perp,0}(s_i) - \beta_\perp(s_i)\right]^2 + \left[\mathcal{W} \times \beta'_\perp(s_i)\right]^2 \right\} \\ \beta_{\perp,0}(s_i) &= \frac{1}{\kappa(s_i)}\sqrt{1+\mathcal{L}^2}, \qquad \frac{1}{\kappa(s_i)} \approx \frac{2\,p_{\text{ref}}[\text{GeV/c}]}{0.3\,B(s_i)}. \end{aligned} \tag{5.3}$$

A weight factor $\mathcal{W}$ is introduced to the betatron correlation $\beta'_\perp(s_i)$ in Eq. (5.3) to ensure optimal results [138]. In this study, the employment of $\mathcal{W} = 100$ was frequently observed. To effectively optimize, choose a few points $s_i$ that are close to the center of the solenoid, which need to be matched.

### Adiabatic field ramping

The 1 m solenoids L1 and L2 operating in the low field regime were selected to achieve a maximum field of approximately 4 T, resulting from a current density of 17 A mm$^{-2}$. Typically, achieving alignment for the beam from L1 to the 40 T Cern-type solenoid, H1, requires some time. The optimizer is sensitive to the initial current densities and, therefore, may require iterative initial solutions prior to a full minimization.

A strategy for discovering quickly optimized parameters is adiabatic ramping from a region with a low magnetic field to a higher one. The initial setup is to match two low-field regions, which rapidly provides a solution for optimized matching coil current densities. After finding the optimal coil parameters for an optimized configuration for both solenoids, the current density in one solenoid of them can be **ramped up**. Once the magnetic field of a solenoid is heightened, the optimizer can be relaunched, but starting with the previously optimized matching coil configuration.

Illustrating the previous setup, Fig. 5.2 shows a matching example using a reference momentum of $p_{\text{ref}} = 112.5\,\text{MeV/c}$. Instead of initiating with the H1, the optimizer uses a geometrically identical solenoid but with a lower field. This is to guide the optimizer to find easier solutions that can be used for the next set of initial conditions. The example in the plot on the left side of Fig. 5.3 begins with a CERN-type solenoid at 10 T. The plots also depict the transitional phases of $\beta_\perp$ and $\beta'_\perp$ until they reach the matched conditions, denoted by a bold line on the graphs. The thin lines are the plots illustrate the intermediate steps of the optimzer. To recapitulate, optimized settings occur when the values of in the center of L1, L2 and H1 are $\beta_\perp = \sqrt{1+\mathcal{L}^2}/\kappa(s)$ and $\beta'_\perp = 0$.

After aligning the matching coils' parameters, an increase in the field strength of the CERN-style solenoid can be re-optimized. The re-optimization will be launched by starting with the previous matched coil conditions. This process can be iterated **adiabatically** until the desired field strength of 40 T is achieved. The outcome for the 40 T solenoid under these aligned conditions is presented in the right plot of Fig. (5.3).

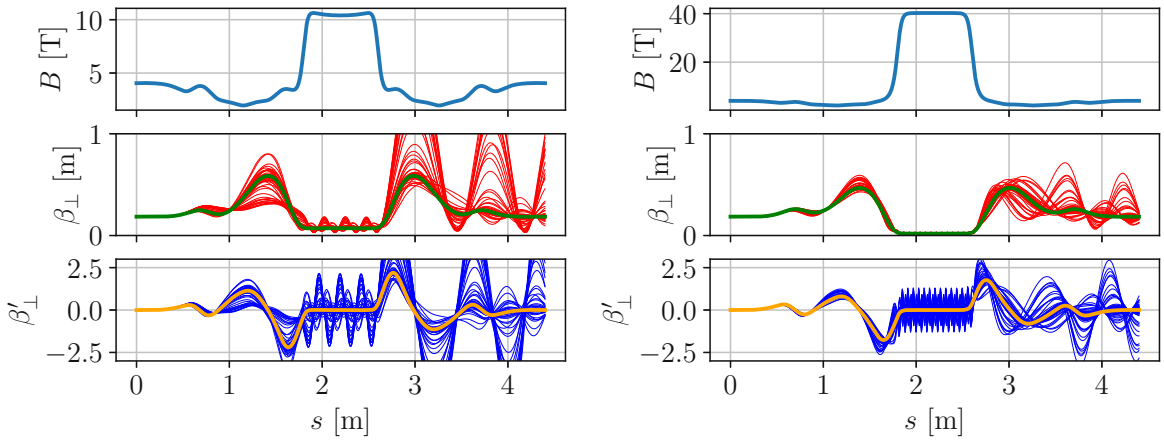


**Figure 5.3.: Adiabatic ramping** of the magnetic field in a CERN-type solenoid is illustrated. Starting at 10 T (**left**), the optimizer minimizes $\beta_\perp$ inside the solenoid while ensuring $\beta'_\perp = 0$, shown as **thick lines**. **Thin lines** represent intermediate optimization steps. Once a solution is found, the solenoid field strength is increased and re-matched, using the previously matched values as a starting point. This process—matching, increasing the field, and re-matching—is repeated in **adiabatic** steps. Once the target field-strength of 40 T (**right**) is reached and the beam is matched, the process ends. The final and matched solutions of the beam parameters are depicted as the **thick lines** in the **right** plots.

Tables 5.2 and 5.3 present the current densities for the four upstream matching coils in both the 10 T and 40 T high-field solenoid scenarios. In particular, current densities are fairly comparable in both situations. It demonstrates that adiabatic ramping effectively transitions beam parameters from low-field to high-field regions while maintaining matched conditions. The current densities for the matching coils for cases 10 T and 40 T are notably similar, highlighting the efficiency of the approach in achieving stable beam matching in high-field solenoids.

For a beam with a single energy (single-particle approach), within a symmetric solenoid setup, achieving beam matching from the region of high magnetic field to the low-field solenoid L2 is straightforward. The key is to apply a symmetric configuration of current density in the corresponding MD1, MD2, MD3, and MD4 alternating coils downstream as opposed to the upstream coils. Four matching solenoids were selected for reasons of comparative analysis, although alternative matching configurations could also result in

| Coil name | $J$ [A mm$^{-2}$ ] |
|---|---|
| MU1 | 24.526 |
| MU2 | 10.314 |
| MU3 | 11.087 |
| MU4 | 24.021 |

**Table 5.2.:** Current densities for the four upstream matching coils in the 10 T solenoid configuration.

| Coil name | $J$ [A mm$^{-2}$ ] |
|---|---|
| MU1 | 22.786 |
| MU2 | 11.389 |
| MU3 | 12.475 |
| MU4 | 19.845 |

**Table 5.3.:** Current densities for the four upstream matching coils in the 40 T solenoid configuration.

viable solutions. Fig. 5.4 presents a comparative histogram of the current density in the matcher coils for both the 10 T and 40 T scenarios.

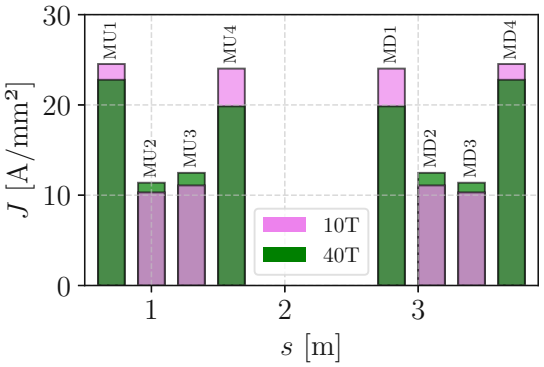


**Figure 5.4.:** Histogram of current density for upstream (MU1-MU4) and downstream matcher (MD1-MD4) solenoids for a 10 T high-field system depicted as violet bars. As comparison, green bars are illustrating the 40 T case.

### 5.1.3 Matching strategy of beams with energy spreads in solenoids

In the discussion before, the matching was performed for a single particle. However, in practical terms, the muon beam displays a momentum spread denoted by $\sigma_{p_z}$. Therefore, the single-particle matching technique needs a slight extension. Before initiating this discussion, it is appropriate to note that the matching of two reference particles requires the optimization of four beam parameters. This optimization is achievable through the selection of four solenoid parameters as variables, with the current density being the parameter selected for this analysis. Note that in the ensuing study, no absorbers were incorporated within the high-field solenoids.

A practical approach involves using two reference particles, defined as

$$p_1 = p_{\text{ref}} - \sigma_{p_z}, \quad p_2 = p_{\text{ref}} + \sigma_{p_z}, \tag{5.4}$$

where $\sigma_{p_z}$ denotes the rms momentum spread of the beam. For beam matching purposes, more than two reference particles can be employed, and momentum deviations other than $\sigma_{p_z}$ may also be considered.

Using the solenoid arrangement illustrated in Fig. 5.2 as a starting point, the objective is now to determine an optimized arrangement for the current densities in the matching coils (MD1-MD4). In this procedure, the error function $f_{\text{err}}(p_1)$ is evaluated for the first reference momentum, along with $f_{\text{err}}(p_2)$ for the second one. The goal of the optimizer is to reduce the sum of these functions, given by the total cost equation:

$$f_{\text{err}}^{\text{total}} = f_{\text{err}}(p_1) + f_{\text{err}}(p_2). \tag{5.5}$$

To initiate optimization, one can employ the adiabatic ramping technique as shown in the prior subsection, facilitating quick results. The study observed that typically when a solution is found for two reference particles, as denoted by $p \pm \sigma_{p_z}$, the macro-particle beam alignment is also achieved. However, in cases where the macro-particle simulation yields a mismatch despite finding a solution for two reference particles, it is advisable to incorporate additional reference momenta. Consequently, the error function becomes generalized to $f_{\text{err}}^{\text{total}} = \sum_i f_{\text{err}}(p_i)$.

Fig. 5.5 illustrates this example, where the initial reference momentum is $p_1 = 109.2\,\text{MeV/c}$, and a second reference particle has a momentum of $p_2 = 115.8\,\text{MeV/c}$. The illustration on the left side of Fig. 5.5 presents the aligned solenoid setup that incorporates the 40 T high-field solenoid. In this beamline, the downstream matching coils (MD1-MD4) are configured with a pattern of symmetric current density. Due to the symmetric optical configuration, this aligns with the present density of the upstream coils. This aids in the beam's transition from the high-field area to the low-field region L2.

Before concluding this discussion, it is worth mentioning the number of matching coils required. When matching two reference particles, four beam parameters need optimization: $\beta_\perp(p_1)$ and $\beta'_\perp(p_1)$, as well as $\beta_\perp(p_2)$ and $\beta'_\perp(p_2)$. In this scenario, four free parameters are required, specifically the current densities of MU1-MU4 to achieve optimal results. The tests were carried out with fewer than four matching coils, but no optimal results were obtained. Hence, it should be clarified that for, e.g., three reference particles, six matching coils should be considered. In summary, for $n$ reference particles, at least $2n$ free parameters are essential to optimize a beamline of solenoids.

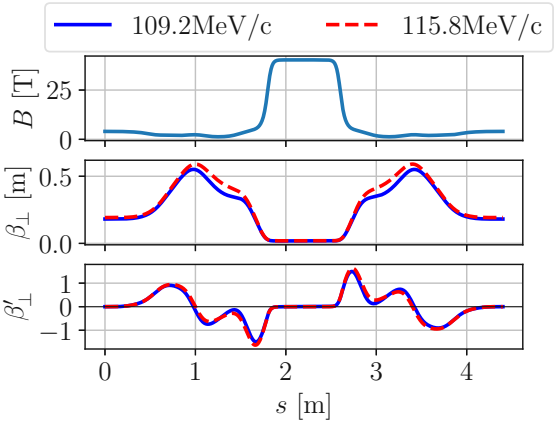


**Figure 5.5.:** Matched beam parameters of two reference momenta with $p_1 = 109.2\,\mathrm{MeV/c}$, $p_2 = 115.8\,\mathrm{MeV/c}$ depicted on the **left** diagram. Illustration of the beam matching setup for a beamline incorporating a 40 T high-field solenoid. **Without absorbers** included, MU1-MU4 equals always MD4-MD1.

### 5.1.4 Dynamical matching including absorbers and RF

In the earlier discussions, the matching methods consistently assumed that the longitudinal momenta of the particles did change within a beamline. However, in ionization cooling, the particles' $p_z$ vary. In ionization cooling, the beam first loses energy in the absorber, and then $p_z$ changes due to acceleration within the cavity system. There is also a third scenario at the solenoid's entrance and exit, where momentum is exchanged between the longitudinal and transverse planes because of fringe-field kicks. This effect can be ignored if the particles have a minimal radial offset relative to the beam axis.

In beam matching, it is essential to incorporate the dynamics of $p_z$, which will affect the focusing strength of the solenoids, denoted as $\kappa$. In the earlier example, $\kappa(s)$ varied due to the alteration of the field of $B(s)$. Now, the momentum changes must also be taken into account, leading to $\kappa(s) \to \kappa(s, p_z) \approx 0.3B(s)/2p_z(s)$.

Two examples will be discussed in the following paragraphs. These examples have been selected because of their critical role in the functioning of a final cooling cell. The first showcases beam matching with a specific energy spread within a high-field solenoid system that incorporates a liquid hydrogen absorber. The second highlights beam matching within a cavity beam acceleration system.

The beamline in the **left** diagram of Fig. 5.6 utilizes a liquid hydrogen (LH) absorber within a 40 T CERN-style solenoid. In a realistic scenario, thick LiH (5 mm) windows are attached to the ends of the absorber to confine the hydrogen. The liquid hydrogen target has a material density of $0.043\,\mathrm{g\,cm^{-3}}$ and a length of 49 cm. This setup was

chosen to maintain the absorber pressure below 30 bar during beam passage. The total length of the absorber, including the beam windows, is 50 cm.

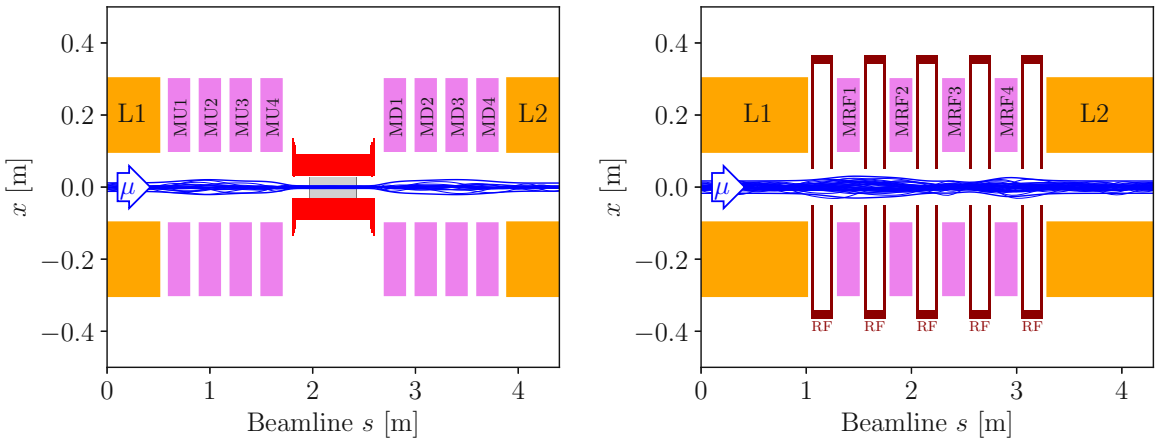


**Figure 5.6.:** The diagram on the **left** shows the arrangement of a solenoid within an ionization cooling cell, with the beam envelope represented by thin blue lines. The center of the left diagram features the high-field CERN solenoid, incorporating an absorber illustrated as the gray surface. On the **right** plot: The setup of a solenoid-cavity configuration includes five 150 MHz RF cavities, each with an accelerating gap of 20 cm powered at 10 MV/m, positioned between two 4 T solenoids (L1 and L2). The cavities are spaced 50 cm apart and interleaved with 20 cm wide matching coils (MRF1-MRF4). The reference particle starts with a momentum of $p_{\text{ref}} = 131.8\,\text{MeV/c}$ and an RF phase of $\varphi_{\text{acc}} = 54°$.

As illustrated in Fig. 5.7 with the appropriate graphs, the initial reference momentum of $p_{\text{ref}}(s_0) = 112.5\,\text{MeV/c}$ decreases approximately linearly to $p_{\text{ref}}(s_1) = 88.25\,\text{MeV/c}$. The beamline starts at $s_0 = 0\,\text{m}$ and extends to $s_1 = 4.4\,\text{m}$; the momentum reduction takes place only in the absorber. Initially, the beam has a momentum spread of $\sigma_{p_z}(s_0) = 3.3\,\text{MeV/c}$, which expands to 5.2 MeV/c due to the absorber highlighted in the previous chapter.

For matching, the adiabatic ramping technique was applied with two reference particles $p_1(s_0) = 109\,\text{MeV/c}$ and $p_2(s_0) = 115.8\,\text{MeV/c}$ that included their dynamical moment changes within the beamline. As can be seen in Fig. 5.7, the matching technique also works for this example, with a minor extension. The downstream matching coils (MD1-MD4) do not have the symmetric current density configuration with respect to the upstream matchers (MU1-MU4). The dynamical momentum change is responsible for this effect. Therefore, an individual set of MD1-MD4 configurations must be optimized to transfer the beam from the high-field area to the low-field solenoid L2. The values of the current density configuration of the matching coils are illustrated as histograms in the right plot of Fig. 5.7.

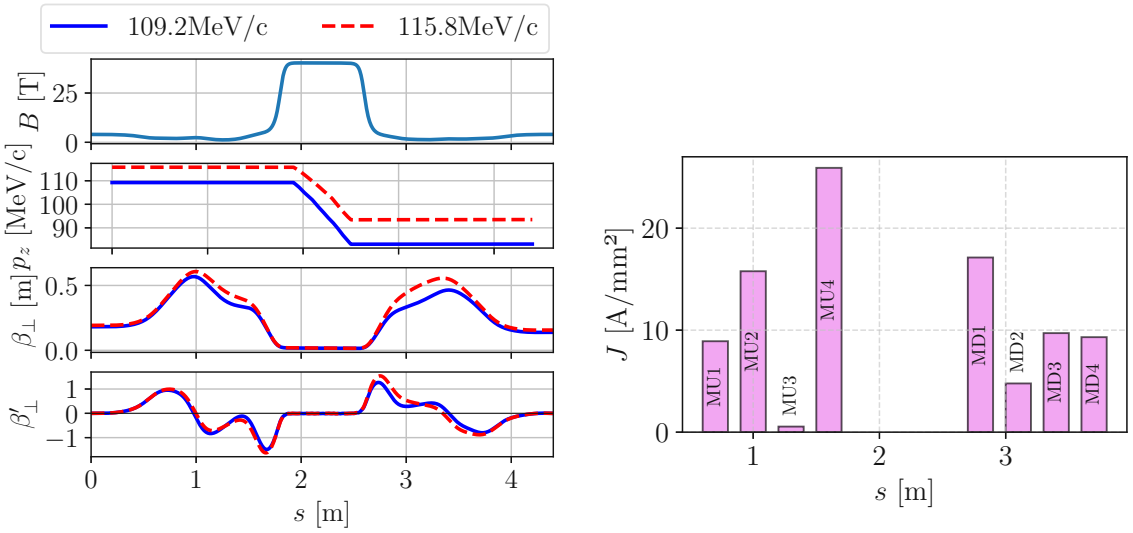


**Figure 5.7.:** Dynamic beam matching in the absorber region: The **left** plots show a momentum decrease of both reference particles (109 MeV/c and 115.8 MeV/c) in the absorber area. The adiabatic ramping of the matching coils (MU1-MU4 & MD1-MD4) establish matched conditions of the beam parametes $\beta_\perp$ and $\beta'_\perp$. The current density configurations are shown as histograms in the **right** plot.

The next example explores the concept of dynamic beam matching within a solenoid-cavity configuration, depicted on the right side of Fig. 5.2. This setup includes five RF cavities situated between two extended low-field ($\sim$ 4 T) solenoids, L1 and L2. Each cavity has an accelerating gap that measures 20 cm and is powered by a gradient of 10 MV/m. The cavities are separated by 50 cm centers and interspersed with wide 20 cm matching coils (identified as MRF1-MRF4). The reference particle initiates with a beam momentum of $p_{\text{ref}} = 131.8$ MeV/c and synchronizes with the RF phase at $\varphi_{\text{acc}} = 54°$. The normalized longitudinal beam emittance of 2 mm was used for this example and the RF frequency is 150 MHz. In Fig. 5.8 left, two reference particles are shown in a matched state, each with a momentum deviation of $\Delta p_z = 3.75$ MeV/c in relation to $p_{\text{ref}}$. The right-hand histogram in Fig. 5.8 presents the current density values for the RF matching coils.

In conclusion, the adiabatic matching method is also applicable in solenoid beamlines where the particle momenta get changed by for example absorbers or RFs. This is crucial to develop an ionization cooling lattice, where such momentum changes occur. The solenoid matching method, which included RF systems and absorbers, was explored and validated, allowing the simulation of a complete simulation of a full final cooling cell. Prior to this, the next discussion highlights the significance of a matched beamline.

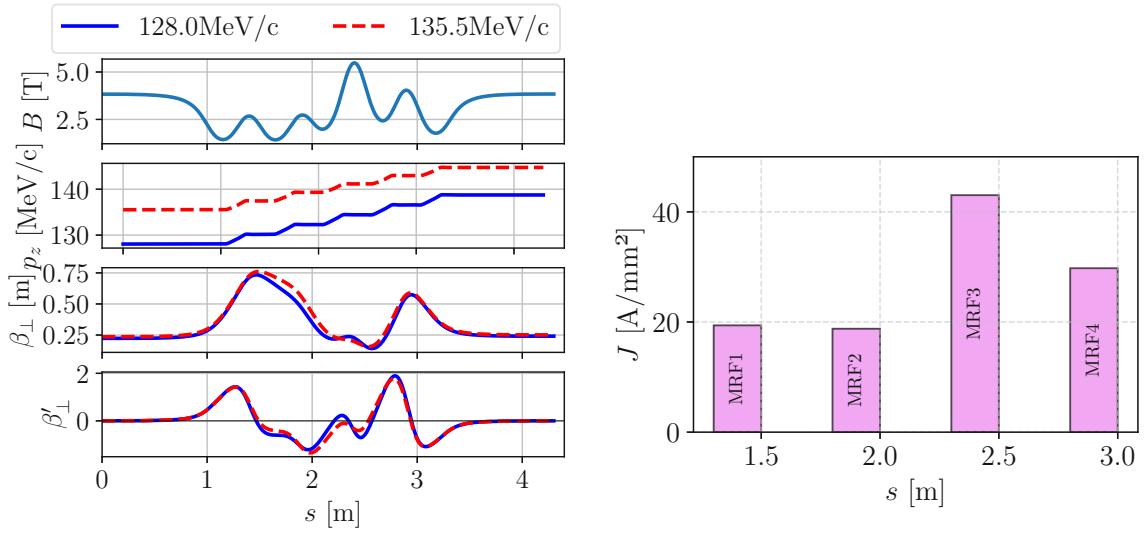


**Figure 5.8.:** Dynamic beam matching in a solenoid-cavity setup with five RF cavities (20 cm gap, 10 MV/m) between low-field solenoids (L1, L2, $\sim 4$ T). The cavity's centers are spaced 50 cm apart, with matching coils (MRF1-MRF4) in between. **Left**: The reference particles with plots showing their momentum increase and the matched beam parameters. **Right**: Current density in the RF matching coils.

### 5.1.5 Mismatches and transverse emittance increase

Finally, this section's concluding discussion highlights the significance of beam matching in terms of the normalized transverse emittance. A simulated example of ionization cooling with G4Beamline is used to compare matched and unmatched beam configurations.

The cooling cell structure comprises of two low field segments, L1 and L2, along with matching coils upstream (MU1-MU4) and downstream (MD1-MD4), as well as a CERN-style solenoid 40 T, denoted as H1. Within H1 lies an absorber-window setup, identical to that mentioned in the earlier discussion. In the first example, an optimized set of coils, MU1-MU4 and MD1-MD4, was identified. Meanwhile, in the second example, only the MU1-MU4 matchers were optimized, with the MD1-MD4 coils selected randomly.

In each case, an initial beam of normalized transverse emittance, $\varepsilon_{\perp,\mathrm{N}} = 124\,\mu\mathrm{m}$ and $10^4$ $\mu^+$, was produced at $s_0 = 0$ m, . For both scenarios, the beam path was tracked using G4Beamline, and the analysis of the normalized transverse emittance incorporated a sigma cut of 5.

In Fig. 5.9, the image on the left illustrates the ionization cooling cell operating under matched conditions. The normalized transverse emittance, $\varepsilon_{\perp,\mathrm{N}}$, is observed to vary strictly within the absorber region and remains steady elsewhere along the beam line.

In contrast, the graph on the right in Fig. 5.9 shows a scenario in which the downstream matching sections (MD1-MD4) are not optimally configured. It becomes apparent that emittance begins to grow rapidly. When the Courant-Snyder parameters of the beam are misaligned with those of the solenoid system, transverse filamentations result in an increase in transverse emittance. In constant solenoid regions, matches appear when $\beta_\perp$ is constant and $\alpha_\perp$ is zero.

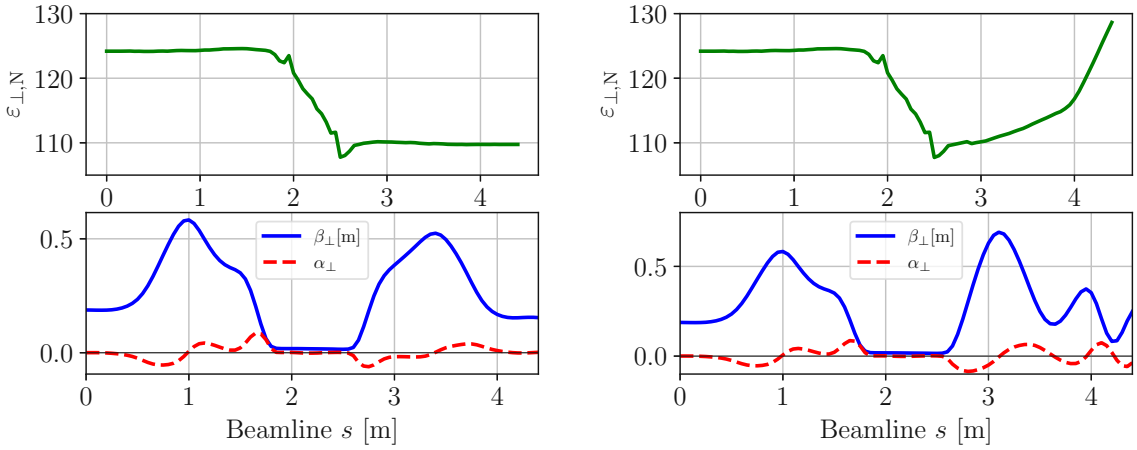


**Figure 5.9.:** Comparison of matched and mismatched Conditions in an Ionization Cooling Cell. The **left up** plot shows the normalized transverse emittance, $\varepsilon_{\perp,\mathrm{N}}$, varying only within the absorber region under matched conditions, with a flat beam envelope in the low and high regions(**left below**). The **right upper** plot illustrates mismatched conditions in the downstream matching sections (MD1-MD4), leading to rapid emittance growth and oscillating $\beta_\perp$ and $\alpha_\perp$ after the high field area(**left below**), highlighting the impact of parameter misalignment.

## 5.2 Beam physics of a field flip

This section details the behavior of the total normalized canonical angular momentum $\mathcal{L}$. Previously, in the theoretical framework of Chapter 4, it was explained that $\mathcal{L}$ increases or decreases in solenoids with absorbers. The increase or decrease depends on the polarity of the solenoid field and the sign of the muon charge.

It is essential to correct this, as outlined by the following reasons. Firstly, the effective betatron function increases with changes in $\mathcal{L}$, since the beta function is scaled by

$$\beta_\perp = \beta_\mathrm{p}\sqrt{1+\mathcal{L}^2}. \tag{5.6}$$

With a higher $\mathcal{L}$, the focus within the solenoid is weakened compared to when $\mathcal{L}$ is lower. Consequently, particle scattering is less suppressed, decreasing the cooling efficiency.

Secondly, additional canonical angular momentum improves the coupling between the transverse $x$ and $y$ planes. This coupling leads to an increase in the determinant value of the non-block diagonal matrices within the four-dimensional covariance matrix, thus increasing the two-dimensional emittances $\varepsilon_y$ and $\varepsilon_y$. This augmentation results in reduced luminosities later in the collider.

This section outlines a proposal for correcting the absorber-induced increase in normalized canonical angular momentum by reversing the field polarity. The study also discusses cooling efficiency and compares the reduction in transverse emittance with and without reversed-field polarities. For simplicity, hereafter the text will refer to it as a canonical angular momentum $\mathcal{L}$, implying its normalized form.

### 5.2.1 Canonical angular momentum correction in field flipped cooling cells

It is practical to allow the beam to transition to the next cooling cell by switching from 40 T to −40 T (or vice versa) to correct the canonical angular momentum. It has not been evaluated, but it is assumed that the forces between these two high-field magnets are negligible since there are separated by a few meters. This alteration in polarity within an ionization cooling cell has been referred to as a **field flip** in earlier studies [139, 140]. The following example demonstrates, in a G4Beamline simulation, the correction of canonical angular momentum. This is achieved by a pair of field-flipped solenoids, including hydrogen absorbers. For comparison, a pair of non-alternating solenoids will be illustrated and discussed.

This example begins with the first cell of the final cooling channel. The starting emittances are determined from the final values of the six-dimensional rectilinear cooling channel by D. Stratakis et al. [36], which are $\varepsilon_{\perp,\mathrm{N}} = 300\,\mu\mathrm{m}$ and $\varepsilon_{\mathrm{L,\,N}} = 1.5\,\mathrm{mm}$.

Assuming a round beam ($\alpha_\perp|_{s=0} = 0$), the only main beam parameters that can be adjusted are the initial energy $E$ and its energy spread $\sigma_E$. In this context, a 25% reduction in the initial normalized transverse emittance was proposed to make the beam parameter changes distinguishable. By analytically optimizing the cost function $-\Delta\varepsilon_{\mathrm{L,\,N}}/\varepsilon_{\perp,\mathrm{N}}$ with this reduction in transverse emittance 25%, the best starting parameters $E_{\mathrm{Kin}} = 120\,\mathrm{MeV}$ and $\Delta E = 3.3\,\mathrm{MeV}$ were determined according to the methodology described in Chapter 4.6.

To decrease the normalized transverse emittance of a muon beam with $E_{\mathrm{Kin}} = 120\,\mathrm{MeV}$ from 300 µm to 225 µm, a liquid hydrogen absorber with specific pressure density is required. This absorber has a length of 1.615 m to operate in a field of 40 T. To manage the correction in canonical angular momentum, the absorber is divided into two segments.

Each segment is housed in separate solenoids of unequal length with reversed-field orientations. Both solenoids are CERN type.

The analytical canonical angular momentum rate was defined in Eq. (4.57) and is

$$\frac{d\mathcal{L}}{ds} = \frac{\sqrt{1+\mathcal{L}^2}}{\beta E^2}\left\langle \frac{\partial E}{\partial s} \right\rangle - \frac{\mathcal{L}}{\varepsilon_{\perp,\mathrm{N}}}\frac{\beta_\perp pc}{2m_\mu c^2}\frac{d\langle\theta^2\rangle}{ds} \tag{5.7}$$

the first segment measures 95 cm in length, while the second is 65.5 cm long. Each absorber has a cylindrical form with diameter 5 cm and features 5 mm thick LiH windows at both ends. The density of liquid hydrogen in the first absorber is 76.8 kg m$^{-3}$, while the second has a density of 69.2 kg m$^{-3}$ to ensure low pressure after passage of the muon beam. In order to ensure high field homogeneity in the absorbers, the total length of the high field solenoid is 1.2 m.

In a G4Beamline simulation, the muon beam was generated in the center of a 1 m low-field 4 T solenoid. This beam is then directed to a CERN-style solenoid absorption system using four matching coils, as detailed previously in 5.1.4, to guarantee the same conditions.

After traversing the first absorber, eight matching coils are strategically placed to ensure proper matching to the second high-field solenoid, which has an opposing field polarity. The field polarity changes adiabatically within these eight-coil setups. Upon exiting the second absorber, the beam is again directed by four matching coils. Then it is transmitted to a 1 m 4 T solenoid, where the simulation concludes. Each matching coil measures 20 cm in length and the dynamic adiabatic ramping technique, as outlined in 5.1.4, was used to ensure matched conditions.

For this specific solenoid configuration, the output of the G4Beamline simulation involving $10^4$ positively charged muons. The plot on the left in Fig. 5.10 presents the configuration of the magnetic field along the beam axis. Positioned below this plot is a depiction of the canonical angular momentum's evolution. It is evident that by appropriately selecting the absorber lengths, the canonical angular momentum can be adjusted to revert to its original value. In this particular scenario, the canonical angular momentum initially had a value of approximately $\mathcal{L} = 0$ and reaches this value again at the end of the simulation.

A similar solenoid beam line to the previous setup was constructed once more; however, this time, without a field flip. The ideal current densities for the matching coils were determined for this set-up. The on-axis field configuration for this scenario is shown in the right plot of Fig. 5.10. Below this illustration, a graph details the canonical angular momentum behavior. With the field polarity unchanged in the second high-field solenoid, the canonical angular momentum continues to rise. Consequently, this scenario

also reduces the cooling efficiency of the beam, which will be discussed in the following section.

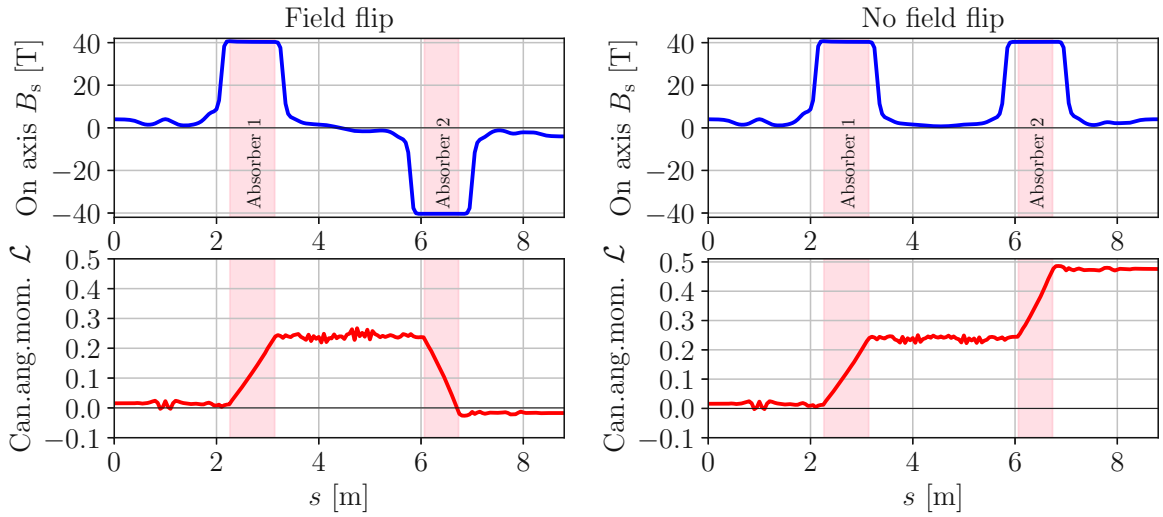


**Figure 5.10.:** The **left** plots depict the magnetic field configuration and canonical angular momentum evolution for a solenoid setup with a field flip, showing how proper absorber lengths restore the angular momentum to its initial value of approximately $\mathcal{L} = 0$. In contrast, the **right** plots represent a configuration without a field flip, where the angular momentum increases continuously due to unchanged field polarity. This continuous rise negatively impacts the cooling efficiency of the beam. These results emphasize the importance of field polarity in ionization cooling.

### 5.2.2 Cooling efficiency of a field-flipped cooling cell

In continuation of the discussion in the previous example, the following paragraphs evaluate the cooling efficiency of solenoid-absorber systems with a flipped magnetic field compared to those without one.

In the left plot of Fig. 5.11, the changes in normalized transverse emittance $\varepsilon_{\perp,\mathrm{N}}$ are shown for both the field-flipped and non-field-flipped configurations. Initially, $\varepsilon_{\perp,\mathrm{N}}$ increases equally in both cases within the first absorber, as expected. However, minor variations appear in the **second absorber**, as depicted to the left of Fig. 5.11. The emittance in the field-flipped configuration is slightly less than that in the non-field-flipped beamline.

The right plot of Fig. 5.11 provides a detailed examination of the betatron function $\beta_\perp$ for both the field-flipped and non-field-flipped modes in the vicinity of the second

absorber. The relationship between both beta functions is

$$\frac{\beta_{\perp}^{\text{noflip}}}{\beta_{\perp}^{\text{flip}}} = \sqrt{\frac{1+\mathcal{L}_{\text{noflip}}^2}{1+\mathcal{L}_{\text{flip}}^2}}. \tag{5.8}$$

In the design where the field is not flipped, $\mathcal{L}_{\text{noflip}}$ increases, while $\mathcal{L}_{\text{flip}}$ reverts to its initial level in the second absorber. In the field-flipped example, the canonical angular momentum returns to its starting value. At the end of the second absorber, the beta function for the configuration without field flip is expressed as $\beta_{\perp}^{\text{noflip}} = \beta_{\perp}^{\text{flip}}\sqrt{1+\mathcal{L}_{\text{noflip}}^2}$, but **only** when the **start value** of the canonical angular momentum was **zero**. This expression indicates that the radius of the beam expands by a factor of $(1+\mathcal{L}_{\text{noflip}}^2)^{1/4}$, respectively, to the field-flipped scenario.

For the non-field-flipped scenario, the reduced focusing due to the induced canonical angular momentum leads to reductions for emittance cooling. As discussed in the previous chapter, this focusing mechanism helps to contain the emittance growth that results from muons scattering against the absorber's atoms. The objective of ionization cooling is to optimize focusing by reducing the canonical angular momentum to its lowest possible value.

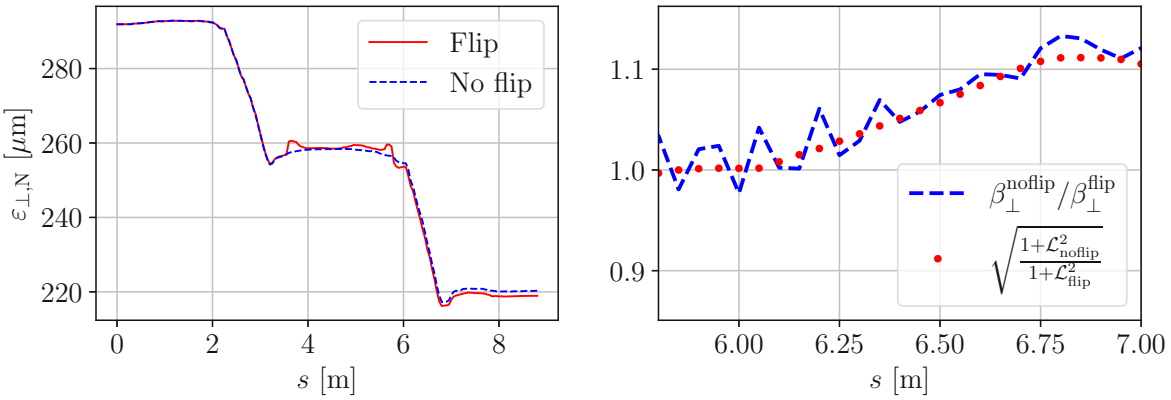


**Figure 5.11.:** The **left** plot illustrates the evolution of normalized transverse emittance $\varepsilon_{\perp,\mathrm{N}}$ for both field-flipped and non-field-flipped configurations. It shows a similar initial increase within the first absorber and minor differences in the second absorber, where the emittance is slightly lower for the field-flipped case. The **right** plot examines the relation of the betatron function $\beta_{\perp}$ for both cases inside the second absorber. Due to the field flip and the associated $\mathcal{L}$ reduction, $\beta_{\perp}^{\text{flip}}$ decreases correspondingly to $\beta_{\perp}^{\text{noflip}}$, following to a higher beam focusing in the absorber and therefore a higher cooling efficiency.

## 5.3 Phase rotation and amplitude correlation

In this section, the rotation of the longitudinal phase space between two solenoid absorber systems with reverse field polarity is discussed. The increase in normalized longitudinal emittance is related to energy spread $\sigma_E$, energy $E$, and normalized longitudinal emittance $\varepsilon_{\mathrm{L,N}}$. Consequently, these parameters must be carefully adjusted to mitigate the increase in longitudinal emittance. The variable $\varepsilon_{\mathrm{L,N}}$ can be modified and reduced only in the earlier stages of the muon production and acceleration chain. The parameter $\varepsilon_{\mathrm{L,N}}$ can be reduced, for example, in the 6D cooling channel [36]. For the final cooling, the longitudinal emittance can no longer decrease as there is no longer any correlation between position and momentum, due to dispersion and wedge-shaped absorbers.

If particles pass through a solenoid system without an absorber included, the longitudinal emittance experiences a small increase. This comes from the correlation effects of the transverse particle's amplitude outlined later in Chapter 5.3.2. To mitigate this effect, one can reduce the transverse emittance of the beam and adjust its energy spread. The adjustment of the energy spread can be accomplished by using phase-rotating cavity systems, which will be discussed in the following section.

### 5.3.1 Longitudinal phase space manipulation

To minimize the energy spread of the bunch, an RF cavity system is used that operates in a reference phase of $\psi = 0°$. The phase of 0° is the rising zero-crossing of the electric field $E_z$ of the cavity, which is the definition used in this thesis. When the RF and gradient are given, the length of the bunch $\sigma_{\mathrm{L}}$ can be adjusted. It can be increased to reduce the energy spread or decreased to increase the energy spread, particularly when the RF phase $\psi = 0°$. This technique is known as phase rotation [141].

Consider an absorber system that incorporates field-flipped solenoids, complemented by matching coils and transfer solenoids, as illustrated in Fig. 5.12. As the beam passes through the absorbers, its energy spread $\sigma_E$ and the normalized longitudinal emittance $\varepsilon_{\mathrm{L,N}}$ increase. As depicted on the left side of Fig. 5.12, the growth rates of $\sigma_E$ and $\varepsilon_{\mathrm{L,N}}$ are more pronounced in the second absorber, although the second absorber is shorter and less dense than the first absorber ($L_{\mathrm{abs1}} = 95\,\mathrm{cm}$, $\rho_{\mathrm{abs1}} = 78.6\,\mathrm{kg\,m^{-3}}$, $L_{\mathrm{abs2}} = 65.5\,\mathrm{cm}$, $\rho_{\mathrm{abs2}} = 69.20\,\mathrm{kg\,m^{-3}}$). This is because the bunch has a lower energy and a larger energy spread in the second absorber, resulting in a larger increase in the normalized longitudinal emittance. When the phase rotator is absent, the normalized longitudinal emittance measures $\varepsilon_{\mathrm{L,N}}^{\mathrm{Rot}} = 2.5\,\mathrm{mm}$, while without rotation, it is $\varepsilon_{\mathrm{L,N}}^{\mathrm{NoRot}} = 2.65\,\mathrm{mm}$. Although these differences seem minor, the longitudinal emittance will increase exponentially throughout the lattice, and phase rotation becomes crucial when dealing with larger longitudinal emittances later in the lattice.

The example presented in the right plot of Fig. 5.12 involves 6 pillbox cavities characterised by a frequency of 300 MHz and a gradient of 12 MV m$^{-1}$ operating in the $TM_{010}$ mode. These pillbox cavities, measuring 15 cm in gap length, were situated between the matching coils of both CERN-type high-field magnet systems. The pillbox cavities are strategically placed, each center located at intervals of 0.5 m, as shown on the right in Fig. 5.12.

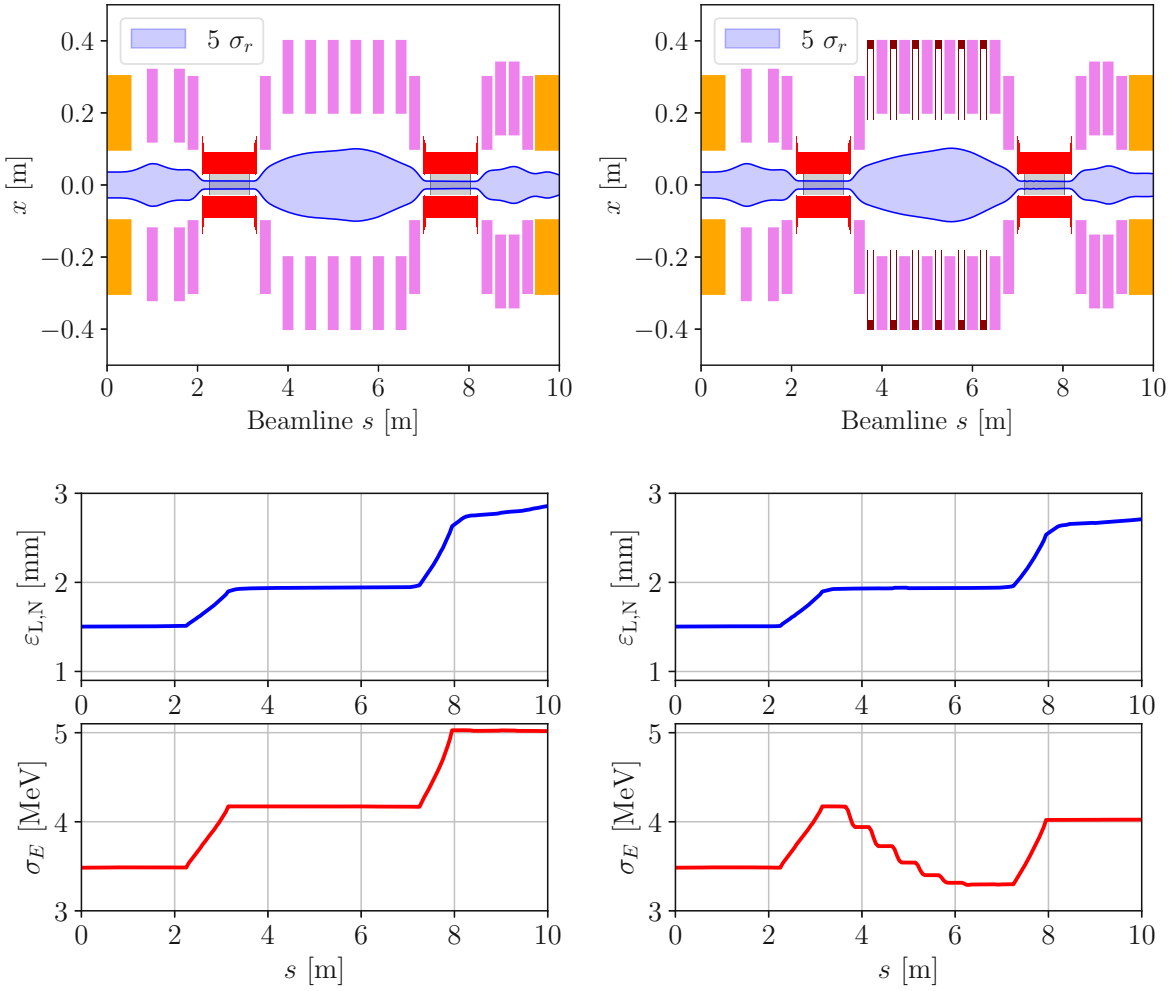


**Figure 5.12.:** An absorber system with field-flipped solenoids, matching coils, and transfer solenoids is illustrated. The **left** panel shows increased energy spread and normalized longitudinal emittance in the second absorber. This occurs despite its shorter length and lower density, due to the bunch's lower energy and greater energy spread. The **right** panel highlights six carefully placed pillbox cavities that reduce energy spread. The normalized longitudinal emittance growth is therefore smaller. The RF system brings the energy spread back to its original value before to entering the second absorber.

To examine the longitudinal phase space, Figure 5.13 on the left illustrates both the particle distribution and the separatrix as observed at the initial stage of the cavity system. This configuration illustrates how the bunch is precisely placed in the center of the stationary bucket. The plot on the right of Fig. 5.13 displays the distribution of the particles after passing through the cavity system.

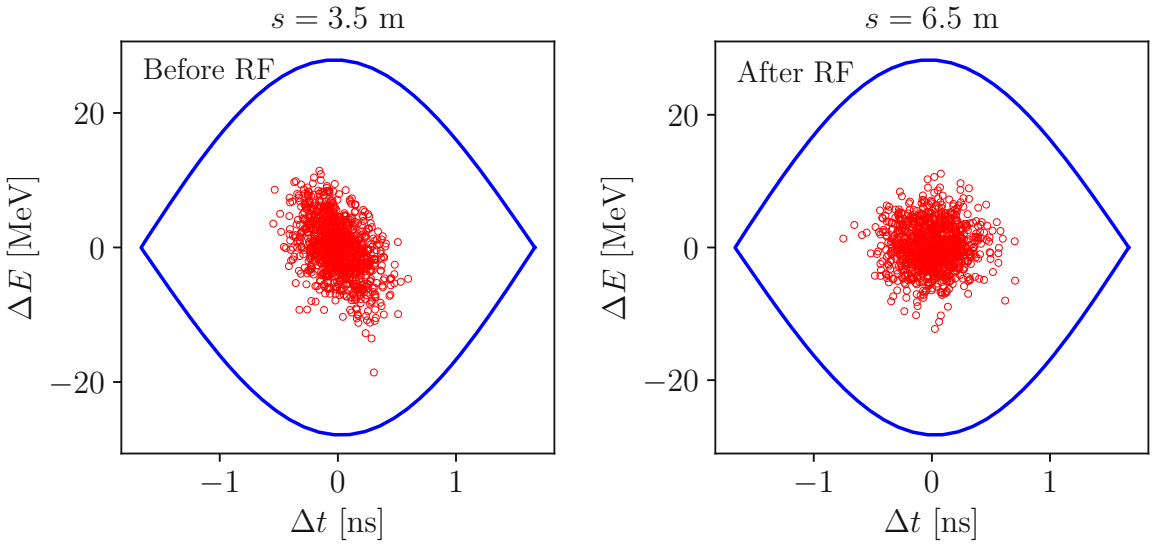


**Figure 5.13.:** The **left** plot illustrates phase-space correlations in $\Delta t$ and $\sigma_E$ after particles exit the first absorber, showing the bunch contained within a stationary bucket. In the plot on the **right**, a longitudinal bunch rotation facilitates the extension of the bunch length and the reduction of the energy spread, thereby correcting the correlation in the longitudinal phase-space. This improvement was achieved by adjusting the RF frequency, gradient, and gap length to align the machine's longitudinal parameters with the beam's requirements.

In the left plot of Fig. 5.12, the longitudinal emittance increases at the end of the study carried out within the solenoid system without absorbers. The energy spread of the beam remained uncorrected, resulting in correlations between the transverse amplitudes and the longitudinal coordinates of the particles. Such nonlinear effects will be addressed in the following discussion.

### 5.3.2 Nonlinear amplitude correlations

In the following sections, the emphasis shifts from examining phase-space rotation to investigating the non-linear correlation between transverse and longitudinal motion. Ac-

cording to a description by G. Penn [142], he noted that particles with higher amplitudes $A_\perp$ tend to lag behind those with smaller $A_\perp$ during their passage through a solenoid.

This phenomenon can be demonstrated with a thought experiment involving a single particle possessing a radial offset from the beam axis. Due to the presence of fringe fields, a particle with a larger radial offset receives a stronger angular momentum kick at the entrance of a solenoid. This leads the particle to gyrate in the solenoid with a larger radius compared to one with a smaller radial offset. Consequently, particles with larger helix radii have path lengths longer than those with smaller radii, causing them to fall behind.

In four dimensions, the amplitude for a single particle is expressed by

$$A_\perp = \left[\mathbf{v}^\top \Sigma^{-1} \mathbf{v}\right] \varepsilon_\perp, \tag{5.9}$$

where $\mathbf{v} = (x, x', y, y')^\top$ represents the four-dimensional transverse coordinates of the particle, and $\Sigma$ denotes the beam's covariance matrix. In Eq. (5.9), the invariant $\varepsilon_\perp$ represents the four-dimensional geometric beam emittance. It is worth mentioning that the amplitude in Eq. (5.9) is occasionally referred to as the four-dimensional single-particle emittance.

The normalized longitudinal emittance in two dimensions was defined in Eq. (4.50). When incorporating the amplitude of particles into the emittance calculation, it is essential to compute the covariance matrix in the $t$-$E$-$A_\perp$ frame and subsequently normalize it using the mean squared amplitude $\langle A_\perp^2 \rangle$, which is defined as

$$\varepsilon_{\mathrm{L,N}}^{\mathrm{corr}} = \sqrt{\frac{\det(\mathrm{Cov}[t, E, A_\perp])}{\langle A_\perp^2 \rangle}}. \tag{5.10}$$

Figure 5.14 illustrates a representative scenario involving a beam exposed to a constant solenoid magnetic field of 4 T. The plots on the **left** side, shown in Figure 5.14, illustrate the discrepancy between $\varepsilon_{\mathrm{L,N}}^{\mathrm{corr}}$ and $\varepsilon_{\mathrm{L,N}}$, as observed in a beam characterized by $\varepsilon_{\perp,\mathrm{N}} = 300\,\mu\mathrm{m}$. One case involves a spread of energy of $\sigma_E = 5.5\,\mathrm{MeV}$, and another scenario involves $\sigma_E = 7.5\,\mathrm{MeV}$. The differences between $\varepsilon_{\mathrm{L,N}}^{\mathrm{corr}}$ and $\varepsilon_{\mathrm{L,N}}$ are clearly visible, demonstrating that particle amplitude increases the normalized longitudinal emittance in the solenoid. Note that this analysis does not incorporate any absorbers.

In the example on the **right**-hand side of 5.14 is the same example demonstrated again but with the transverse beam emittance reduced by an order of magnitude. This example clearly demonstrates that the amplitude dependency in the longitudinal plane vanishes. In Fig. 5.14 can also be noticed that there is even with the amplitude corrected expression still a nonlinear longitudinal emittance increase. This non-linear effects are not symplectic and therefore phase space densities are not conserved.

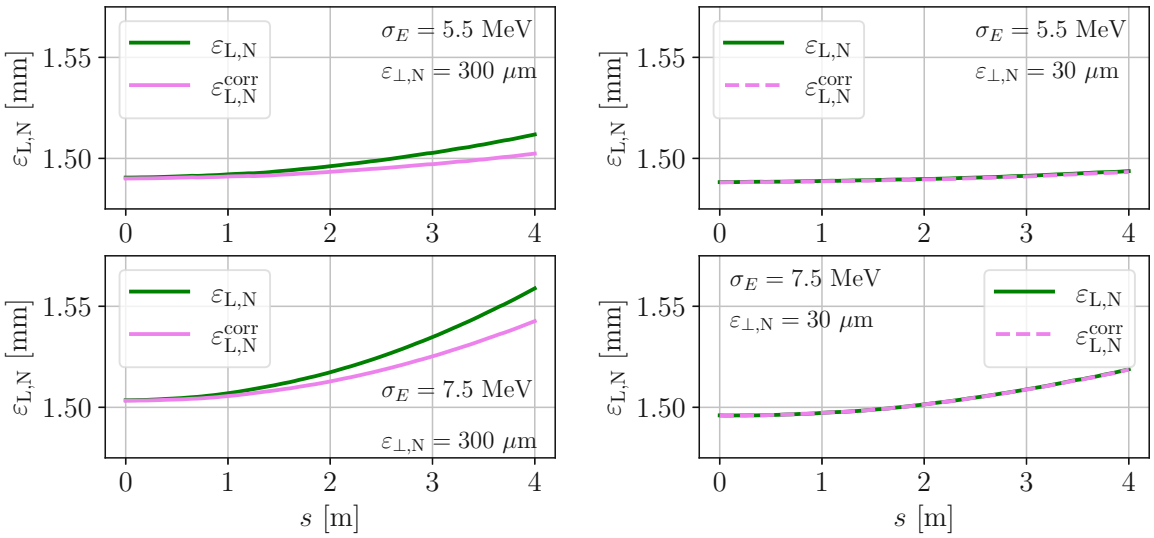


**Figure 5.14.:** A long solenoid subjected to a 4 T magnetic field shows the impact of particle amplitude on normalized longitudinal emittance, with distinct energy variances of 5.5 MeV and 7.5 MeV analyzed for a beam with $\varepsilon_{\perp,N} = 300\,\mu$m. On the right, reducing transverse beam emittance by an order of magnitude eliminates the amplitude dependency in the longitudinal plane. This analysis excludes beam-stopping materials like absorbers.

Given the manifestation of these amplitude-correlated dependencies in large normalized transverse emittances, it is advisable to expedite the cooling of the beam by employing a short beam line. This strategy mitigates the supplementary longitudinal emittance growth observed in non-absorber regions within a solenoid and contributes to an efficient cooling rate within the design.

Armed with a thorough examination of these technical aspects in ionization cooling and a plan for

1. minimization of emittance increase with matched beam within a solenoid system within absorbers and RF cavities,
2. Optimization of the RF cavity parameters,
3. angular momentum cancellation with field-flipped solenoids,
4. awareness of longitudinal emittance amplitude correlation,

the next phase involves developing an initial model of an ultimate cooling channel.

## 5.4 Final cooling channel including liquid and vapor hydrogen absorbers

Upon examining the beam dynamics is examined within a final cooling setup, the design of a potential final cooling cell can be conceptualized. This chapter therefore suggests a structure for a single cell of the final cooling channel, consisting of:

- a high-field solenoid with uniform field distribution
- a pair of absorbers separated by an arrangement of field-reversed and 40 T solenoids for canonical angular momentum correction,
- phase rotation cavities for energy spread adjustments, and
- matching coils in conjunction with low-field transport solenoids.

To advance the design of an individual cooling cell, this part additionally includes

- beam windows tailored for the absorbers, and
- modifications of hydrogen densities to counteract over pressurized conditions in the absorber caused by the muon beam.

This section gives a general overview of a potential final cooling channel composed of nine cooling cells. Each final cooling cell approximately reduces the normalized transverse emittance by 25%. The 25%-emittance reduction was an intuitive choice and did not follow any results from optimization algorithms. The design was focused on optimizing the hydrogen densities and limiting the solenoid length at 1.2 m. This study aims primarily to execute and evaluate the technical elements of a final cooling cell that were previously mentioned.

The following discussion presents a technical configuration for a single final cooling cell and reviews earlier studies on a final cooling design. The study will illustrate the selection of hydrogen absorber densities and their state, either as saturated liquid or as vapor. The section continues with a discussion about beam windows, followed by a thorough examination of the hydrogen density configuration choices for each cell. Ultimately, the resulting beam parameters from the G4Beamline simulations will be presented, highlighting promising outcomes for the future advancement of a final cooling channel.

### 5.4.1 Novel setup approach of a final cooling cell and comparisons to previous designs

#### Conceptual design of a final cooling cell

Using the field-flip configuration is beneficial to adjust the acquired canonical angular momentum as the beam moves through the material-filled solenoid. This setup slightly enhances the cooling efficiency due to its improved focusing abilities. Another purpose of a field-flipped cooling cell is to minimize the coupling effects between $x$- and $y$-planes. Achieving this goal enables the transfer of a decoupled beam to the next accelerator section in the muon collider framework [25].

After the beam exits the absorber, the phase rotating RF cavities adjust the energy spread $\sigma_E$ while preserving the normalized longitudinal emittance $\varepsilon_{\mathrm{L,N}}$. Lower energy spreads are beneficial to keep the growth of $\varepsilon_{\mathrm{L,N}}$ low in the absorbers and even in solenoids, due the to non-linear effects in Fig. 5.14.

Furthermore, in between the solenoid and RF components, the matching coils ensure aligned conditions between the machine and beam parameters. If the conditions are not matched, the transverse emittance increases, leading to decreased cooling efficiency of the cell.

In summary, a single final cooling cell comprises a configuration of **two window-absorber-window setups**, utilizing **hydrogen** as the absorber material. These are separated by **field-flipped solenoids** and operate at high magnetic field strength. Alternating **RF cavities** and **matching coils** located right next to the field-flipped solenoid ensure optimized performance for both **longitudinal** and **transverse emittance**.

#### Past final cooling design proposals

In prior iterations of the final cooling lattice designs [131, 132], the configuration of a single cell within the lattice was conceptualized differently. Specifically, a single cell comprised an individual absorber located within a high-field solenoid module, followed by a sequential phase rotation and acceleration via an RF system. Indeed, a final cooling cell could incorporate re-accelerating RF cavities positioned between two field-flipped solenoid-absorber systems. However, the primary objective of this study is to examine and elaborate on a final cooling cell from a more technical, e.g. the inclusion of beam windows and hydrogen absorber adjustments. Another goal is to examine the beam

dynamic in the final cooling cell with the inclusion of innovative field-flipped and RF systems.

In these past studies, a field polarity switch was proposed and even implemented in H. Sayed's [132] and B. Palmer's [131] design. However, in Sayed's work details concerning the exact methodology used to determine when the field-polarity changes occurred were notably omitted.

The design of Sayed incorporated an RF system within the bore of large low-field solenoids. In contrast, the design proposed in this thesis positions the RF cavities between smaller coil components. Applying pillbox geometry, the radius of the cavity is inversely scaled with its frequency [143]. In a vacuum, this relationship can be approximately expressed as

$$r_{\text{Cavity}} = \frac{c}{2\pi}\frac{2.40483}{f[\text{Hz}]}. \tag{5.11}$$

In Sayed's design, the maximum frequency used is $f = 325\,\text{MHz}$, which corresponds to a cavity diameter of 70 cm. As frequencies decrease along the channel, this necessitates transport solenoids with larger core radii. This chapter demonstrates, for the first time, the proof of RF-cavities that are not situated inside solenoids, a scenario not previously investigated in prior final cooling studies.

The designs proposed by Sayed and Palmer could further benefit from a more detailed consideration of the adjustments in hydrogen density within the absorber. According to their studies, liquid hydrogen was assumed to be utilized at constant densities of $\rho = 70.8\,\text{kgm}^{-3}$. However, this assumption may result in pressures reaching several hundreds of bar within the absorber after the passage of the beam, as evaluated in Fig. 4.12.

Additionally, their lattice proposals do not currently incorporate beam windows at both ends of the absorber. Furthermore, both papers could provide greater clarity regarding the behavior of the magnetic field generated by solenoids within the absorber, as well as more comprehensive technical specifications of the high-field solenoid.

In the following lattice design discussion, the technical aspects of ionization cooling will be discussed in a detailed and technical way. The key design components of technical relevance are the following:

- beam windows for the absorbers, and
- adjustments of the absorber densities to mitigate pressure increases induced by the muon beam.

In addition, the beam optical aspect of the cooling cell design involves implementing the following:

- RF-cavities not inside transport solenoids;

- a high-field solenoid with uniform field distribution, similar to the CERN design.

These CERN-type solenoids [136] have already been incorporated into beam dynamics studies earlier in this chapter 5.1.1.

### 5.4.2 Beam windows for absorbers

The beam windows play a critical role in the containment of hydrogen, ensuring that it remains isolated from the vacuum conditions in the rest of the beam pipe. As the beam deposits energy in the absorber via ionization, the hydrogen pressure along the beam path inside the absorber rises. This pressure increase correlates with the initial density of the hydrogen, which must be adjusted in advance of the beam's entry into the absorber.

To minimize Coulomb scattering, these windows should be **thin** and composed of a material with a **low atomic number Z**. **Lithium hydride** (**LiH**) and **silicon nitride** (**$Si_3N_4$**) are promising materials for such windows.

The final cooling channel will be performed in its initial cells using a higher beam energy (50-120 MeV), due to a better cooling performance. At increased beam energies, saturated **liquid hydrogen** (**LH**) will be used as an absorber. In this preliminary final cooling lattice design, 5 mm LiH windows are used for LH absorbers [144]. To a moderate extent, this type of window equipped with an LH absorber setup can withstand stresses up to 30 bar. The densities of LH will initially be calibrated so that the pressure levels remain below 30 bar after the muon beam passes through.

In the later cells in the final cooling channel, lower beam energies have to be used to reach low transverse emittances. The combination of low energy levels and reduced transverse beam dimensions necessitates the employment of **vapor hydrogen** (**VH**) as an absorber equipped with extremely thin windows. VH is used because of its lower density compared to LH in order to prevent beam-induced high pressures. The application of ultra-thin windows primarily serves to minimize muon losses caused by particles getting stopped inside the window. The aim of the system is also to minimize the growth of the transverse emittance because of the substantially higher equilibrium emittance inherent in the window material.

Very thin membranes, like $Si_3N_4$, have been used as X-ray windows [145]. The initial pressure tests at CERN involved a sample of 1 µm thick $Si_3N_4$ foil with a square size of 6 mm × 6 mm [146]. It shows that this membrane starts to fail at 6.5 bar at a temperature of 77 K.

In another setup, a equivalent $Si_3N_4$ sample was irradiated by 400 GeV proton beams with a beam intensity of $2.6 \cdot 10^{13}\,p^+/mm$ [144]. Apart from minor deformation on the $Si_3N_4$-membrane caused by the proton beam hitting it, the pressure inside the test chamber remained constant at 5 bar, implying that the $Si_3N_4$ window remained intact. $Si_3N_4$ windows with a thickness of 1 µm have been shown to withstand a pressure of 6.5 bar [146]. It is plausible to hypothesize that windows with increased thickness, in the range of 2-3 µm, could endure pressures exceeding 10 bar. However, an empirical validation is required to confirm this assumption.

In the preliminary final cooling lattice study, the density of the VH absorbers, which incorporate $Si_3N_4$ windows, will be fine-tuned. This adjustment will ensure that the pressure after the muon beam passes through the VH does not exceed 10 bar.

### 5.4.3 Properties of the LH and VH absorbers in a final cooling channel

On the basis of its initial density and pressure, hydrogen can exist as a liquid or a vapor. A list in Table 5.4 of initial absorber conditions is provided, including density, temperature, and pressure, in a final cooling channel, starting from a beam with $\varepsilon_{\perp,N} = 300\,\mu m$ and $\varepsilon_{L,N} = 1.5\,mm$. The thermodynamic properties within the absorber, as dictated by the beam characteristics, were assessed utilizing CoolProp [133]. As a preliminary illustration, the aim was to decrease 25% of $\varepsilon_{\perp,N}$ per cooling cell while maintaining the solenoid length within the range of $1.0 \pm 0.2\,m$.

The **vapor quality factor** for a **saturated liquid** is characterized by $Q_{vap} = 0$, while for a **saturated vapor**, it is defined as $Q_{vap} = 1$. In any intermediate phase ($0 < Q_{vap} < 1$), the hydrogen absorber would comprise both liquid and vapor, leading to varying density regions. These diverse density areas would cause the beam to release its energy unevenly, complicating the analysis of ionization cooling.

Each individual cell in the final cooling section contains **two absorbers** as a result of corrections for the canonical angular momentum. To ensure that the absorbers remain in a single phase ($Q_{vap} = 0$ or $Q_{vap} = 1$), adherence to the saturation curve is required. The saturation lines are presented in Fig. 5.15 and Fig. 5.16, indicating ones for pressure $p$ and those for temperature $T$ in relation to internal energy $U$. Fig. 5.15 illustrates the $p$ and $T$ for the first absorber in each cell, while Fig. 5.16 corresponds to the cell's second absorber.

The initial pressures and temperatures are marked down on the saturation curve in Fig. 5.15 and Fig. 5.16. The maximum in the saturation curves is represented by the critical pressure $P_c$ and the critical temperature $T_c$. The saturation line to the **left of these critical points** corresponds to the saturated-liquid state and is marked as blue

| Cell | $\rho$ [kg m$^{-3}$] | Abs. [cm] | Sol. [m] | $Q_{\text{sat}}$ | $p_0$ [bar] | $p_1$ [bar] | $T_0$ [K] | $T_1$ [K] |
|---|---|---|---|---|---|---|---|---|
| 1 | 78.60 | 95.0 | 1.2 | 0 | 0.08 | 22.03 | 14.21 | 16.50 |
| | 69.20 | 65.5 | | | 1.49 | 24.38 | 21.75 | 24.38 |
| 2 | 76.54 | 70.5 | 1.0 | 0 | 0.10 | 28.67 | 14.52 | 17.51 |
| | 69.18 | 49.0 | | | 1.50 | 25.61 | 21.77 | 25.61 |
| 3 | 58.80 | 60.0 | 1.0 | 0 | 6.00 | 29.84 | 28.26 | 32.35 |
| | 45.16 | 40.0 | | | 11.50 | 31.89 | 32.33 | 38.31 |
| 4 | 43.00 | 50.0 | 0.8 | 0 | 12.00 | 31.33 | 32.61 | 38.81 |
| | 34.16 | 31.5 | | | 12.77 | 33.02 | 33.04 | 41.211 |
| 5 | 6.87 | 87.6 | 1.2 | 1 | 5.60 | 9.51 | 27.87 | 39.92 |
| | 4.48 | 75.5 | | | 3.70 | 7.23 | 25.69 | 43.11 |
| 6 | 5.71 | 81.5 | 1.2 | 1 | 4.70 | 9.11 | 26.92 | 43.65 |
| | 3.76 | 64.5 | | | 3.10 | 7.8 | 24.83 | 53.06 |
| 7 | 3.06 | 35.4 | 1.0 | 1 | 2.50 | 7.89 | 23.86 | 64.25 |
| | 1.96 | 28.1 | | | 1.55 | 5.94 | 21.9 | 74.28 |
| 8 | 2.48 | 43.6 | 1.0 | 1 | 2.00 | 8.33 | 22.91 | 82.19 |
| | 1.61 | 34.3 | | | 1.25 | 8.62 | 21.1 | 93.63 |
| 9 | 2.08 | 52.1 | 1.0 | 1 | 1.65 | 8.86 | 22.15 | 101.24 |
| | 1.38 | 40.0 | | | 1.05 | 9.23 | 20.5 | 161.24 |

**Table 5.4.:** Every final cooling cell comprises a pair of absorbers. The initial cells (1-4) incorporates liquid hydrogen (LH) absorbers, denoted by blue values and $Q_{\text{sat}} = 0$. The red values represent the absorber characteristics for hydrogen vapor (VH) (cell 5-9) with $Q_{\text{sat}} = 1$. Within each cell, the initial absorber's density $\rho$, pressure, and temperature are presented in the first line, and those for the second absorber are displayed in the second line. The starting values of pressure and temperature are denoted by $p_0$ and $T_0$, respectively, whereas the concluding values after the beam's passage are denoted by $p_1$ and $T_1$. In the table Abs. and Sol. stand for the lengths of the absorber and the solenoid.

lines. On the **right**, it indicates the saturated vapor state, and these are marked as red lines.

Liquid hydrogen (LH) is observed to be used as the absorbers in each of the first four final cooling cells. These cells have starting pressures ranging from 0.8 bar to 12.77 bar, just below $P_c$. Meanwhile, for final cooling cells five through nine, hydrogen vapor (VH) is utilized for the absorbers, with pressures ranging from 5.6 bar to 1.05 bar.

Upon depositing its energy into the absorber, the beam causes an increase in pressure. The objective of this study is to maintain the pressure in the LH absorbers, equipped with LiH windows, around 30 bar after the beam passes through. For VH absorbers, the pressure after the beam passage is kept below 10 bar due to the proposed limitations of the ultra thin $Si_3N_4$ windows.

Figure 5.15 depicts the pressures and temperatures recorded following the beam's passage through each cell's primary absorber. Dashed lines in the diagram on the left of Fig. 5.15 connect the initial and final pressures in each cell. Similarly, the initial and final temperatures are connected in the right plot of Fig. 5.15. This analysis is also applied for the second absorber of each cell, as shown in Fig. 5.16. For each absorber within each cell, both figures illustrate the regulation of pressure for the LH and VH absorbers.

Table 5.4 presents a summary of the densities chosen for each final cooling cell, along with the initial and concluding pressure and temperature values. Table 5.4 indicates that after the conclusion of each cell, specifically cells 2 to 9, it is necessary to adjust the absorber density. This adjustment ensures that the pressure remains reasonably below a specific threshold after the passage of the muon beam.

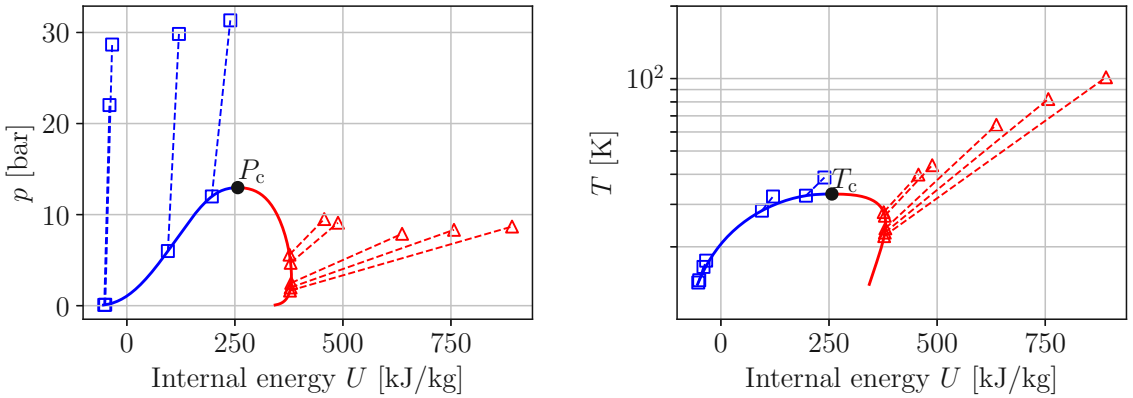


**Figure 5.15.:** The saturation curves delineate the boundaries between hydrogen's saturated-liquid (blue) and saturated-vapor (red) states, plotted against internal energy. Initial and final pressures (left) and temperatures (right) for the absorbers in each cooling cell are connected with dashed lines, showing the progression through the system. LH is used in the first four cooling cells, with pressures from 0.8 to 12.77 bar, while VH is used in cells five through nine, spanning pressures from 5.6 to 1.05 bar. The data highlights the conditions following beam passage through the initial absorber of each cell.

After the fourth cell in the final cooling channel, the absorber phase changes to VH. Due to the lower densities in VH compared to LH, the density starting at cell 5 decreases, as illustrated in Fig. 5.17. Consequently, a longer absorber is required to dissipate the beam energy, affecting the transverse emittance. In addition, extended absorbers require the use of longer solenoids. The lengths of high-field solenoids in cooling cells, including LH absorbers, are summarized in Table 5.5, while the solenoids containing VH absorbers are detailed in Table 5.4. In LH, the length of the absorbers reduced

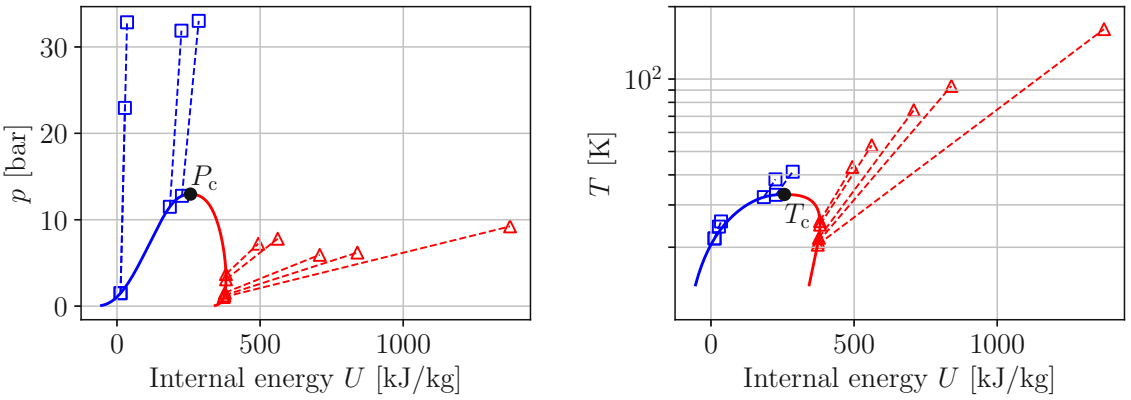


**Figure 5.16.:** The second absorbers of each cooling cell operates within the saturation boundaries, transitioning from an initial to a final state along the saturation curve. Its pressure and temperature changes are connected by dashed lines, illustrating the system's progression through the absorber.

from 95 cm to 31.5 cm. For VH, the original length of 87.6 cm also decreased, with the shortest absorbers measuring 28.1 cm. Table 5.4 lists the absorber densities relative to their lengths, while Fig. 5.17 provides a visual representation.

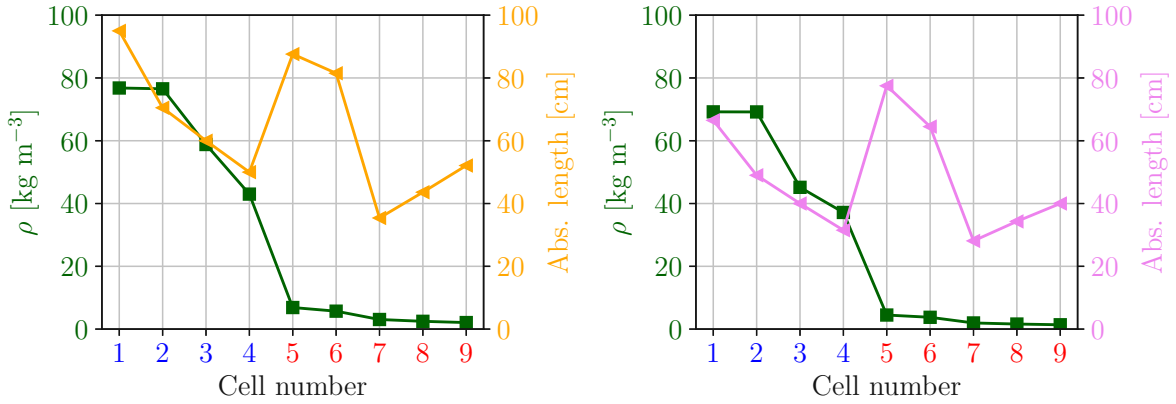


**Figure 5.17.:** The **left** plot depicts the density and length of the first absorber in each cell, whereas the **right** plot illustrates these parameters for the second absorber in each cell. Subsequent to cell 4, the absorbers are composed of VH with significant lower hydrogen densities. Owing to the reduced densities, the absorber lengths are extended to maintain a substantial reduction in transverse emittance.

The absorbers that demonstrate the highest sensitivity are located in the final cell of the channel. A significant amount of energy is deposited by the beam within a very small volume, as a result of the reduced beam radius achieved in the preceding cells. Fig-

ure 5.18 provides a representation of the pressure distribution from a lateral perspective of both absorbers in the last cooling cell. It is evident that the internal pressure can be maintained within the range described in 10 bar.

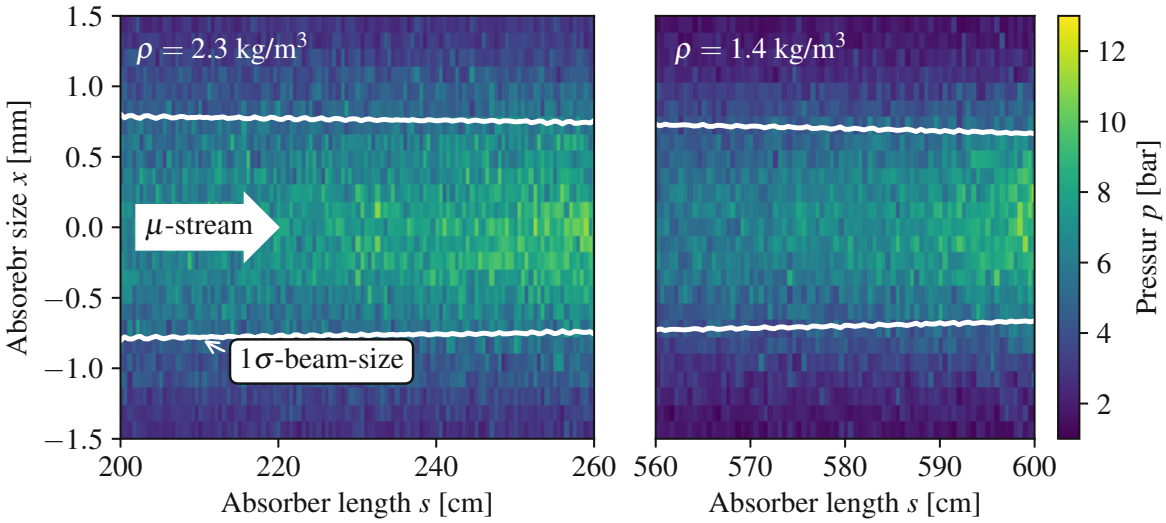


**Figure 5.18.:** The absorbers in the final cell exhibit the highest sensitivity. The pressure distribution from a lateral view of the absorbers in the last cooling cell, shown in the heatmap, demonstrates that internal pressure remains within the specified range of 10 bar.

In light of the substantial temperature rise within the VH absorber (164 K), it is necessary to demonstrate that the temperature can increase rapidly despite the high viscosity of hydrogen. The absorber must be adjusted to its initial pressure and temperature within 200 ms, which is the time frame for the passage of a new muon bunch. Establishing a continuous VH flow (and potentially LH) within the absorber, linked with an external loop, may aid in conducting heat out of the absorber.

### 5.4.4 Beam energies and energy spread choice for each cell

This section discusses the results of optimizations of a beam cooling process through a series of cooling cells. It focuses on reducing the beam's transverse emittance while minimizing longitudinal emittance growth. Adjustments to initial kinetic energy, energy spread, and use of phase-rotating cavities were key strategies. Technical constraints such as solenoid length, hydrogen pressure in the absorbers, and cavity specifications were carefully managed. The study concludes that phase rotation is unnecessary beyond the sixth cooling cell due to reduced beam energy levels and manageable non-linear effects, avoiding complications from extended beamline requirements.

A first attempt of a re-accelerating beamline between two cooling cells will be discussed in Section 5.5 later. Yet, between cells, at the end of each cell, the energy was raised and the energy distribution fine-tuned by artificially adjusting the macro-particles. Once this artificial modification was completed, the beam was directed to pass through the subsequent final cooling cell.

In this final cooling beamline, calculations were performed for 9 cooling cells, which reduce the beam's transverse emittance from $\varepsilon_{\perp \mathrm{N}}$ : 300 µm to 25 µm. This results in a roughly 25% reduction in transverse emittance per cell. The aim was to achieve the target normalized transverse emittance of 25 µm by incorporating both LH and VH absorbers along with the necessary beam windows. Furthermore, it was essential to maintain the high-field solenoid within a range of less than 1.2 m. A future study proposes to adjust the normalized longitudinal emittance.

The initial kinetic energy $E^0_{\mathrm{Kin}}$ and the initial energy spread $\sigma^0_E$ were adjusted and a reduction of 25% in the transverse emittance in each cell was made. This adjustment was made while keeping the growth of the longitudinal emittance minimal. The values for $E^0_{\mathrm{Kin}}$ and the final kinetic energy $E^1_{\mathrm{Kin}}$ for each final cooling cell are tabulated in Table 5.5, as well es the $\sigma^0_E$ and the final energy spread $\sigma^1_E$.

Furthermore, it was ensured that the solenoid does not exceed the length of 1.2 m. Every cooling cell is initialized with a distinct starting energy and a specific energy spread, alongside two absorbers. Modifications outlined in $E_{\mathrm{Kin}}$ and $\sigma_E$ are simulated for each cell employing G4Beamline and are depicted in Fig. 5.19.

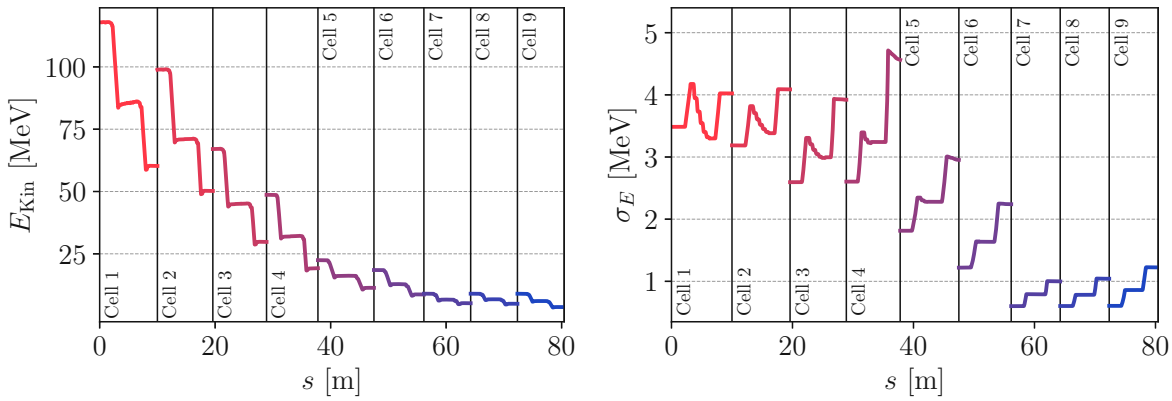


**Figure 5.19.:** The evolution of kinetic energy $E_{\mathrm{Kin}}$ in a G4Beamline simulation is depicted in the **left** plot, whereas the **right** plot illustrates the progression of the energy spread $\sigma_E$. The adjustments of $E_{\mathrm{Kin}}$ and $\sigma_E$ between each cell were executed artificially, without employing a complex RF system.

The energy spread between the two absorbers in each cell was adjusted by employing phase-rotating cavities. This approach aimed to suppress longitudinal emittance

| Cell | $\varepsilon_{\perp,\mathrm{N}}^{\mathrm{start}}$ | $\varepsilon_{\perp,\mathrm{N}}^{\mathrm{final}}$ [µm] | $E_{\mathrm{Kin}}^{0}$ [MeV] | $E_{\mathrm{Kin}}^{1}$ [MeV] | $\sigma_E^0$ [MeV] | $\sigma_E^1$ [MeV] |
|---|---|---|---|---|---|---|
| 1 | 300.0 | 260.1 | 120.0 | 83.6 | 3.5 | 4.3 |
| | 260.9 | 225.3 | 84.0 | 58.6 | 3.3 | 4.0 |
| 2 | 227.0 | 200.2 | 97.2 | 70.0 | 3.2 | 3.8 |
| | 200.3 | 174.2 | 70.0 | 48.66 | 3.4 | 4.1 |
| 3 | 174.5 | 150.9 | 65.7 | 43.9 | 2.6 | 3.3 |
| | 151.1 | 131.6 | 43.9 | 28.6 | 3.0 | 3.9 |
| 4 | 133.5 | 116.0 | 47.7 | 31.0 | 2.6 | 3.4 |
| | 116.6 | 94.0 | 31.0 | 20.6 | 3.3 | 4.7 |
| 5 | 94.1 | 85.2 | 21.5 | 15.1 | 1.8 | 2.4 |
| | 89.0 | 76.6 | 15.4 | 10.6 | 1.8 | 2.3 |
| 6 | 76.6 | 69.4 | 17.6 | 11.9 | 2.2 | 2.9 |
| | 70.2 | 60.2 | 12.4 | 8.2 | 1.6 | 2.2 |
| 7 | 60.2 | 53.5 | 9.0 | 6.6 | 0.6 | 0.8 |
| | 53.5 | 47.5 | 6.6 | 5.2 | 0.8 | 1.0 |
| 8 | 47.5 | 42.7 | 9.0 | 6.7 | 0.6 | 0.8 |
| | 42.7 | 37.7 | 6.7 | 5.1 | 0.8 | 1.0 |
| 9 | 38.2 | 33.8 | 9.0 | 6.6 | 0.6 | 0.9 |
| | 34.0 | 27.2 | 6.0 | 3.6 | 0.9 | 1.2 |

**Table 5.5.:** The table presents the initial and final kinetic energy ($E_{\mathrm{Kin}}^{0}$ and $E_{\mathrm{Kin}}^{1}$) and energy spread ($\sigma_E^0$ and $\sigma_E^1$) for each final cooling cell. It also includes the initial and final normalized transverse emittance ($\varepsilon_{\perp,\mathrm{N}}^{\mathrm{start}}$ and $\varepsilon_{\perp,\mathrm{N}}^{\mathrm{end}}$). Cells 1-4, which use LH absorbers, are highlighted in blue, while cells 5-9, using VH absorbers, are marked in red. The evolution of longitudinal emittance will be illustrated in Fig. 5.25

growth caused by non-linear effects and longitudinal emittance in the absorber. For the G4Beamline simulation, pillbox cavities with $\mathrm{TM}_{010}$ mode fields were used for the phase rotating cavities. The technical specifications for these cavities are provided in Table 5.6.

Beyond cooling cell 6, no other phase rotation systems were implemented. At this point, the beam has very low energies and small transverse emittances. Implementing any form of phase rotation would necessitate a long drift or additional RF gymnastics, elongating the beamline and resulting in more muon decay. The extended bunch lengths would require cavities with very low frequencies, which presents technical challenges. At this stage, the non-linear effects are manageable. Hence, employing phase rotation at later cooling stages becomes unnecessary.

| Cell | Freq. [MHz] | Cav. Num. | Gap. len. [cm] | Grad. [MV m$^{-1}$] |
|---|---|---|---|---|
| 1 | 300 | 6 | 15 | 12.0 |
| 2 | 200 | 6 | 15 | 7.5 |
| 3 | 140 | 6 | 15 | 6.0 |
| 4 | 60 | 4 | 20 | 8.8 |
| 5 | 55 | 3 | 15 | 2.8 |
| 6 | 20 | 1 | 10 | 4.0 |

**Table 5.6.:** Phase rotating cavities were necessitated up to cooling cell 6. The parameters for each cell, including frequency, number of cavities, accelerating gap length, and field gradient, are presented in the accompanying table.

### 5.4.5 Preliminary design and optimization of the final cooling channel

This study investigates a preliminary final cooling design aimed at reducing normalized transverse emittance from 300 µm to 25 µm, achieving a final value of 27.2 µm with muon transmission greater than 70%. The canonical angular momentum was adjusted by using optimized absorber lengths and densities, enhancing beam focusing and cooling efficiency. However, discrepancies in emittance reduction and muon losses in later cells highlight areas for further refinement. Furthermore, the normalized longitudinal emittance increased to 300 mm, which requires further optimization to achieve the target of 70 mm. A global optimization algorithm will be required to evaluate what are the best initial solenoid, absorber and beam parameter to keep $\varepsilon_{\mathrm{L,N}}$ growth low, but this went beyond the scope of this work.

In G4Beamline, the simulations utilized $10^4$ $\mu^+$, saving the positions of the particle phase space every 1 mm. In this initial cooling arrangement, the field flips were utilized to adjust the canonical angular momentum, which is altered as the beam traverses the absorber. Figure 5.20 provides a summary of the magnetic field on the axis for the beamline composed of 9 final cooling cells. The field flip was executed solely within a single cell and did not span two successive cells. This is because the canonical angular momentum should be completely adjusted after the second absorber of a cooling cell, in order to archive maximum cooling efficiency in the consecutive cell.

Modifying the canonical angular momentum $\mathcal{L}$ is essential for improving the cooling efficiency in a high-field solenoid that contains an absorber. Enhanced focusing effects ensure greater cooling efficiency. They also improve the decoupling effects between both transverse planes, which is significant for high luminosities in the collider. The modification of $\mathcal{L}$ was executed through a precisely derived analytical selection of the two absorber lengths. The absorbers' density, temperature, and pressure were determined

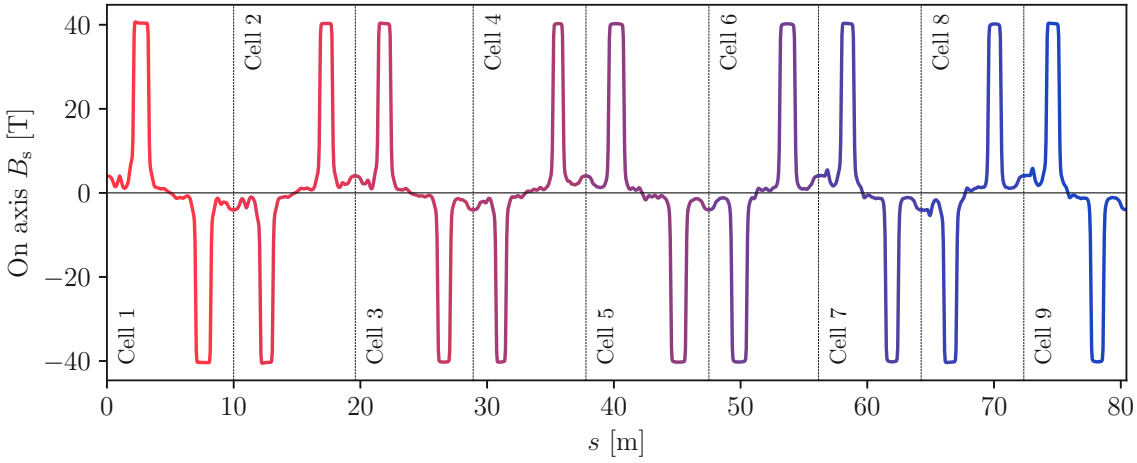


**Figure 5.20.:** This graph illustrates the magnetic field along the axis of nine final cooling cells. The inversion of the magnetic field occurs exclusively within a single cell and not between successive cells, to optimize the cooling efficiency in the cell and to correct the decoupling between $x$ and $y$ planes.

to ensure that the beam windows are not subjected to excessive stresses as the beam passes through.

The plot in Fig. 5.21 shows the dynamical evolution of the canonical angular momentum in each cell analyzed by G4Beamline simulations. Beginning with $\mathcal{L} = 0$, the two absorbers within each cell, located in opposing field polarities, nearly return the beam to zero. To achieve $\mathcal{L} = 0$ after each cell, it is advisable to manually adjust the absorber length. The reason for this is that the analytical expression in Eq. (5.7) offers merely approximate solutions for the optimal length and density configurations of the hydrogen absorber.

In the scenario depicted in Fig. 5.21, the beam was reset after each cell, which means $\mathcal{L} = 0$ at the beginning. The final cell in Fig. 5.21 exceeds the intended correction of the canonical angular momentum, and the underlying cause of this deviation will be analyzed in subsequent paragraphs.

It is imperative for a muon bunch to traverse a matched solenoid system of the final cooling. In regions of high-field magnets, the symmetric cylinder beta function $\beta_\perp$ must reach a minimal and constant value. Furthermore, the correlation parameter $\alpha_\perp$ should be zero within these regions to optimize cooling efficiency. Both independent beam parameters of the final cooling channel are depicted in Fig. 5.22.

The objective of this preliminary final cooling design was to decrease the normalized transverse emittance from 300 µm to 25 µm. The evolution of the normalized transverse emittance $\varepsilon_{\perp,\mathrm{N}}$ within the final cooling channel is illustrated in Fig. 5.23. The ultimate

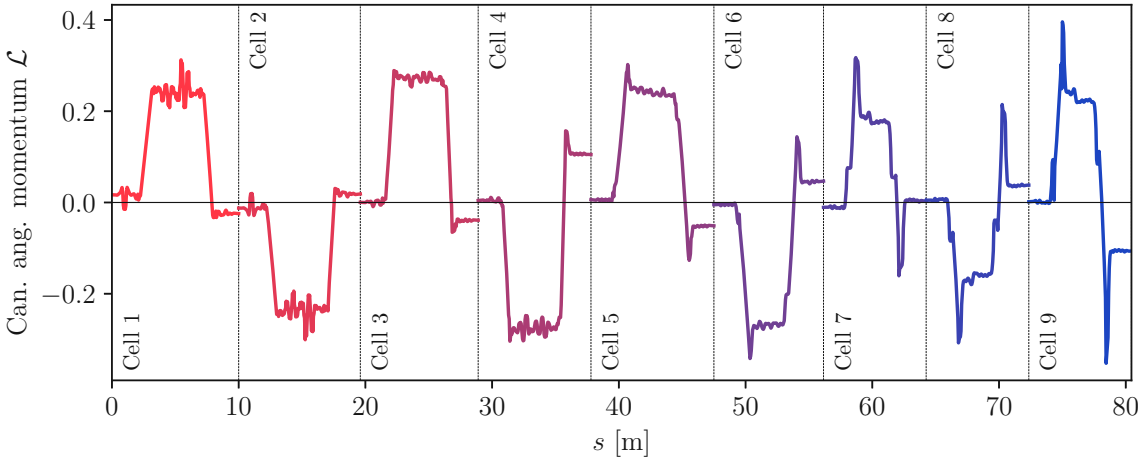


**Figure 5.21.:** The plot of a G4Beamline simulation illustrates the dynamical evolution of canonical angular momentum, starting with $\mathcal{L} = 0$ in each cell and showing how absorbers in varying polarities nearly restore $\mathcal{L}$ to its initial state. Manual adjustment of absorber lengths should be used to fine-tune $\mathcal{L}$-corrections.

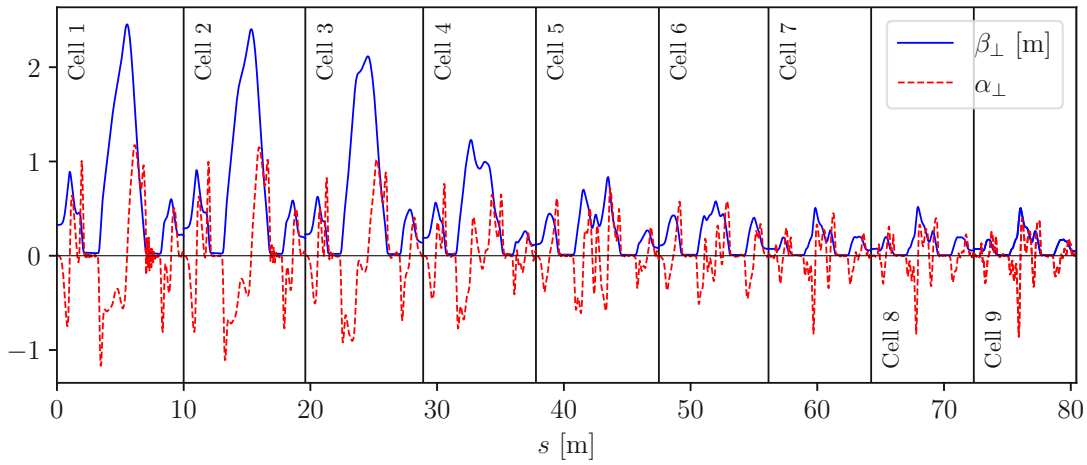


**Figure 5.22.:** This graph illustrates the beam parameters within the final cooling lattice. Efficient cooling requires a matched system with minimal cylinder symmetric betatron function $\beta_\perp$ and zero $\alpha_\perp$ in high-field regions.

emittance achieved was $\varepsilon_{\perp,\mathrm{N}} = 27.2\,\mu\mathrm{m}$, which might necessitate either adjustment of the design or the addition of an extra cell. The table 5.5 provides the values of the initial and final transverse emittance, $\varepsilon_{\perp,\mathrm{N}}^{\mathrm{start}}$ and $\varepsilon_{\perp,\mathrm{N}}^{\mathrm{end}}$, for each cell.

A slight discrepancy can be observed in cell 5 of Fig. 5.23, where the normalized transverse emittance increases around 4 µm. According to investigations, the adiabatic

matching technique provides a theoretically matched configuration in Cell 5. However, G4Beamline simulations using macro-particle bunches might still show mismatches. To mitigate this, one might consider redoing the matching with alternative initial beam parameters or adjusting the matching coils using multiple reference particles.

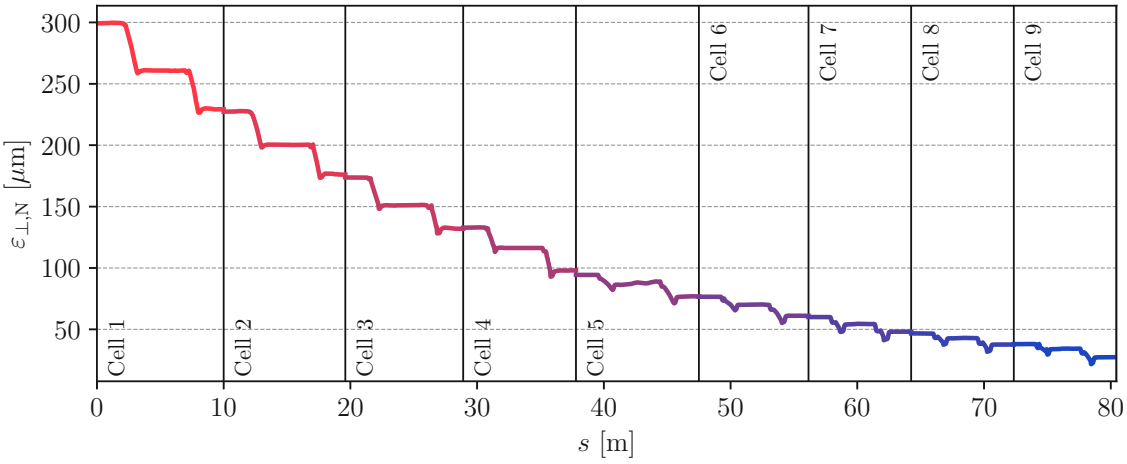


**Figure 5.23.:** The normalized transverse emittance $\varepsilon_{\perp,\mathrm{N}}$ evolution highlights a reduction target from 300 to 25 µm, achieving a final value of 27.2 µm. A notable increase in emittance around Cell 5 suggests potential mismatches, prompting considerations for design adjustments or additional optimization techniques.

Particle losses primarily occur due to muon decay, with occasional contributions from magnetic-mirror effects that may cause muons to deflect backward. The dependency of muon decay is correlated with the relativistic factor of muon $\gamma$. The survival rate of muons is quantitatively described by transmission, which is defined as the ratio of the actual number of muons in the bunch to the initial number of muons at the beginning of the channel. It should also be noted that precise beam matching and aperture examination contribute to reducing muon losses as well.

It is evident that transmission in LH-containing cells (1-4) does not decrease as significantly as illustrated in Fig. 5.24. This phenomenon is attributable to the higher density of LH, which facilitates the passage of muons with higher beam energies. In contrast, in cells containing VH (cells 5-9), the muon energy must be reduced to decrease the transverse emittance within the low-density vapor. A marked decrease in transmission is observed starting at cell 5. In cell 9, efforts were made to increase the last absorber to achieve the target emittance. However, unfortunately, this approach resulted in a substantial loss of muons, causing the transmission increase observed in the final cell of Fig. 5.24.

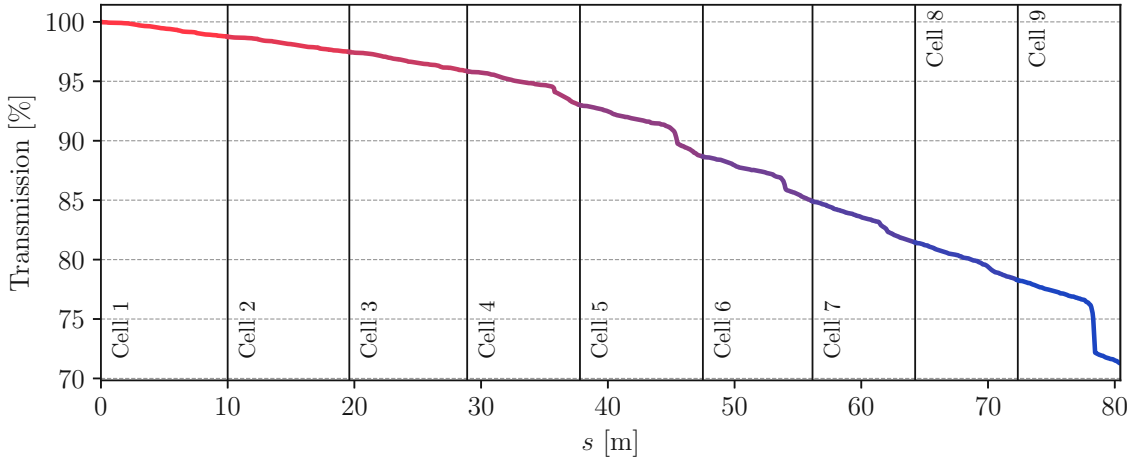


**Figure 5.24.:** Muon transmission throughout the channel is mainly influenced by decay, with higher transmission observed in LH-containing cells (1-4) due to their ability to accommodate higher beam energies. Starting at cell 5, where VH is used to reduce the transverse emittance, a marked decrease in transmission occurs, culminating in significant losses in cell 9 due to adjustments aimed at achieving the target emittance.

Finally, the normalized longitudinal emittance $\varepsilon_{\mathrm{L,N}}$ will be addressed in the this paragraph. The primary objective of this preliminary study was to achieve a 25% reduction in normalized transverse emittance within each cell. This was accomplished without exceeding the specified high-field solenoid length, including adjusted absorber densities. Consequently, less emphasis was placed on the normalized longitudinal emittance. As illustrated in Fig. 5.25, the final measured value is approximately 300 mm, compared to the target value of 70 mm. This requires further investigation of an final cooling channel to align the longitudinal parameters with the target value. One potential approach could involve lengthening the solenoids and initiating with higher energies in the cells, including VH. An alternative proposition involves the utilization of high-pressure VH absorbers featuring thick LiH windows. However, the optimal strategy remains to be determined in future studies.

## 5.5 Cell to cell beam transfer and re-acceleration

In the earlier discussion, re-acceleration was omitted between the final cooling cells. Rather, the beam was artificially adjusted to its optimal energy, energy distribution, and optimal canonical angular momentum. In the following sections, an initial concept for a potential acceleration structure is introduced. This encompasses various cavity configurations operated under particular RF parameters. Subsequently, an examination

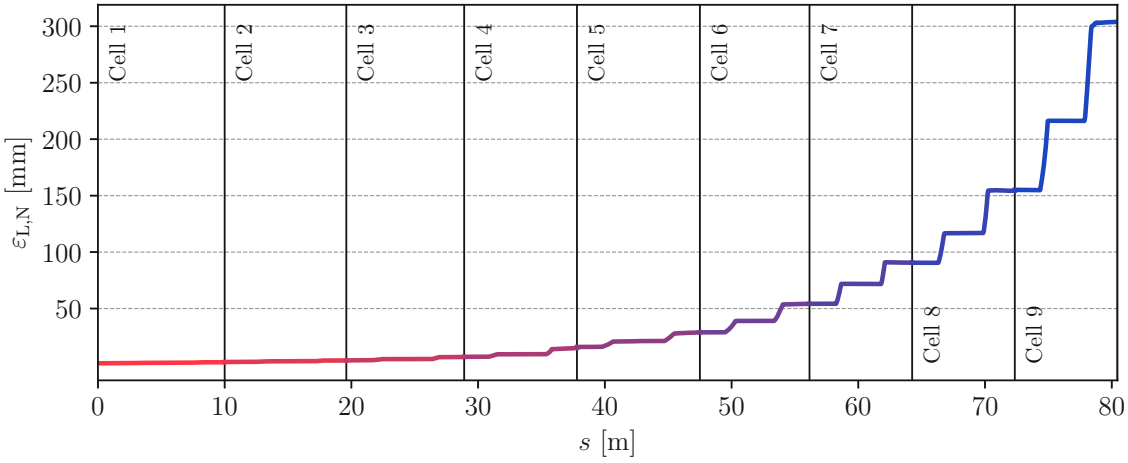


**Figure 5.25.:** The normalized longitudinal emittance, with a final measured value of approximately 300 mm compared to the target of 70 mm, highlights a need for further optimization. Achieving alignment with target parameters may involve lengthening solenoids, starting with higher cell energies, or refining the cooling channel design.

of the longitudinal phase space dynamics will be undertaken within these RF systems.

### 5.5.1 RF system components

Nevertheless, the final cooling design has only incorporated the phase rotating cavity system. These cavities do not accelerate the reference particle, as the synchronized reference phase of the electric sine wave is set at $\psi = 0°$. The phase rotation intends not only to suppress the longitudinal emittance increase within the absorber but also mitigate non-linear increase in the transfer lines.

This section goes a step further and discusses a possible design of a re-accelerating structure between two final cooling cells. For ease of explanation, this discussion focuses on the connecting beamline between cell 1 and cell 2. Unlike previous studies [131, 132], in this setup, the cavities are positioned outside the solenoids, which act as transport and matching components. For its computational design, the cavity elements from G4Beamline pillbox [78] were utilized. These cavities operate with the electromagnetic field in the $TM_{010}$ mode, where the positive slope of the field's sine wave intersects at $\psi = 0°$.

Two cooling cells are designed with six cavity systems, as shown in Fig. 5.26. The system labeled **RF1** acts as a phase rotation system positioned after the initial absorber in the first cell. Another phase rotation system, **RF2**, is situated following the second absorber of the same cell. Both RF1 and RF2 systems serve to reduce the energy spread of the

muon beam post-absorbers. The cavities of these systems are installed between the matching coils, maintaining a separation of 5 cm. This gap was empirically determined but may be fine-tuned in future cooling studies.

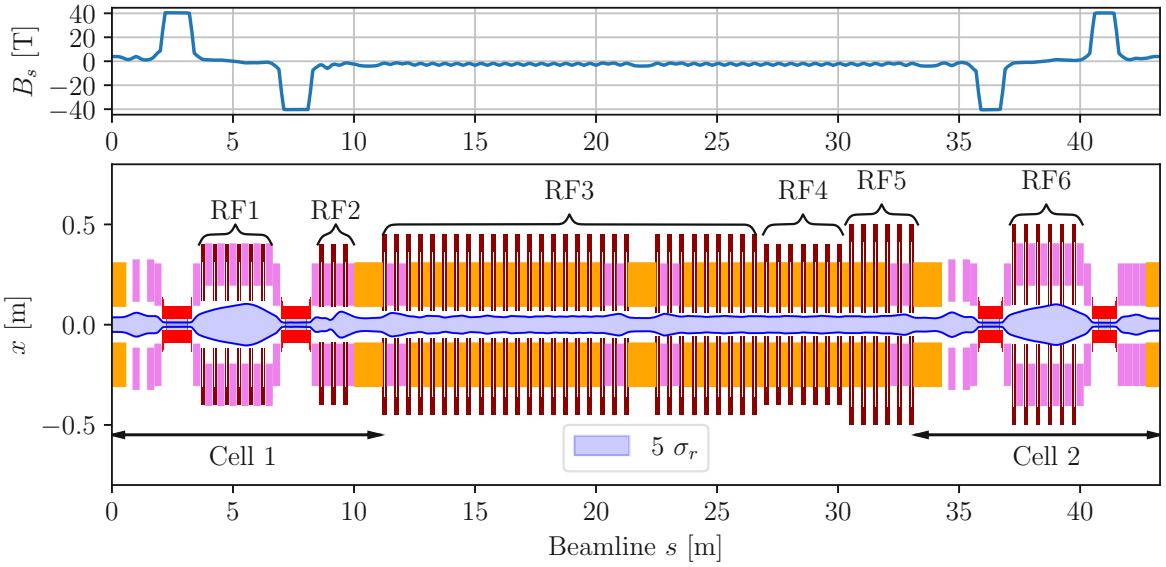


**Figure 5.26.:** Depiction of a cooling system with six cavity configurations: **RF1** and **RF2** serve as phase rotation systems located after the first and second absorbers in the initial cell. **RF3** incorporates pillbox cavities for beam acceleration. The bunch-stretchers, part of **RF4**, are followed by the phase rotator in **RF5**. **RF6**, another phase rotation system, is positioned after the primary absorber in the second cooling cell.

After RF2, the beam enters the system labeled **RF3**, which consists of pillbox cavities configured for acceleration. This process boosts the beam's kinetic energy from 60 MeV to 97 MeV. Each acceleration gap within the RF3 cavities spans 20 cm, and the centers of these cavities are spaced 50 cm apart. There are a total of 30 RF3 cavities, interspersed with low-field transport solenoids that steer the beam toward the subsequent cooling cell. Table 5.7 outlines all other crucial technical parameters of the cavity system.

As the beam undergoes acceleration, its energy spread widens. As the beam reference energy rises, the bucket height grows, which will be detailed in Fig. 5.28. To reduce the energy spread and optimize the cooling performance in the second cell, two solutions are available. The first involves allowing the beam to drift within a long solenoid, where the bunch length extends while the energy spread remains unchanged. Subsequently, the beam is directed into a phase rotating system for an exchange between bunch length and energy spread. However, this method requires a very long solenoid ($\sim 10$ m), which is detrimental to the transmission of the muon beam.

| System | Freq. [MHz] | Cav. Num. | Gap. len. [cm] | Grad. [MV m$^{-1}$] | Phase [deg] |
|---|---|---|---|---|---|
| **RF1** | 300 | 6 | 12 | 12.0 | 0 |
| **RF2** | 300 | 3 | 12 | 12.0 | 0 |
| **RF3** | 200 | 30 | 13 | 13.0 | 32.4 |
| **RF4** | 300 | 6 | 15 | 15.0 | 180 |
| **RF5** | 200 | 6 | 12 | 12.0 | 0 |
| **RF6** | 200 | 6 | 7.5 | 7.5 | 0 |

**Table 5.7.:** Each cavity system, labeled RF1 to RF6, operates at a distinct RF frequency. The Table outlines the number of cavities, the individual cavity's accelerating gap length, and the accelerating gradient applicable to each system. The phase for each system indicates whether the operation is in rotation (0°), stretching (180°), or accelerating mode ($0 < \psi < 180°$) for the muon bunch.

An advanced approach involves the use of stretching cavities with a reference phase of $\psi = 180°$. The **bunch-stretchers** [147] belong to the **RF4** system and are succeeded by the phase rotator in the **RF5** system. This set-up of stretchers and rotators minimizes the beamline for energy spread adjustment by a few meters. The cavity parameters for both RF4 and RF5 are detailed in 5.7. The goal is to provide an energy spread of $\sigma_E = 3.2\,\text{MeV}$ for the next cooling cell, as recommended by Tabel 5.5.

Finally, a phase-rotating system known as **RF6** is positioned immediately after the primary absorber of the second cooling cell. A similar system is also necessary after the second absorber, which would be a possible RF7 system. However, this was no longer considered because the primary focus was muon transport between two final cooling cells. The evolution of kinetic energy $E_{\text{Kin}}$ and $\sigma_{\text{E}}$ is shown in Fig. 5.27.

The subsequent section will provide a detailed analysis of the behavior of the longitudinal phase space within the RF systems. Particular attention will be paid to the evolution of the bunch after RF2, during which the beam traverses the intermediate beam line between the final cooling cells 1 and 2.

### 5.5.2 RF gymnastics between two cooling cells

This section will outline the evolution of the longitudinal phase space within RF systems, with a particular focus on the transition from RF3 to RF5 cavity systems. The primary objective is to modify the energy and energy spread of the muon bunch prior to its transfer to the next cooling cell. Proper adjustments in the beam's energy and energy spread maximize the efficiency of ionization cooling.

After modifying the energy spread in RF2, the bunch proceeds to the RF3 system for re-acceleration. The RF3 system is configured at a frequency of 200 MHz, chosen because

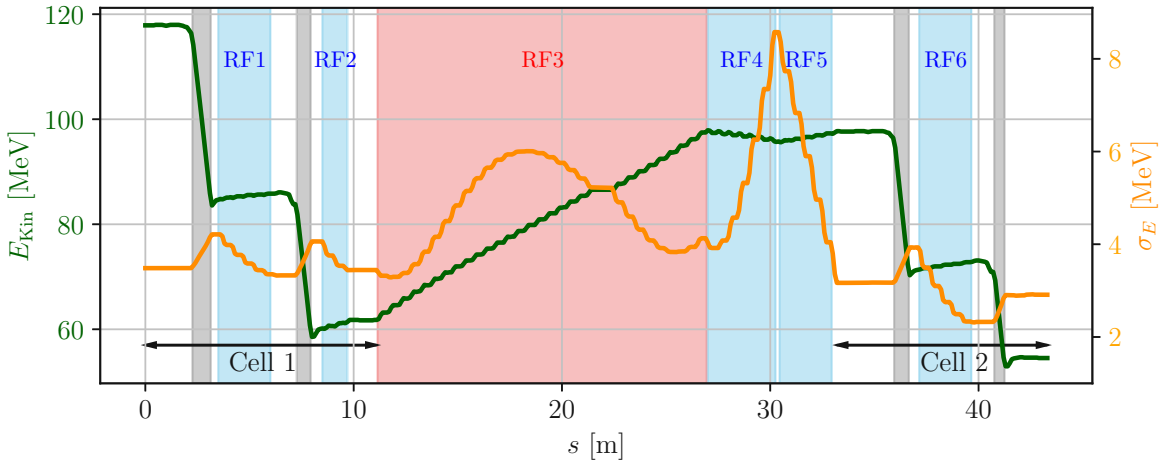


**Figure 5.27.:** The energy will be decreased in both the first cooling cell's absorber and in the two absorbers within the second cooling cell. Energy recovery occurs at **RF3**. The energy spread is fine-tuned following the absorber in **RF1**, **RF2**, and **RF6**. To achieve the ideal energy spread for the second cooling cell, **RF4** and **RF5** are designed to modify this using the technique of bunch stretching followed by a phase rotation.

the area of the running buckets ($0 < \psi < 180°$) is narrower than the stationary ones ($0°$). Muons located outside of the designated buckets experience phase de-focusing, which results in longitudinal tails and potentially losses, and should be avoided. The acceleration phase in RF3 is set to $\psi = 32.4°$ in order to avoid emittance growth and beam acceleration within a short distance. The longitudinal phase space distribution along with its separatrix is illustrated in Fig. 5.28 left. The separatrix defines the boundary of the region within the bucket in which the particles undergo phase focusing.

The muon bunch undergoes an energy increase of 36 MeV over a span of less than 17 m. This process involves RF3-type pillbox cavities that alternate with transport solenoids. The increase in energy during acceleration leads to a significant increase in the bucket height, as shown in the right phase-space plot of Fig. 5.28, depicting the beam's exit from the RF3 system.

The height of the bucket depends on the beam's reference energy, as detailed in Chapter 4. Consequently, this also results in a widening of the energy spread of the bunch form 3.5 to 4.0 MeV, which must be adjusted afterward. For future studies, it is recommended to improve the gymnastics RF within the RF3 section to help reduce the increase in energy spread and to shorten the overall length of the system.

Following section RF3, the energy spread will be adjusted in RF4. The objective is to refine the energy spread from 4.0 to 3.2 MeV to optimize the cooling performance in the following cell. A compact approach is to direct the beam through a bunch stretching

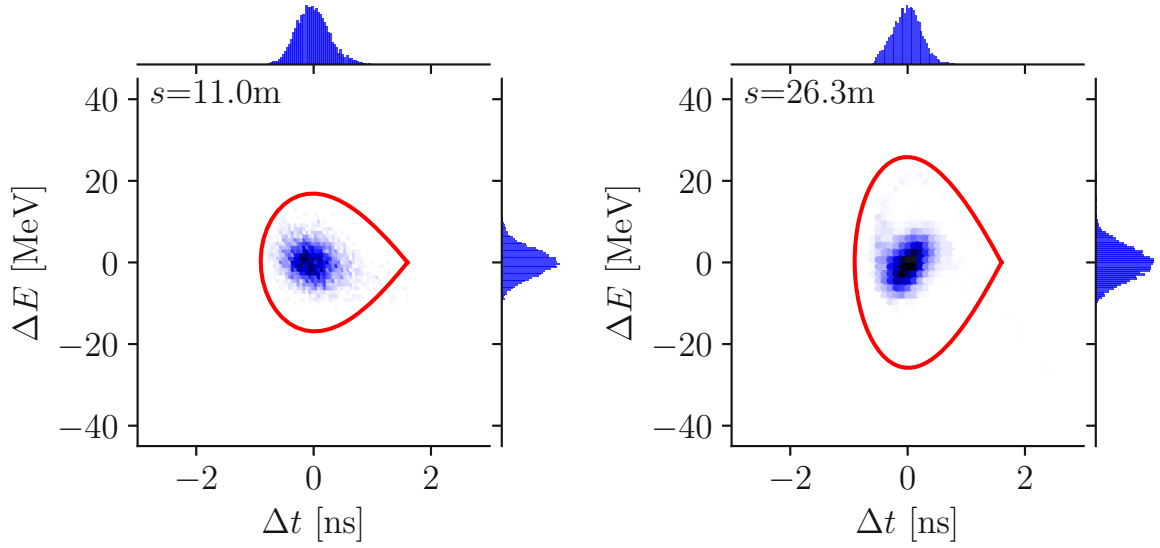


**Figure 5.28.:** Illustration of the longitudinal phase space distribution and separatrix in the **RF3** system: The **left** plot shows the initial configuration at the acceleration phase of $\psi = 32.4°$, where the separatrix outlines the phase-focusing region within the bucket. The **right** plot demonstrates the phase space at the exit of the RF3 system, highlighting the increased bucket height and the widened energy spread following a 36 MeV energy gain over less than 17 m.

cavity system by placing the reference particle at $\psi = 180°$. The bunch is somehow placed off-stationary, as illustrated in the left plot of Fig. 5.29. This image captures a snapshot of the longitudinal phase space at the RF4 entry point.

RF4 is made up of six 300 MHz pillbox cavities. These cavities extend the muon horizontally and vertically in the $\Delta t$-$\Delta E$ phase space across a span of 3 m. In Fig. 5.29, the right panel displays a snapshot at the end of RF4. This snapshot illustrates the alignment of the bunch with the contours of two adjacent stationary buckets. The energy distribution increases from 3.9 MeV at the beginning of RF4 to 8.6 MeV at its conclusion.

From RF4 the bunch will guided into six 200 MHz cavity systems which enhance the system RF5. In this beamline, the energy spread will be reduced by increasing the bunch length. The system decreases the energy spread from 8.6 MeV to 3.2 MeV, which is the target value for the consecutive cooling cell. In Fig. 5.30, the diagram on the left illustrates the evolution of the longitudinal phase space at the entrance of RF5, while the evolution at the end of the system is shown on the right.

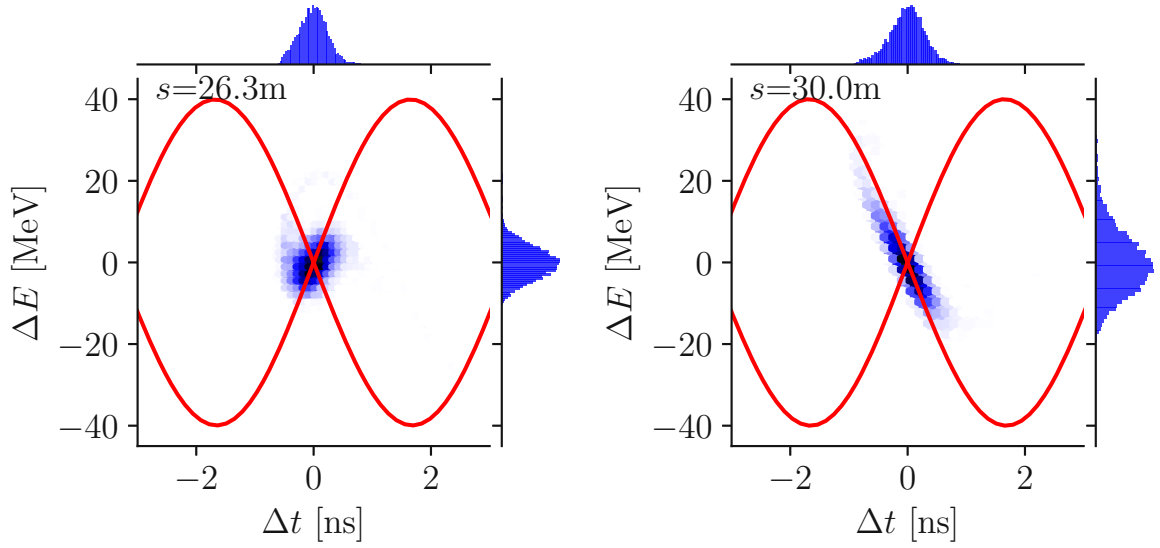


**Figure 5.29.:** Depiction of the longitudinal phase space evolution in RF4: The **left** plot shows the phase space at the RF4 entry, where the reference particle is positioned off-stationary at a phase of 180°. The **right** plot illustrates the phase space at the RF4 exit, where the beam aligns with the contours of two adjacent stationary buckets.

### 5.5.3 Evolution of the emittances in the re-acceleration chain

Fig. 5.31 shows the development of normalized transverse and longitudinal emittances, $\varepsilon_{\perp,\mathrm{N}}$ and $\varepsilon_{\mathrm{L,\,N}}$. The final transverse emittance is 200 µm, although it could potentially be reduced to 174 µm, compared to Table 5.5. As illustrated in Fig. 5.31, the increase of $\varepsilon_{\perp,\mathrm{N}}$ observed in the transfer line spanning cell 1 to cell 2 is attributed to mismatches.

Eight matching coils are installed between these cells, represented by the magenta sections between RF3 and RF5 in Fig. 5.26. This suggests that additional matchers could be installed to maintain the transverse emittance constant.

The longitudinal emittance undergoes a slight increase, notably in RF3, which shows both an upward and downward trend. Figure 5.31 illustrates that this emittance growth is attributed to non-linear effects within the solenoid transport lines as well as the RF systems. These RF systems further contribute to emittance expansion because of the beam to a RF-bucket misalignment.

In summary, this example is at an initial stage, and further modifications are necessary. However, unlike previous studies [131, 132], it represents the first attempt at longitudinal beam gymnastics, which yields very encouraging results. Increasing the gradients in the RF system would reduce the beamline length. However, this change would require higher frequencies, which would result in greater mismatches and an increase in longitudinal

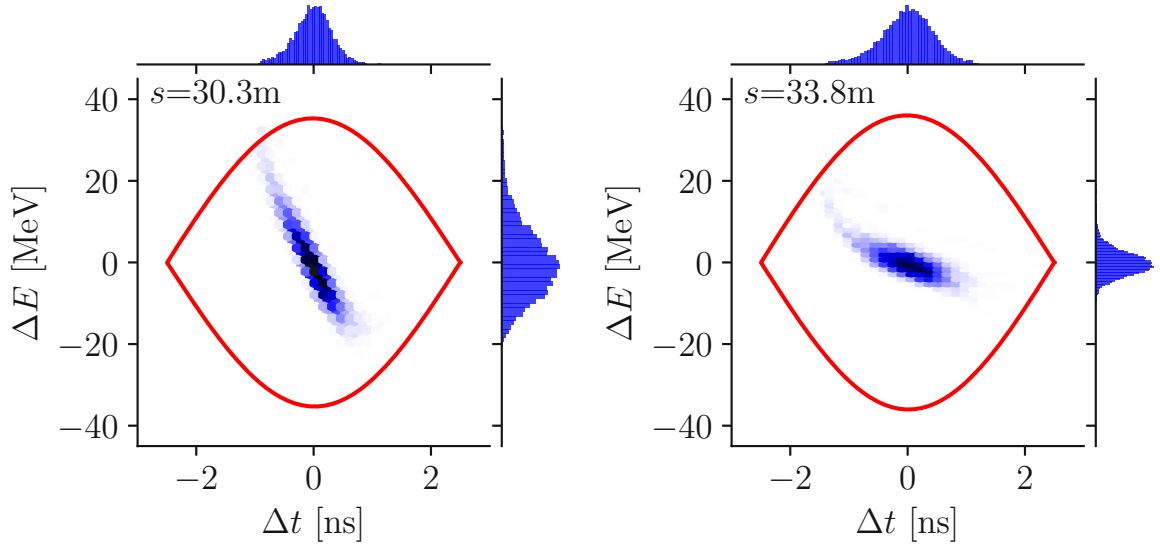


**Figure 5.30.:** Illustration of the longitudinal phase space evolution in **RF5**: The **left** diagram shows the phase space at the entrance of RF5, where the energy spread is 8.6 MeV. The **right** diagram depicts the phase space at the system's end, where the energy spread is reduced to the target value of 3.2 MeV.

emittance. This issue is complex and demands both time and technical innovation to optimize the re-acceleration process. Achieving the highest efficiency involves maintaining constant emittance values, longitudinal and transverse, with minimal muon loss.

At this point, the chapter concludes with promising results. These results demonstrate that final cooling, a bottleneck in muon collider technology, is feasible. This finding bolsters the motivation for a further study of muon colliders. The acceleration of muons within the final initial cooling cells has been demonstrated. In subsequent cells, the nature of acceleration will differ due to the anticipated increase in longitudinal emittances and bunch lengths. This aspect requires further investigation, as it extends beyond the scope of this thesis.

## 5.6 Summary of an ionization cooling lattice design

Achieving effective ionization cooling in the final cooling channel requires the use of extremely strong solenoid fields. The CERN high-field solenoid, which utilizes ReBCO high-temperature superconductors, is capable of generating fields up to 40 T while maintaining a high quality of field uniformity. Due to the inclusion of long gas absorbers, the lattice design requires a CERN-type solenoid with a maximum length of 1.2 m.

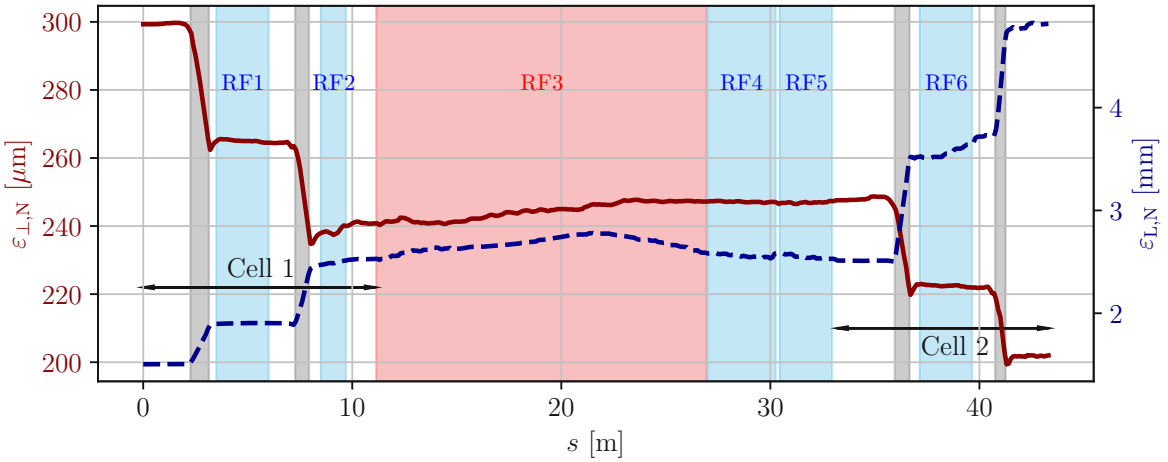


**Figure 5.31.:** Development of normalized transverse and longitudinal $\varepsilon_{\perp,N}$ and $\varepsilon_{L,\,N}$: The transverse emittance shows a noticeable inconsistency between cooling cells 1 and 2, achieving a final value of 200 µm, with potential reduction to 174 µm. This inconsistency arises from the limited number of matching coils (eight). The growth in longitudinal emittance results from nonlinear dynamics and mismatches occurring within the cavity regions.

A key aspect of this study is the method of adiabatic ramping a single particle in a solenoid-based beamline. This technique ensures optimal transverse conditions for muon beam ionization cooling. This method of matching shifts the beam from low-field solenoids to solenoids with fields that are gradually increased adiabatically, all while keeping the matching conditions consistent. In addition to matching single particles, the adiabatic ramping method is effective for macro-particle bunches within solenoid beamlines that incorporate absorbers and RF systems, where the longitudinal momentum of the beam is dynamically altered.

The chapter also investigates the impact of field flipping on the canonical angular momentum in a final cooling system. By reversing the solenoid field polarity, the canonical angular momentum can be restored to its initial value. This action enhances cooling efficiency and decouples the muon beam. Ultimately, these improvements contribute to higher luminosity values for the collider.

Controlling energy spread is essential for mitigating longitudinal emittance growth. Phase rotation, implemented using RF cavity systems, plays a critical role in adjusting energy spread. Additionally, non-linear amplitude correlations in solenoids contribute to further emittance growth. These contributions are predominantly observed at the initial phases of the final cooling channel, where the transverse emittance exhibits higher values. Managing the energy spread through RF phase rotating systems at these early stages is advantageous for controlling the growth of the longitudinal emittance.

This study primarily addressed the installation of beam windows at the absorber in the final cooling design. The beam windows play a critical role in containing hydrogen within the absorbers and preventing it from leaking into the beam pipe vacuum. These windows must be made from low-atomic number materials such as lithium hydride (LiH) or ultra-thin materials such as silicon nitride ($Si_3N_4$) to minimize Coulomb scattering or muon losses.

This chapter initially discussed the critical role of maintaining pressure regulations within hydrogen absorbers to avert potential window damage and subsequent leakages. As the muon beam passes, the absorber pressure increases, necessitating careful initial hydrogen density calibration to maintain pressure control.

Due to a careful choice of hydrogen pressures and absorber windows, a preliminary design and optimization of a final cooling channel was carried out. This design aimed to reduce the normalized transverse emittance from 300 µm to 25 µm. The process achieved a final value of 27.2 µm with muon transmission exceeding 70%. The process of optimization entailed altering the canonical angular momentum $\mathcal{L}$ by modifying the lengths and densities of the absorbers. The normalized longitudinal emittance increased to 300 mm, deviating from the target of 70 mm, necessitating additional optimization. Future improvements may include extending the solenoid lengths and initiating cooling with higher beam energies.

A beam transfer with acceleration between the final cooling cells was presented. This design suggested an alteration of the cavities and solenoid modules. The cavity systems re-accelerate the beam between two cells and adjust the energy spread. During the procedure, the evolution of both longitudinal and transverse emittance is examined, underscoring the necessity for enhanced matching. Although some emittance growth is observed, the system shows promising results in addressing the final cooling challenges. This study marks an important step toward the feasibility of muon colliders, encouraging further investigation into advanced beam dynamics in a final cooling channel.

# Chapter 6.

# Conclusion

This work has presented high-precision Standard Model (SM) calculations, a contributing development of the advanced particle tracking software RF-Track, detailed solenoid beam dynamics studies, and an optimization strategy for a final cooling cell, all aimed at motivating and shaping the design of a final cooling stage for a muon collider. The thesis introduces significant breakthroughs in six key areas:

- The prediction of measuring the lepton-parton distribution functions (LePDFs) in muon colliders is another method for the precise examination of the SM.
- Developing and testing a novel semi-Gaussian deflection model for charged particle scattering in materials for simulating relisting beam dynamics in ionization cooling.
- The first quantitative evaluation of hydrogen pressure throughout a final cooling lattice, including mitigation strategies that preserve cooling performance, demonstrates that acceptable operating conditions are achievable.
- The first analytical formulation of transverse emittance evolution in absorbers using an improved model, enabling accurate predictions of optimal beam parameters in final cooling cells.
- Demonstrating the positive effect of magnetic field flips on beam dynamics, resulting in a fully designed final cooling cell with matched optics and field-reversed solenoids with the inclusion of lithium hydride (LiH) or silicon nitride ($Si_3N_4$) at the hydrogen absorbers.
- Identification of non-linear longitudinal emittance growth in drift spaces and high-field solenoids, along with initial mitigation strategies employing phase-rotating cavities between field-flipped solenoids.

RF-Track offers a new method for simulating particle scattering in absorbers and solenoids, achieving better alignment with experimental results and consistent deflection patterns, even with small integration steps. These advancements are essential for RF-Track to be reliably compared with standard simulation toolkits. The primary motivation for upgrading RF-Track at CERN to simulate ionization cooling is its ability to model collective effects. RF-Track will allow for the first systematic study of collective effects in ionization cooling.

This thesis also provides a comprehensive analysis of the beam dynamics within the final cooling channel, incorporating realistic components that are often neglected in earlier studies. These include thermodynamic modifications of hydrogen absorbers, implementation of thin-beam windows, realistic high-field solenoid models, and transverse-beam entanglements. This work enables the evaluation of a complete lattice designs for the final cooling, incorporating all critical effects. Without such realistic models, predicting the performance of a muon collider and the corresponding technological requirements for beam acceleration and steering would be impossible.

The muon collider is presented as a unique environment for precision SM measurements, such as the determination of the triple-Higgs coupling. Chapter 2 analyzes lepton-parton distribution functions (LePDFs), derived from SM principles, through the detection of final-state photons in processes involving partonic muon and neutrino interactions. Enhanced differential cross sections at small forward angles offer a means for high-precision measurements of the neutrino LePDF in a muon collider setting. Furthermore, the muon collider serves as a Higgs factory, predominantly producing Higgs bosons via vector boson fusion (VBF). Although LePDF effects are included in the analysis, their impact on the Higgs production cross section is shown to be negligible because of the low exchange energies.

A critical focus of this thesis is the modeling of interactions relevant to ionization cooling, including electronic energy losses, their fluctuations, and nuclear multiple Coulomb scattering (MCS), all implemented within RF-Track. Benchmark comparisons with ICOOL and G4Beamline show excellent agreement in energy loss simulations, with discrepancies below 0.15%. The deflection of charged particles within materials is modeled using a semi-Gaussian mixture distribution parameterized by the Bethe-Wentzel scattering model, a novel approach developed in this work. This method is in strong agreement with existing models, with relative errors below 8% in liquid hydrogen (LH) and LiH. Moreover, RF-Track delivers even greater accuracy in scattering patterns for small integration steps compared to that of ICOOL, establishing RF-Track as a powerful tool for ionization cooling research. However, further refinements are necessary in the energy-straggling model to achieve even higher physical accuracy.

Chapter 4 validates the reliability of RF-Track to simulate particle motion in solenoids by comparing the results with G4Beamline, which shows strong agreement despite slight deviations at larger radial offsets. This chapter also introduces a refined analytical model for ionization cooling, incorporating Bethe-Wentzel scattering into the transverse emittance rate equation, which achieves better consistency with ICOOL simulations than previous versions of the analytical cooling equation. Beyond minimizing transverse and longitudinal emittances to maximize collider luminosity, an analytical framework was developed to determine the optimal initial beam energy. Critical thermal challenges within hydrogen absorbers were also addressed, highlighting the importance of optimizing their initial temperature, pressure, and density, an aspect that was overlooked in

previous studies. Analytical estimates of radial heat transport in LiH windows indicate that sufficient thermal dissipation keeps window temperatures below 37 K during operation.

Chapter 5 presents the design and analysis of an ideal final cooling cell. A major innovation introduced here is the method of adiabatic ramping, a beam-matching technique that allows for the smooth transition between solenoids of different strengths, preventing beta-beating, and thus avoiding emittance growth. This method enables precise and efficient beam matching, which is essential for the lattice design of a final cooling channel.

Furthermore, a systematic and novel final cooling cell design is proposed, which features two high-field solenoids equipped with hydrogen absorbers. A key innovation is the use of reversed field polarities between cells, which is crucial to nullifying canonical angular momentum accumulation across multiple solenoids. Such a canonical angular momentum degrades the cooling efficiency and induces beam coupling between both transverse planes. The design also incorporates LiH and $Si_3N_4$ beam windows and thermodynamically optimized hydrogen absorbers. For the first time, absorbers are modeled as liquid or vapor based on thermodynamic conditions, preventing excessive pressure increases after beam passage. Optimal parameters for initial pressure, density, temperature, and absorber length were determined through analytical estimations using CoolProp software simulations.

This work presents a preliminary design for a final cooling channel capable of reducing the normalized transverse emittance from 300 µm to 25 µm with a transmission efficiency exceeding 70%, a performance not previously achieved. Although the longitudinal emittance exceeds the target value, improvements in the cooling rates per cell offer potential for further optimization. Chapter 5 also demonstrates a method for transferring the beam between two final cooling cells using a phase-rotating and re-accelerating cavity system. The tracking simulations show promising results in preparing the beam's momentum and energy spread for successive cooling stages.

In summary, this thesis demonstrates the rich physics opportunities enabled by a muon collider, ranging from probing the existence of LePDFs to precision Higgs studies. It also highlights the critical importance of precise engineering and beam dynamics in achieving the required emittance reductions. The advances made here lay the groundwork for the realization of final cooling lattices. These advances include improved MCS modeling in low-$Z$ materials, optimized thermal management of hydrogen absorbers, beam window, and adiabatic matching strategies in high-field solenoids. Continued refinement of these techniques is expected to bring ionization cooling technologies closer to implementation, thereby enabling the unprecedented precision of SM tests and opening pathways to discoveries beyond it.

# Appendix A.

# Luminosity

## A.1 Luminosity of muon colliders

To derive the expression for the luminosity of the muon collider $\mathcal{L}$, two Gaussian-distributed particle bunches are considered which cross at the **interaction point** (**IP**). The particle density in each bunch is given by

$$\rho_{\mathbf{i}}(x, y, s, \pm s_0) = N_{\mathrm{i}}, \rho_{x,\mathbf{i}}(x), \rho_{y,\mathbf{i}}(y), \rho_{z,\mathbf{i}}(s \pm s_0), \tag{A.1}$$

where $\mathbf{i} = \mathbf{a}, \mathbf{b}$ and $N_{\mathbf{i}}$ is the number of particles per bunch. Assuming identical Gaussian distributions for both beams:

$$\rho_u(x) = \frac{1}{\sqrt{2\pi}\sigma_u} \exp\left(-\frac{u^2}{2\sigma_u^2}\right), \tag{A.2}$$

with $u = x, y, z$. The luminosity per bunch crossing is defined as

$$\mathcal{L}_{\mathrm{Lum}} = K \int dt\, d^3x\, \rho_{\mathbf{a}}\rho_{\mathbf{b}}, \tag{A.3}$$

with the kinematic factor

$$K = v_{\mathbf{a}} + v_{\mathbf{b}} = \sqrt{(\vec{v}_{\mathbf{a}} - \vec{v}_{\mathbf{b}})^2 - \frac{1}{c^2}(\vec{v}_{\mathbf{a}} \times \vec{v}_{\mathbf{b}})^2}. \tag{A.4}$$

For head-on collisions at relativistic speeds ($|\vec{v}_{\mathbf{a}}| \approx |\vec{v}_{\mathbf{b}}| \approx c$), this simplifies to $K = 2c$ [148], and with $dt = ds_0/c$, the expression becomes

$$\mathcal{L}_{\mathrm{Lum}} = 2\frac{N_{\mathbf{a}}N_{\mathbf{b}}}{(2\pi)^3\sigma_x^2\sigma_y^2\sigma_s^2} \int dx\, dy\, ds\, e^{-\frac{x^2}{\sigma_x^2}} e^{-\frac{y^2}{\sigma_y^2}} e^{-\frac{(s-s_0)^2+(s+s_0)^2}{2\sigma_s^2}}. \tag{A.5}$$

Evaluating the integrals yields

$$\mathcal{L}_{\text{Lum}} = \frac{N^2}{4\pi\sigma_x\sigma_y}, \tag{A.6}$$

assuming $N\mathbf{a} = N_\mathbf{b} = N$ and a symmetric beam ($\sigma_x = \sigma_y = \sigma_\perp$).

Since the beam is accelerated to near-light speed ($\beta \approx 1$), we substitute $\sigma_\perp = \sqrt{\epsilon_{\perp,\text{N}}\beta^*_\perp/\gamma}$ to obtain:

$$\mathcal{L}_{\text{Lum}} = \frac{N^2\gamma}{4\pi\epsilon_{\perp,\text{N}}\beta^*_\perp}. \tag{A.7}$$

In a circular circular collider of circumference $C$ with a single interaction point and a bunch repetition rate $f_\text{r}$, the time between collisions is $t = C/c$. Including muon decay ($N(t) = N_0 e^{-t/\gamma\tau_0}$), the time-integrated luminosity becomes:

$$\mathcal{L} = \frac{\gamma^2\tau_0 c}{2C}\frac{N_0^2}{4\pi\epsilon_{\perp,\text{N}}\beta^*_\perp} \tag{A.8}$$

## A.2 Hourglass effect

The hourglass effect refers to the reduction in collider luminosity due to the finite length of particle bunches and the variation of the beam's transverse size near the IP. As a bunch travels through the final focus region, the transverse beam size changes according to the beta-function, which reaches a minimum at the collision point and increases parabolically with distance from it as demonstrated in Fig. (A.1) **left**.

If the bunch length is comparable to or larger than the region over which the beam remains tightly focused, only a fraction of the particles experience optimal overlap during collision. This spatial mismatch leads to a decrease in the effective luminosity. The hourglass effect is quantified by a correction factor $F_\text{h}$ and the muon collider luminosity scales to

$$\mathcal{L}_{\text{Lum}} = \frac{\gamma^2\tau_0 c}{2C}\frac{N_0^2}{4\pi\ \varepsilon_{\perp,\text{N}}\ \beta^*} f_\text{r}\ F_\text{h} \tag{A.9}$$

The hourglass factor depends on the ratio of the IP beta function $\beta^*$ to the bunch length $\sigma_z$. The ration $(\beta^*/\sigma_z)$ versus the hourglass factor is illustrated as a graph on the **right** side of Fig. (A.1).

## A.3 Pinch effect

The pinch effect in collider physics refers to the mutual electromagnetic attraction between charged particle bundles that move in opposite directions during a collision, which

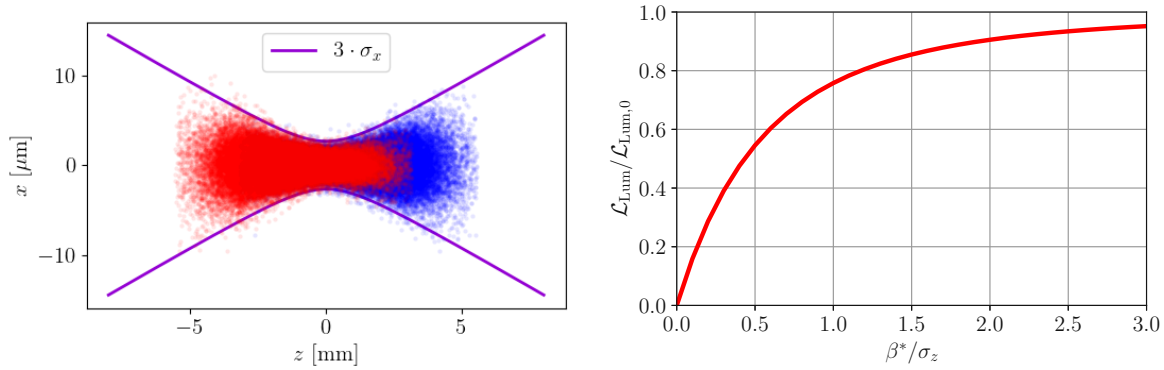


**Figure A.1.: Left**: Visualization of the hourglass effect, where the transverse beam size varies along the beam axis $s$. The minimum size occurs at the IP, and grows parabolically away from it. This spatial variation, combined with the finite bunch length, leads to a reduction in collider luminosity characterized by the hourglass factor, which depends on the ratio $\beta^*/\sigma_z$, illustrated in the **right** plot.

can lead to dynamic focus of the beams. As two high-intensity bunches pass through each other, the electromagnetic fields generated by one beam can compress or **pinch** the other, reducing its transverse size and increasing the local particle density. In other words, its an beam induced extra focusing effect.

This self-focusing enhances the overlap of the beams at the interaction point. It effectively boosts the instantaneous luminosity beyond what would be expected from static beam parameters alone. The strength of the pinch effect is characterized by the disruption parameter

$$D = \frac{N r_\mu \sigma_z}{\gamma \sigma_x^2}, \tag{A.10}$$

which depends on the number charges in the bunch, the beam, and transverse beam size [149]. The constant $r_\mu$ is the muon radius. The muon collider luminosity expanses to

$$\mathcal{L}_{\mathrm{Lum}} = \frac{\gamma^2 \tau_0 c}{2C} \frac{N_0^2}{4\pi\ \varepsilon_{\perp,\mathrm{N}}\ \beta^*} f_\mathrm{r}\ F_\mathrm{h} H_\mathrm{D} \tag{A.11}$$

with the enhancement factor

$$H_\mathrm{D} = 1 + D^{\frac{1}{4}} \frac{D^3}{1+D^3} \log\left(\sqrt{D}+1\right) + 2\log\left(0.8\frac{\beta^*}{\sigma_\mathrm{z}}\right). \tag{A.12}$$

## A.4 Luminosity summary

The luminosity was calculated based on the assumption of head-on collisions of particle bunches exhibiting Gaussian distributions in the transverse phase space. The longitudinal distribution of these particle bunches, along with the focusing effects induced by the collider optics, alters the collision cross section. This alteration results in a reduction in luminosity. This modified cross-section exhibits a characteristic form known as the hourglass effect. The mutual attraction of the charged collider bunches induces an additional focusing effect. This effect is referred to as the pinch effect, which leads to an increase in luminosity.

# Appendix B.

# Selected precession measurement events

## B.1 Extended derivation of the Lorentz invariant phase space

In particle physics, the **Lorentz invariant phase space** (**LIPS**) provides a framework for describing the kinematics of multi-particle systems in a way that is independent of the reference frame. It ensures that calculations of physical observables, such as cross sections and decay rates, remain consistent under Lorentz transformations.

### B.1.1 $\mathrm{d}^2$Lips

The phase space volume element is constructed to be invariant by incorporating both the momentum conservation delta function and the relativistically correct integration measures over the final state momenta. Specifically, for a process that involves 2 final-state particles with total momentum $P = p_1 + p_2$.

To derive the LIPS for a 2-particle final state, the general expression for the differential phase space element for a final state of 2 particles is

$$\mathrm{d}^2\mathrm{Lips}(P, p_1, p_2) = (2\pi)^4 \delta^{(4)}(P - p_1 - p_2) \frac{d^3 p_1}{(2\pi)^3 2p_1^0} \frac{d^3 p_2}{(2\pi)^3 2p_2^0} \tag{B.1}$$

The total energy is $E^2 = P^2 + M^2$ and in the frame, where $P^2 = 0$, the state momenta are defined as $p_1^* = -p_2^* = p$ and the center of mass energy (cm) is $M = \sqrt{s}$. The LIPS in the cm frame yields then

$$\mathrm{d}^2\mathrm{Lips}(P, p_1, p_2) = \mathrm{d}^2\mathrm{Lips}(0, p, -p) = \frac{1}{(2\pi)^2} \delta(\sqrt{s} - E_1 - E_2) \frac{d^3 p}{2E_1 2E_2} \tag{B.2}$$

Switch to spherical coordinates for integrating over the angular part is $d^3p = p^2 dp\, d\Omega = p^2 dp\, \sin(\vartheta) d\vartheta d\varphi$ and taking the definition

$$\int_{\tilde{p}} \delta(f(p)) \cdot g(p)\, dp = g(\tilde{p}) \left| \frac{df}{dp} \right|^{-1}_{\tilde{p}}, \tag{B.3}$$

with the Dirac-Delta function $\delta$. The LIPS for of 2 final state particles results to

$$\mathrm{d}^2\mathrm{Lips}(P, p_1, p_2) = \frac{1}{(2\pi)^2} \int \frac{p}{4\sqrt{s}} d\Omega = \frac{1}{(2\pi)^2} \int \frac{\lambda^{1/2}(s, m_1^2, m_2^2)}{8s} d\Omega \tag{B.4}$$

with the Källén function $\lambda$ explained in detail in the next section.

### B.1.2 Källén Function

The Källén function, also known as the triangle function, frequently arises in the kinematics of two-body decays and scattering processes. It provides a compact expression for combinations of masses and invariant quantities and is particularly useful in calculating momenta and phase-space factors.

Consider the decay of a particle with mass $M$ into two daughter particles with masses $m_1$ and $m_2$. In the rest frame of the parent particle, the energy of each daughter particle satisfies the relativistic energy-momentum relation:

$$E_i^2 = m_i^2 + p_i^2, \quad i = 1, 2,$$

where $p_i$ is the magnitude of the 3-momentum of the particle $i$.

The four-momenta of the system in the rest frame of the decaying particle are given by:

$$P^\mu = \begin{pmatrix} M \\ \vec{0} \end{pmatrix}, \quad p_1^\mu = \begin{pmatrix} E_1 \\ \vec{p} \end{pmatrix}, \quad p_2^\mu = \begin{pmatrix} E_2 \\ -\vec{p} \end{pmatrix}, \tag{B.5}$$

where $\vec{p}$ is the momentum of particle 1 in the center-of-mass (CM) frame, and $-\vec{p}$ that of particle 2, due to momentum conservation.

According to the kinematics in the CM frame, as illustrated in Fig. B.1, we have:

$$\begin{aligned} M &= \sqrt{s} = E_1 + E_2, \\ \vec{0} &= \vec{p}_1 + \vec{p}_2. \end{aligned} \tag{B.6}$$

From this it follows that $\vec{p}_1^* = -\vec{p}_2^* = \vec{p}$. Although the momenta are equal in magnitude and opposite in direction, the energies depend on the respective masses and are generally not equal.

To compute the energies, we use the invariant-mass condition. Starting with:

$$m_2^2 = (M - E_1)^2 - p^2,$$

and using $E_1^2 - p^2 = m_1^2$, we find:

$$m_2^2 = M^2 - 2ME_1 + m_1^2,$$

which can be solved for $E_1$ to yield:

$$E_1 = \frac{M^2 + m_1^2 - m_2^2}{2M}. \tag{B.7}$$

Now, the magnitude of the momentum is obtained via:

$$\begin{aligned} p^2 &= E_1^2 - m_1^2 \\ &= \frac{(M^2 + m_1^2 - m_2^2)^2}{4M^2} - m_1^2 \\ &= \frac{M^4 + m_1^4 + m_2^4 - 2M^2m_1^2 - 2M^2m_2^2 - 2m_1^2m_2^2}{4M^2} \\ &= \frac{\lambda(M^2, m_1^2, m_2^2)}{4M^2}, \end{aligned} \tag{B.8}$$

where $\lambda$ is the Källén function. Finally, for a general invariant mass $\sqrt{s}$ of the decaying system, the momentum of the decay products in the CM frame becomes:

$$p = \frac{\sqrt{\lambda(s, m_1^2, m_2^2)}}{2\sqrt{s}}. \tag{B.9}$$

This result is fundamental in analyzing two-body decays, and the Källén function provides a concise way to express the dynamics of the available phase space.

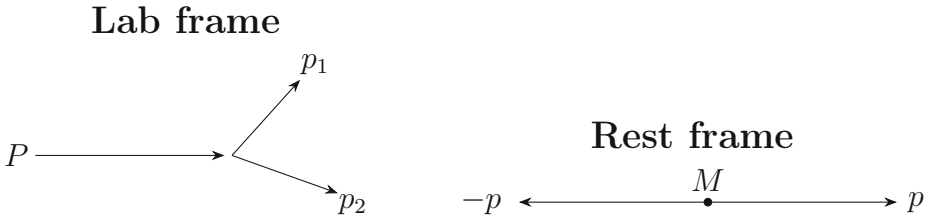


**Figure B.1.:** Lorentz transformation from the lab frame to the rest frame.

## B.2 Average squared matrix element of $\mu^- \bar{\nu}_\mu \to \gamma W^-$

The derivation of the average squared matrix element for process $\mu^- \bar{\nu}_\mu \to \gamma W^-$ will be conducted at the parton level. This process is equivalent to $\mu^+ \nu_\mu \to \gamma W^+$. The s-channel amplitude will be introduced initially, followed by the presentation of the t-channel amplitude.

### B.2.1 t-Channel

The t-channel is depicted in Fig. B.2 with a $\mu^-$ as the exchanged particle. The matrix element of the process shown in Fig. B.2, under the assumption of $m_\mu \approx 0$, scales to

$$M_{fi} = \xi\, \overline{v}(p_2) \left[\gamma^\nu (1-\gamma^5)\right] \not{q} \gamma^\mu u(p_1) \epsilon^*_\mu(p_3) \epsilon^*_\nu(p_4), \tag{B.10}$$

with

$$\xi = -\frac{g\, e}{2\sqrt{2}\, t}, \tag{B.11}$$

where $e$ denotes the electrical charge, $g$ represents the coupling constant of the $W$-boson, and $t = q = (p_1 - p_3)^2$ refers to the Mandelstam variable. In Eq. (B.10), the Dirac spinors corresponding to the fermion and anti-fermion are designated as $u$ and $v$, respectively, while the spinor associated with the boson is indicated as $\epsilon$. The Dirac gamma matrices are represented by $\gamma^\mu$, and the chiral matrix is defined as $\gamma^5 = i\gamma^0\gamma^1\gamma^2\gamma^3$. Slashed tensors are defined as $\not{q} = \gamma^\mu q_\mu$.

The average squared matrix element is the product of Eq. (B.10) with its conjugation $M^\dagger_{fi}$ averaged by all possible initial spin states. Spin average spared matrix element is

$$\begin{aligned}\left\langle |M|^2_t \right\rangle =& \frac{1}{2} \sum_{\text{Spin}} |M_{fi} M^\dagger_{fi}| = \frac{\xi^2}{4} \left( \underbrace{\sum_{\text{Spin}} \epsilon^*_\lambda(p_3) \epsilon_\mu(p_3)}_{-g_{\lambda\mu}} \right) \left( \underbrace{\sum_{\text{Spin}} \epsilon^*_\sigma(p_4) \epsilon_\beta(p_4)}_{-g_{\sigma\nu} + p_{4\sigma} p_{4\nu}/m^2_W} \right) \\ & \cdot \left( \underbrace{\sum_{\text{Spin}} u(p_1)\overline{u}(p_1)}_{\not{p}_1} \right) \left(\gamma^\lambda \not{q} \gamma^\sigma (1-\gamma^5)\right) \left( \underbrace{\sum_{\text{Spin}} v(p_2)\overline{v}(p_2)}_{\not{p}_2} \right) \left(\gamma^\nu \not{q} \gamma^\mu (1-\gamma^5)\right).\end{aligned} \tag{B.12}$$

The summation over the spinor in Eq. (B.12) can be summerized to matrices, where $g_{\alpha\beta}$ is the metric tensor. The sum over the initial states can further solved with the trace

formalism, leading to

$$\left\langle |M|_t^2 \right\rangle = -\xi^2 \left( g_{\sigma\nu} - \frac{p_{4\sigma} p_{4\nu}}{m_W^2} \right) p_{1\alpha} q_\beta p_{1\gamma} q_\delta \, \mathrm{Tr}\left( \gamma^\alpha \gamma^\beta \gamma^\sigma \gamma^\gamma \gamma^\nu \gamma^\delta (1 - \gamma^5) \right) . \tag{B.13}$$

By means of the trace rules, summarized in [7], the final result for the average squared matrix element yields to

$$\left\langle |M|^2 \right\rangle = \frac{g^2 \, e^2}{2 t m_W^2} \left[ 2m_W^4 - 2m_W^2 (s + t) + st \right] . \tag{B.14}$$

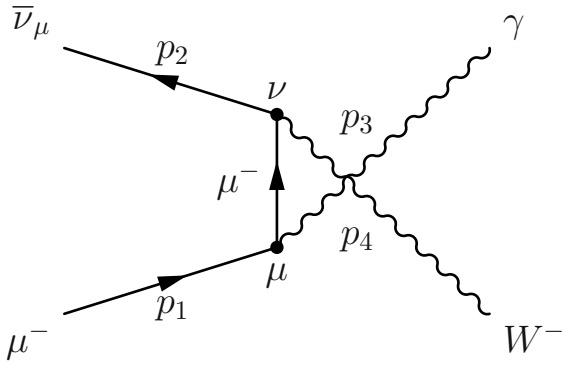


**Figure B.2.:** Feynman diagram of the t-channel process of $\mu^- \bar{\nu}_\mu \to \gamma W^-$.

### B.2.2 s-Channel

The s-channel process is illustrated in the Feynman diagram on the **left** of Fig. B.3. The triple gauge boson vertex necessary for the calculation is detailed in the **right** diagram of Fig. B.3 and is sourced from H. Eberl's lecture notes [49], which is

$$-ig \begin{pmatrix} \cos\vartheta_W, \text{ for } Z^0 \\ \sin\vartheta_W, \text{ for } \gamma \end{pmatrix} \left[ g^{\sigma\nu} (p_4 + q)^\lambda - g^{\sigma\lambda} (2p_4 - q)^\nu - g^{\nu\lambda} (2q - p_4)^\sigma \right] . \tag{B.15}$$

According to the Feynman rules, the matrix element $M_{fi}$ for the process is written as:

$$\begin{aligned} -iM_{fi} = & \overline{v}(p_2) \left[ -\frac{ig}{\sqrt{2}} \gamma^\mu \frac{1}{2} (1 - \gamma^5) \right] u(p_1) \frac{-i \left( g_{\mu\nu} - q_\mu q_\nu / m_W^2 \right)}{(q^2 - m_W^2) - i m_W \Gamma_W} \cdot (-ig \sin\vartheta_W) \\ & \left[ g^{\sigma\nu} (2p_4 + p_3)^\lambda - g^{\sigma\lambda} (p_4 - p_3)^\nu - g^{\nu\lambda} (2p_3 + p_4)^\sigma \right] \cdot \epsilon_\lambda^*(p_3) \epsilon_\sigma^*(p_4) \end{aligned} \tag{B.16}$$

The electric charge is articulated as $e = g \sin\vartheta_W$, where $\vartheta_W$ denotes the Weinberg angle. The mass and decay width of the $W$ boson is represented as $m_W$ and $\Gamma_W$. The matrix

element simplifies when the muon mass is negligible[1] to

$$M_{fi} = \xi \cdot \overline{v}(p_2)\left[\gamma^{\mu}(1-\gamma^5)\right] u(p_1)\left[g_{\mu}^{\sigma}(2p_4+p_3)^{\lambda} - g^{\sigma\lambda}(p_4-p_3)_{\mu} - g_{\mu}^{\lambda}(2p_3+p_4)^{\sigma}\right] \epsilon_{\lambda}^{*}(p_3)\epsilon_{\sigma}^{*}(p_4), \tag{B.17}$$

with

$$\xi = -\frac{eg}{2\sqrt{2}[(s-m_W^2) - im_W\Gamma_W]} \tag{B.18}$$

The average squared matrix element can be evaluated by the trace technique and is

$$\left\langle |M|_s^2 \right\rangle = \frac{e^2g^2}{2\left[(s-m_W^2)^2 + m_W^2\Gamma_W^2\right]}\left[\frac{s(s^2+st+t^2)}{m_W^2} - m_W^2(s-5t) - 4s^2 - 6st - 5t^2\right], \tag{B.19}$$

with the Mandelstam[2] variable $t$ and $s = (p_1+p_2)^2$.

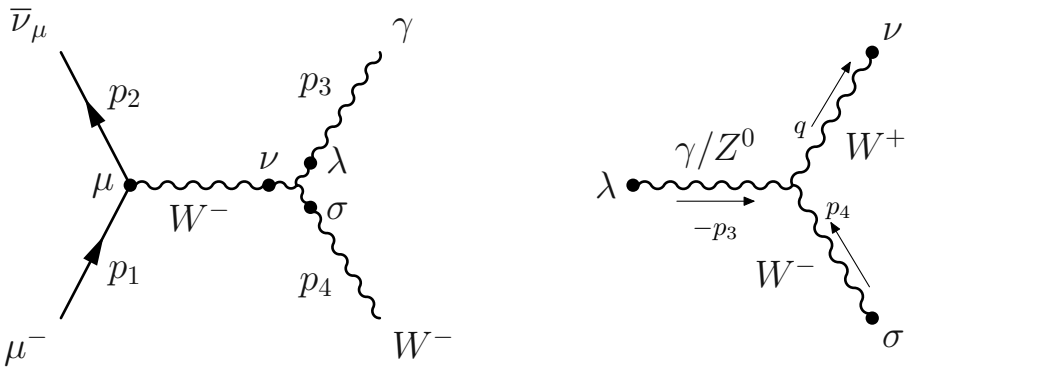


**Figure B.3.:** The **left** Feynman diagram illustrates the s-channel process of $\mu^-\bar{\nu}_\mu \to \gamma W^-$. The **right** diagram provides a more detailed summary of the kinematics associated with the triple gauge vertex.

### B.2.3 Interference term and total squared amplitude

The matrix element is also called the amplitude. In order to determine the total squared amplitude of the process, it is necessary to evaluate the crossing term of the s- and t-channel. This term is referred to as the interference term in the results $\langle |M|^2 \rangle_{\text{Int}} = \text{Re}(M_s M_t^{\dagger})$. The total squared amplitude of the $\mu^-\bar{\nu}_\mu \to \gamma W^-$ process is $\langle |M| \rangle = \langle |M| \rangle_s + \langle |M| \rangle_t + 2\langle |M| \rangle_{\text{Int}}$, derived by disregarding $\Gamma_W$

$$\langle |M| \rangle = \frac{2e^2g^2}{t(s-m_W^2)^2}(m_W^2 - s - t)\left[m_W^4 - 2m_W^2t + s^2 + 2t(s+t)\right]. \tag{B.20}$$

[1] Dirac equation: $\overline{v}(p_2)(\not{p}_2 + m_\mu) = 0,\ (\not{p}_1 - m_\mu)u(p_1) = 0,\ (\not{p}_1 - m_\mu)u(p_1) = 0$

[2] $s + t + u = m_W^2$

These findings can be compared with reference [150] and are identical.

## B.3 Vector boson fusion cross sections

Vector boson fusion (VBF) studies offer a robust approach to understanding the structure of matter and testing the SM. VBF plays a crucial role in generating the Higgs boson at muon colliders, which offer a cleaner environment compared to hadron colliders.

This section presents a comprehensive overview of the procedure for calculating the total cross section of VBF. An emphasis will be placed on the Lorentz invariant phase space for three particles, along with the derivation of the average squared matrix element using Feynman rules.

### B.3.1 Three body scattering kinematics

The Lorentz-invariant phase space (Lips) is essential when calculating cross sections and decay rates in particle physics. For three final-state particles, the LIPS these particles will be derived which can be applied for the calcuation of the total cross section of the VBF in a muon colliders[3].

The lip for three particles is written as $\mathrm{d}^3\mathrm{Lips}$. Calculating $\mathrm{d}^3\mathrm{Lips}$ is need for determine $1+2 \to 3+4+5$ scattering processes, such as VBF. In $W^+W^-$-fusion, involving $\nu_\mu, \bar{\nu}_\mu$ and $H$, the process simplifies to two-body $1+2 \to 3+4$ scattering[4]. Neutrinos $\nu_\mu$ and $\bar{\nu}_\mu$ are unified as a single virtual particle with mass $m_{12}$ and momentum $\vec{k}$. The kinematics of this interaction are shown in Fig. B.4. Incoming particles $\mu^-$ and $\mu^+$ have momenta $p_1$ and $p_2$, with a virtual outgoing particle $k_{12}$ and a Higgs boson $k_3$. The 4-momenta in the cm frame are defined as

$$p_1^\mu = \begin{pmatrix} p \\ 0 \\ p\sin(\vartheta) \\ p\cos(\vartheta) \end{pmatrix}, \quad p_2^\mu = \begin{pmatrix} p \\ 0 \\ -p\sin(\vartheta) \\ -p\cos(\vartheta) \end{pmatrix}, \quad k_{12}^\mu = \begin{pmatrix} E_{12} \\ 0 \\ 0 \\ k \end{pmatrix}, \quad k_3^\mu = \begin{pmatrix} E_H \\ 0 \\ 0 \\ -k \end{pmatrix} \tag{B.21}$$

where $p = \frac{\sqrt{s}}{2}$, $E_H = \sqrt{m_H^2 + k^2}$ and $E_{12} = \sqrt{m_{12}^2 + k^2}$. The outgoing momentum $k$ can be evaluated by the Källén function, summarized in Appendix B.1.2, and results to

$$k = \frac{\lambda^{1/2}\left(s, m_{12}^2, m_H^2\right)}{2\sqrt{s}} \tag{B.22}$$

[3] Equivalent to Higgs production via VBF in $e^+e^-$ linear colliders.
[4] Also valid for $Z^0Z^0$-fusion.

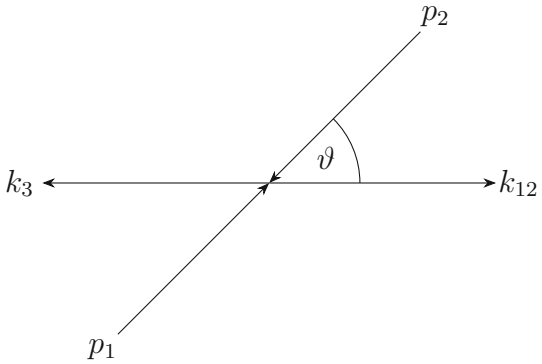


**Figure B.4.:** The kinematics of the three-body process have been reduced to a two-scattering event. The momenta labeled as $p_1$ and $p_2$ correspond to the incoming muons, whereas $k_{12}$ represents that of a virtual particle, and $k_3$ pertains to the Higgs boson. This virtual particle is responsible for combining the two outgoing muon-neutrinos.

The artificially introduced virtual particles decay into $\nu_\mu$ and $\bar{\nu}_\mu$. Within the rest frame of this virtual particle, the neutrino's 4-momenta are denoted as $k_1^*$ and $k_2^*$. In particular, the rest frame of the virtual particle differs from the center-of-momentum frame of the collision $\mu^+\mu^-$. The muon-neutrinos have equal spatial momentum values $k^*$. However, this spatial momentum occurs with polar and azimuthal angles, given by $\vartheta^*$ and $\varphi^*$, respectively to the cm frame. The relevant kinematic details are depicted in Fig. B.5.

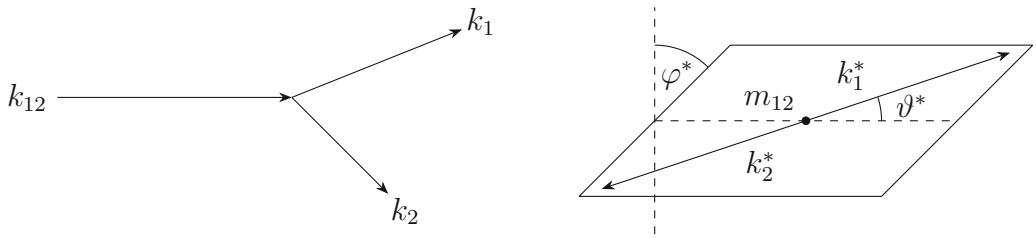


**Figure B.5.:** On the **left** side, within the cm frame, the virtual particle characterized by momentum $k_{12}$ undergoes a decay process resulting in the formation of a pair of muon-neutrinos with momenta $k_1$ and $k_2$. The rest frame of this virtual particle is illustrated in the **right** sketch, presenting the associated momentum definistions.

The four-momenta of the muon-neutrinos, as observed in the rest frame of the virtual

particle and subsequently in the cm frame, are defined as

$$k_1^{\mu *} = \begin{pmatrix} k^* \\ k^* \sin(\vartheta^*) \sin(\varphi^*) \\ k^* \sin(\vartheta^*) \cos(\varphi^*) \\ k^* \cos(\vartheta^*) \end{pmatrix}, \quad k_2^{\mu *} = \begin{pmatrix} k^* \\ -k^* \sin(\vartheta^*) \sin(\varphi^*) \\ -k^* \sin(\vartheta^*) \cos(\varphi^*) \\ -k^* \cos(\vartheta^*). \end{pmatrix} \tag{B.23}$$

The determination of the spatial momentum within the rest frame of the virtual particle is provided in

$$k^* \approx \frac{\lambda^{1/2}\left(m_{12}^2, 0, 0\right)}{2m_{12}} = \frac{m_{12}}{2}, \tag{B.24}$$

under the assumption that both muon masses $m_{\nu_\mu}$ and $m_{\bar{\nu}_\mu}$ are negligible. The essential step involves performing a Lorentz transformation $k_i^* = \Lambda^{-1} k_i$ of muon neutrinos into the cm frame, as indicated by $i = 1, 2$. The inverse Lorentz boost matrix is derived as

$$\Lambda^{-1} = \begin{pmatrix} \gamma & 0 & 0 & \gamma\beta \\ 0 & 1 & 0 & 0 \\ 0 & 0 & 1 & 0 \\ \beta\gamma & 0 & 0 & \gamma \end{pmatrix}, \tag{B.25}$$

utilizing the Lorentz factors $\gamma = E_{12}/m_{12}$ and $\beta = k/E_{12}$. The muon-neutrinos' momenta in the cm frame results in

$$k_1^{\mu} = \frac{1}{2} \begin{pmatrix} E_{12} + k\cos\vartheta^* \\ m_{12}\sin(\vartheta^*)\sin(\varphi^*) \\ m_{12}\sin(\vartheta^*)\cos(\varphi^*) \\ k + E_{12}\cos(\vartheta^*) \end{pmatrix}, \quad k_2^{\mu} = \frac{1}{2} \begin{pmatrix} E_{12} - k\cos\vartheta^* \\ -m_{12}\sin(\vartheta^*)\sin(\varphi^*) \\ -m_{12}\sin(\vartheta^*)\cos(\varphi^*) \\ k - E_{12}\cos(\vartheta^*) \end{pmatrix} \tag{B.26}$$

### B.3.2 Three body decay phase space

The $\mathrm{d}^3$Lips can be analytically evaluated through the convolution of two two-body Lorentz-invariant phase spaces, denoted as $\mathrm{d}^2$Lips. One of these, $\mathrm{d}^2$Lips, corresponds to the simplified VBF process illustrated in Fig. B.4, while the second pertains to the decayed virtual particle depicted in Fig. B.5. The $\mathrm{d}^3$Lips is defined as

$$\begin{aligned} \mathrm{d}^3\mathrm{LIPS} &= (2\pi)^4 \delta^{(4)}(k^\mu - k_1^\mu - k_2^\mu - k_3^\mu) \prod_{i=1}^{3} \frac{d^3 k_i}{(2\pi)^3 2E_i} \\ &= \frac{1}{(2\pi)^5} \delta^{(4)}(p_1^\mu + p_2^\mu - k_3^\mu - k_1^\mu - k_2^\mu) \frac{d^3 k_1\, d^3 k_2\, d^3 k_3}{2E_1\, 2E_2\, 2E_3} \end{aligned} \tag{B.27}$$

with the total momentum of VBF process is $k^\mu = p_1^\mu + p_2^\mu = k_1^\mu + k_2^\mu + k_3^\mu$. The Dirac-delta function is $\int \prod_i \delta(x_i)\, dx_i = 1$ which results to the unity of

$$\int \delta^{(4)}(k_{12}^\mu - k_1^\mu - k_2^\mu)\, dE_{12}\, d^3k = 1 \tag{B.28}$$

Due to $E_{12}\, dE_{12} = m_{12}\, dm_{12}$ of the virtual particle, the unity is reshaped to

$$2 \int \delta^{(4)}(k_{12}^\mu - k_1^\mu - k_2^\mu)\, m_{12} \frac{dm_{12}\, d^3k_{12}}{2E_{12}} = 1. \tag{B.29}$$

This unity will be inserted into Eq. (B.27) resulting to

$$\begin{aligned} \mathrm{d}^3\mathrm{LIPS} = \frac{1}{(2\pi)} 2 \int m_{12}\, dm_{12} \frac{(2\pi)^4}{(2\pi)^6} \delta^{(4)}(k^\mu - k_3^\mu - k_{12}^\mu) \frac{d^3k\, d^3k_3}{2E_{12}\, 2E_3} \\ \cdot \frac{(2\pi)^4}{(2\pi)^6} \delta^{(4)}(k_{12}^\mu - k_1^\mu - k_2^\mu) \frac{d^3k_1\, d^3k_2}{2E_1\, 2E_2} \end{aligned} \tag{B.30}$$

As discussed in Appendix B.1.1, the equation above can be decomposed into two $\mathrm{d}^2$Lips

$$\mathrm{d}^3\mathrm{LIPS} = \frac{1}{(2\pi)} 2 \int_0^{\sqrt{s}-m_H} m_{12}\, dm_{12}\, \mathrm{d}^2\mathrm{LIPS}(\sqrt{s}, k_3, k_{12})\, \mathrm{d}^2\mathrm{LIPS}(k, k_1, k_2) \tag{B.31}$$

with the lower integration limit of $m_{\nu_\mu} + m_{\bar{\nu}_\mu} \approx 0$ and the upper limit as cm energy reduced with the Higgs mass. The 2-body phase space expressions are

$$\begin{aligned} \mathrm{d}^2\mathrm{LIPS}(\sqrt{s}, k_3, k) &= \frac{1}{(2\pi)^2} \int d\Omega \frac{k}{4\sqrt{s}} = \frac{1}{(2\pi)^2} \frac{\lambda^{1/2}(s, m_H^2, m_{12}^2)}{8s} \int d\Omega \\ \mathrm{d}^2\mathrm{LIPS}(k, k_1, k_2) &= \frac{1}{(2\pi)^2} \int d\Omega^* \frac{k^*}{4m_{12}} = \frac{1}{(2\pi)^2} \frac{1}{8} \int d\Omega^*, \end{aligned} \tag{B.32}$$

with $d\Omega = \sin(\vartheta)\, d\vartheta\, d\varphi$. Given that the Matrix element is independent of $\varphi$, the integral can be solved without complication. Consequently, the $\mathrm{d}^3$Lips results in

$$\mathrm{d}^3\mathrm{LIPS} = \frac{1}{(2\pi)^4} \frac{1}{16\sqrt{s}} \int_0^{2\pi} d\varphi^* \int_0^{\pi} \sin(\vartheta^*)\, d\vartheta^* \int_0^{\pi} \sin(\vartheta)\, d\vartheta \int_0^{\sqrt{s}-m_H} m_{12}\, k\, dm_{12}, \tag{B.33}$$

the final result of Lorentz invariant phase space of three final state particles.

### B.3.3 Amplitude of the $W^+W^-$-Fusion

In the upcoming section, an extensive elaboration of the squared amplitude (matrix element) of the $W^+W^-$ fusion will be conducted, employing the Feynman rule framework and the trace technique [7]. Previously, the Feynman diagram depicting the $W^+W^-$ fusion was illustrated in Fig. 2.4 on the left. It should be noted that the invariant eigenproduct of each 4-momentum is zero due to the negligible particle masses relative to the cm energy $\sqrt{s}$, with the exception of $(k_3^\mu)^2 = m_H$. The definition of the 4-momenta of the W boson is according to Fig. 2.4 is defined as

$$q_1^\mu = (p_1 - k_1)^\mu, \qquad q_2^\mu = (p_2 - k_2)^\mu. \tag{B.34}$$

The matrix element may be derived using the Feynman rules and results in

$$\begin{aligned} -iM_{fi} = &\left[\frac{-ig}{\sqrt{2}}\bar{u}(k_1)\gamma^\mu\frac{1}{2}(1-\gamma^5)u(p_1)\right] \times \left[\frac{-i\,(g_{\mu\nu} - q_{1\mu}q_{1\nu}/m_W^2)}{q_1^2 - m_W^2}\right] \times \\ &ig_{\nu\lambda}\, g\, m_W \times \left[\frac{-i\,(g_{\lambda\sigma} - q_{1\lambda}q_{1\sigma}/m_W^2)}{q_1^2 - m_W^2}\right] \times \left[\frac{-ig}{\sqrt{2}}\bar{v}(p_2)\gamma^\sigma\frac{1}{2}(1-\gamma^5)v(k_2)\right]. \end{aligned} \tag{B.35}$$

Within this equation, one can identify two fermion currents, delineated as

$$J_1^\mu = \bar{u}(k_1)\gamma^\mu(1-\gamma^5)u(p_1), \qquad J_2^\sigma = \bar{v}(p_2)\gamma^\sigma(1-\gamma^5)v(k_2). \tag{B.36}$$

The interaction constants and associated denominator terms are encapsulated in

$$\xi = \left(\frac{g^3}{8}\right)\frac{m_W}{(q_1^2 - m_W^2)(q_2^2 - m_W^2)}. \tag{B.37}$$

Subsequently, the matrix element can be further simplified to

$$\begin{aligned} M_{fi} = &\xi\left[\underbrace{J_1^\mu\, g_{\mu\nu}\, g_{\nu\lambda}\, g_{\lambda\sigma}\, J_2^\sigma}_{A} + \frac{1}{m_W^4}\underbrace{J_1^\mu q_{1\mu}q_{1\nu}\cdot g_{\nu\lambda}\cdot q_{2\lambda}\, q_{2\sigma}J_2^\sigma}_{B}\right] - \\ &\xi\left[\frac{1}{m_W^2}\underbrace{J_1^\mu g_{\mu\nu}\, g_{\nu\lambda}\cdot q_{2\lambda}\, q_{2\sigma}J_2^\sigma}_{C} + \frac{1}{m_W^2}\underbrace{J_1^\mu q_{1\mu}\, q_{1\nu}\cdot g_{\nu\lambda}\, g_{\lambda\sigma}J_2^\sigma}_{D}\right], \end{aligned} \tag{B.38}$$

yielding four distinct terms, namely $A, B, C$ and $D$. The following procedure involves the elimination of the metric tensors via the application of the Einstein summation

convention to each term

$$\begin{aligned} A &= J_1^\mu \underbrace{g_{\mu\nu}\, g_{\nu\lambda}\, g_{\lambda\sigma}}_{g_{\mu\sigma}} J_2^\sigma = J_1^\mu J_{2\,\mu} = (J_1 J_2), \quad C = \frac{1}{m_W^2}(J_1 q_2)(q_2 J_2), \\ B &= \frac{1}{m_W^4}\,(J_1 q_1)\,(q_1 q_2)(q_2 J_2), \qquad\qquad D = \frac{1}{m_W^2}(J_1 q_1)(q_1 J_2), \end{aligned} \tag{B.39}$$

where the Lorentz product is specified as $a^\mu b_\mu = (ab)$. The Dirac equation, described in $[\not{q} - m_\mu]u = 0$, assumes the muon and neutrino masses to be negligible, allowing for the Dirac equation to be approximated as $\not{q}u \approx 0$. The Lorentz product of any current $J_i$ with a W-boson momentum $q_j$, given $i, j = 1, 2$, yields

$$\begin{aligned} (J_i q_j) &= \bar{u}(k_i)\gamma^\mu(1-\gamma^5)u(p_i)\cdot q_{j\,\mu} = \bar{u}(k_i)[\gamma^\mu q_{j\,\mu} u(p_i) - \gamma^\mu\gamma^5 q_{j\,\mu} u(p_i)] \\ &= \bar{u}(k_i)[\not{q}_j u(p_i) + \gamma^5 \not{q}_j u(p_i)] = 0, \end{aligned} \tag{B.40}$$

whereby the terms $B, C$ and $D$ are reduced to zero. The squared amplitude is

$$|M_{fi}|^2 = M_{fi}^\dagger M_{fi} = \xi^2 (J_2^\dagger \cdot J_1^\dagger)(J_1 \cdot J_2), \tag{B.41}$$

with the hermitian conjugated currents

$$J_1^{\mu\dagger} = \bar{u}(p_1)\gamma^\mu(1-\gamma^5)u(k_1), \quad J_2^{\sigma\dagger} = \bar{v}(k_2)\gamma^\sigma(1-\gamma^5)v(p_2). \tag{B.42}$$

The spin averaged matrix element is

$$\begin{aligned} \langle |M|^2 \rangle = \frac{1}{4}\sum_{\text{spins}} |M_{fi}|^2 = \frac{\xi}{4}\sum_{\text{spins}} &[\bar{v}(k_2)]_{\text{a}} \left[\gamma_\nu(1-\gamma^5)\right]_{\text{ab}} [v(p_2)]_{\text{b}} [\bar{u}(p_1)]_{\text{c}} \left[\gamma^\nu(1-\gamma^5)\right]_{\text{cd}} \\ &[u(k_1)]_{\text{d}} [\bar{u}(k_1)]_{\text{e}} \left[\gamma^\mu(1-\gamma^5)\right]_{\text{ef}} [u(p_1)]_{\text{f}} [\bar{v}(p_2)]_g \left[\gamma_\mu(1-\gamma^5)\right]_{\text{gh}} [v(k_2)]_{\text{h}} \end{aligned} \tag{B.43}$$

The completeness relation is denoted as $\sum_{\text{spins}} u(p)\bar{u}(p) = \not{p} + m$ and $\sum_{\text{spins}} v(p)\bar{v}(p) = \not{p} - m$. Assuming the muon and neutrino mass is negligible and reordering the terms leads to

$$\begin{aligned} &\Big(\sum v(k_2)\bar{v}(k_2)\Big)_{\text{ha}} \left[\gamma_\nu(1-\gamma^5)\right]_{\text{ab}} \Big(\sum v(p_2)\bar{v}(p_2)\Big)_{\text{bg}} \left[\gamma_\mu(1-\gamma^5)\right]_{\text{gh}} \\ &\Big(\sum u(p_1)\bar{u}(p_1)\Big)_{\text{fc}} \left[\gamma^\nu(1-\gamma^5)\right]_{\text{cd}} \Big(\sum u(k_1)\bar{u}(k_1)\Big)_{\text{de}} \left[\gamma^\mu(1-\gamma^5)\right]_{\text{ef}} \end{aligned} \tag{B.44}$$

The averaged squared amplitude contains two trace terms

$$\langle |M_{fi}|^2 \rangle = \frac{\xi}{4}\ \text{Tr}\Big\{\not{k}_2\gamma_\nu(1-\gamma^5)\not{p}_2\gamma_\mu(1-\gamma^5)\Big\}\ \text{Tr}\Big\{\not{p}_1\gamma^\nu(1-\gamma^5)\not{k}_1\gamma^\mu(1-\gamma^5)\Big\}. \tag{B.45}$$

An application demonstrating the resolution of the initial trace in the aforementioned equation will be presented. The chirality operator rules are: $(\gamma^5)^2 = 1$, $\gamma^\mu\gamma^5 = -\gamma^5\gamma^\mu$. The formulation of the first trace in the equation is as follows:

$$\begin{aligned}
&\mathrm{Tr}\Big\{\not{k}_2\gamma_\nu\not{p}_2\gamma_\mu(1-\gamma^5)^2\Big\} = 2\,k_{2,\alpha}\,p_{2,\beta}\;\mathrm{Tr}\big\{\gamma^\alpha\gamma_\nu\gamma^\beta\gamma_\mu(1-\gamma^5)\big\} = \\
&2\,k_{2,\alpha}\,p_{2,\beta}\;\big(\mathrm{Tr}\big\{\gamma^\alpha\gamma_\nu\gamma^\beta\gamma_\mu\big\} - \mathrm{Tr}\big\{\gamma^\alpha\gamma_\nu\gamma^\beta\gamma_\mu\gamma^5\big\}\big) = \\
&2\,k_{2,\alpha}\,p_{2,\beta}\;\big(4\;\big(g^\alpha_\nu g^\beta_\mu - g^{\alpha\beta}g_{\nu\mu} + g^\alpha_\mu g^\beta_\nu\big) - i4\epsilon^\alpha{}_\nu{}^\beta{}_\mu\big) = \\
&8\;\big(k_{2,\nu}\,p_{2,\mu} - (k_2\,p_2)g_{\nu\mu} + k_{2,\mu}\,p_{2,\nu} - i\,k_{2,\alpha}\,p_{2,\beta}\,\epsilon^\alpha{}_\nu{}^\beta{}_\mu\big)\,.
\end{aligned} \tag{B.46}$$

A similar approach applied to the second term results in

$$\mathrm{Tr}\Big\{\not{p}_1\gamma^\nu(1-\gamma^5)\not{k}_1\gamma^\mu(1-\gamma^5)\Big\} = 8\;\big(p_1^\nu\,k_1^\mu - (p_1\,k_1)g_{\nu\mu} + p_1^\mu\,k_1^\nu - i\,p_1^\lambda\,k_1^\sigma\,\epsilon^{\lambda\nu\sigma\mu}\big)\,. \tag{B.47}$$

Moreover, the average matrix element gets the form of

$$\langle|M|^2\rangle = 16\xi\,\big(2\,(p_1\,k_2)(p_2\,k_1) + 2\,(p_1\,p_2)(k_1\,k_2) - k_{2,\alpha}\,p_{2,\beta}\,p_1^\lambda\,k_1^\sigma\,\epsilon^{\lambda\nu\sigma\mu}\,\epsilon^\alpha{}_\nu{}^\beta{}_\mu\big)\,. \tag{B.48}$$

A detailed examination of the epsilon tensor product reveals that it manifests as a product of Kronecker deltas

$$\epsilon^{\lambda\nu\sigma\mu}\,\epsilon^\alpha{}_\nu{}^\beta{}_\mu = \delta^{\lambda\nu\sigma\mu}_{\alpha\nu\beta\mu} = \delta^{\lambda\sigma}_{\alpha\beta} = -2\,(\delta^\lambda_\alpha\delta^\sigma_\beta - \delta^\lambda_\beta\delta^\sigma_\alpha), \tag{B.49}$$

resulting in

$$\langle|M|^2\rangle = m_W^2\,g^6\frac{(p_1k_2)\cdot(p_2k_1)}{\left[2(p_1k_1)+m_W^2\right]^2\left[2(p_2k_2)+m_W^2\right]^2} \tag{B.50}$$

with the eigen-production of the boson momenta

$$\begin{aligned}
q_1^2 &= (p_1 - k_1)^2 = -2\,(p_1k_1), \\
q_2^2 &= (p_2 - k_2)^2 = -2\,(p_2k_2).
\end{aligned} \tag{B.51}$$

The derivation for the production of a single Higgs boson via $W^+W^-$ fusion is equally applicable to the $Z^0Z^0$ fusion process.

### B.3.4 Higgs strahlung contribution and its interference

Higgs strahlung refers to a production mechanism in which a Higgs boson is emitted simultaneously with a $Z^0$ boson, predominantly during fermion-anti-fermion collisions at $240\,\mathrm{GeV} < \sqrt{s} < 250\,\mathrm{GeV}$. For example, this mechanism is the predominant process for Higgs production in the proposed $e^-e^+$ ring colliders [151, 152].

Higgs strahlung has a minor role in multi-TeV muon colliders, yet it is worth mentioning. The final state $\nu_\mu \bar{\nu}_\mu H$ is not produced solely by the process $W^+W^-$; Higgs strahlung also contributes, as shown in the Feynman diagram in Fig. B.6 **left**, with $Z^0$ decaying into neutrinos. The production of the Higgs boson through $Z^0Z^0$ fusion, along with the Higgs strahlung process resulting in final states of $\mu^-$, $\mu^+$, and $H$, is illustrated in Fig. B.6 **right**.

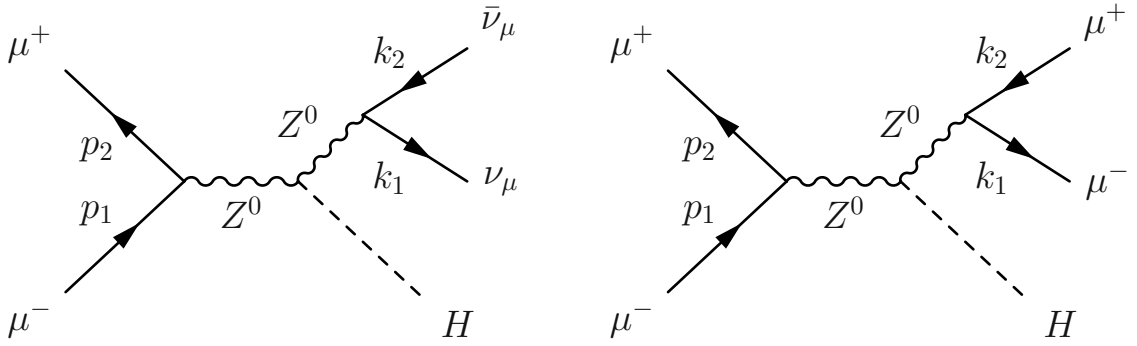


**Figure B.6.:** The contribution of Higgs strahlung with a final state consisting of a neutrino pair (**left**) and a muon pair (**right**).

The amplitude of the left process depicted in Fig. B.6 is given by

$$\overset{HZ\to\nu\bar{\nu}H}{M_{fi}} = \xi_2 \left[\bar{u}(k_1)\gamma^\mu(1-\gamma^5)v(k_2)\right] \cdot \left[\bar{v}(p_2)\gamma^\nu(c_V - c_A\,\gamma^5)u(p_1)\right], \tag{B.52}$$

with the vector- and axial vector coupling, $c_V$ and $c_A$, of the muon to $Z^0$. In Eq. (B.52),

$$\xi_2 = \frac{g'^3}{8}\frac{m_Z}{(\tilde{q}_1^2 - m_Z^2)(\tilde{q}_2^2 - m_Z^2)} \tag{B.53}$$

where $g'$ is the coupling constant and $m_Z$ the mass of the $Z^0$ boson. The intermediate momenta fulfill the kinematics $\tilde{q}_1^2 = s$ and $\tilde{q}_2^\mu$ equals $k_{12}^\mu$ in Eq. (B.21). The decay rate of the $Z^0$ boson is denoted as $\Gamma_Z$. Executing the squared sum of Eq. (B.52) follows to

$$\overset{HZ\to\nu\bar{\nu}H}{\langle|M|^2\rangle} = g'^6 m_Z^2\,(m_{12}^2 - m_Z^2)^2 \frac{(c_A - c_V)^2(p_1k_1)(p_2k_2) + (c_A + c_V)^2(p_1k_2)(p_2k_1)}{4(s - m_Z^2)^2\left[(m_{12}^2 - m_Z^2)^2 + m_Z^2\Gamma_Z^2\right]^2} \tag{B.54}$$

For an exhaustive computation of Eq. (B.52) and Eq. (B.54), the mathematical methods outlined in the preceding section can be utilized.

For the total cross section of the scattering process of $\mu^-\mu^+ \to W^-W^+ \to \nu_\mu\bar{\nu}_\mu H$, the

total average and square amplitude has to be evaluated first which is

$$\begin{aligned}\langle|\overset{\nu\bar{\nu}H}{M}|^2\rangle &= \left\langle \left| \overset{WW\to\nu\bar{\nu}H}{M_{fi}} + \overset{HZ\to\nu\bar{\nu}H}{M_{fi}} \right|^2 \right\rangle \\ &= \overset{WW\to\nu\bar{\nu}H}{\langle|M|^2\rangle} + \overset{HZ\to\nu\bar{\nu}H}{\langle|M|^2\rangle} + 2\overset{\text{Interference}}{\langle|M|^2\rangle}\end{aligned} \tag{B.55}$$

where $\langle|\overset{\nu\bar{\nu}H}{M}|^2\rangle$ is equal to Eq. (B.50) and the interference term is defined as

$$\overset{\text{Interference}}{\langle|M|^2\rangle} = \text{Re}\left(\overset{WW\to\nu\bar{\nu}H}{M_{fi}} \cdot \overset{HZ\to\nu\bar{\nu}H}{M_{fi}^{\dagger}}\right). \tag{B.56}$$

### B.3.5 Higgs rate in different collider types

In the following, Table B.1 compares the muon collider as a Higgs factory with other future lepton collider concepts. Depending on the collider type and operation energy, Higgs particles are generated by different leading processes.

| **Linear colliders** | Leading process | $\sigma_{\text{tot}}$ [fb] | $\mathcal{L}_{\text{Lum}} \times 10^{34}$ [$\text{cm}^{-2}\text{s}^{-1}$] | Higgs Rate [$\text{s}^{-1}$] | $\frac{1}{\text{Rate}}$ |
|---|---|---|---|---|---|
| CLIC 1.5 TeV | $W^-W^+$ | 309.7 | 3.7 | 0.012 | 1.5 min |
| CLIC 3 TeV | $W^-W^+$ | 496.6 | 5.9 | 0.029 | 34.1 s |
| ILC 250 GeV | $HZ^0$ | 242.9 | 1.5 | 0.004 | 3.5 min |
| ILC 1 TeV | $W^-W^+$ | 210.3 | 4.9 | 0.010 | 41.1 s |
| **$e^+e^-$ ring colliders** | | | | | |
| FCC-ee 240 GeV | $HZ^0$ | 242.7 | 8.5 | 0.021 | 48.4 s |
| CEPC 240 GeV | $HZ^0$ | 242.7 | 8.3 | 0.020 | 49.7 s |
| LEP3 240 GeV | $HZ^0$ | 242.7 | 1.0 | 0.002 | 6.9 min |
| **µ-colliders** | | | | | |
| µ-collider 3 TeV | $W^-W^+$ | 496.6 | 2.0 | 0.010 | 1.6 min |
| µ-collider 10 TeV | $W^-W^+$ | 845.1 | 21.5 | 0.182 | 5.5 s |

**Table B.1.:** An overview of lepton collider concepts as Higgs factories is presented. At lower energies, Higgs strahlung dominates, while at higher energies, $W^-W^+$ fusion acts as the leading process. The 3 TeV muon collider is comparable to linear colliders, whereas the 10 TeV machine produces a Higgs every 5 s, an order of magnitude faster than other concepts.

Within the low energy spectrum (240 GeV-250 GeV), the prevalence of Higgs strahlung

as the dominant mechanism is observed. For collider systems operating within the TeV energy range, such as muon colliders, $W^-W^+$ predominantly facilitates the production of Higgs particles. A 3 TeV muon collider is compatible with the linear collider as shown in Table B.1. A muon collider operating at 10 TeV has the potential to produce a significantly high event rate, generating a Higgs every 5 s. This performance surpasses that of other lepton collider concepts, making it a key motivation for ongoing research and development efforts within the muon collider study [25].

# Appendix C.

# Specific calculations relevant for ionization cooling

## C.1 From Maxwell's equations to the magnetic field of a finite current sheet

The analytical model for describing realistic solenoids can be derived from Maxwell's equations. In the following a brief overview of these equations will be discussed.

### C.1.1 Maxwell equation

Charges and currents are responsible for creating electromagnetic fields that influence the space around them. In 1864, James Clerk Maxwell combined these processes into four differential equations, now famously known as Maxwell's equations. They explain the link between the electric field $\vec{E}(\vec{x},t)$ and the magnetic field $\vec{B}(\vec{x},t)$, and also their connection to their generating sources through variables of time $t$ and position $\vec{x}$. The fields carry energy and momentum and exert influence over charges and currents on the basis of their location. Presented below is a concise summary of Maxwell's equations in a vacuum.

Gauss's law is illustrated by the first equation, indicating that the divergence of the electric field is directly related to the charge density $\varrho(\vec{x},t)$:

$$\nabla \cdot \vec{E}(\vec{x},t) = \frac{\varrho(\vec{x},t)}{\varepsilon_0}. \tag{C.1}$$

In this context, $\nabla$ denotes the vector differential operator, while $\varepsilon_0$ represents the vacuum permittivity. The second equation, referred to as Gauss's law for magnetism, states that

magnetic monopoles do not exist, or if they do, they have yet to be found. Consequently, the magnetic field $\vec{B}(\vec{x},t)$ invariably creates closed loops:

$$\nabla \cdot \vec{B}(\vec{x},t) = 0. \tag{C.2}$$

The third Maxwell equation, referred to as Faraday's law of electromagnetic induction, articulates that a temporally varying magnetic field generates a circulating electric field. In essence, temporal alterations in the magnetic field engender a rotational or "curl" configuration within the electric field.

$$\nabla \times \vec{E}(\vec{x},t) = -\frac{\partial \vec{B}(\vec{x},t)}{\partial t}. \tag{C.3}$$

The Ampère-Maxwell law is an essential equation illustrating that a magnetic field with a curl arises from both electric currents and changing electric fields. This law conservatively extends Maxwell's equations by incorporating the displacement current, crucial for describing electromagnetic waves:

$$\nabla \times \vec{B}(\vec{x},t) = \mu_0 \vec{J}(\vec{x},t) + \mu_0 \varepsilon_0 \frac{\partial \vec{E}(\vec{x},t)}{\partial t}. \tag{C.4}$$

In Eq. (C.4), $\mu_0$ refers to the vacuum permeability, while $J(\vec{x},t)$ represents the current density. According to the third Maxwell equation, $\nabla \cdot \vec{B} = 0$, the magnetic field $\vec{B}$ can be mathematically be expressed as the curl of a vector potential, which is given by

$$\vec{B}(\vec{x},t) = \nabla \times \vec{A}(\vec{x},t). \tag{C.5}$$

### C.1.2 Current sheet model derivation

This section aims to analytically derive the axial and radial components of the field both inside and outside a finite solenoid. A solenoid is a coiled wire, typically cylindrical, which generates a magnetic field when an electric current passes through it. To analyze the magnetic field of a solenoid, one begins by examining the field created by a single current-carrying loop. Given the cylindrical symmetry of a solenoid, it is advantageous to perform additional calculations in cylindrical coordinates $\vec{x} = (\varrho\ \varphi\ z)^\top$.

A given point $P$ is exposed to a magnetic field generated by a loop carrying a current density $\vec{J}$ positioned in the $(x,y)$-plane, as depicted in the diagram to the left in Fig. C.1. At a point $Q$ within this loop, the separation $\overline{PQ}$ can be determined using trigonometric methods as $|\vec{x} - \vec{x}'| = \sqrt{z'^2 + \varrho^2 + r^2 - 2\varrho r \cos\varphi}$. This derivation is sourced from [153]. The solenoid is constructed by integrating the contributions from numerous identical coaxial loops, evenly distributed along its length $L$. For simplification purposes, these

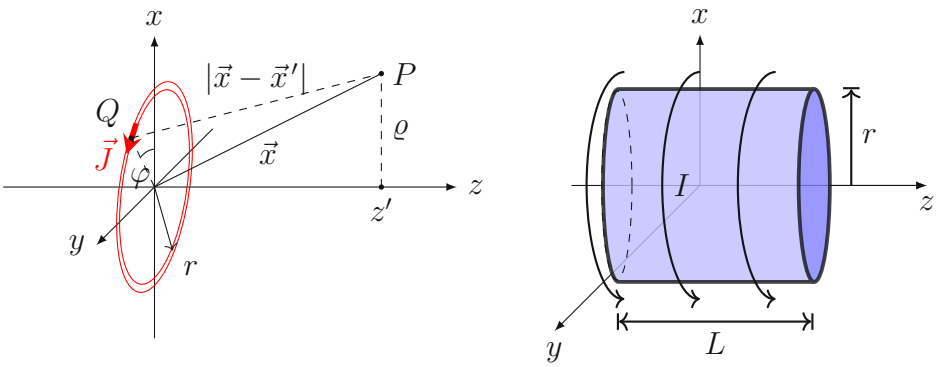


**Figure C.1.: Left**: Distance $|\vec{x}-\vec{x}'|$ between a point $Q$ on a wire loop of radius $r$ and point $P$. **Right**: Multiple coils can be simplified as a single current sheet of length $L$.

loops can be represented as an infinitesimally thin conductive current sheet, illustrated on the right in Fig. C.1. The surface current density of this cylindrical sheet is expressed as

$$J = \frac{I}{L}\delta(r-\varrho')\cos\varphi. \tag{C.6}$$

In Eq. (C.6), $r$ denotes the radius of the sheet, and $\delta$ represents the Dirac-Delta function. The vector potential for this cylindrical current sheet can be determined using Eq. (C.5) with the functional determinant $d^3x' = \varrho' d\varrho'\, d\varphi\, dz'$ and is expressed as

$$A_\varphi = \frac{\mu_0}{4\pi}\frac{I}{L}\int_{-L/2}^{L/2} dz' \int_0^{2\pi} d\varphi \int_0^{\infty} d\varrho' \frac{\varrho'\,\delta(r-\varrho')\,\cos\varphi}{\sqrt{\varrho^2+\varrho'^2+(z-z')^2-2\varrho'\varrho\cos\varphi}}. \tag{C.7}$$

By performing the integration over $\varrho'$, the $\delta$ vanishes, and substituting $\zeta = z - z'$, we obtain

$$A_\varphi = \frac{\mu_0 I r}{2\pi L}\int_{\zeta_-}^{\zeta_+} d\zeta \int_0^{\pi} d\varphi \frac{\cos\varphi}{\sqrt{\varrho^2+r^2+\zeta^2-2r\varrho\cos\varphi}}, \tag{C.8}$$

where the integration bounds are defined as $\zeta_- = z - L/2$ and $\zeta_+ = z + L/2$. Proceeding with the evaluation of the double integral, we have

$$\int_{\zeta_-}^{\zeta_+} d\zeta \int_0^{\pi} d\varphi \frac{\cos\varphi}{\sqrt{\varrho^2+r^2+\zeta^2-2r\varrho\cos\varphi}} = \int_0^{\pi} d\varphi \cos\varphi \left[\ln\left(\zeta+\alpha(\zeta)\right)\right]_{\zeta_-}^{\zeta_+}, \tag{C.9}$$
$$\text{where} \quad \alpha(\zeta) = \sqrt{\varrho^2+r^2+\zeta^2-2r\varrho\cos\varphi}.$$

Next step, the integral of the angle $\varphi$ will be executed where the in partial integration

is performed

$$A_\varphi = \frac{\mu_0}{2\pi}\frac{I\,r}{L}\left[\cancel{\left[\sin\varphi\,\ln\left(\zeta+\alpha(\zeta)\right)\right]_0^\pi} - \int_0^\pi d\varphi\,\sin\varphi\,\ln\left(\zeta+\alpha(\zeta)\right)\right]_{\zeta_-}^{\zeta_+}. \tag{C.10}$$

The initial term of Eq. (C.10) is nullified owing to the inherent asymmetry of the sine function, whereas the subsequent term may be simplified through the application of a mathematical technique as described in [154]. Consequently, the vector potential adjusts to

$$A_\varphi = \frac{\mu_0}{2\pi}\frac{\varrho\,I\,r^2}{L}\left[\zeta\int_0^\pi \frac{\sin^2\varphi\,d\varphi}{(r^2+\varrho^2-2r\varrho\cos\varphi)\sqrt{r^2+\varrho^2+\zeta^2-2r\varrho\cos\varphi}}\right]_{\zeta_-}^{\zeta_+}. \tag{C.11}$$

By implementing the substitution of $\varphi = 2\vartheta$, the form of the integral becomes

$$\begin{aligned}&\int_0^\pi \frac{\sin^2\varphi\,d\varphi}{(r^2+\varrho^2-2r\varrho\cos\varphi)\sqrt{r^2+\varrho^2+\zeta^2-2r\varrho\cos\varphi}}\\ &=\int_0^{\frac{\pi}{2}} \frac{8\left(\sin^2\vartheta-\sin^4\vartheta\right)d\vartheta}{\left[(\varrho+r)^2-4r\varrho\sin^2\vartheta\right]\sqrt{(\varrho+r)^2+\zeta^2-4r\varrho\sin^2\vartheta}}.\end{aligned} \tag{C.12}$$

At this juncture, the new variables will be introduced

$$\begin{aligned}k^2 &= \frac{4\varrho\,r}{(\varrho+r)^2},\\ h^2 &= \frac{4\varrho\,r}{(\varrho+r)^2+\zeta^2},\end{aligned} \tag{C.13}$$

with the result that the integral in Eq. (C.12) is simplified to

$$\frac{h^2k}{\sqrt{r\varrho}^3}\int_0^{\frac{\pi}{2}} \frac{8\left(\sin^2\vartheta-\sin^4\vartheta\right)d\vartheta}{\left(1-h^2\sin^2\vartheta\right)\sqrt{1-k^2\sin^2\vartheta}}, \tag{C.14}$$

which can be resolved using complete elliptical integrals. In the context of elliptic integrals, "complet" refers to evaluating the integral over the full range of the independent variable, typically from 0 to $\pi/2$. Complete elliptic integrals are special functions that arise in the study of the arc length of ellipses and other problems in mathematical

physics. They are categorized into three types of complete elliptic integrals:

$$\begin{aligned}\text{First kind:}\quad K(k^2) &= \int_0^{\frac{\pi}{2}} \frac{d\vartheta}{\sqrt{1-k^2\sin^2\vartheta}},\\ \text{Second kind:}\quad E(k^2) &= \int_0^{\frac{\pi}{2}} \sqrt{1-k^2\sin^2\vartheta}\,d\vartheta,\\ \text{Third kind:}\quad \Pi(h^2,k^2) &= \int_0^{\frac{\pi}{2}} \frac{d\vartheta}{\left(1-h^2\sin^2\vartheta\right)\sqrt{1-k^2\sin^2\vartheta}}.\end{aligned} \tag{C.15}$$

Improved numerical calculations of these integrals are documented in [59, 155].

$$A_\varphi = \frac{\mu_0 I}{2\pi L}\sqrt{\frac{r}{\varrho}}\left[\zeta\, k\left(K(k^2)\frac{h^2+k^2-h^2k^2}{h^2k^2} - E(k^2)\frac{1}{k^2} + \frac{h^2-1}{h^2}\Pi(h^2,k^2)\right)\right]_{\zeta_-}^{\zeta_+} \tag{C.16}$$

which full derivation is over viewed in appendix C.1.2. **Curl in cylinder coordinates**

$$\nabla\times\vec{F} = \begin{pmatrix} \frac{1}{r}\frac{\partial F_z}{\partial\varphi} - \frac{\partial F_\varphi}{\partial z} \\ \frac{\partial F_r}{\partial z} - \frac{\partial F_z}{\partial r} \\ \frac{1}{r}\frac{\partial (r F_r)}{\partial r} - \frac{1}{r}\frac{\partial F_r}{\partial\varphi} \end{pmatrix} \tag{C.17}$$

follows to

$$B_\varrho = -\frac{\partial A_\varphi}{\partial\zeta},\quad B_\varphi = 0,\quad B_z = \frac{1}{\varrho}\frac{\partial}{\partial\varrho}(\varrho\, A_\varphi) \tag{C.18}$$

Evaluating the derivatives of elliptical integrals with respect to $\zeta$ and $\varrho$ is not a simple task, yet these can be readily found in literature.

$$B_\varrho = \frac{\mu_0 I}{2\pi L}\sqrt{\frac{r}{\varrho}}\left[\frac{k^2-2}{k}K(k^2) + \frac{2}{k}E(k^2)\right]_{\zeta_-}^{\zeta_+} \tag{C.19}$$

Special attention is required when $\varrho = 0$ in Eq. (C.19), resulting in $B_\varrho = 0$. Furthermore, when $\varrho = r$ and $z = \pm L/2$, the radial B field vanishes, indicating the edges of the sheet.

$$B_z = \frac{\mu_0 I}{4\pi L}\frac{1}{\sqrt{r\varrho}}\left[\zeta\, k\left(K(k^2) + \frac{\varrho - r}{r+\varrho}\Pi(h^2,k^2)\right)\right]_{\zeta_-}^{\zeta_+} \tag{C.20}$$

According to Eq. (C.20), the axial field components are zero when $r = \varrho$. Field maps for both axial and radial components are depicted in Fig. C.2. When $\varrho = 0$, Eq. (C.20) reduces to the on-axis longitudinal field:

$$B_z(\varrho = 0) = \frac{\mu_0 I}{2L}\left(\frac{z + L/2}{\sqrt{r^2 + (z+L/2)^2}} - \frac{z - L/2}{\sqrt{r^2 + (z-L/2)^2}}\right) \tag{C.21}$$

In the finite current sheet model, it was presumed that the sheet had an infinitesimally

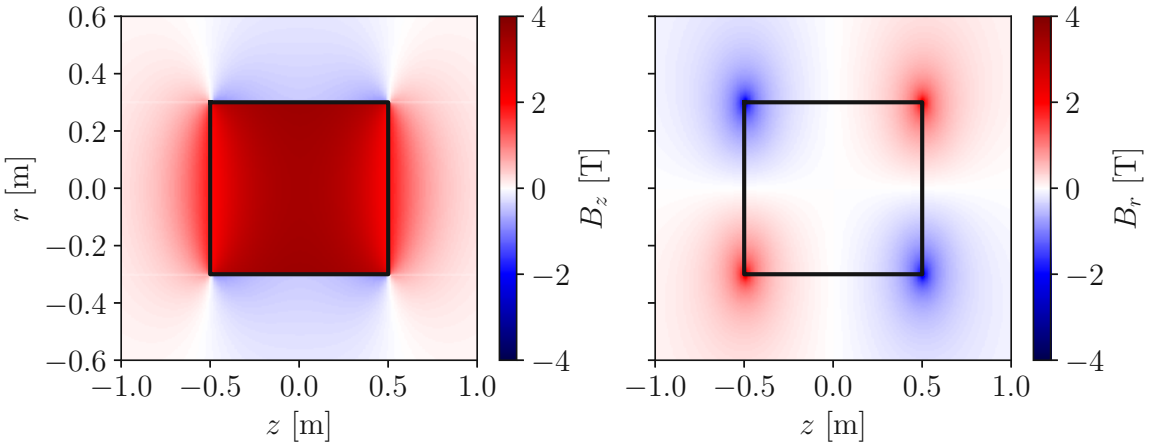


**Figure C.2.:** The maps illustrate the spatial distribution of both radial (**left**) and axial (**right**) field components.

small size. As illustrated in Fig. C.3, the field lines curl around the sheet, and the total magnetic field's intensity amplifies as it approaches the symmetry axis within the current sheet.

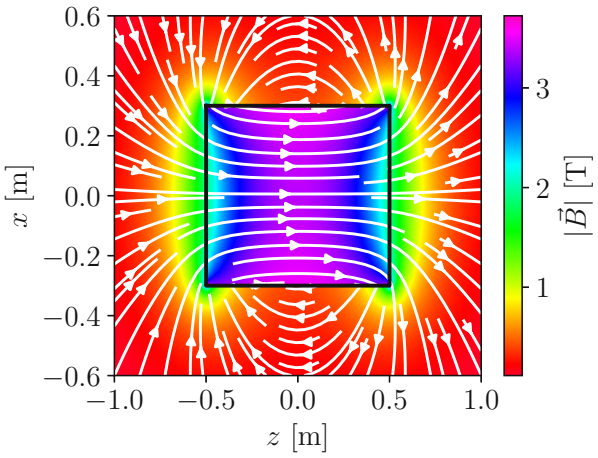


**Figure C.3.:** Magnetic field lines curling around the finite current sheet, with the total magnetic field intensity increasing toward the symmetry axis.

## C.2 Hamiltonian of solenoids

The Hamiltonian for a particle carrying charge $q$ within a relativistic framework is delineated in the context of an electromagnetic field. It is denoted as

$$H(x, p_x, y, p_y, s, p_s; t) = \sqrt{c^2 \left(\vec{P} - \frac{e}{c}\vec{A}\right)^2 + m_0^2 c^4} + e\Phi, \tag{C.22}$$

where $\Phi$ represents the electric field potential and $\vec{A}$ signifies the vector potential from the magnetic field. The canonical momentum is defined as

$$\vec{P} = m\vec{v} + e\vec{A} = \beta\gamma m_0 c + e\vec{A}, \tag{C.23}$$

where $m_0$ is the mass of the particle in its rest frame. Eq. (C.23) differs from the kinetic momentum $m\vec{v}$. As stated in Wolski's textbook [117], a series of transformations are performed on Eq. (C.22), which will be subsequently listed:

- Change the independent time variable $t$ to the spatial variable $s$.
- Express the longitudinal coordinates of time as

$$z = \frac{s}{\beta} - ct, \quad \tilde{\delta} = \frac{E}{c\beta} - \frac{1}{\beta}. \tag{C.24}$$

- Scaling Eq. (C.22) by applying the paraxial approximation

$$\tilde{H} = \frac{H}{p_0}, \quad \vec{a} = \frac{e}{p_0}\vec{A}, \quad \tilde{p}_{x,y} = \frac{P_{x,y}}{p_0} = \frac{p_{x,y} + eA_{x,y}}{p_0}. \tag{C.25}$$

The Hamiltonian subsequently assumes the form

$$\tilde{H}(x, \tilde{p}_x, y, \tilde{p}_y, z, \tilde{\delta}; s) = \frac{\tilde{\delta}}{\beta} - \sqrt{\left(\tilde{\delta} + \frac{1}{\beta}\right)^2 - (\tilde{p}_x - a_x)^2 - (\tilde{p}_y - a_y)^2 - \frac{1}{\beta^2\gamma^2}}. \tag{C.26}$$

The Hamiltonian of Eq. (C.26) is non-linear. The paraxial approximation $\tilde{p}_{x,y} \ll 1$ allows the construction of the linearized version of Eq. (C.26). Considering the field of a simplified solenoid with only a longitudinal and static component $\vec{B} = (0,\ 0,\ B_0)^\top$, the Eq. (4.1) simplifies in Cartesian coordinate to

$$\vec{A} = \left(-\tfrac{B_0}{2}y,\quad \tfrac{B_0}{2}x,\quad 0\right)^\top. \tag{C.27}$$

Substituting Eq. (C.27) into Eq. (C.26) and linearize it yields to the second order Hamiltonian

$$\tilde{H}_2 = \frac{p_x^2}{2} + \frac{p_y^2}{2} + \frac{\delta^2}{2\beta^2\gamma^2} + \frac{\kappa^2 x^2}{2} + \frac{\kappa^2 y^2}{2} - \kappa(xp_y + yp_x), \tag{C.28}$$

where kappa is $\kappa = cB_0/2p_0$.

## C.3 Normalized transverse emittance rate equation

The derivative of the normalized emittance in the transverse space with respect to the reference orbit $s$ results in two terms

$$\frac{d}{ds}\varepsilon_{\perp,\mathrm{N}} = \varepsilon_\perp \frac{d(\beta\gamma)}{ds} + \beta\gamma\frac{d\varepsilon_\perp}{ds}. \tag{C.29}$$

The first term in Eq. (C.29) involves the derivative of the Lorentz factors, expressed using relativistic kinematics

$$\frac{d(\beta\gamma)}{ds} = \frac{1}{mc^2}\frac{d(pc)}{ds} = \frac{1}{mc^2}\frac{d}{ds}\sqrt{E^2 - m^2c^4} = \frac{1}{\beta\cdot mc^2}\frac{dE}{ds}. \tag{C.30}$$

The change of the beam energy follows the Bethe formula in Eq. (3.17). The second term is

$$\frac{d\varepsilon_\perp}{ds} = \frac{d}{ds}\sqrt{\det\boldsymbol{\Sigma}} = \frac{1}{2\varepsilon_\perp}\left(\sigma_{x'}^2\frac{d\sigma_x^2}{ds} + \sigma_x^2\frac{d\sigma_{x'}^2}{ds} - 2\sigma_{xx'}\frac{d\sigma_{xx'}}{ds}\right). \tag{C.31}$$

The assumptions include the beam in an absorber within a solenoid with a strong, homogeneous magnetic field along the longitudinal direction. The beam is matched with the machine ellipse of the solenoid, which nullifies $\sigma_{xx'}$ and $d\sigma_x^2/ds$. Therefore, the remaining term in Eq. (C.31) is the change in transverse angular distribution, where $\sigma_{x'}^2$ represents small angle deflections of the muon caused by Coulomb scattering. Finally, the cooling equation results in

$$\frac{d\varepsilon_{\perp,\mathrm{N}}}{ds} = -\frac{\varepsilon_{\perp,\mathrm{N}}}{E\beta^2}\left\langle\frac{\partial E}{\partial s}\right\rangle + \beta\gamma\frac{\beta_\perp}{2}\frac{d\sigma_{x'}^2}{ds}. \tag{C.32}$$

# Bibliography


[1] F. Tikhonin and G. Budker, "On the effects with muon colliding beams," *JINR Report P2-4120 (Dubna, 1968)*, 1968.

[2] G. I. Budker, "An effective method of damping particle oscillations in proton and antiproton storage rings," *Soviet Atomic Energy*, vol. 22, pp. 438–440, May 1967.

[3] G. I. Budker, "Proceedings of the 7th internationalconference on high-energy accelerators," Academy of Sciences of Armenia, Yerevan,1970, 1969.

[4] D. Cline and D. Neuffer, "A muon storage ring for neutrino oscillations experiments," in *AIP Conference Proceedings Volume 68*, p. 856–857, AIP, 1980.

[5] G. Aad *et al.*, "Observation of a new particle in the search for the standard model Higgs boson with the ATLAS detector at the LHC," *Physics Letters B*, vol. 716, p. 1–29, Sept. 2012.

[6] S. Chatrchyan *et al.*, "Observation of a new boson at a mass of 125 GeV with the CMS experiment at the LHC," *Physics Letters B*, vol. 716, p. 30–61, Sept. 2012.

[7] M. Thomson, *Modern Particle Physics*. Cambridge University Press, Sept. 2013.

[8] W. Demtröder, *Experimentalphysik 4*. Springer Berlin Heidelberg, 2017.

[9] F. Zwicky, "Die Rotverschiebung von extragalaktischen Nebeln," *Helvetica Physica Acta, Vol. 6, p. 110-127*, vol. 6, pp. 110–127, 1933.

[10] V. C. Rubin and W. K. Ford Jr, "Rotation of the andromeda nebula from a spectroscopic survey of emission regions," *Astrophysical Journal, vol. 159, p. 379*, vol. 159, p. 379, 1970.

[11] S. Perlmutter *et al.*, "Measurements of $\omega$ and $\lambda$ from 42 high-redshift supernovae," *The Astrophysical Journal*, vol. 517, no. 2, p. 565, 1999.

[12] A. G. Riess *et al.*, "Observational evidence from supernovae for an accelerating universe and a cosmological constant," *The astronomical journal*, vol. 116, no. 3, p. 1009, 1998.

[13] A. Linde, "Particle physics and inflationary cosmology," vol. 5, 1990.

[14] B. S. DeWitt, "Quantum theory of gravity. i. the canonical theory," *Physical Review*, vol. 160, no. 5, p. 1113, 1967.

[15] G. Arcadi, A. Djouadi, and M. Raidal, "Dark matter through the higgs portal," *Physics Reports*, vol. 842, p. 1–180, Feb. 2020.

[16] M. Ruhdorfer, E. Salvioni, and A. Weiler, "A global view of the off-shell Higgs portal," *SciPost Phys.*, vol. 8, p. 027, 2020.

[17] M. Reichert *et al.*, "Probing baryogenesis through the higgs boson self-coupling," *Physical Review D*, vol. 97, apr 2018.

[18] R. K. Ellis *et al.*, "Physics Briefing Book: Input for the European Strategy for Particle Physics Update 2020," tech. rep., Geneva, 2019.

[19] O. Brüning and L. Rossi, *The High Luminosity Large Hadron Collider: The New Machine for Illuminating the Mysteries of Universe*. WORLD SCIENTIFIC, Feb. 2015.

[20] I. Agapov *et al.*, "Future Circular Lepton Collider FCC-ee: Overview and Status," 3 2022.

[21] H. Yang, "Status of the cepc project," in *Proceedings of 42nd International Conference on High Energy Physics — PoS(ICHEP2024)*, ICHEP2024, p. 821, Sissa Medialab, Jan. 2025.

[22] A. P. Blondel, F. Zimmermann, M. Koratzinos, and M. Zanetti, "LEP3: A High Luminosity $e^+e^-$ Collider in the LHC Tunnel to Study the Higgs Boson," in *3rd International Particle Accelerator Conference*, 5 2012.

[23] M. J. Boland *et al.*, *Updated baseline for a staged Compact Linear Collider*. CERN Yellow Reports: Monographs, Geneva: CERN, 2016. Comments: 57 pages, 27 figures, 12 tables.

[24] "The International Linear Collider Technical Design Report - Volume 1: Executive Summary," 6 2013. arxiv.org/abs/1306.6327.

[25] C. Accettura *et al.*, "Towards a muon collider," *The European Physical Journal C*, vol. 83, Sept. 2023.

[26] B. Stechauner, "First study of beam-beam interactions," in *IMCC and MuCol Annual Meeting 2024*, CERN, 2024.

[27] R. Taylor, A. Chance, D. Giove, N. Milas, R. Losito, D. Lucchesi, C. Rogers, L. Rossi, and D. Schulte, "Preliminary parameters," 2024. https://zenodo.org/doi/10.5281/zenodo.13970100.

[28] FCC collaboration, "FCC-hh: the hadron collider: future circular collider conceptual design report volume 3," *European Physical Journal Special Topics*, vol. 228, no. 4, pp. 755–1107, 2019.

[29] A. C. Canbay *et al.*, "SppC based energy frontier lepton-proton colliders: Luminosity and physics," *Advances in High Energy Physics*, vol. 2017, no. 1, p. 4021493, 2017.

[30] K. Long *et al.*, "Muon colliders to expand frontiers of particle physics," *Nature Physics*, vol. 17, no. 3, pp. 289–292, 2021.

[31] O. Amram and G. Cummings, "United states early career researchers in collider physics input to the european strategy for particle physics update," 2025. https://arxiv.org/abs/2503.22834.

[32] J. P. Delahaye *et al.*, "Muon colliders," 2019. arxiv.org/abs/1901.06150.

[33] S. Johannesson *et al.*, "Initial design of a proton complex for the Muon Collider," *JACoW IPAC*, vol. 2024, p. WEPR24, 2024.

[34] F. Saura *et al.*, "Muon Collider Graphite Target Studies and Demonstrator Layout Possibilities at CERN," *JACoW IPAC*, vol. 2022, pp. 2895–2898, 2022.

[35] C. T. Rogers *et al.*, "Muon front end for the neutrino factory," *Physical Review Special Topics - Accelerators and Beams*, vol. 16, Apr. 2013.

[36] D. Stratakis and R. B. Palmer, "Rectilinear six-dimensional ionization cooling channel for a muon collider: A theoretical and numerical study," *Phys. Rev. ST Accel. Beams*, vol. 18, p. 031003, Mar 2015.

[37] Y. Bao, G. Hanson, R. B. Palmer, and D. Stratakis, "Conceptual design and modeling of a six-dimensional bunch merging scheme for a muon collider," *Physical Review Accelerators and Beams*, vol. 19, Mar. 2016.

[38] A. Chance *et al.*, "Parameter ranges for a chain of rapid cycling synchrotrons for a muon collider complex," *JACoW IPAC*, vol. 2023, p. MOPL162, 2023.

[39] K. Skoufaris *et al.*, "First design of a 10 TeV centre of mass energy muon collider," *JACoW IPAC*, vol. 2023, p. MOPL064, 2023.

[40] S. L. territoire Genevoise à la carte Nicole Wiedmann, "Geneva city," 2020.

[41] Global Administrative Areas (GADM), "Database of global administrative areas," 2024. Accessed: 2024-02-07.

[42] swisstopo, "SwissBoundaries3D – Das Landschaftsmodell der Schweiz," 2024. Accessed: 2024-02-07.

[43] K. Jordahl *et al.*, "geopandas/geopandas: v0.8.1," July 2020.

[44] E. MacTavish, "Siting overview: Cern." https://indico.desy.de/event/45968/contributions/186581/, May 2025. Talk presented at the IMCC and MuCol Annual Meeting 2025.

[45] G. Lerner *et al.*, "FLUKA simulations of neutrino-induced effective dose at a Muon Collider," *JACoW IPAC*, vol. 2024, p. WEPR27, 2024.

[46] C. Desponds, "Geoprofiler update and investigation of potential collider placement solution," in *IMCC and MuCol Annual Meeting 2024*, (CERN, Geneva, Switzerland), 2024. https://indico.cern.ch/event/1325963/contributions/5837738/.

[47] C. Accettura *et al.*, *Interim report for the International Muon Collider Collaboration*, vol. 2 of *CERN Yellow Reports: Monographs*. Geneva: CERN, 2024. This document summarises the International Muon Collider Collaboration (IMCC) progress and status of the Muon Collider RD programme.

[48] IMCC Collaboration, "The muon collider: European strategy for particle physics update," *Unpublished Springer*, 2025. https://indico.cern.ch/event/1513450/attachments/3042022/.

[49] H. Eberl, "Einführung in die Modelle der Elementarteilchenphysik 2," 2022. Lecture notes, TU Wien.

[50] J. C. Romão and J. P. Silva, "A resource for signs and feynman diagrams of the standard model," *International Journal of Modern Physics A*, vol. 27, p. 1230025, Oct. 2012.

[51] M. E. Peskin and D. V. Schroeder, *An Introduction to quantum field theory*. Reading, USA: Addison-Wesley, 1995.

[52] K. Cheung and Z. S. Wang, "Physics potential of a muon-proton collider," *Physical Review D*, vol. 103, June 2021.

[53] C. F. v. Weizsaecker, "Ausstrahlung bei Stoessen sehr schneller Elektronen," *Zeitschrift für Physik*, vol. 88, p. 612–625, Sept. 1934.

[54] R. Capdevilla, F. Garosi, D. Marzocca, and B. Stechauner, "Testing the neutrino content of the muon at muon colliders," *Journal of High Energy Physics*, vol. 2025, no. 4, p. 168, 2025.

[55] P. Virtanen *et al.*, "SciPy 1.0: Fundamental Algorithms for Scientific Computing in Python," *Nature Methods*, vol. 17, pp. 261–272, 2020.

[56] D. Marzocca, "LePDF: Lepton Parton Distribution Functions." https://github.com/DavidMarzocca/LePDF, 2023. Accessed: 2025-04-01.

[57] D. Calzolari *et al.*, "Machine-detector interface design for a 10-TeV muon collider," *PoS*, vol. ICHEP2024, p. 819, 2025.

[58] G. Peter Lepage, "A new algorithm for adaptive multidimensional integration," *Journal of Computational Physics*, vol. 27, p. 192–203, May 1978.

[59] W. H. Press, S. A. Teukolsky, W. T. Vetterling, and B. P. Flannery, *Numerical Recipes 3rd Edition: The Art of Scientific Computing*. USA: Cambridge University Press, 3 ed., 2007.

[60] A. Latina, *RF-Track Reference Manual,* `https://gitlab.cern.ch/rf-track`, 2023.

[61] R. Frühwirth, M. Regler, R. Bock, H. Grote, and D. Notz, *Data analysis techniques for high-energy physics; 2nd ed.* Cambridge monographs on particle physics, nuclear physics,and cosmology, Cambridge: Cambridge Univ. Press, 2000.

[62] R. Frühwirth and A. Strandlie, *Pattern Recognition, Tracking and Vertex Reconstruction in Particle Detectors*. Springer International Publishing, 2021.

[63] C. Rogers, "Software mini-workshop." Workshop conducted at CERN, October 2024.

[64] R. Palmer and J. Gallardo, "High luminosity muon collider design," *Conf. Proc. C*, vol. 9608262, pp. 887–891, 1996.

[65] N. V. Mokhov and C. C. James, "The MARS code system user's guide version 15(2016)," 2 2017.

[66] R. C. Fernow, "ICOOL: a simulation code for ionization cooling of muon beams," in *Proc. PAC'99*, pp. 3020–3022, JACoW Publishing, Geneva, Switzerland, 1999.

[67] P. Gruber *et al.*, "The Study of a European Neutrino Factory Complex," tech. rep., CERN, Geneva, 2002.

[68] E. Holzer, "Simulation of the pion decay channel of a neutrino factory," *Nuclear Instruments and Methods in Physics Research Section A: Accelerators, Spectrometers, Detectors and Associated Equipment*, vol. 503, no. 1, pp. 360–362, 2003. Proceedings of the 3rd International Workshop on Neutrino Factories based on Muon Storage Rings.

[69] H. S. Deaven and K. C. Chan, "Computer codes for particle accelerator design and analysis: A compendium. second edition," 5 1990.

[70] G. Penn and J. S. Wurtele, "Beam envelope equations for cooling of muons in solenoid fields," *Physical Review Letters*, vol. 85, p. 764–767, July 2000.

[71] E. B. Holzer, "Figure of merit for muon cooling—an algorithm for particle counting in coupled phase planes," *Nuclear Instruments and Methods in Physics Research Section A: Accelerators, Spectrometers, Detectors and Associated Equipment*, vol. 532, p. 270–274, Oct. 2004.

[72] R. Fernow, *ICOOL Reference Manual*, 2009.

[73] R. Brun and F. Carminati, *Geant3: A Simulation Toolkit for Particle Physics*. CERN, 1994. CERN Program Library Long Writeup W5013.

[74] D. Attwood *et al.*, "The scattering of muons in low-z materials," *Nuclear Instruments and Methods in Physics Research Section B: Beam interactions with materials and atoms*, vol. 251, p. 41–55, Sept. 2006.

[75] R. Fernow, "Physics analysis performed by ecalc9," *NFMCC-doc-280. Sept*, vol. 30, 2003.

[76] T. J. Roberts and D. M. Kaplan, "G4beamline simulation program for matter-dominated beamlines," in *2007 IEEE Particle Accelerator Conference (PAC)*, pp. 3468–3470, 2007.

[77] S. Agostinelli *et al.*, "Geant4— a simulation toolkit," *Nuclear Instruments and Methods in Physics Research Section A: Accelerators, Spectrometers, Detectors and Associated Equipment*, vol. 506, p. 250–303, July 2003.

[78] T. Roberts, *G4beamline Users Guide,* `http://www.gnu.org/copyleft/gpl.html`, 2022.

[79] S. Benedetti, A. Grudiev, and A. Latina, "High gradient linac for proton therapy," *Phys. Rev. Accel. Beams*, vol. 20, p. 040101, 2017.

[80] C. Rossi *et al.*, "The deep electron flash therapy facility," in *Proc. LINAC2024*, 2024.

[81] V. Favaudon *et al.*, "Ultrahigh dose-rate flash irradiation increases the differential response between normal and tumor tissue in mice," *Sci. Transl. Med.*, 2014.

[82] Y. Han *et al.*, "Optimization of the clic positron source using a start-to-end simulation approach involving multiple simulation codes," *Nucl. Instrum. Methods Phys. Res.*, vol. 928, p. 83–88, 2019.

[83] Y. Zhao *et al.*, "Comparison of Different Matching Device Field Profiles for the FCC-ee Positron Source," in *Proc. IPAC'21*, pp. 2617–2620, JACoW Publishing, 2021.

[84] *Python3 reference manual*, 2024. Accessed: 2024-10-14.

[85] *GNU Octave*, 2024. Accessed: 2024-10-14.

[86] V. Mușat, A. Latina, and G. D'Auria, "A high-energy and high-intensity inverse compton scattering source based on compactlight technology," *Photonics*, vol. 9, p. 308, Apr. 2022.

[87] N. F. Mott and H. S. W. Massey, "Theory of atomic collisions," *Theory of Atomic Collisions*, 1933.

[88] H. Bethe, "Zur theorie des durchgangs schneller korpuskularstrahlen durch materie," *Annalen der Physik*, vol. 397, p. 325–400, Jan. 1930.

[89] H. Bethe, "Bremsformel fuer elektronen relativistischer geschwindigkeit," *Zeitschrift füer Physik*, vol. 76, p. 293–299, May 1932.

[90] N. Bohr, "On the theory of the decrease of velocity of moving electrified particles on passing through matter," *Philos. Mag. 25, 10*, Jan. 1913.

[91] N. Bohr, "On the decrease of velocity of swiftly moving electrified particles in passing through matter," *The London, Edinburgh, and Dublin Philosophical Magazine and Journal of Science*, vol. 30, no. 178, pp. 581–612, 1915.

[92] R. L. Workman *et al.*, "Review of particle physics," *Progress of Theoretical and Experimental Physics*, vol. 2022, Aug. 2022.

[93] W. Allison *et al.*, "Ab initioliquid hydrogen muon cooling simulations with elms," *Journal of Physics G: Nuclear and Particle Physics*, vol. 34, p. 679–685, Mar. 2007.

[94] R. C. Fernow, "Scattering in icool," 4 2006.

[95] M. Bogomilov *et al.*, "Demonstration of cooling by the muon ionization cooling experiment," *Nature*, vol. 578, p. 53–59, Feb. 2020.

[96] M. Bogomilov *et al.*, "Performance of the mice diagnostic system," *Journal of Instrumentation*, vol. 16, p. P08046, Aug. 2021.

[97] M. Bogomilov *et al.*, "Multiple coulomb scattering of muons in lithium hydride," *Phys. Rev. D*, vol. 106, p. 092003, Nov 2022.

[98] D. Kaplan, "Private communication," 2024. Personal communication with the author.

[99] R. C. Fernow, *Introduction to Experimental Particle Physics*. Cambridge University Press, Nov. 2022.

[100] R. Fernow, "iCool: A simulation code for ionization cooling, source code," 2011. Last updated in 2013. Available at: https://www.cap.bnl.gov/ICOOL/.

[101] L. Landau, *On the Energy Loss of Fast Particles by Ionisation*. J.Phys.(USSR) 8 (1944) 201, 1944.

[102] P. V. Vavilov, "Ionization losses of high-energy heavy particles," *Sov. Phys. JETP*, vol. 5, pp. 749–751, 1957.

[103] U. Fano, "Penetration of protons, alpha particles, and mesons," *Annual Review of Nuclear Science*, vol. 13, p. 1–66, Dec. 1963.

[104] G. Moliere, "Theorie der streuung schneller geladener teilchen i. einzelstreuung am abgeschirmten coulomb-feld," *Zeitschrift für Naturforschung A*, vol. 2, p. 133–145, Mar. 1947.

[105] H. A. Bethe, "Molière's theory of multiple scattering," *Physical Review*, vol. 89, p. 1256–1266, Mar. 1953.

[106] W. T. Scott, "The theory of small-angle multiple scattering of fast charged particles," *Reviews of Modern Physics*, vol. 35, p. 231–313, Apr. 1963.

[107] G. R. Lynch and O. I. Dahl, "Approximations to multiple coulomb scattering," *Nuclear Instruments and Methods in Physics Research Section B: Beam Interactions with Materials and Atoms*, vol. 58, p. 6–10, May 1991.

[108] V. L. Highland, "Some practical remarks on multiple scattering," *Nuclear Instruments and Methods*, vol. 129, p. 497–499, nov 1975.

[109] B. Rossi and K. Greisen, "Cosmic-ray theory," *Reviews of Modern Physics*, vol. 13, p. 240–309, Oct. 1941.

[110] J. D. Jackson, *Classical electrodynamics; 2nd ed.* New York, NY: Wiley, 1975.

[111] T. Carlisle, J. Cobb, and D. Neuffer, "Multiple Scattering Measurements in the MICE Experiment," *Conf. Proc. C*, vol. 1205201, pp. 1419–1421, 2012.

[112] T. Carlisle, *Step IV of the muon ionization cooling experiment (MICE) and the multiple scattering of muons.* PhD thesis, Oxford University, UK, 2013.

[113] G. Wentzel, "Zwei Bemerkungen ueber die Zerstreuung korpuskularer Strahlen als Beugungserscheinung," *Zeitschrift füer Physik*, vol. 40, p. 590–593, Aug. 1926.

[114] R. Frühwirth and M. Liendl, "Mixture models of multiple scattering: computation and simulation," *Computer Physics Communications*, vol. 141, p. 230–246, Nov. 2001.

[115] R. Frühwirth and M. Regler, "On the quantitative modelling of core and tails of multiple scattering by gaussian mixtures," *Nuclear Instruments and Methods in Physics Research Section A: Accelerators, Spectrometers, Detectors and Associated Equipment*, vol. 456, p. 369–389, Jan. 2001.

[116] R. Frühwirth and M. Regler, *Modelling of Multiple Scattering Distributions by Mixture Models*, p. 571–576. Springer Berlin Heidelberg, 2001.

[117] A. Wolski, *Beam Dynamics in High Energy Particle Accelerators.* WORLD SCIENTIFIC, 2nd ed., 2023.

[118] S. Y. Lee, *Accelerator Physics*. WORLD SCIENTIFIC, Nov. 2011.

[119] F. Hinterberger, *Physik der Teilchenbeschleuniger und Ionenoptik*. Springer Berlin Heidelberg, 1997.

[120] E. Courant and H. Snyder, "Theory of the alternating-gradient synchrotron," *Annals of Physics*, vol. 3, p. 1–48, Jan. 1958.

[121] R. Q. Twiss and N. Frank, "Orbital stability in a proton synchrotron," *Review of Scientific Instruments*, vol. 20, no. 1, pp. 1–17, 1949.

[122] M. Sands, "Physics of electron storage rings: An introduction.," tech. rep., SLAC National Accelerator Lab., Menlo Park, CA (United States), 1970.

[123] D. A. Edwards and L. C. Teng, "Parametrization of linear coupled motion in periodic systems," *IEEE Transactions on Nuclear Science*, vol. 20, no. 3, pp. 885–888, 1973.

[124] B. Stechauner, "Final cooling scheme for muon colliders: a door opener for future discovery machines," 2021. Presented 16 Dec 2021.

[125] G. Penn, "Muon capture and cooling dynamics, capture in solenoidal channels," in *PACS2001. Proceedings of the 2001 Particle Accelerator Conference (Cat. No. 01CH37268)*, vol. 1, pp. 132–136, IEEE, 2001.

[126] G. Penn and J. Wurtele, "Simulation of the ionization cooling of muons in linear rf systems," in *Electronic Conference Proceedings C*, p. TH203, 2000.

[127] D. Neuffer, "Principles and applications of muon cooling," in *Proceedings of the Third LAMPF II Workshop: Los Alamos National Laboratory, Los Alamos, New Mexico, July 18-28, 1983*, vol. 1, p. 470, Los Alamos National Laboratory, 1983.

[128] P. B. Jurj, *Normalised transverse emittance reduction via ionisation cooling in MICE'Flip Mode'*. PhD thesis, Imperial College London, 2022.

[129] D. Neuffer, "Low-energy ionization cooling of ions for beta beam sources," *Nuclear Instruments and Methods in Physics Research Section A: Accelerators, Spectrometers, Detectors and Associated Equipment*, vol. 585, no. 3, pp. 109–116, 2008.

[130] H. Bichsel and R. P. Saxon, "Comparison of calculational methods for straggling in thin absorbers," *Physical Review A*, vol. 11, no. 4, p. 1286, 1975.

[131] R. B. Palmer, R. C. Fernow, and J. L. Lederman, "Muon Collider Final Cooling in 30-50 T Solenoids," *Conf. Proc. C*, vol. 110328, pp. 2061–2063, 2011.

[132] H. Sayed, R. B. Palmer, and D. Neuffer, "High field – low energy muon ionization cooling channel," *Phys. Rev. ST Accel. Beams*, vol. 18, p. 091001, Sep 2015.

[133] I. H. Bell, J. Wronski, S. Quoilin, and V. Lemort, "Pure and pseudo-pure fluid thermophysical property evaluation and the open-source thermophysical property library coolprop," *Industrial & Engineering Chemistry Research*, vol. 53, no. 6, pp. 2498–2508, 2014.

[134] W. Demtröder, *Experimentalphysik 1: Mechanik und Wärme*. Springer Berlin Heidelberg, 2021.

[135] A. V. Shestakov, S. V. Stankus, and N. A. Krasnikova, "Thermal conductivity of lithium hydride in the temperature range 6–399 k," *High Temperature*, vol. 7, no. 5, pp. 828–830, 1969. Data retrieved via INIS (International Nuclear Information System).

[136] B. Bordini *et al.*, "Conceptual design of a ReBCO non/metal-insulated ultra-high field solenoid for the muon collider," *IEEE Transactions on Applied Superconductivity*, vol. PP, pp. 1–12, 05 2024.

[137] J. A. Nelder and R. Mead, "A simplex method for function minimization," *The Computer Journal*, vol. 7, p. 308–313, Jan. 1965.

[138] C. Rogers, "Private communication," July 2024. Didcot.

[139] V. Balbekov *et al.*, "Double field flip cooling channel for the neutrino factory," *PACS2001. Proceedings of the 2001 Particle Accelerator Conference*, vol. 5, pp. 3870–3872 vol.5, 2001.

[140] V. Balbekov, "Comparison of alternate solenoid and long solenoid cooling channels," *Nuc. Inst. Meth. in Phys. Res. Sec. A*, vol. 472, p. 571–576, Oct. 2001.

[141] K. Wille, *The physics of particle accelerators: an introduction,*. Oxford Univ. Press, 2009.

[142] G. Penn, "Muon capture and cooling dynamics, capture in solenoidal channels," in *PACS2001. Proceedings of the 2001 Particle Accelerator Conference (Cat. No.01CH37268)*, vol. 1 of *PAC-01*, p. 132–136, IEEE, 2001.

[143] H. Padamsee, T. Hays, and J. Knobloch, *RF superconductivity for accelerators*. Wiley series in beam physics and accelerator technology, New York, NY: Wiley, 1998.

[144] J. A. Ferreira, "Absorbers (and windows) for final cooling," *Muon coolider annual meeting 2024*, 2024.

[145] P. T. Torma *et al.*, "Performance and properties of ultra-thin silicon nitride x-ray windows," *IEEE Transactions on Nuclear Science*, vol. 61, p. 695–699, Feb. 2014.

[146] V. Giovinco *et al.*, "Innovative bulge test setup to characterize thin beam vacuum windows," *JACoW*, vol. IPAC2024, p. WEPR33, 2024.

[147] H. Damerau, "Rf manipulations i. cas course on," *CAS proceedings*, 2023.

[148] W. Herr and B. Muratori, "Concept of luminosity," 2006.

[149] M. Pivi, "Beam-beam effects in particle collider," 2011. US Particle Accelerator School.

[150] R. W. Brown, D. Sahdev, and K. O. Mikaelian, "$W^{\pm}Z^0$ and $W^{\pm}\gamma$ pair production in $\nu e$, pp, and $\overline{p}p$ collisions," *Physical Review D*, vol. 20, p. 1164–1174, Sept. 1979.

[151] A. A. et al. (FCC Collaboration), "FCC-ee: The lepton collider - future circular collider conceptual design report volume 2," *Eur. Phys. J. ST*, vol. 228, pp. 261–623, 2019.

[152] CEPC Study Group, "CEPC Conceptual Design Report: Volume 2 - Physics & Detector," *arXiv e-prints*, 2018.

[153] E. E. Callaghan and S. H. Maslen, "The magnetic field of a finite solenoid," 10 1960.

[154] Wordpress.com, "Finite length solenoid potential and field," *NuclearPhysics101*, 2011.

[155] B. C. Carlson, "Numerical computation of real or complex elliptic integrals," *Numerical Algorithms*, vol. 10, p. 13–26, Mar. 1995.